



INVESTIGATION INTO LASER SELF-MIXING FOR  
ACCELERATOR APPLICATIONS

Thesis submitted in accordance with the requirements of  
the University of Liverpool for the degree of Doctor in Philosophy by

**Alexandra Alexandrova**

March 2017



# Contents

<b>Notations</b>	<b>xi</b>
<b>Abstract</b>	<b>xiii</b>
<b>Acknowledgements</b>	<b>xv</b>
<b>1 Self-Mixing Technique</b>	<b>1</b>
1.1 Introduction . . . . .	1
1.2 Optical Diagnostics . . . . .	2
1.2.1 Interferometry . . . . .	2
1.2.2 Particle Imaging Velocimetry (PIV) . . . . .	3
1.2.3 Laser Doppler Velocimetry (LDV) . . . . .	5
1.3 The Sources of Light in Laser Doppler Velocimetry . . . . .	7
1.3.1 Laser Light and its Properties . . . . .	7
1.3.2 Semiconductor Lasers: Bandgap . . . . .	9
1.3.3 Semiconductor Lasers: Different Types . . . . .	10
1.4 Self-Mixing Effect, or Optical Feedback . . . . .	12
1.4.1 Introduction . . . . .	12
1.4.2 Self-Mixing: Theory . . . . .	13
1.4.3 Free Running State of the Laser . . . . .	14
1.4.4 Lang-Kobayashi Model: Single Mode Laser Diode with Weak Feed- back . . . . .	15
1.4.5 Laser Diode under Optical Feedback (Three-Mirror Cavity Model)	16
1.4.6 Equivalent Cavity Model: Modulation of the Laser Optical Fre- quency . . . . .	17
1.4.7 Laser Diode under the Self-Mixing Effect: Common Case . . . . .	19
1.4.8 Modulation of the Output Power under the Self-Mixing Effect . . . . .	19
1.5 Self-Mixing Interferometry Applications . . . . .	23
1.5.1 Displacement and Vibration Measurement . . . . .	24
1.5.2 Different Reflectivity and Speckles Influence . . . . .	24
1.5.3 Self-Mixing Technique as LDV for Velocity Measurement . . . . .	25
1.5.4 Flow Measurements in Self-Mixing and Seeding Particles . . . . .	26
1.5.5 Coupling of Scattered Light . . . . .	28
1.5.6 Important Laser Parameters for Optical Feedback . . . . .	28
1.5.7 Types of Lasers Used in Self-Mixing Measurements . . . . .	29
1.6 Conclusion . . . . .	30

<b>2</b>	<b>Laser Light Scattering for Self-Mixing Sensors</b>	<b>33</b>
2.1	Light Scattering . . . . .	33
2.1.1	Light Scattering off Motionless Particles . . . . .	34
2.1.2	Light Scattering: Different Seeding Particles for Self-Mixing Sensor Experiments . . . . .	39
2.2	Light Scattered off Moving Particles: Expected Spectrum from an Arbitrary Moving Target . . . . .	47
2.2.1	Introduction . . . . .	47
2.2.2	Expected Spectrum of Light Scattered off Rotating Targets . . . . .	49
2.2.3	Spectrum of the Scattered Light from a Rotating Target when the Target is at an Angle . . . . .	51
2.2.4	Self-Mixing Velocimeter: Flow Measurements . . . . .	52
2.2.5	Signal Spectrum of Scattered Light from a Fluid . . . . .	53
2.2.6	Simulation (Model Application): the Influence of the Distribution of Velocities within the Measured Area . . . . .	55
2.2.7	Model Application: the Influence of the Waist Beam Size within the Measuring Area on the Spectrum . . . . .	58
2.3	Conclusion . . . . .	63
<b>3</b>	<b>Application of the Self-Mixing Technique to Solid Targets</b>	<b>65</b>
3.1	Light Sources for Self-Mixing Measurements . . . . .	65
3.1.1	Introduction . . . . .	65
3.1.2	Optical Bandwidth Measurements . . . . .	67
3.1.3	Detection Schemes in the Self-Mixing Technique . . . . .	70
3.2	Application of Self-Mixing Technique to Solid Targets . . . . .	72
3.2.1	Set-up Description . . . . .	72
3.2.2	Signal Processing for Velocity Measurements . . . . .	73
3.3	Application of the Self-Mixing Technique to a Translational Stage . . . . .	75
3.3.1	Different Regimes of the Self-Mixing Signal . . . . .	75
3.3.2	Self-Mixing for Displacement Measurements . . . . .	80
3.3.3	Mirror and White Paper on a Translation Stage: Reflectivity Effect	82
3.3.4	Mirror and White Paper on a Translation Stage: Velocity and Distance Variation . . . . .	83
3.3.5	The Influence of Different Levels of Feedback on the Spectra . . . . .	85
3.3.6	Self-mixing Velocimeter Based on 1550 nm Laser . . . . .	86
3.4	The Self-Mixing Technique with a Rotating Target of Low Reflectivity . . . . .	88
3.4.1	Set-up Description . . . . .	88
3.4.2	Rotating Target with Low Reflectivity: Spectra . . . . .	89
3.4.3	Variation of the Target Angular Velocity with a Fixed Position of the Laser Spot . . . . .	92
3.4.4	Variation of the Position of the Laser Spot with a Fixed Angular Velocity . . . . .	94
3.4.5	Variation of the Angle between Laser Axis and Velocity Vector . . . . .	94
3.4.6	Other Contribution to the Spectra . . . . .	96
3.4.7	Studies into the Accuracy of Velocity Measurements . . . . .	96
3.4.8	Discussion . . . . .	98
3.5	Application of Self-Mixing Sensors for Accelerators . . . . .	99

3.6	Conclusion . . . . .	101
<b>4</b>	<b>Self-Mixing Technique Applied to Fluids</b>	<b>103</b>
4.1	Introduction . . . . .	103
4.2	Fluid as a Target . . . . .	104
4.2.1	Set-up Description . . . . .	104
4.2.2	Milk and Titanium Dioxide as Seeders: Verification of the Measurements . . . . .	105
4.3	Effects of Variation of Different Parameters of the Flow . . . . .	107
4.3.1	Velocity of the Laminar Flow . . . . .	108
4.3.2	The Shape of the Spectrum . . . . .	108
4.3.3	Concentration of the Seeding Materials . . . . .	111
4.3.4	Size of Seeding Materials . . . . .	115
4.3.5	Focus Point of the Laser Light . . . . .	118
4.3.6	Angle Variation . . . . .	124
4.3.7	Water without Seeders . . . . .	127
4.3.8	Flow Velocity Profile Measurements and Resolution Discussion . . . . .	127
4.4	On the Properties of Spectra from an SM Sensor . . . . .	129
4.5	Application in Accelerators . . . . .	135
4.6	Conclusion . . . . .	136
<b>5</b>	<b>Gas Jets in Accelerators and Their Characterisation</b>	<b>139</b>
5.1	Gas Jets . . . . .	139
5.1.1	Gas Jets: Basic Definitions . . . . .	139
5.1.2	Application of Gas Jets in Accelerators . . . . .	141
5.2	Gas Jets for Beam Diagnostic . . . . .	143
5.2.1	Beam Diagnostics: Gas Jet Set-up . . . . .	143
5.2.2	Currently Used Methods for Characterisation of the Gas Jet . . . . .	144
5.2.3	Installation of the Self-Mixing Sensor into the Existing Set-up . . . . .	145
5.2.4	Self-mixing Technique: Expected Backscattered Light in Gas jets . . . . .	148
5.3	Conclusion . . . . .	151
<b>6</b>	<b>Conclusion and Outlook</b>	<b>153</b>
6.1	Conclusion . . . . .	153
6.2	Outlook . . . . .	156
<b>A</b>	<b>Characterisation of Gas Jets</b>	<b>159</b>
A.0.1	Characterisation of Gas Jets . . . . .	159
	<b>Bibliography</b>	<b>165</b>



# Illustrations

## List of Figures

1.1	Interferometers . . . . .	2
1.2	Particle Imaging Velocimetry . . . . .	4
1.3	Schematic representation of the optical Doppler velocimetry . . . . .	6
1.4	Variety of semiconductor lasers: bandgap energy and bandgap wavelength as a function of the lattice constant . . . . .	10
1.5	Output power and wavelength dependence on the injected current for the DFB laser diode . . . . .	11
1.6	Different geometries of lasers . . . . .	12
1.7	Schematic representation of the laser diode . . . . .	14
1.8	Solution of the phase equation for different levels of feedback . . . . .	20
1.9	Simulation of the emitted optical power modulation for weak and moderate feedback . . . . .	21
1.10	Simulation of the emitted optical power modulation for strong feedback . . . . .	22
1.11	Shapes of the self-mixing signal for different levels of feedback . . . . .	22
2.1	Light scattering scheme . . . . .	34
2.2	Schematic representation of Mie theory . . . . .	36
2.3	Mie efficiency function for a wavelength of 650 nm for 0 absorption coefficient . . . . .	38
2.4	Mie efficiency function for a wavelength of 650 nm for different refractive indices . . . . .	40
2.5	Complex refractive index for $\text{TiO}_2$ and Ag . . . . .	41
2.6	Angular distribution of the scattered power . . . . .	42
2.7	Calculated Mie efficiency functions for $\text{TiO}_2$ . . . . .	43
2.8	Calculated Mie efficiency functions dependence on wavelength for $\text{TiO}_2$ . . . . .	44
2.9	Backscattering efficiency distribution for Ag . . . . .	46
2.10	Backscattering efficiency distribution for Ag of size 80 nm and 300 nm . . . . .	47
2.11	Geometry of the scattering of laser light beam on rotating ground glass . . . . .	49
2.12	Geometry of the SM system for rotating disc experiments . . . . .	51
2.13	Schematic arrangement for the fluid interaction with an LD for an SM system . . . . .	52
2.14	Schematic representation of the interaction of the laser light with fluid . . . . .	54
2.15	Schematic representation of the different velocities of the points on the disc . . . . .	56
2.16	Simulated spectra for rotating disc as a target for angles of $70^\circ$ and $40^\circ$ . . . . .	57
2.17	Calculation of the spectrum of the light scattered off the target with the narrow velocities distribution . . . . .	59
2.18	Calculation of the spectrum of the light scattered off the target with the wide velocities distribution . . . . .	60
2.19	Schematic interpretation of the interaction of a Gaussian laser beam with fluid . . . . .	61

3.1	Measured spectrum of a DFB laser diode at fixed injection current . . . . .	68
3.2	Measured spectrum of a DFB laser diode at varied injection currents . . . . .	68
3.3	Measured spectra of MQW InGaAsP LD light at room temperature at various injection currents . . . . .	69
3.4	Measured spectra of MQW InGaAsP LD light at room temperature at fixed injection currents . . . . .	70
3.5	Illustration of the layout of the experiments with SM sensor and a target . . .	73
3.6	Influence of discontinuity at the endpoints on the FFT of real signals . . . . .	75
3.7	SM set-up with a mirror on a translation stage as a target . . . . .	76
3.8	First experimental results obtained from the SM set-up . . . . .	76
3.9	Experimentally obtained self-mixing signals for mirror and white paper for various feedback levels . . . . .	78
3.10	Displacement measurement using SM sensor . . . . .	81
3.11	Two types of the light reflection depending on the roughness of the surface . .	82
3.12	Examples of SM signals for a strong feedback for mirror and white paper as targets . . . . .	83
3.13	Velocity measurements for the mirror and the white paper and showed . . . . .	84
3.14	Spectrum of an SM signal for a strong feedback . . . . .	85
3.15	Spectrum of an SM signal for a strong feedback in case of misalignment of the system . . . . .	86
3.16	Set-up used for testing the 1550 nm fibre-based laser . . . . .	86
3.17	Examples of SM signals for different types of fibres . . . . .	87
3.18	Examples of the spectra of signals for 1550 nm laser for various velocities . .	88
3.19	SM sensor set-up with a rotating disc at a target in two different geometries .	89
3.20	Example of SM signal from a rotating disc for different velocities . . . . .	90
3.21	Velocity measurements of the rotating disc: SM signal and obtained spectrum .	90
3.22	Experimental and simulated spectra for varied velocity below 2 m/s . . . . .	93
3.23	Experimental and simulated spectra for varied velocity higher than 3 m/s up to 8 m/s . . . . .	93
3.24	Experimental and simulated spectra for varied location of the laser spot on the disc . . . . .	94
3.25	Experimental and simulated spectra for varied angle between the laser axis and the velocity vector . . . . .	95
3.26	Theoretical and experimental relative error dependence on the angle between the disc and the laser . . . . .	97
3.27	Examples of typical SM signals and their FFTs for a relative error of above and below 5% . . . . .	99
3.28	Experimental results from measurements of a rotating disc covered with white paper . . . . .	100
4.1	Set-up of the SM sensor used for velocity measurements with a fluid as a target	105
4.2	Experimental results from measuring the velocity of fluids . . . . .	106

4.3	Spectrum of typical SM signals for laminar flow and their result: various pump speeds . . . . .	109
4.4	Schematic explanation of the spectrum obtained in the experiments with different velocities . . . . .	111
4.5	Spectrum of typical SM signals for laminar flow: various concentrations of seeders . . . . .	112
4.6	Result from experimental spectra: influence of the concentration of seeders .	114
4.7	Spectrum of typical SM signals for laminar flow and their result: various size of seeders and concentration of seeders . . . . .	116
4.8	Result from experimental spectra: influence of the concentration of seeders and their size . . . . .	117
4.9	Set-up of the focus point study . . . . .	120
4.10	Schematic representation of the set-up for focus point study and obtained results . . . . .	120
4.11	Obtained spectra for studying the focus point . . . . .	121
4.12	Obtained spectra for studying the focus point and fitting the data with theory	123
4.13	Obtained spectra when varying the point of the laser light focus for different angles $70^\circ$ and $60^\circ$ . . . . .	125
4.14	Obtained spectra when varying the point of the laser light focus for an angle of $55^\circ$ . . . . .	126
4.15	Obtained spectra when varying the point of the laser light focus for an angle of $80^\circ$ for pure water . . . . .	127
4.16	The points of maximum and inflection on the function similar to one obtained from SM sensor . . . . .	132
4.17	Numerically calculated functions of the system of the equations for finding the velocity range based on two frequency points of experimental spectrum .	134
4.18	Numerical solution the system of the equations for finding the velocity range based on two frequency points of experimental spectrum . . . . .	135
5.1	Schematic representation of a beam monitor based on a gas jet . . . . .	144
5.2	Example of alternative estimation of the gas jet velocity . . . . .	146
5.3	Implementation of the SM sensor into the existing gas jet monitor set-up for beam diagnostic . . . . .	147
5.4	Optical feedthrough as a way to deliver light from the SM sensor to the gas jet	148
A.1	Pitot probe for the gas jet . . . . .	160
A.2	Schlieren photograph of the gas expansion . . . . .	161
A.3	Absorption sensors in a turbulent jet . . . . .	162
A.4	Michelson interferometer for the gas cell characterisation . . . . .	163
A.5	Three optical diagnostics for the characterisation of a gas flow . . . . .	164

## List of Tables

1.1	Parameters of the system used for the simulation presented in Figure 1.8, when solving Eq. 1.34. . . . .	19
1.2	Parameters of the system used for the simulation presented in Fig. 1.9 and 1.10, using Eq. 1.40. . . . .	22
1.3	Liquid flow velocity measurements using the self-mixing technique . . . . .	27
1.4	Seeding material for liquid and gas flows . . . . .	28
2.1	Parameters used in the simulation of the spectrum in Fig. 2.16. . . . .	57
2.2	Parameters of the system used for the simulation presented in Fig. 2.17 and 2.18. . . . .	61
3.1	Influence of different parts of an SM sensor on the limitation of measurable velocities. . . . .	66
4.1	Results of the theoretically calculated frequency and measured frequency based on the velocity value of 1.654 m/s. . . . .	126

# Notations

The following notations and abbreviations are found throughout this thesis:

BIF	Beam Induced Fluorescence,
CCD	Charge-Coupled Device,
CMOS	Complementary Metal-Oxide Semiconductor,
DBR	Distributed Bragg Reflector,
DFB	Distributed Feedback,
DFT	Discrete Fourier transformation,
EM	Electromagnetic,
FFT	Fast Fourier Transformation,
FP	Fabry-Perot,
FT	Fourier Transformation,
FWHM	Full Width at Half Maximum,
GC	Gain-Coupled (laser),
HC	Horizontal Cavity,
HWA	Hot-Wire Anemometry,
IPM	Ionisation Profile Monitor,
LD	Laser Diode,
LDV	Laser Doppler Velocimetry/Velocimeter,
LED	Light-Emitting Diode,
LSV	Laser Speckle Velocimetry,
MQW	Multiple Quantum Well,
MCP	MicroChannel Plate,
PD	Photodiode,
PIV	Particle Imaging Velocimetry,
PTV	Particle Tracking Velocimetry,
RF	Radio Frequency,
ReMi	Reaction Microscope,
SM	Self-Mixing,
SRRS	Spectrally Resolved Rayleigh Scattering,
VC	Vertical Cavity,
VCSEL	Vertical-Cavity Surface-Emitting Laser.



# Abstract

Sensors play an important role in many areas of science, ranging from fundamental research to the automotive industry. These areas are pushing the development of more compact, sensitive and affordable sensors which can provide reliable information on displacement, velocity, density, and other key parameters.

In this thesis a compact laser-based sensor, based on the self-mixing effect in semiconductor lasers, was studied and assessed in detail with regards to its use for a number of applications. The work includes the development of the self-mixing sensor itself, studies into its intrinsic limitations from a physics and engineering point of view, and investigations into ways to optimise signal level and quality; of specific interest were studies into the use of the sensor in the context of particle accelerators.

The self-mixing phenomenon occurs inside a laser cavity and influences the wavelength of the light and its power fluctuation. The interaction of the backscattered light with the initial light is amplified within the cavity. This means that the sensor is very sensitive to external variation of the coupled back light; hence it does not require high power lasers, and there is no need for a complex optical system. The development of the sensor addresses the choice of laser and light delivery system, the detection system, and the data analysis. The detection system includes a photodiode which is part of a commercially available laser, a custom-built current delivery system to a transimpedance amplifier, and the transimpedance amplifier for converting and amplifying the current into a voltage. The data analysis system consists of a custom-written Matlab code.

This thesis contains the combination of a new theory for modelling the self-mixing signal in order to extract the velocity profile, with an experimental study into its limitations. These include velocities, the experimental parameters of the measured target and the environment. Research into the limitations of the self-mixing technique complemented the study. It was shown that the sensor can be applied for numerous applications in a particle accelerator environment, as well as in many other areas. These are highlighted across the thesis.

This thesis consists of five chapters which describe the self-mixing sensor in great detail. After a general introduction in Chapter 1, Chapter 2 presented developments of the theory behind the self-mixing technique. The subsequent Chapters 3 and 4 described experiments relating to different applications of the technique. Chapter 5 focused on applications using the sensor in a completely new area of supersonic gaseous targets. Finally, Chapter 6 presents conclusion and outlook.



# Acknowledgements

I would like to thank my supervisor, Professor Carsten P. Welsch, for providing me with the opportunity to work on this incredibly interesting project. I am thankful for the regularity of our meetings through which I have received support in all areas of my PhD. The creation of this thesis would not have been possible without his encouragement to explore the scientific world and the freedom he granted me pursuing my research.

I am grateful to the University of Liverpool, Marie Curie European Grant (LA<sup>3</sup>NET project in particular), and my scientific group QUASAR; these groups have enabled me to achieve in the scientific arena. Additionally, I am glad to have been part of the Cockcroft Institute and have enjoyed working in such a welcoming environment.

I would like to thank those people who have helped me in this journey; from scientific support to simply being there when I ask. With special thanks to (in alphabetic order) Bruno Muratori, Chris Edmonds, Emilia Cruz Alaniz, Emmy Sharples, Javier Resta Lopez, Lee Devlin, Louis Bizel-Bizellot, Massimiliano Putignano, Sam Jones, Sonal Mistry, Sue Davies, Tomas Cybulski, and Vasilis Tzoganis. I have become who I am today and have created this piece of work because of you. Thank to you.

I will be always grateful to my parents for their kindness, support and faith in me.

My thanks extend to the United Kingdom, which has become a home for me. I have made many friends, and I have grown as a person in the time I have been here. My current scientific achievements and potential future opportunities may not have happened had I not been here. This amazing four year adventure has been a great pleasure every single day. The nature of the UK inspired me to give my all each day, the typically British series “Doctor Who” brightened up so many of my evenings, and Neil Gaiman’s books and actually meeting him has made my life in the UK a unique experience. I am looking forward to experiencing the future which is awaiting for me.



# Chapter 1

## Self-Mixing Technique

Chapter 1 introduces the physical principle and theory of the self-mixing (SM) effect together with a general introduction into standard optical diagnostics. It includes an overview of the main parameters influencing the formation of the self-mixing phenomenon, including the different SM feedback regimes, and the signal which can be received for these regimes. The chapter then proceeds by presenting state-of-the-art applications of the self-mixing technique with emphasis on velocity measurements for different types of targets. Possible ways to improve the level of feedback which can be obtained for characterising fluid velocities with seeding particles are listed. An overview of the different types of lasers which can be used for the SM technique and their properties is also discussed.

### 1.1 Introduction

Accurately describing a physical process is a complicated task which may require the use of dynamic or kinematic equations to fully understand the situation or to obtain a simplified solution. Measuring the distances and velocities of a system provides essential information of its behaviour and also how it may evolve over time. Equations of motion are essential for studying any type of physical media. Laser based techniques are well established and are used in many fields ranging from industrial to research laboratory environments. The engineering side of any facility might require information on displacement and vibration of any part of equipment.

Laser light can be considered as a probe with a set of individual parameters; each of which could be used for characterisation. Changes in parameters of the laser light such as power density, polarisation, wavelength, spectrum, phase, and light propagation direction as a result of interaction with a target can provide information of a variety of processes.

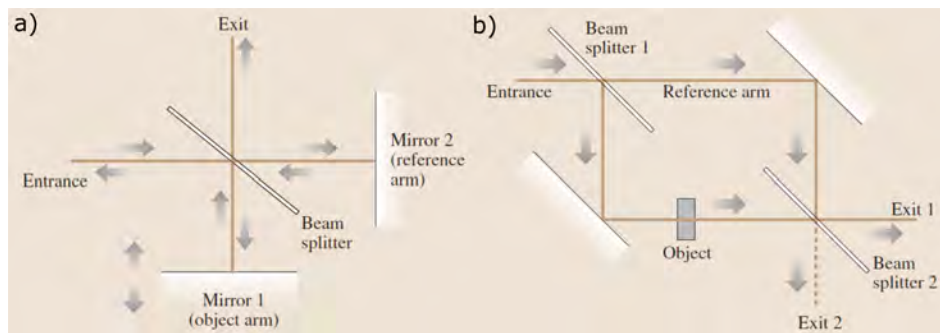


FIGURE 1.1: Basic principle of a) a Michelson interferometer and b) a Mach-Zehnder interferometer [1]. The reference arm and the object arm are formed using beam splitters.

## 1.2 Optical Diagnostics

Laser optical diagnostics are based on various properties which are unique to laser light such as monochromaticity and monodirectionality. Optical techniques allow precise non-invasive measurements to be taken of properties of the object under consideration. Depending on the physical phenomenon on which the technique is based, various properties can be measured, for example in the case of a flow these can be its: temperature, pressure, ionisation, luminescence, refraction, absorption, etc. Utilising a combination of different unique characteristics of laser light allows measurements to be taken of many target parameters at the same time.

### 1.2.1 Interferometry

Interferometry presents a group of techniques which uses the phenomenon of interference of waves to extract information about some of the properties of those waves. Interferometry has many different applications including surface deviations, wavefront characterisation, high-precision length measurements, etc [1, 2]. The basic principle of any interferometer is a superposition of two waves with the same wavelength. The resulting intensity of this superposition is determined by the difference in phase of the two waves. Constructive interference happens when the waves are in phase. Out of phase waves undergo destructive interference. The basic idea behind the simplest interferometer is to split the incident light into two waves, which then can interfere with each other.

A Michelson interferometer and a Mach-Zehnder interferometer, see Fig. 1.1 (a) and (b), are two of the most commonly used interferometers and consist of two arms: a reference arm and an object arm [1, 3]. The object arm contains the object under study, and which changes the property of the incident wave. When the wave from the object arm interferes with the unchanged wave from the reference arm, the resulting interference pattern contains the desired information about the object. In these examples only two waves interfere, however, variation across different interferometers is extensive, and some have three or more waves interfere, for example a Fabry-Perot interferometer.

If two beams are coherent [4], an interference pattern is formed where they cross, and the pattern is divided into bright and dark zones, i.e. due to constructive and destructive interference. If the light scatters off a particle passing through the volume and is collected in a detector, the signal on this detector experiences an amplitude modulation. The properties of the interference pattern depend on the size, optical properties and velocity of the scattering particle.

One very common example where interferometry can be employed for flow characterisation is in measuring the density of a flow by using the variation of the index of refraction with density. When one of the arms of the interferometer is located within the area of the studied object, a variation of refractive index results in a change of the optical path of the laser beam. It interferes with a reference beam and as a result, an interference pattern is created. Based on this, the refraction index can be obtained, and hence the density of the measured flow [1].

### 1.2.2 Particle Imaging Velocimetry (PIV)

A significant group of sensors is based on analysing the displacement of the moving particles as a whole. In such techniques, the flow is seeded with tracer particles, which scatter the light. The region of interest is illuminated by the laser, whose output is made to form a sheet by a cylindrical lens. The instantaneous flow is recorded by short light flashes with known separation time. The picture of scattered light is visualised, for example by a charge-coupled device (CCD) or a complementary metal-oxide semiconductor (CMOS) camera. The flash should be rather short to image the particle. If the pulses are too long, the particle images streak and the exact location of the particles in the flow cannot be determined. A set of pictures as a function of time allows for the calculation of velocities within the flow with a certain time and spatial resolution. An example of a typical set-up where this method was applied was a study into gaseous targets in vacuum [5]. The results obtained in this study are presented in Fig. 1.2.

The image particle density  $NI$  is the ratio of the length of the particles path between illuminations and the distances between individual particles. The source density  $NS$  is the number of particles per interrogating window or area of interest, and it represents wherever the particles can be recognised individually or as a group of particles. The source density can be described as  $NS = C \cdot Z(D/M)^2$ , where  $C$  is the concentration of seeding particles,  $Z$  is the thickness of laser light sheet,  $M$  is the lateral magnification, and  $D$  is the area of interest or interrogation window. If the tracer particles are assumed to faithfully follow the flow, a statement on the average velocity within the flow can be made. Depending on the image particle density and the source density, qualitatively, three different ways of approach for the calculation can be distinguished.

#### a) Particle Tracking Velocimetry (PTV)

If the density of illuminated particles is low ( $NS < 1$  and  $NI \ll 1$ ), the images of particles seldom overlap. The illumination from each particle can be obtained from each

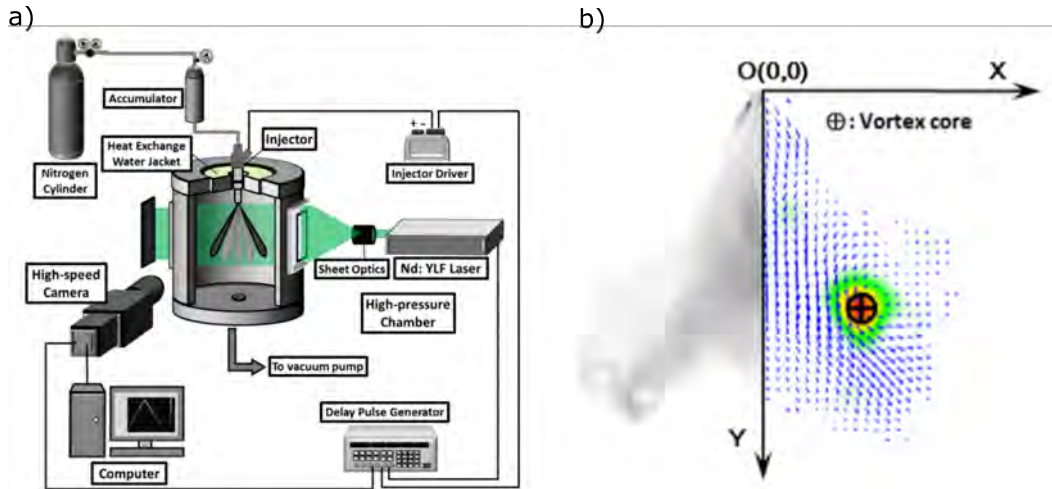


FIGURE 1.2: (a) Example of the experimental set-up used for PIV used in vacuum. (b) The spray image on the left hand side of the vertical axis with the corresponding flow field obtained using PIV on the right hand side of the axis [5].

image taken during the PTV. However, complex algorithms for coordinates determination and reliable identification of each particle tracks are required [6]. Often, dedicated software is needed for this. In summary, PTV is based on a coordinate measurement, and each individual particle can be detected and tracked using this method.

#### b) Particle Imaging Velocimetry (PIV)

PIV is used in the case of a high density of particles  $NI > 1$ . It is impossible to recognise individual tracks of particles when the density is too high. However, the average displacements of particles within a small interrogation window can be traced. Moreover, information about the velocity can be calculated using statistical correlations. Individual particles travel the distance between interrogation windows with time, which can be found by cross-correlation of the scattered light at different locations. If more interrogation windows are located in the flow the average velocity can be sampled in many points along the flow providing better accuracy. A very high density of illuminated particles is needed for good performance of the PIV method.

One of the major advantages of the PIV is that a two-dimensional picture can be obtained. This 2D mapping of the sections illuminated by the laser sheet is achieved by photographing the flow with two CCDs and some statistical calculations. However, it usually involves cross-correlation decision making algorithms [7]. PIV is applied to study vortices in turbulent and transonic flows and a thermal convection within the flow [8, 9].

#### c) Laser Speckle Velocimetry (LSV)

A speckle is formed by the interference of light waves which have the same frequency, but different phases and amplitudes. This is usually the case when the amplitude and intensity of light vary randomly. Such an interference pattern can be observed on a screen as a picture consisting of bright and dark spots, i.e. speckles [10]. This phenomenon can be observed when coherent light is scattered off any obstacles whose topographical sizes are greater than the wavelength of the incident light.

In the case of PIV, the topographical properties of the target influence the statistical properties of the speckle patterns. This effect occurs when particles overlap, i.e. for  $NS > 1$  and  $NI \gg 10$ . The principle of measurement and calculation for LSV is the same as for PIV, and it is based on the statistical properties of obtained images. The only difference is the mathematical algorithms used for the calculations and analysis of collected data [11].

A variety of other techniques are based on PTV, PIV, and LSV [12, 13] which use different equipment to achieve their goals.

### 1.2.3 Laser Doppler Velocimetry (LDV)

One of the most common laser based sensors is the Laser Doppler Velocimeter (LDV) [14, 15]. LDV based on the Doppler shift experienced by a wavelength of the laser light which is scattered off a moving target. The Doppler shift principle implies the laser light undergoes a shift in frequency proportional to the component of the velocity parallel to the direction of propagation of the light.

Doppler shift is the shift in frequency/wavelength observed from a moving object by a receiver in a different rest frame. The source of light, which frequency undergoes a Doppler shift, moves with a velocity  $\vec{v}$  with respect to the receiver. The source of light in the case of LDV is a monochromatic laser. The stationary receiver registers a shift in wavelength,  $\lambda$ , of the incident light with frequency  $\nu$  as:

$$\lambda' = \frac{c - \vec{v} \cdot \vec{n}}{\nu}.$$

Where  $\vec{n}$  is the unit vector in the direction from the source to the receiver and  $c$  is the speed of light in vacuum. In terms of the change in frequency, it can be written as:

$$\nu' = \frac{c}{\lambda'} = \frac{\nu}{\nu - \frac{\vec{v} \cdot \vec{n}}{c}}, \quad (1.1)$$

when the light source and/or the light receiver moves. The difference in frequencies between stationary receiver and moving sources of light is:

$$\nu' - \nu = \Delta\nu = \frac{\nu}{c} \frac{\vec{v} \cdot \vec{n}}{1 - \frac{\vec{v} \cdot \vec{n}}{c}}.$$

For the nonrelativistic case, i.e.  $|\vec{v}| \ll c$ , the difference is equal to:

$$\Delta\nu = \frac{\vec{v} \cdot \vec{n}}{\lambda}.$$

The change in frequency also appears when the light source is stationary, but the receiver moves:

$$\nu' = \frac{1}{\lambda} [c - \vec{v} \cdot \vec{n}]. \quad (1.2)$$

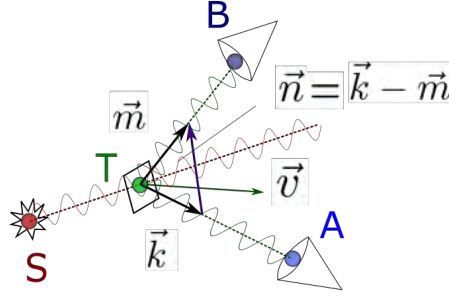


FIGURE 1.3: Schematic representation of the optical Doppler velocimetry technique in terms of vector representation.  $S$  (red dot) is the source of the light.  $T$  (green dot) is moving target with a velocity ( $\vec{v}$ ). The light scattered on the moving target  $T$  has a Doppler shift, and it is received by receivers  $A$  (purple dot) and  $B$  (blue dot), and they are characterised by the unit vectors ( $\vec{k}$ ) and ( $\vec{m}$ ) respectively.  $\vec{n}$  is the sensitivity vector.

These equations are correct when the Doppler effect is accounted for once. In the case of optical Doppler velocimetry, the Doppler effect occurs twice because the source of the radiation together with the receiver are in a stationary lab frame whilst the target, which reflects or scatters the source light, is in the moving lab frame.

Figure 1.3 shows a schematic interpretation of the Doppler effect. The light from the source  $S$  scatters off the target  $T$ , which moves with the velocity  $\vec{v}$ . The moving target becomes a receiver of light from the source  $S$ . Generally, the light scatters off the target  $T$  in all directions, and can be received at any point. Hence, the moving target  $T$  becomes a re-emitter of light. There are two receivers  $A$  and  $B$  whose directions can be characterised by the unit vectors  $\vec{k}$  and  $\vec{m}$ , respectively. Each of these receivers detects shifts in the frequency differently since they are at different locations in space. The moving target  $T$  can be referred to as the receiver of the light coming from the stationary source  $S$  and at the same time as a re-emitter of the light to the two stationary receivers located at the points  $A$  and  $B$  [2]. The frequency of the radiated light from the target is equal to the frequency of received light according to following relation, based on Eq. 1.2:

$$\nu_r = \nu_0 \left( 1 - \frac{\vec{v} \cdot \vec{n}}{c} \right).$$

Two receivers at the points  $A$  and  $B$  register an additional change in the frequency that appears due to moving of the re-emitter  $T$ :

$$\nu_B = \frac{\nu_r}{1 - \frac{\vec{v} \cdot \vec{m}}{c}} = \nu_0 \frac{1 - \frac{\vec{v} \cdot \vec{n}}{c}}{1 - \frac{\vec{v} \cdot \vec{m}}{c}},$$

$$\nu_A = \frac{\nu_r}{1 - \frac{\vec{v} \cdot \vec{k}}{c}} = \nu_0 \frac{1 - \frac{\vec{v} \cdot \vec{n}}{c}}{1 - \frac{\vec{v} \cdot \vec{k}}{c}}.$$

Direct measurements of these shifts in frequencies are difficult due to the slow response of photodetectors. However, the interference of two wavefronts, which are scattered off in different directions, are more suitable for detection. The resulting signal has

a frequency equal to the difference between the frequencies of the two scattered waves. In this case, the frequency of the Doppler shift is equal to:

$$\Delta\nu = \nu_A - \nu_B = \nu_0 \frac{1 - \frac{\vec{v} \cdot \vec{n}}{c}}{\left(1 - \frac{\vec{v} \cdot \vec{k}}{c}\right) \left(1 - \frac{\vec{v} \cdot \vec{m}}{c}\right)} \frac{\vec{v} \cdot (\vec{k} - \vec{m})}{c}. \quad (1.3)$$

In case of  $|\vec{v}| \ll c$ , the registered signal has a Doppler frequency equal to:

$$\nu_D = \Delta\nu = \frac{\nu_0}{c} \vec{v} \cdot (\vec{k} - \vec{m}) = \frac{1}{\lambda} \vec{v} \cdot \vec{n}. \quad (1.4)$$

Equation 1.4 is the non-relativistic expression for the Doppler shift for any kind of moving target including moving particles. It is very precise since all its components do not depend on the properties of the media such as temperature, pressure, contamination, etc., and does not require calibration with the reference velocity, since all components can be calculated precisely and independently.

According to Eq. 1.1, the frequency of the signal depends on the wavelength of light, the geometry of the optics of the system, and the velocity of the target. In this context, the geometry of the optics is defined by the vector  $\vec{n}$ . The signal frequency dependence on the three parameters is valid assuming that in the media the following two conditions are met. Firstly, the frequency of the light source does not change and is stable. Secondly, the velocity with which the wave propagates does not change and is stable. Using laser light as the source, the first condition is true with an accuracy better than  $10^{-5}\%$  [1, 15, 16]. The second condition is correct for most liquids and gases, for example for water it is valid with an accuracy better than  $10^{-5}\%$  [15, 17]. Hence, the LDV is a relatively precise device which is limited in performance by the precision of the frequency,  $\nu_D$ , which is defined by the properties of the detector. In the case of flows, the target from which the light scatters off can either be added to the flow or is part of the flow itself, i.e. water molecules in a water flow. If the moving target is in the area of the laser light, it scatters some part of the light, i.e. it receives and at the same time re-emits the light [10, 15, 18].

## 1.3 The Sources of Light in Laser Doppler Velocimetry

### 1.3.1 Laser Light and its Properties

The main source of light for a Doppler Velocimeter is light from lasers since they allow precise and accurate measurements of Doppler shift to be taken. A laser produces a light beam which is monochromatic, coherent, intense, and polarised. A typical laser consists of three key components:

1. A gain medium or active medium, which amplifies light in the process of stimulated emission.
2. A pump source, which produces the population inversion within the gain medium.

3. Two mirrors, forming a laser cavity, which traps lights inside and aids the emission process.

Spontaneous emission occurs due to the spontaneous decay of an atom into the ground state. Stimulated emission arises when an incident photon interacts with the excited atom and causes it to decay. In this case the emitted photon has the same properties as the incident photon. In the case of a high level of population inversion within the gain medium locked between two mirrors, all emitted photons have the same properties leading to coherent laser light. The spontaneous emission within the laser appears before a certain level of population inversion is reached.

Depending on the property of the active media of the laser, the laser radiation can be obtained in different parts of the emitted spectrum. The emitted laser light has discrete quasi-monochromatic equidistant components, the distance between which depends on the length of the resonator and is equal to [1]

$$\Delta\nu/\nu' = \lambda/(2L) = 10^{-6} - 10^{-4},$$

where  $L$  is the length of the resonator. Each of the components is quasi-monochromatic radiation with natural emission linewidth of  $\Delta\nu = 10^2 - 10^{-1}$  Hz, or  $\Delta\nu/\nu' = 10^{-13} - 10^{-16}$  [1, 15, 16].

The broadening of the Doppler signal, based on Eq. 1.4, can be derived as:

$$\delta\nu_D = \frac{1}{\lambda} \vec{n} \cdot \delta\vec{v} + \frac{1}{\lambda} \vec{v} \cdot \delta\vec{n} - \frac{1}{\lambda^2} \vec{n} \cdot \vec{v} \delta\lambda. \quad (1.5)$$

The first term describes a change of frequency due to a change of velocity  $\delta\vec{v}$ ; the second term is the change of frequency due to an optical imperfection  $\delta\vec{n}$  of the geometry of the system which is described by vector  $\vec{n}$ ; and the third term is due to temporal incoherence of the light source  $\delta\lambda$ . In the case of laminar flows, the third term is negligibly small.

Laser light, when applied in Doppler shift experiments, has several benefits including monodirectionality and monochromaticity. The Doppler shift is set in the range  $\nu_D \approx 10^5 - 10^{10}$  Hz [19] in the case of turbulent flows. To achieve a high, better than 0.1%, accuracy during measurements, the resolution of a method or a tool used for measurements should be better than  $\delta\nu_D \leq 10^2 - 10^4$  Hz. A laser meets these criteria. For example, the radiation linewidth is about  $10^{-3} - 10^{-4}$  nm for gas lasers,  $10^{-1} - 10^{-4}$  nm for solid-state and semiconductor lasers, and  $10^{-7} - 10^{-9}$  nm for gas lasers [15].

Noise influences the properties of the laser beam dramatically including its power. The main sources of noise are spontaneous emission and modal interference [1]. The first leads to a fluctuation of the intensity known as white noise, and is relatively small with respect to the intensity of the beam itself [15]. The interference of different modes of the laser can have a much bigger effect on the laser beam. Most lasers produce multi-mode output with lots of frequency components with properties strongly dependent on small changes in gain, length of the cavity, temperature, and others factors [1]. Different modes can interfere with each other, which leads to a bias and fluctuation of the output

power rather than noise. Multimode emission results in a decrease of the coherence length of the beam. The frequency difference between modes is usually given in the datasheet of each laser. It can also be calculated using  $\delta\nu_{sep} = c/(2L)$  [16]. The number of modes within the gain bandwidth of a laser can be found from:

$$N_m \approx \frac{\delta\nu}{\delta\nu_{sep}} = \frac{\delta\nu 2L}{c}, \quad (1.6)$$

where  $\delta\nu$  is the gain bandwidth. In the case of a typical Helium-Neon laser with wavelength  $\lambda = 632.8$  nm, the gain bandwidth follows the Doppler-broadened emission linewidth with a full width at half maximum (FWHM) of  $\delta\nu = 1.5$  GHz [1]. Typical numbers for a semiconductor diode laser are a wavelength  $\lambda = 0.35$   $\mu\text{m}$  to  $24$   $\mu\text{m}$ , and gain bandwidth of  $\delta\nu = (2.5$  to  $10) \times 10^{12}$  Hz or  $\delta\lambda_{ul} = 5$  to  $20$  nm [15, 20].

One of the main properties of laser light is its directivity and corresponding angular divergence. Without an additional optical system, the angular divergence is around several angular minutes for a gas laser beam, several minutes for a solid-state laser beam, and up to several degrees in the case of semiconductor lasers [20]. The precision of the geometrical beam centre estimation is inversely proportional to the angular divergence of the beam.

A laser can emit on one wavelength or on several wavelengths, depending on the properties of active media and the properties of the laser cavity. Multi-mode lasers are easier to produce, but the behaviour of lasing light is more difficult to predict. Hence, a single mode laser is preferably to use for any kind of detection instrumentation unless the multi-mode itself is specifically used for the detection. However, the single mode semiconductor lasers have less power and, generally, are more expensive compared to multi-mode lasers.

### 1.3.2 Semiconductor Lasers: Bandgap

Semiconductor lasers are unique in their efficiency, compact size and relatively low power input in comparison with other lasers. The principle of their operation is based on the merging of different, at least two, semiconductor materials. The emission occurs at the interface between the materials. One has an excess of electrons, known as n-type, the other has an excess of holes, a deficiency of electrons, known as p-type. Applying a forward voltage to the materials, electrons from the n-type material are forced into the region of the holes of the p-type material. In the process of collision, they neutralise each other and emit recombination energy. The principle of the n-type semiconductor laser is that collisions only happen when applying an additional voltage across the device, otherwise there will be no gain in energy. Thus, the merging of different materials is made to design a bandgap of the materials. The bandgap is the difference between the lower conduction-band edge energy and the upper valence-band edge energy, and that is the exact energy, which is released during recombination. Depending on the combination of materials, the bandgap is different leading to different wavelengths of

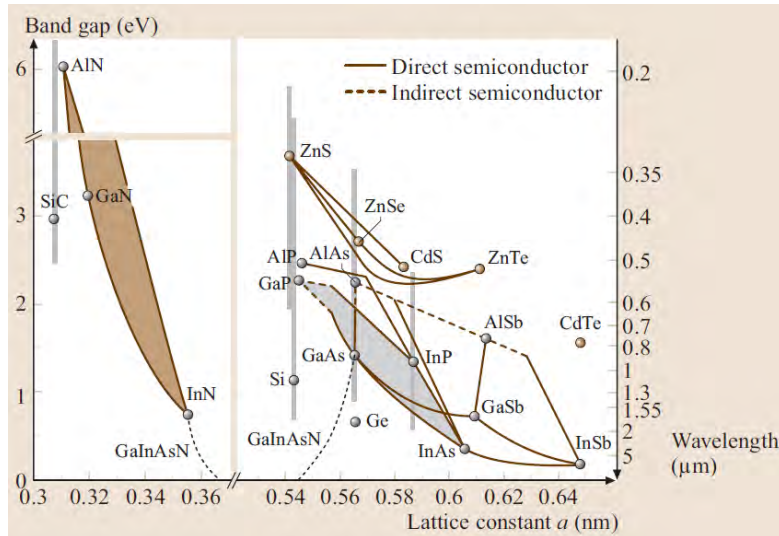


FIGURE 1.4: Bandgap energy and bandgap wavelength as a function of the lattice constant demonstrating the variety of different semiconductor lasers [1]. The shaded areas represent the tunability of wavelength for the specific type of the laser.

the emitted light, and it is usually presented as a function of the lattice constant of the materials, see Fig. 1.4 [1].

### 1.3.3 Semiconductor Lasers: Different Types

When a low voltage is applied, a laser produces spontaneous emission, which is not coherent. During the spontaneous emission, when the absorption exceeds the gain, the emission increases linearly. As soon as the gain exceeds the loss at the threshold current  $I_{th}$ , lasing action starts, and, as it can be seen from Fig. 1.5, the output power increases dramatically with the current.

Typical gain coefficients of semiconductor lasers are between  $5,000$  and  $10,000 \text{ m}^{-1}$ . The gain coefficient is responsible for the excess of the emitted light over losses. With a usual gain length of  $1 \text{ mm}$  and less, it is enough to overcome rather significant distributed losses, of the order of  $2,000 \text{ m}^{-1}$  within the gain media. A typical number of gain bandwidth for semiconductor lasers is of the order of  $10^{13} \text{ Hz}$ . Correspondingly the emission linewidth of the recombination radiation is approximately  $20 \text{ nm}$ . Quantum-well lasers are an exception of this with narrower bandwidth of around  $5 \text{ nm}$  [1, 20].

The cavity for the semiconductor laser can be designed in two ways. The first one is the Fabry-Perot (FP) cavity. The mirror for a FP laser is made at the end of the gain medium by cleaving the edge of the crystal which the semiconductor laser is made from. The reflectivity of such cleaved mirrors is around  $30\%$  because of a relatively high index of refraction for that type of material, usually  $n = 3.5$ . The typical length of the cavity of such a laser is  $0.2 - 1 \text{ mm}$ . This leads to a relatively broad spectrum of the laser output with many longitudinal modes [17]. In order to have single longitudinal mode lasers, frequency-selective elements are usually used [15].

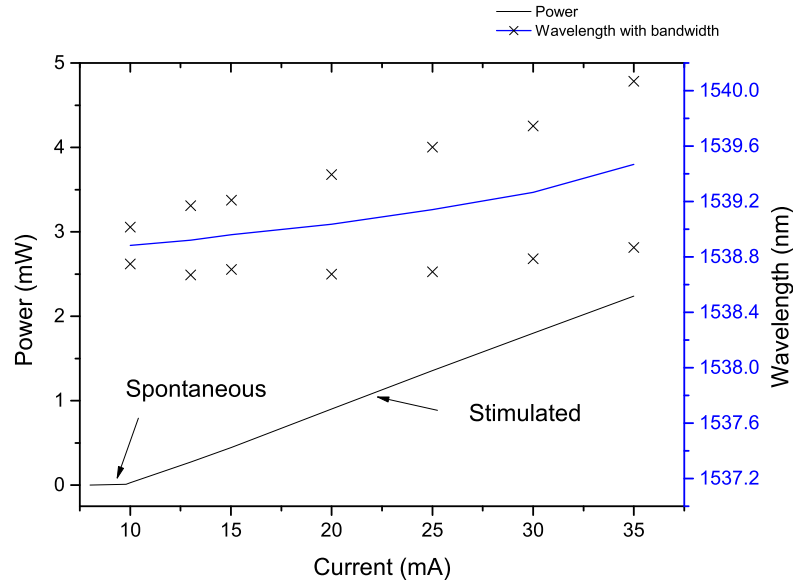


FIGURE 1.5: Dependence of the output power and the wavelength of the DFB laser diode (PL15N0021FCA-0-0-.5, Laser Components) at room temperature on the injected current with  $I_{th} = 9.8$  mA. The behaviour of the laser power during spontaneous and stimulated emission is different.

Another way to classify semiconductor lasers is according to the geometry of their cavities, horizontal (HC) and vertical (VC) [1], see Fig. 1.6. The difference between those two types is the way the laser cavity is defined. The laser cavity mirrors are either perpendicular (for HC) or parallel (for VC) to the plane of the heterostructure of the layer. The orientation of the cavity determines the way in which the light emits from the laser.

FP cavities and structures with distributed feedback (DFB) have horizontal cavities. The usual way to provide feedback in a laser oscillation is to put mirrors at each end of the cavities, as in the FP laser. This leads to standing waves with discrete longitudinal modes, and the lasers tend to support lasing action on a number of longitudinal cavity modes, see the right part of Fig. 1.6. This appears due to boundary condition requirements that the fields at the mirrors should be zero. For example, the typical separation of the equidistant mode frequency is around 150 GHz for a 300  $\mu\text{m}$ -long cavity with a typical width gain curve of 5 THz, which leads to multimode operation of the laser [1].

The methods to achieve single-mode operation can be split into two main groups: short lasers, an effective example of this is the vertical-cavity surface-emitting laser (VCSEL), and frequency-selective feedback, which can be realised by using coupled cavities, an external grating (quite expensive technique), or a Bragg grating. In the case of the latter, the wavelength selection is done by distributing the boundary condition throughout the gain medium. Bragg grating is employed in three main categories of devices: distributed Bragg reflector (DBR), DFB and gain-coupled (GC) lasers [1, 20].

In DFB lasers the index grating occupies the entire cavity length. The waves are scattered off a Bragg grating, and the waves, the wavelength of which corresponds to the

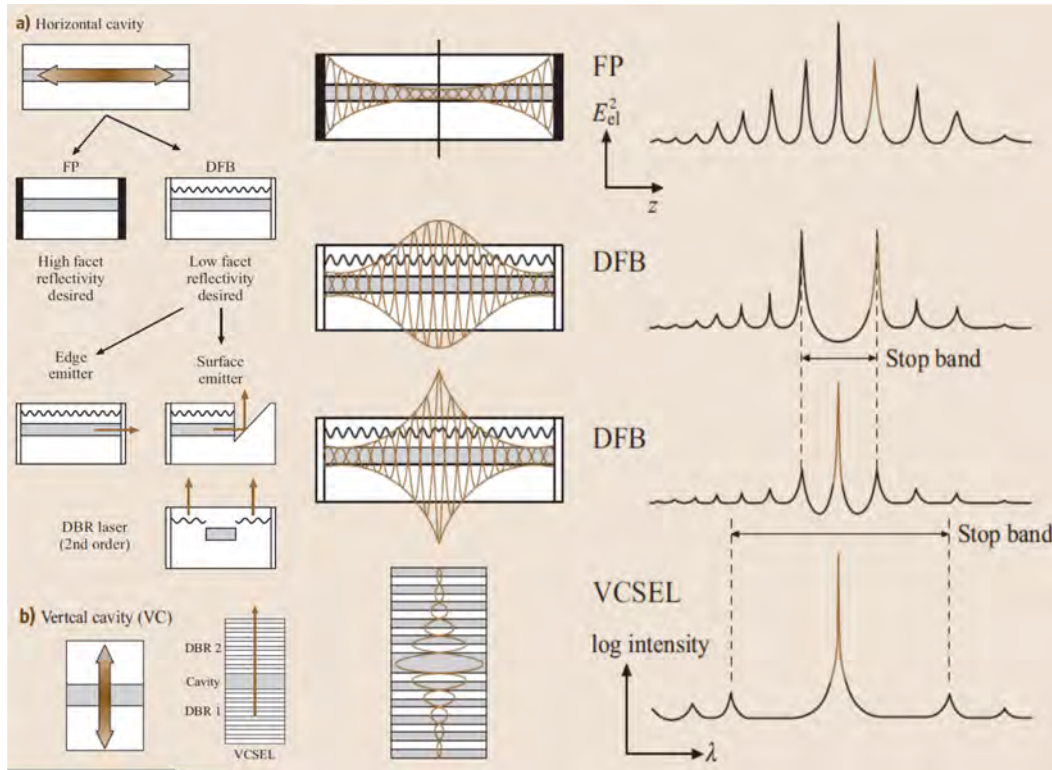


FIGURE 1.6: Different geometries of lasers with (a) horizontal and (b) vertical resonators (left part of the figure); and their schematic structural cross section (central part) and the corresponding emission spectra (right part) [1].

corrugation period of the grating, are gathered in the central part of the resonator. As a result, the mirror losses are a function of the wavelength, and the longitudinal mode with the lowest mirror losses is the most effective one for the resonator selection in terms of the concentration of photons. Typical emission spectra for different lasers are shown in Fig. 1.6. The right part of Fig. 1.6 shows the emission spectra for different lasers, and these can be compared with FP lasers, for the wavelength at which the laser emits the light, which is important for many applications.

## 1.4 Self-Mixing Effect, or Optical Feedback

### 1.4.1 Introduction

Demonstrated for first time in 1962 [21], laser diodes have revolutionised many fields of physics. Laser diodes have been used as an easy-to-apply coherent source of light for applications such as optical fibre telecommunications, non-linear optics and dynamics studies [20]. Their importance has triggered considerable scientific research effort into semiconductor laser properties. The physics of a semiconductor laser is different compared to conventional lasers. The typical length of a laser diode is of the order of a millimetre, while a helium-neon laser is of the order of a quarter of a metre. Diode lasers are relatively easy to build, very reliable and cheap. Furthermore, they are more

“open” or “transparent” than conventional lasers. Typical lasers emit a small, 1-5%, fraction of the total light intensity whilst semiconductor lasers typically emit 70% [20]. The amount of emitted light depends on the reflectivity of the laser’s cavity mirrors. Semiconductor lasers allow more light to exit, which leads to more light being coupled back into the laser. As a result, laser diodes are extremely sensitive to the external environment. Usually, such influences are undesirable, so the system is protected from it with, for example, optical isolators; however, non-linear response due to optical feedback has been an active area of research for several years [17]. For example, the laser diode can go into a chaotic dynamic regime when exposed to external optical feedback [17, 22]. In 1975, a strong mathematical similarity between laser diode dynamics and the chaotic behaviour of turbulent flows was shown [23], which triggered interest in this area and led to many publications, and to the study of the phenomenon known as optical feedback or induced-modulated interferometry or the self-mixing (SM) effect [22, 24].

Self-mixing has been studied for a long time in other laser systems as well. In the case of semiconductor lasers, the theory is different compared to the self-mixing effect in gas (CO<sub>2</sub> [25], He-Ne [26, 27]) lasers. The difference arises from the non-linear nature of the semiconductor active medium coupled to the optical gain and the carrier density due to the property of the p-n junction, which leads to different field equations and solutions compared to conventional lasers [20].

The first analysis of the self-mixing phenomenon in the case of a laser diode (LD) was performed by R. Lang and K. Kobayashi [24], which became a foundation work in this area. A useful review of different theories and practical approach to the SM effect in semiconductor lasers is given in [22], demonstrating theoretical investigations into the SM effect and developments of various applications.

The first approach to explain the self-mixing effect, which are known as the Lang-Kobayashi equations [24], describes the behaviour of a single-mode laser diode in the case of weak and moderate optical feedback through one round trip between the laser and the target, i.e. the external cavity. By considering multiple round trips in the external cavity a multimode iterative model has been developed [28, 29], this model is valid for an arbitrary level of feedback. The multimode coupled-cavity model [30] describes the SM effect for any level of feedback and views the system as a whole determining many parameters such as mode behaviour, phase perturbation, optical power variation, polarisation modulation, etc. [30, 31]. This model includes the Lang-Kobayashi solution in the limit of one round trip and one longitudinal mode of the laser diode.

### 1.4.2 Self-Mixing: Theory

The working principle of the SM effect is that light from the laser scatters off a target and returns back into the laser cavity. The laser plays multiple roles in the functioning of the SM sensor. It detects the signal being both a coherent heterodyne receiver and amplifier at the same time. This means there is no need for additional optics for a signal to be obtained and recorded.

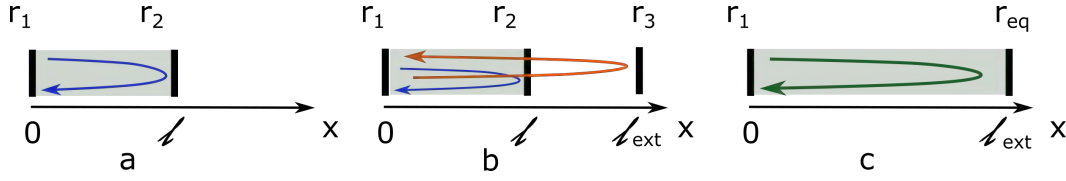


FIGURE 1.7: Schematic representation of the laser diode operation a) in a free space b) under optical feedback in a three-mirror cavity model c) under the feedback in an equivalent cavity model.

The SM system can be described by a set of field and rate equations obtained by adding an additional external feedback term into the standard equations [24, 32]. The standard equations are obtained for a laser diode operating in a free space, see Fig 1.7 (a). The additional external feedback term appears due to the coupling of the scattered light back into the laser cavity. There, the influence of the feedback is traceable through this additional term.

The target can be seen as an additional mirror for the laser system. In this way the system can be described as a three-mirror laser [16] with an external cavity length equal to the distance between the laser and the target. The schematic representation of this is shown in Fig. 1.7 (b).

Another approach is to consider the system as a two-mirror laser with a modified complex reflection coefficient or effective reflection coefficient, and use standard solutions derived for semiconductor laser systems [33]. As a result, the solution is based on replacing the parameters without feedback, see Fig. 1.7 (a), with parameters which depends on an additional mirror [34], i.e. a target, see Fig. 1.7 (c). In the case of the two-mirror laser with a modified complex reflection coefficient approach, the target is seen as an additional boundary, or space, and an initial, or time, condition. The details of these approaches are given below.

### 1.4.3 Free Running State of the Laser

The self-mixing, or optical feedback, effect can be studied based on the operation of a standalone laser diode, or a laser diode in free space [16, 20]. Schematically, a free running state of the laser diode can be represented as a two-facet Fabry-Perot cavity with an active layer of length  $l$ , see Fig. 1.7 (a). The facets have reflection coefficients  $r_1$  and  $r_2$  with respect to the amplitude of the electric field. The active media inside the laser cavity has a power gain  $g$ , a power loss  $\alpha_0$ , and thus an absorption gain coefficient:

$$\gamma_0 = g - \alpha_0. \quad (1.7)$$

The electromagnetic wave travelling in the longitudinal direction ( $x$ ) of the cavity can be written as:

$$E(x) = E_0 \exp(-ik_0x) \exp\left(-\frac{1}{2}\gamma_0x\right), \quad (1.8)$$

where  $k_0$  is a wavenumber, and it is equal to:

$$k_0 = \frac{2\pi\eta_0\nu_0}{c}, \quad (1.9)$$

where  $\eta_0$  is the refractive index of the active medium and  $\nu_0$  is the angular frequency of the wave.

The emission condition for the laser is reached when the optical gain in the media is balanced with all losses within one round trip inside the laser cavity. The parameters for such condition are usually called threshold parameters, for example a current threshold, and they are denoted with a subscript *th* later on. Considering that  $E(0)$  is injected through the first facet, then after one round trip Eq. 1.8 becomes:

$$E(0) = E(0)r_1 \exp(-ik_0l) \exp\left(-\frac{1}{2}\gamma_0l\right) \cdot r_2 \exp(ik_0(-l)) \exp\left(-\frac{1}{2}\gamma_0(-l)\right), \quad (1.10)$$

leading to:

$$1 = r_1r_2 \exp(-2ik_0l) \exp(-\gamma_0l). \quad (1.11)$$

It can then be shown that the emission condition of the laser diode without feedback is [20]:

$$r_1r_2 \exp\left(-\frac{4\pi\eta_0\nu_0}{c}l + (g_{th0} - \alpha_0)l\right) = 1. \quad (1.12)$$

Solving this equation, the emitting frequency equation can be found:

$$1 = r_1r_2 \exp(-\gamma_0l),$$

$$g_{th0} = \alpha_0 - \frac{\ln(|r_1r_2|)}{l}, \quad (1.13)$$

$$2k_0l = q \cdot 2\pi,$$

$$\nu_0 = q \frac{c}{2l\eta_0}, \quad (1.14)$$

where  $q$  is an integer number and corresponds to a longitudinal emission mode. These conditions are frequently referred to as threshold conditions for the laser [1, 16, 20]. Depending on the configuration of the laser and its cavity, the laser can have several oscillating wavelengths. If the cavity is designed in a way that only one wavelength can oscillate, such a laser is called a single mode laser, which is assumed in the theory presented above. However, the effect of multimode regimes of the laser under the SM effect will be discussed as well.

#### 1.4.4 Lang-Kobayashi Model: Single Mode Laser Diode with Weak Feedback

The initial SM analysis by Lang-Kobayashi described the evolution of the electric field of a single mode laser diode under the influence of a weak time-delayed portion of an optical field coupled back into the laser system. The electric field changes with time

because of additional delayed feedback [24]:

$$\frac{d}{dt}E(t)e^{-i2\pi\nu_0 t} = i2\pi\nu_q E(t)e^{-i2\pi\nu_0 t} + \frac{1}{2}(g - \alpha_0)E(t)e^{-i2\pi\nu_0 t} + \tilde{k}E(t - \tau_D)e^{-i2\pi\nu_0(t - \tau_D)}. \quad (1.15)$$

The electric field inside the cavity is assumed to be a product of an envelope function  $E(t)$  and a rapidly oscillating optical field  $e^{-i2\pi\nu_0 t}$  with a central frequency  $\nu_0$ . The amount of light coupled back into the laser corresponds to  $\tilde{k}$ .  $\tau_D$  is the time of flight of the wave and  $\nu_q$  is the longitudinal mode frequency of the laser, which is equal to  $\nu_q = qc/2l\eta$ , where  $\eta$  is the refractive index of the medium. The refractive index in the case of SM effect can vary with the density carried due to plasma loading [22].

The time-dependent equation represents a possible difference between the assumed frequency of the emitted light  $\nu_0$  and the instantaneous frequency of the laser light within the cavity as a first term on the right side of the equation (green). The amplification through stimulated emission is presented as the second term (blue) of the equation, and the external feedback influence on the result optical field as the third term (orange). The last term represents the self-mixing effect. For a steady solution, the electric field  $E$  is considered to be constant with time. The real and imaginary part respectively can be written as:

$$g - \alpha_0 + 2\tilde{k} \cos(2\pi\nu_0\tau) = 0, \quad (1.16)$$

$$2\pi\nu_q - 2\pi\nu_0 - \tilde{k} \sin(2\pi\nu_0\tau) = 0. \quad (1.17)$$

These two equations are coupled to each other via the refractive index  $\eta$ , since it is different for inside and outside the cavity and used for calculation of the frequency. The expressions for power, phase, and frequency can be obtained from Eq. 1.15, and the expressions will be shown later.

#### 1.4.5 Laser Diode under Optical Feedback (Three-Mirror Cavity Model)

Considering a target as an additional mirror with reflection coefficient  $r_3$  located at a distance  $l_{ext}$ , as was shown in Fig. 1.7 (b), the same concept of the round trip inside the cavity can be applied. Therefore, the same threshold condition of the balance between gain and losses within the longer external cavity should be fulfilled. The equation can be split into two parts:

$$E(0) = E(0)r_1r_2 \exp(-2ik_{in}l) \exp(-\gamma_{in}l) + E(0)r_1(1 - r_2^2) \exp(-2ik_{in}l) \exp((- \gamma_{in}l)r_{ext} \exp(-2ik_{ext}l_{ext})). \quad (1.18)$$

The first term (blue in the equation and it represents blue wave in Fig. 1.7 (b)) of the equation describes the wave propagation within the initial cavity. The second part (orange in the equation and orange wave in Fig. 1.7 (b)) of the equation represents the propagation of the optical field outside the cavity and its reflection off the external facet or target. The subscripts in the equations refer to the wave travelling inside (*in*) and outside (*ext*) the laser cavity. In the reflection coefficient, the effect of the attenuation,

$a$ , of the reflected light are taken into account, so  $r_{ext} = afr_3$ . Where  $f$  is the fraction of the reflected field which is coupled back into the laser cavity [32]. This equation leads to:

$$1 = r_1 r_2 \exp(-2ik_{in}l) \exp(-\gamma_{in}l) [1 + \zeta \exp(-2ik_{ext}l_{ext})], \quad (1.19)$$

where a coupling parameter,  $\zeta$ , between the internal and external cavity is equal to:

$$\zeta = \frac{(1 - r_2^2)r_{ext}}{r_2}. \quad (1.20)$$

Equation 1.19 can be written for the parameter  $r_{eq}$ , which describes the system of the three-mirror cavity, with the “equivalent” ( $eq$ ) reflectivity  $r_{eq}$  as:

$$r_{eq} = |r_{eq}| \exp(i\Phi_{eq}) = r_2(1 + \zeta \exp(-2ik_{ext}l_{ext})), \quad (1.21)$$

where its modulus  $|r_{eq}|$  and phase  $\Phi_{eq}$  are equal to:

$$|r_{eq}| = r_2(1 + \zeta \cos(2k_{ext}l_{ext})), \quad (1.22)$$

$$\Phi_{eq} = -\zeta \sin(2k_{ext}l_{ext}). \quad (1.23)$$

#### 1.4.6 Equivalent Cavity Model: Modulation of the Laser Optical Frequency

Approaching it differently and considering the feedback as an additional initial condition for the laser [22], the equivalent reflectivity coefficient can be written as:

$$r_{eq}(t) = r_2 \left( 1 + \exp \left( i \int_t^{t-\tau_D} \omega_F(t, 0) dt \right) \right). \quad (1.24)$$

Then Eq. 1.12 under feedback can be written as:

$$r_1 r_{eq} \exp \left( -\frac{4\pi\eta_F\nu_F}{c}l + (g_{thF} - \alpha_0)l \right) = 1. \quad (1.25)$$

The subscript terms, denoted as  $F$ , mean that these parameters are obtained under feedback. Combining Eq. 1.12, 1.13 and 1.21 leads to the following relation:

$$\left| \frac{r_{eq}}{r_2} \right| \exp \left( -i \left( \frac{4\pi\eta_F\nu_F}{c}l + \Phi_{eq} - \frac{4\pi\eta_0\nu_0}{c}l \right) \right) \exp((g_{thF} - g_{th0})l) = 1. \quad (1.26)$$

Resolving Eq. 1.26 in terms of the modulus part and the phase part, the emission frequency under feedback can be expressed as:

$$g_{thF} - g_{th0} = -\zeta/l \cos(2k_{ext}l_{ext}), \quad (1.27)$$

$$\Delta\Phi = \frac{4\pi l}{c}(\eta_F\nu_F - \eta_0\nu_0) + \zeta \sin(2k_{ext}l_{ext}). \quad (1.28)$$

By definition [16]:

$$\eta_F \nu_F - \eta_0 \nu_0 = \Delta(\eta \nu) = \nu_0 \Delta \eta + \eta_F \Delta \nu, \quad (1.29)$$

where the change of refractive index is:

$$\Delta \eta = \frac{\partial \eta}{\partial g} (g - g_0) + \frac{\partial \eta}{\partial \nu} (\nu - \nu_0), \quad (1.30)$$

and considering the linewidth enhancement factor [16]  $\alpha = -\frac{4\pi\nu_0}{c} - \frac{\partial \eta}{\partial g}$ , Eq. 1.29 can be written as:

$$\begin{aligned} \Delta(\eta \nu) &= \nu_0 \left[ -\frac{\alpha c}{4\pi\nu_0} (g_F - g_0) + \frac{\partial \eta}{\partial \nu} (\nu_F - \nu_0) \right] + \eta_F (\nu_F - \nu_0) = \\ &= (\nu_F - \nu_0) \left[ \nu_0 \frac{\partial \eta}{\partial \nu} + \eta_F \right] - \frac{\alpha c}{4\pi} (g_F - g_0). \end{aligned} \quad (1.31)$$

For the threshold condition and using Eq. 1.27, this equation can be written as

$$\Delta(\eta \nu) = (\nu_F - \nu_0) \eta_{eff} + \frac{\alpha c}{4\pi l} \zeta \cos(2k_{ext} l_{ext}). \quad (1.32)$$

Then the parameter  $\eta_{eff}$  can be defined as:

$$\eta_{eff} = \nu_0 \frac{\partial \eta}{\partial \nu} + \eta_F. \quad (1.33)$$

The emission frequency can be obtained from Eq. 1.28 for a phase difference equal to 0 or to an integer multiple of  $2\pi$ , then:

$$\begin{aligned} 0 = \Delta \Phi &= \frac{4\pi l}{c} \left( (\nu_F - \nu_0) \eta_{eff} + \frac{\alpha c}{4\pi l} \zeta \cos(2k_{ext} l_{ext}) \right) + \zeta \sin(2k_{ext} l_{ext}) = \\ &= (\nu_F - \nu_0) + \zeta \frac{c}{4\pi l \eta_{eff}} \sqrt{1 + \alpha^2} \sin(2k_{ext} l_{ext} + \arctan(\alpha)). \end{aligned} \quad (1.34)$$

So:

$$(\nu_F - \nu_0) = \frac{C}{4\pi \tau_D} \sqrt{1 + \alpha^2} \sin(2\pi \nu_F \tau_D + \arctan(\alpha)), \quad (1.35)$$

where  $C$  is called the coupling coefficient [22],  $\tau_D$  is the time of flight inside the external cavity (so up to the target) and  $\tau_l$  is the time of flight in the laser cavity, which are equal to:

$$\begin{aligned} C &= \frac{\tau_D}{\tau_l} \zeta \sqrt{1 + \alpha^2}, \\ \tau_D &= \frac{2l_{ext}}{c}, \\ \tau_l &= \frac{2l_{laser}}{c}. \end{aligned} \quad (1.36)$$

It needs to be stated that all solutions are obtained for weak feedback and may be derived from Eq. 1.15-1.17.

TABLE 1.1: Parameters of the system used for the simulation presented in Figure 1.8, when solving Eq. 1.34.

Parameter name	Value
Laser wavelength	$\lambda = 650 \text{ nm}$
Linewidth enhancement factor	$\alpha = 5$
External cavity length	$l_{ext} = 10 \text{ cm}$

### 1.4.7 Laser Diode under the Self-Mixing Effect: Common Case

The first study of the self-mixing effect was performed for single-mode laser diodes under weak feedback assuming that there was only one round-trip within the external cavity. When the multimode structure of the laser diode and multiple round trips within the external cavity are taken into account, the dynamics of the SM system leads to many solutions including those which are chaotic. However, even with the approach of only one round trip, the chaotic regime can be described and studied since the parameter  $C$  defines the solution of Eq. 1.35 when finding the phase difference from Eq. 1.27. An example of the solution of Eq. 1.27 for different values of the parameter  $C$  is shown in Fig. 1.8. The parameters used as inputs to the simulation are shown in Table 1.1. The dependence of the phase difference on the change in the frequency of the laser when it is under feedback is calculated for three cases: weak feedback ( $C < 1$ , yellow line), moderate feedback ( $C = 1$ , red line), and strong feedback ( $C > 1$ , blue line). The solution for the equation can be found from the crossing of the curve with a horizontal black line, i.e.  $\Delta\Phi = 0$ . The dotted line shows the case when the laser is under no influence of feedback. It can be seen that as soon as  $C > 1$ , there are three solutions to Eq. 1.34 and Eq. 1.35, while for weak and moderate feedbacks only one solution exists. It means that for strong feedback, the laser can enter the chaotic regime, and its behaviour is difficult to predict.

Generally, the description and solution of the equations governing the SM effect can be done for any kind of feedback and for multimode laser diodes [22]. The diode cavity mode and external cavity mode influence each other [32] leading to a change in the laser diode emitting wavelength or to potential instabilities. In the case when the LD length is equal to an integral multiple of the length of the external cavity, the laser frequency jumps between modes, i.e. mode-hopping appears. This can lead to not only an instability of the system but also a decrease of the LD current. However, the simplified solution describes the system relatively well, as soon as weak feedback is achieved.

### 1.4.8 Modulation of the Output Power under the Self-Mixing Effect

Within both ways of approaching the SM system, the modulation of light as a result of the interaction with the target can be written as:

$$P_F = P_0 \left( 1 + mF(2\pi\nu_F\tau_D) \right), \quad (1.37)$$

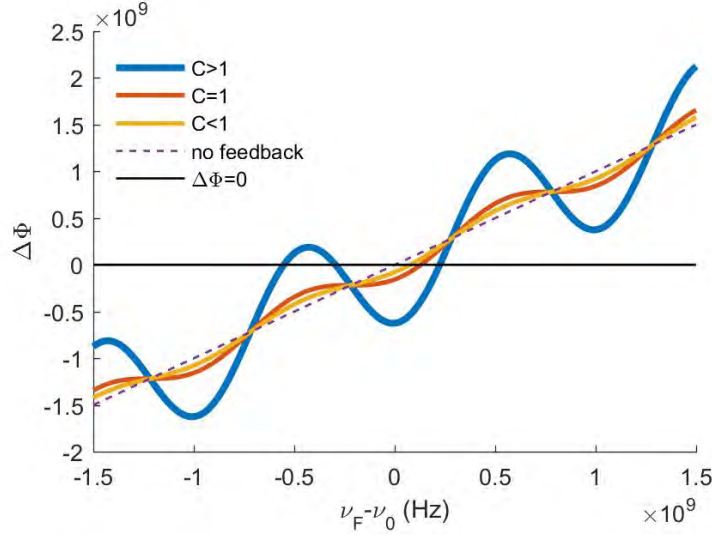


FIGURE 1.8: Solution of Eq. 1.34 or Eq. 1.35 for different levels of feedback represented by different values of  $C$ :  $C > 1$  (blue line),  $C = 1$  (red line),  $C < 1$  (orange line), and the black solid line represents the solution of the equation. In the case of  $C > 1$  (blue line), Eq. 1.33 has more than one solution, with three solutions in the presented case. The parameters which were used for the simulation of the phase function are presented in Table 1.1.

where  $P_0$  and  $P_F$  are the optical power without and with feedback, respectively. The periodic function  $F$  describes the interferometric signal waveform. The modulation index  $m$  is equal to:

$$m = C \frac{\tau_p C}{l_{ext} \sqrt{1 + \alpha^2}}. \quad (1.38)$$

The photon lifetime is  $\tau_p$ . The modulation index  $m$  and the shape of  $F$  are functions of feedback parameter  $C \propto r_3 l_{ext}$ . The parameter  $C$  depends on the level of feedback, which is the portion of light returned back into the internal laser cavity.  $C$  is defined by the reflectivity coefficient  $r_3$  together with coupling optics, and by the target distance  $l_{ext}$  [32–34]. For the case of one trip inside the cavity, Eq. 1.35 for both approaches can be solved, and Eq. 1.37 takes the form:

$$P_F = P_0 \left( 1 + m \cos(2\pi \nu_F \tau_D) \right), \quad (1.39)$$

which can be directly obtained from the Lang-Kobayashi Eq. 1.15.

The influence of the parameter  $C$  on the output power can be analysed based on Eq. 1.39 with the parameter  $m$  defined by Eq. 1.38. The optical power changes with time due to time modulation of two parameters. Firstly, the length of the equivalent cavity  $l_{ext}$  in the case of the velocity and displacement measurements changes in time. This directly affects the time for the wave to travel back and forth and hence the optical power, see Eq. 1.36. It can be shown as  $l_{ext}(t) \Rightarrow \tau_D(t) \Rightarrow P(t)$ , i.e. the time dependence of one function implies the time dependence of another. Secondly, the time dependence of the optical power can be seen from the solution of Eq. 1.35 from the emitted frequency of the laser under feedback, i.e.  $\nu_F(t) \Rightarrow P(t)$ . Equation 1.39 describes the behaviour

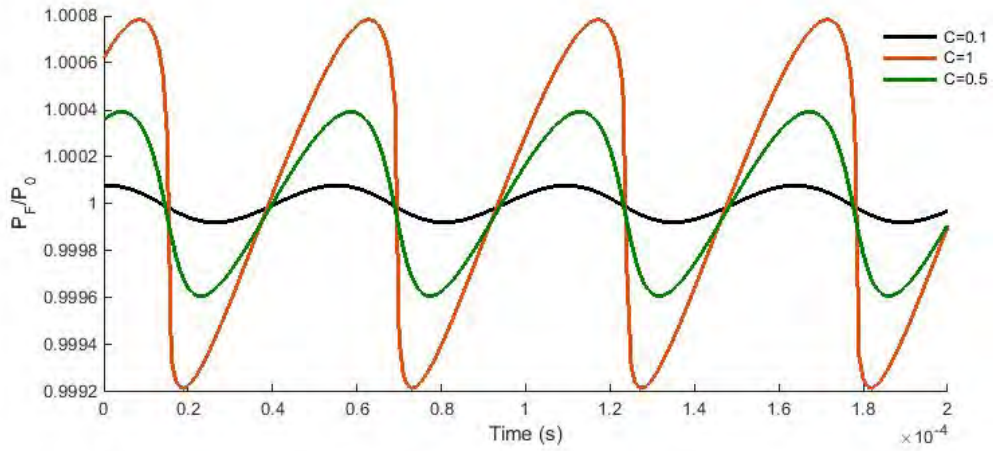


FIGURE 1.9: Simulation of the emitted optical power modulation depending on the coupling factor  $C$  using Eq. 1.40. In case of weak feedback ( $C = 0.1$ , black line), the signal is close to a sinusoidal function. When the amount of coupled-back light increases, the shape of the signal disturbs from the sinusoidal. Its leaning denotes the direction of the moving target, in here-presented case the target presumably moves away from the laser. The parameters used for the simulation are listed in Table 1.2.

of the SM system under any level of feedback. When the target moves with a certain velocity  $v$ , taking into account that the length of external cavity changes in time, using Eq. 1.36, Eq. 1.39 can be written as:

$$P_F = P_0 \left( 1 + m \cos \left( 2\pi \frac{2(l_{ext} + vt)}{c} \nu_F \right) \right). \quad (1.40)$$

The simulations of Eq. 1.39 when solving Eq. 1.35 for different levels of feedback  $C$  are shown in Fig. 1.9 for weak feedback and in Fig. 1.10 for strong and moderate feedbacks. The parameters used for the simulations are shown in Table 1.2. As seen in Fig. 1.8, in the case of strong feedback, the system can have several solutions in the case of instabilities of the SM system or multiple values of the optical power function. This means that, when simulated, the optical power function should demonstrate all possible solutions which exist for the phase function. However, the actual waveform of the interferometric signal, or the actual SM signal, follows the optical power function in real time, and jumping between different stable branches of the optical power function appears. Figure 1.11 shows the schematic representation of different shapes of the optical power function and actual SM signals which can be obtained. Depending on the amount of backscattered light coupled into the cavity, four different types of function (dotted line) and hence of the SM signals can be obtained, see Fig. 1.11. The blue line shows the actual SM signal which can be seen experimentally on an oscilloscope.

Gradually increasing the level of feedback, the shape of the signal can be deformed from a sinusoidal for  $C \ll 1$ , Fig. 1.11 (a), to a non-symmetrical sinusoidal-like shape for  $0.1 < C < 1$ , Fig. 1.11 (b), and then into an asymmetrical sawtooth-like form for

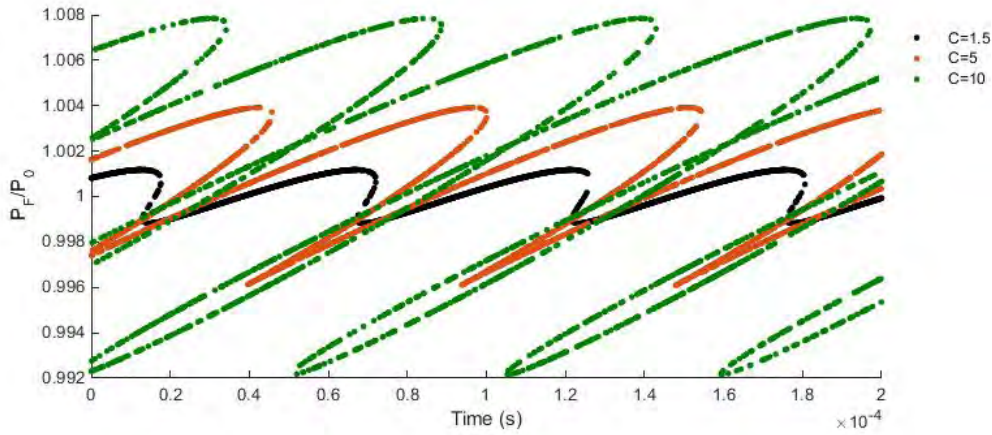


FIGURE 1.10: Simulation of the emitted optical power using Eq. 1.40 for the case of strong feedback. The function describing the optical power now has multiple values at any given time. The parameters used for the simulation are listed in Table 1.2.

TABLE 1.2: Parameters of the system used for the simulation presented in Fig. 1.9 and 1.10, using Eq. 1.40.

Parameter name	Value
Laser wavelength	$\lambda = 650 \text{ nm}$
Linewidth enhancement factor	$\alpha = 5$
External cavity length	$l_{ext} = 10 \text{ cm}$
Photon life time	$\tau_p = 10^{-12} \text{ s}$
Velocity of the target	$v = 4 \text{ mm/s}$

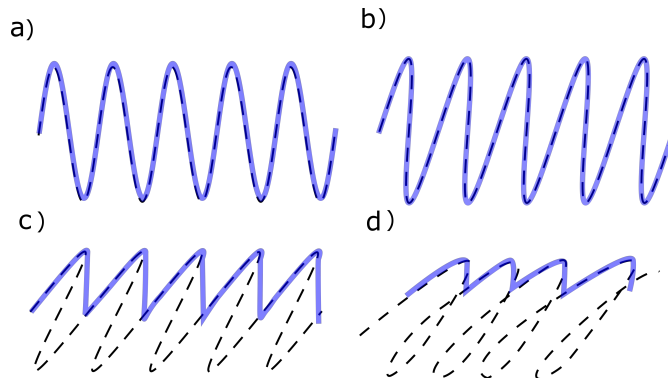


FIGURE 1.11: Illustration of different shapes of the self-mixing signal depending on the amount of light coupled back into the laser cavity. The dotted line shows the optical power function. The blue line shows the result of the signal which can be seen in the experiments on an oscilloscope. a) For weak feedback with  $C \ll 1$ , the optical power function and actual signal are sinusoidal; b) for weak feedback with  $0.1 < C < 1$ , the optical power function and the signal have a non-symmetrical shape; c) moderate feedback ( $1 < C < 5$ ), the system is bistable with a three-valued function resulting in a sawtooth-like signal; d) strong feedback ( $C > 5$ ) with a five-valued or a seven-valued function, when the laser can go into the mode-hopping regime. The corresponding signal is a sawtooth-like signal with lower amplitude compared to case c). The orientation in which the function leans is directly related to the direction in which the target moves.

$C > 1$ , Fig. 1.11 (c), (d). The orientation of the optical power function depends on the sign of the phase, so the direction of the target movements can be discerned [35–37].

In the case of a low amount of coupled back light with  $C \ll 1$  the optical power function is a sinusoid and so is the actual signal, see Fig. 1.11 (a) and Fig. 1.9 (black line). The SM signal follows thoroughly the optical power function, see the blue line in Fig. 1.11 (a).

For the weak feedback with  $0.1 < C < 1$ , the function is disturbed from the sinusoid, but it is still one-valued, and the signal follows it, see Fig. 1.11 (b). The examples of simulated optical power function are shown in Fig. 1.9 with orange and green lines.

An asymmetrical sawtooth-like form of the optical power function appears for strong feedback for the parameter  $C > 1$ , see Fig. 1.11 (c) and (d) for the schematic illustration and Fig. 1.10 for the simulations. The simulated functions of the optical power which are shown by a red and green line in Fig. 1.10 correspond to the cases in Fig. 1.11 (c) and (d), respectively. The actual signal follows the optical power function in time and, in particular, the branches along it until the point of instability, see Fig. 1.11. Then, after reaching this point, the signal falls on the next adjacent stable branch of the optical power function and follows it once more until the next point of instability. The resulting signal on the oscilloscope can be seen as a step-like or sawtooth-like transition. The leaning of the optical power function depends on the direction of movement of the target. If the direction changes, the signal has a sawtooth-like shape with a step turned in the opposite direction. Experimental study of this effect will be presented later in Chapter 3) in greater detail.

The absolute amplitude of the emitted optical power grows with the level of feedback, see Fig. 1.9 and 1.10. This suggests that the stronger feedback is more desirable due to higher amplitudes. However, as soon as the function becomes multiple-valued for strong feedback, the real signal becomes sawtooth-like. The amplitude of the observed signal for strong feedback is reduced from the calculated one as a result of the hysteresis of the SM function, see Fig. 1.11. Hence, there is a finite limit as to how much feedback is optimal and desirable for the best performance of the sensor.

## 1.5 Self-Mixing Interferometry Applications

The self-mixing technique is based on LDV, and it is basically a modified Michelson interferometer [1, 22]. The self-mixing scheme can be employed in nearly every situation where traditional interferometers, such as the Michelson or the Mach-Zender interferometer, are used. However, the SM sensor is a self-aligned interferometer without additional lenses, prisms and mirrors. Therefore, it can be applied much more easily for many purposes, including measurements of displacement [37–41] and velocity of different objects [33, 42–45]. SM sensors have been applied for various other applications, including studying materials with complex indices of refraction [46] and their change [47]; imaging

of different objects [48, 49]; measuring the thickness of transparent objects [50]; and for the purposes of alignments of solid objects [41].

### 1.5.1 Displacement and Vibration Measurement

The SM effect appears in both emitted frequency and optical power. If the distance between the laser and the target stays constant and the LD current remains constant, then both parameters have fixed properties. When the back-reflected light from a moving object is coupled into the LD cavity, the optical length of the external cavity changes, hence the optical power and the spectral properties of the emitted light change as well.

The SM effect is easy to use for the measurements of large, when compared to the laser light wavelength, displacements ( $\Delta l_{ext} \gg \lambda/(2n_{ext})$ ), This corresponds to a small change of the position of the external cavity. The change in the feedback level is negligible,  $C$  remains constant, and the phase is equal to:

$$\phi(t) = \omega\tau_{ext}(t) = \frac{2\pi c}{\lambda} \frac{2n_{ext}l_{ext}(t)}{c} = \frac{4\pi n_{ext}l_{ext}(t)}{\lambda}. \quad (1.41)$$

By changing the external cavity length  $l_{ext}$  by half of the wavelength taking into account its refractive index  $n_{ext}$ , the phase  $\phi$  changes by  $2\pi$ , similar to traditional interferometry. The peak of a sawtooth-like signal appears within the target moving over a distance  $\lambda/2$  along the laser light axis, and then every time it moves an additional distance of  $\lambda/2$ . The basic precision of this measurements is considered to be  $\lambda/2$  when no additional algorithms are applied. The example of such measurements will be shown in Chapter 3).

The SM effect can also be applied to measure small, less than  $\lambda/(2n_{ext})$  displacements, and these measurements are usually aimed at vibration studies [51, 52]. The principle of the measurement in this case is to achieve the same phase change of  $2\pi$  by exerting an external influence on the phase. For example, by adjusting the length of the external cavity (i.e.  $l_{ext} = l_{ext0} + \Delta l_{ext} \sim \lambda/(2n_{ext})$ ) or by tuning the lasing frequency, by modulation of the injection current [51–54]. The precision of the vibration measurements can be improved up to  $\lambda/12$ .

### 1.5.2 Different Reflectivity and Speckles Influence

The operation of the SM sensor is directly affected by the properties of the light which is coupled back into the cavity. For example, in the case of mirrors, or other surfaces with low roughness, the amount of reflected light can be very high, leading to strong feedback for an SM sensor with  $C \gg 1$ . When SM measurements require a lower level of feedback such as weak feedback, additional filters can be placed between the mirror and the LD cavity to reduce the amount of light entering back into the cavity.

The nature of the reflection off a mirror is such that additional alignment of the system might be required to obtain the SM effect. However, the SM technique can be applied without additional alignment and it can be performed at any angle, if a rough

surface is used as a target. Light scatters off a rough surface in all directions; this is in contrast with smooth surfaces where light reflects mainly in one direction. However, due to random interference of light scattered off the rough surface, speckles [10] are observed affecting the shape of the received SM signal, causing errors in measurements [55]. Speckles appear when light interacts with any kind of object causing such interference. For example, light scattering off a rough surface produces secondary spherical waves, and their interaction with each other and the initial beam produces the speckles. When light travels through a liquid or gas, the interaction between the light and particles randomly changes the phase and amplitude of the scattered light [10], resulting in speckles in the propagating media. An ideal case of an SM signal is a harmonic function with a constant amplitude and a single peak in the frequency domain. In the presence of speckles, the amplitude and the phase of the SM signal are modulated which leads to spectral broadening and additional noises in the signal [56].

The speckle effect in SM can be used not only for a displacement measurement [57], but also for surface classification [58], as well as length measurements of a moving object [59].

### 1.5.3 Self-Mixing Technique as LDV for Velocity Measurement

An SM signal is the result of mixing the initial lasing field with a portion of the light which is coupled back into the cavity. Since the SM sensor is fundamentally similar to LDV, the same principle and equations can be used for the description of the sensor behaviour. For an SM system, the source of the light and the receiver of the light are the same object. Hence, the difference between two vectors in Eq. 1.4 is equal to double the magnitude of the velocity vector in the direction of the propagation of light, leading to

$$f = 2 \frac{\vec{n} \cdot \vec{v}}{\lambda}. \quad (1.42)$$

At the same time, the SM theory showed that the spectrum of the laser changes due to the interaction between the lasing field and the small back-scattered field, which re-enters the laser cavity leading to the SM effect. When the target moves with velocity  $\vec{v}$ , the backscattered light is Doppler-shifted in frequency, see Eq. 1.40. The simplest way to obtain an expression for the Doppler shift of the SM signal is from Eq. 1.39 and 1.40. The Doppler shift of the periodic optical power fluctuation is given by Eq. 1.42.

Equation 1.42 shows the shift in frequency at the moment of scattering. In general, both parameters  $\vec{v}$  and hence  $f$  depend on time, which results in a frequency and time modulated SM signal [60]. The information on the displacement, velocity, and acceleration can be obtained if the signal from the SM sensor is analysed the right way depending on the parameter of the interest.

A range of articles are dedicated to measuring the velocity of solid objects, see for example [44, 59]. The SM sensor was successfully applied for measuring velocities up to 25 m/s with a rotating disc covered with white paper as a target [61].

#### 1.5.4 Flow Measurements in Self-Mixing and Seeding Particles

The SM technique is used not only for the detection of velocity of solids, but also for liquid targets. In the case of fluids, the light scatters off particles moving within the measurable volume. These particles can be natural molecules of the fluid, for example H<sub>2</sub>O in water. They can also be added or seeded particles. For example, blood consists of around 50% water, 45% red blood cells, and 5% of other elements. In this case, the red blood cells can be considered as seeders for water when analysing the scattering process. Seeders can be artificially added to the underlying liquid for the improvement of scattering effects. Here and throughout the thesis, the scattering particles within the underlying liquid will be referred to as seeders or seeding particles. Water is the most common liquid used which is seeded. Further, the natural mix of particles in the fluid can also be referred to as a seeding material, for example milk or blood.

The main purpose for most studies within SM technique are medical applications, hence most of the literature focuses on blood flow rate measurements. A wide range of works within the field of velocimetry using the SM effect have been dedicated to this [43, 59, 62–66]. SM fluid velocity measurements are mainly aimed at biological applications such as blood characterisation [65] and molecular dynamics [59]. The measurements of blood flow in a tube [43] and in vivo in human fingertips [62] were demonstrated as well. In the literature milk [43, 62, 63, 65] and polystyrene (latex) spheres [43, 59, 66–68] are the most commonly used materials for seeding the water. A list of previous experiments which can be found in the literature including the seeding materials with their size and concentration and properties of the laser system used in experiments are presented in Table 1.3.

One of the most common methods for velocity mapping of fluids and gases is PIV [9]. The technique is based on the analysis of the displacement of the net movement of the seeding particles within the measured flow. Hence, a substantial amount of research into the seeding materials and seeding techniques has been conducted for PIV applications [2, 62, 73, 74]. The main seeding materials and their sizes are presented in Table 1.4. Also shown in the table are the range of different materials which have been used for seeding both liquids and gases, among which are solid, liquid and gaseous types of seeders. In PIV, the seeding particles are usually referred to as tracing particles.

The diameter of the polystyrene particles in SM experiments varies from 110 nm [70] up to 1.23  $\mu\text{m}$  [66], compared to the size of the polystyrene seeders used in fluid PIV experiments which ranges from 10  $\mu\text{m}$  to 500  $\mu\text{m}$ . The concentration of the seeders in water varied across different experiments with a minimum concentration of 0.05% of polystyrene seeders in water [70]. An SM system for velocity detection is more sensitive to scattered light, so smaller seeding particles can be used for velocimetry. The main and easy-to-use seeding material is milk. The velocity measurements demonstrated in recent published papers do not exceed more than 15 cm/s for milk as seeders [43], 17 cm/s with polystyrene spheres as seeders of 1.23  $\mu\text{m}$  size (and with lower velocities in case of the

TABLE 1.3: Liquid flow velocity measurements using the self-mixing technique. Here, the seeding materials and their concentrations, range of measured velocities along with the properties of the laser system are shown. All lasers listed in the table are LDs. VCSEL is a vertical-cavity surface-emitting laser, which is a type of semiconductor LD. The last row, which is separated from the others, is from published articles which form part of the work presented in this thesis. These results are shown to give an up-to-date account of the literature on velocity measurements of fluids using the self-mixing effect.

Seeding material	Concentration	Velocities range	Laser system
Milk	2%	1-18 mm/s	VCSEL, 667 nm,
Milk with Xanthan gum [62]	2%	2-15 mm/s	1.8 mA, 80° and 25°
Milk [63]	100% 10% 1% 0.2%	0.5-52 mm/s 0.5-43 mm/s 0.9-17 mm/s 0.9-6.9 mm/s	VCSEL, 850 nm, 4.3 mA, 74°
Polystyrene beads, 1.15 $\mu\text{m}$ [67]	< 0.5%	20 mm/s	785 nm, 25 mA, close to 90° and 60°
Intralip, 100 nm [69] Blood [65] Milk (as reference)	0.5% and 1.5%	22-300 mm/s	Superluminescent LD, 836 nm, 85°
Polystyrene, 950 nm	$5 \cdot 10^{-4} \mu\text{m}^{-2}$	0.9-4 cm/s (3 mW), up to 15 cm/s	780 nm, 44 mA 75° Upstream fibre
Milk, 4 $\mu\text{m}$ [43]			
Polystyrene spheres, 1.23 $\mu\text{m}$ Blood [66]	$2.8 \cdot 10^{-2} \mu\text{m}^{-2}$ $5 \cdot 10^{-2} \mu\text{m}^{-2}$	up to 17 cm/s	820 nm, 35 mA, fibre in the flow
Polystyrene spheres, (with glycerol) 262 nm, 110 nm [70]	0.05%	up to 72 mm/s	1064 nm, 30 mW, 10°
Milk, 3-6 $\mu\text{m}$ [71] TiO <sub>2</sub> , 0.5-1 $\mu\text{m}$ [72]	< 0.5% < 0.5%	1-20 cm/s 10-110 cm/s	650 nm, 25 mA, different angles

smaller sizes of the seeders) [66], and up to 35 cm/s for blood measurements at a very high concentration and without specific verification of the experimental results [66].

Together with the size, shape and orientation of seeders, scattering efficiency is a function of the ratio of the refractive index of the seeders and surrounding area (to be discussed in Chapter 2). In the case of gaseous targets, using the same types of seeding particles might bring the scattering efficiency to an even higher level due to the indices ratio. Since the refractive index of air is considerably less than that of water, the amount of light scattered off small particles of the same size in air is at least one order of magnitude higher than in water [18]. Furthermore, in the case of gases the size of the seeders can be even smaller. This is demonstrated in Table 1.4 which shows the sizes of seeding particles for a PIV system for liquid and gas flows where the same type of laser and measuring system are used for velocimetry.

The SM system applies homodyne detection, so that the reference source of light is derived from the same source before and after detection. Moreover, the amplification of

TABLE 1.4: Seeding material for liquid and gas flows in PIV measurements mostly with 532 nm laser light [9, 73, 74] and other lasers [2, 62].

Type	Material	Mean diameter of seeders, $\mu\text{m}$	
		in liquid flows	in gas flows
Solid	Polystyrene	10-500	0.5-10
	Alumina $\text{Al}_2\text{O}_3$	2-10	0.2-5
	Titanium dioxide $\text{TiO}_2$	0.5-2	0.1-5
	Carbon dioxide $\text{CO}_2$		5-15
	Glass spheres	0.53-100	0.2-30
	Granules for synthetic coatings	10-500	10-50
	Diethylphthalate		1-10
	Smoke		< 1
Liquid	Different oils	1-500	0.5-10
	Di-ethyl-hexyl-sebacate		0.5-1.5
	Helium-filled soap bubbles		1,000-3,000
	Fluorescent dyes in glycol/water	0.2-10	0.1-5
Gaseous	Oxygen bubbles	50-1,000	
	Hydrogen bubbles	50-1,000	

the light occurs inside the cavity. As a result the SM system depends on the amount of light coupled back into the cavity in relation to the initial light so powerful lasers are not required. PIV systems, on the other hand, require more powerful laser systems as it is the absolute amount of scattered light which is needed for the PIV to work correctly.

### 1.5.5 Coupling of Scattered Light

If the laser has a beam divergence half-opening angle  $\Delta\Theta$ , the power of the laser beam  $P_R$  at a distance  $R$  is [2]:

$$P_R = \frac{1}{R^2 \Delta\Theta^2}. \quad (1.43)$$

The light scatters on the moving target. The power of scattered light  $P_S$  is proportional to the initial laser power  $P_L$  and the scattering cross section  $\sigma$ :

$$P_S = \frac{P_L \sigma}{R^2 \Delta\Theta^2}. \quad (1.44)$$

The power is distributed over  $4\pi$ . The detector system can detect the scattered part of light  $D^2/R^2$ , where  $D$  is the diameter of the detecting optics. The light loss of the optical detecting system can be characterised by the coefficient  $\tilde{\xi}$ . As a result, when taking into account the optics and laser light properties, the detectable power of the light is given by:

$$P_S = P_L \frac{\sigma}{R^2 \Delta\Theta^2} \frac{1}{4\pi} \frac{D^2}{R^2} \tilde{\xi}. \quad (1.45)$$

### 1.5.6 Important Laser Parameters for Optical Feedback

The self-mixing method implies that the laser system responds to the oscillation of the coupled back light which was scattered off a moving object at a frequency proportional

to the velocity of the target. The properties of the laser system should be adequate to achieve the aim of the measurements.

From the Lang-Kobayashi model, the common behaviour of the dynamics of the single-mode diode laser was studied. First of all, it is important to understand the difference between different modes which can occur in a laser system under an SM effect.

1. The laser can be single mode or multi-mode, and modes can be longitudinal and transverse.
2. The external cavity adds possible modes, which the laser can switch between.

The relaxation processes in a laser define such an important parameter of a laser system as a relaxation frequency. It is the oscillation with which the inversion population decay to the stable energy state, or it is the frequency with which the photon population can oscillate [1]. All modulation processes in a laser are limited by this frequency, because the system cannot respond any faster. Time relaxation of the diode laser is of the order of nanoseconds, the quantum cascade laser time relaxation is of the order of picoseconds, for solid-state lasers it is of the order of picoseconds [1].

The possible modes which a laser can generate are solutions to Eq. 1.13, 1.16, and 1.30. Depending on the gain of the laser, the laser can produce more than one mode. Under feedback, additional terms appear in Eq. 1.14. Therefore, there are further solutions which correspond to new modes which can be seen as new points in the solutions of the equations, see Fig. 1.8. Any kind of perturbation, even very weak, causes a change in the behaviour of the laser system. Depending on the amount of feedback (weak, moderate, or strong), the solution can be stable or unstable. In the case of a stable solution, the SM system returns to the stable point with the relaxation oscillation frequency [17], see possible solution in Fig. 1.8. In the case of strong feedback, a laser enters the unstable unpredictable regime of work.

Hopping between stable and unstable regimes can occur quickly depending on different parameters such as the amount of light and the distance between the laser and the target, see Fig. 1.10. As a result, the laser can switch immediately from a regime of moderate feedback to one of strong feedback, leading to chaotic motion as opposed to returning the stable regime with one working mode of the laser [22]. In some specific cases of unstable regimes a collapse of the coherence can occur [75].

### 1.5.7 Types of Lasers Used in Self-Mixing Measurements

Table 1.3 lists laser systems which have been used in SM for flow characterisation. Some lasers show better performance for the SM effect than others. A list of advantages and disadvantages for lasers used for SM measurements of solids and flows follows.

A DFB laser with a 1.31  $\mu\text{m}$  [41] wavelength is potentially suitable for measurements. It does not have a locked single wavelength, however, only a small variation of the 0.01 nm per degree wavelength occurs, which is an advantage for an SM system. Moreover, it can be stabilised by temperature control. The only problem was it was difficult to achieve

a stable repeatable signal and the signal-to-noise ratio was low. Using this particular laser, the measurements can be done in two dimensions, both for the target displacement and the target rotation [41].

Fibre pigtailed lasers were used at a wavelength of  $1.3\ \mu\text{m}$  and  $1.55\ \mu\text{m}$  [66]. Fibre lasers can deliver light to any point, which is a big advantage for a sensor. In the case of a fibre pigtailed laser, the divergence of the beam is applied for better motion diagnostics of rotated targets. If the light is not focused at one point, a part of scattered light comes from different angles. It allows to detect the change in the position of the target in several dimensions using just one light source. However, some effects from the curvature of the fibre can occur [68]. When the fibre is bent the delivery system does not provide a total reflection of the light beam. As a result, part of the optical power can be lost. This is equivalent to applying a filter, moreover the bending of the fibre is difficult to adjust.

VCSELs have become popular for SM studies, and lasers with the wavelength of  $780\ \text{nm}$  [66],  $667\ \text{nm}$  [74], and  $850\ \text{nm}$  [64] have been used for fluid measurements. The surface of emission for VCSEL lasers is large, so VCSEL is a multimode laser. The disadvantages of using these lasers were the difficulties encountered in obtaining a stable signal due to the change in polarisation occurring during the measurements.

Quantum cascade lasers are more stable, in terms of fluctuation of wavelength and power, but not in terms of SM signal [76]. This laser was not used in many measurements.

A FP laser with a wavelength of  $650 - 670\ \text{nm}$  and  $830\ \text{nm}$  was used in some experiments, as they are the simplest and most stable. However, the problem of mode hopping can appear, and other longitudinal modes can also oscillate [75] causing the perturbation of the laser dynamic under feedback. So far, these lasers are the most suitable to use for SM measurements.

## 1.6 Conclusion

This thesis was focused on a new laser-based method for measuring different parameters such as the displacement and velocity of solid and fluid targets and its potential application for particle accelerators. It is based on the laser diode, and is known as the self-mixing technique. There is an increasing demand in the detection and further understanding of solid and fluid properties, such as distances, velocities, temperature, etc. The main methods to measure these properties are through various optical diagnostics due to their accuracy and mostly non-invasive nature. Lasers are powerful tools which are ideally suited for measurements due to their unique characteristics.

For velocity measurements, the Doppler effect is the main phenomenon used in diagnostics, such as LDV. Another popular technique is PIV, which is based on laser light scattering off added seeding particles, or tracing particles. This Chapter has presented an introduction into SM sensors and the self-mixing phenomenon on which they are

based, as well as various applications in which they are used. SM sensors combine the principles of LDV and PIV together.

The SM phenomenon occurs when reflected or scattered laser light is coupled back into the cavity and interacts with the laser light inside the cavity. The backscattered light's wavelength is shifted due to the Doppler effect and the intensity of the backscattered light depends on the particulars of the target i.e. optical properties etc. The SM phenomenon is a non-linear effect which influences both the wavelength of the light and its power fluctuation. The interaction within the cavity causes backscattered light to be amplified, so the sensor does not require a powerful laser and there is no need for a complex optical system, as in the case of PIV or other typical interferometers.

The SM technique has previously been used for displacement or small velocity measurements. Velocimetry sensors which exploit the self-mixing effect have attracted growing interest in recent years, resulting in a wealth of publications trying to optimise a sensing technique for different purposes [77]. The velocity of a target can be calculated from the power spectrum of the SM signal. This Chapter contains a review on the velocity range SM sensors have so far been applied to; velocities of up to 25 m/s for solid targets and up to 30 cm/s for fluids, and this technique was never applied to gaseous targets. These limitations are going to be investigated in following Chapters. Techniques which allow velocities to be measured beyond upper velocity limits of previous SM studies will be presented in the following chapters. The main advantage of an SM sensor with respect to traditional methods is the possibility of an unambiguous measurement from a single interferometric channel. Sensors based on SM compared to other techniques are compact, less expensive and are easier to align.

The review presented in this Chapter on different light sources which can be used in LDV together with information on laser systems used for SM sensors demonstrates why LDs are used for SM experiments presented in this thesis. Since the SM sensor when applied to fluids is based on light scattering off seeding particles, the review on tracing particles for PIV systems gave an indication on which is the best seeding material to use. Moreover, this information has shown which seeders have already worked successfully for SM velocity measurements. Seeding particles are available in different diameters and with different reflective properties, so detailed study of them is essential, which is covered in the next Chapter.



## Chapter 2

# Laser Light Scattering for Self-Mixing Sensors

In this chapter an overview of scattering processes is presented. This includes Rayleigh and Mie theory for one motionless particle which the light scatters off. Within this chapter calculations of scattering parameters for different types of particles are given with a focus on the specific particles which are used in experiments presented in later chapters. The second part of this chapter addresses light scattering off a surface and off multiple particles, which are set in motion, with the expected spectrum of light after scattering derived from basic theory. Simulations of the possible overall spectra which can be obtained from different targets in experiments with an SM sensor are presented. This addresses the interaction between light and a rotating disc as well as between light and a fluid channel. The chapter concludes with a study into the influence from a distribution of velocities and the size of the laser spot on the overall spectrum for an SM sensor.

### 2.1 Light Scattering

Self-mixing operates on the principle that a proportion of scattered light is coupled back into the cavity of the laser. The scattering process influences the amount of feedback, which determines the type of SM signal that is obtained. In addition, scattering also affects the backscattered light spectrum and hence the spectrum of the signal measured during experiments. The scattering media, including seeding particles, need to be accounted for when characterising the SM signal. The characteristics of the signal can then be used for the accurate calculation of the experimental parameters. These include the displacement of objects, the velocities of solid and fluid targets, and the concentration of scattering particles in the case of flows.

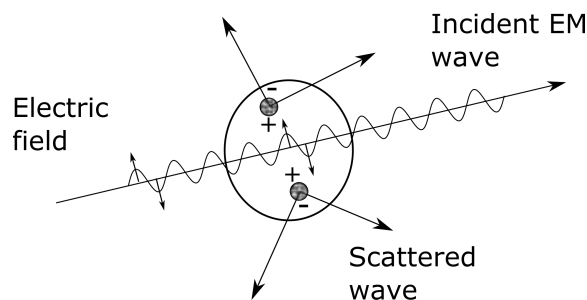


FIGURE 2.1: Light scattered by an induced dipole moment caused by the incident EM field.

### 2.1.1 Light Scattering off Motionless Particles

Scattering can be described as the redirection of light when an electromagnetic (EM) wave encounters an obstacle in its path. Scattering involves the excitation of elementary charges, i.e. the electron cloud, of matter, which are set into an oscillatory motion by an incident EM field. The perturbation of the electron cloud causes a periodic separation of the charges within the molecule, resulting in a dipole moment. Accelerated electric charges, or oscillating induced dipoles, radiate (re-emit) EM energy (secondary radiation) in all directions, i.e. the EM wave is scattered off the matter. The scattering process is usually described by Maxwell's equations.

In summary, scattering is not limited to bouncing or reflection of an EM field off surface or particles, but it is a complex interaction between the EM field and the molecular/atomic structure of the scattering media, see Fig. 2.1. When an EM wave interacts with matter, two main processes are involved: one proportion of the light participates in the excitation, while the remaining light does not interact with the matter at all.

The scattering process is historically described by two main theories. The first is Rayleigh scattering, which was originally formulated and applied only to light scattering off small, non-absorbing (dielectric) spherical particles [78], which are the limitation of its usage. The second is Mie theory which was developed by Gustav Mie in 1906 [79] to describe scattered intensity of light as a function of the scattering angle and is valid for any kind of particle. Mie theory is not limited in its usage in regards to the size, shape and optical properties of particles it is applied to. For this reason, it is possible to formulate Rayleigh scattering theory from Mie theory.

Scattering occurs when light interacts with an object, which, as a unit of scattering, will hence be called a scattering particle. Scattering particles are assumed to be spherical, from which more complicated scattering particles can be built, such as scattering particles of any shape, agglomerations of particles, refraction gradients, temperature gradients, and density gradients, etc. The EM constants are functions of the radius of these spherical particles. Differences in the EM constants result in an optical heterogeneity of the particles.

In general, the scattering particle is not spherical and not homogeneous, so the properties of the scattered light are defined by:

1. The EM constants of the matter, i.e. permeability and permittivity.
2. Shape and size of scattering obstacles or scattering particles.
3. Orientation with the respect to the incident light.

These properties define the fraction of light that is involved in excitation and then in the scattering process. In the case of an ensemble of scattering particles, the following should also be accounted for:

4. Concentration of the scattering particles.
5. The size distribution of the particles (including agglomerations of particles if applicable).
6. The physical and chemical properties of the particles.

In general, Mie theory describes the scattering patterns from a spherical isotropic particle illuminated by a monochromatic plane wave. It consists of a series of approximations which are solutions to Maxwell's equations. Mathematically, the simplest case can be found by approximating size parameters and refractive index relations. The size parameter is usually given by the expression [80]:

$$q = \frac{2R}{\lambda_0 m_0}, \quad (2.1)$$

where  $R$  is the characteristic size (spherical radius) of the scattering particles,  $\lambda_0$  is the wavelength of the incident light with respect to vacuum, and  $m_0$  is the refractive index of the surrounding area. The refractive index of the scattering particles is usually presented in complex notation:

$$m = n - i \cdot k, |m| = \sqrt{n^2 + k^2}, \quad (2.2)$$

where  $n$  refers to refraction of light and  $k$  to absorption. The absorption coefficient is usually equal to  $4k/\lambda$ . While  $k$  is never exactly equal to zero for any material, it is close to zero for dielectric materials. Both  $n$  and  $k$  depend on the wavelength of the light.  $q$  and  $m$  are usually used for identifying the appropriate method for calculating the scattering process. Figure 2.2 subdivides Mie theory into simplified models for the range of refractive indices and particle sizes.

Depending on the value of the size parameter  $q$ , the following scattering theories can be applied [80, 82].

$q \ll 1$  **and**  $|m|q \ll 1$ : **Rayleigh scattering**. This theory is typically applied to particles that are small relative to the wavelength of the impinging light. The particles encounter a uniform electric field around themselves since the penetration time is significantly less than the period of oscillation of the EM field. The intensity of the scattered light is proportional to the size of the scattering particles ( $\propto R^2$ ) and strongly

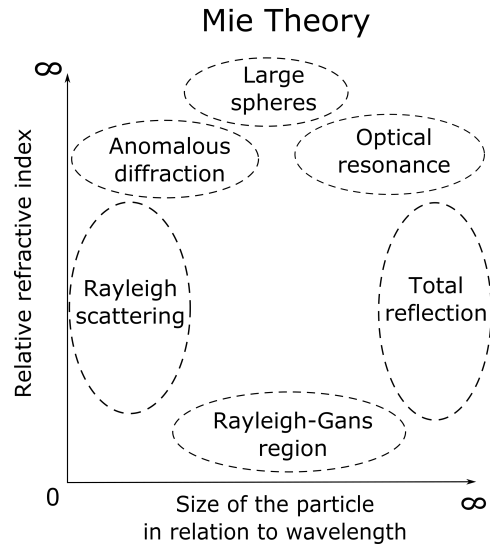


FIGURE 2.2: Schematic representation of Mie theory subdivided into simplified theories, which are derived depending on the size of the particles in relation to the wavelength and the refractive index [81].

depends on the wavelength of the incident light ( $\propto \lambda^{-4}$ ). A typical scatterer with a size in the range of 1 - 100 nm for light of wavelength 650 nm falls under this theory. For example, the size of DNA is 1 - 4 nm, and ink particles are of 45 - 100 nm, hence Rayleigh scattering theory can be applied to such particles. Light scattering off gases can also be described by Rayleigh scattering.

$q \gg 1$ : **Total reflection.** For this theory, the size of the particles is significantly larger than the wavelength of the incident light. The solution can usually be found using the Huygens-Fresnel principle [3]. This theory usually includes the reflection and refraction off a common boundary between two different phases of matter. Examples include a solid and a liquid, two liquids with different refractive indices, a liquid and a vacuum, etc. The intensity of the scattered light is not strongly dependent on the size of the particles, but is a function of the refractive index and the incident light angle. This case can also be referred to as geometrical optics, and hence it can describe the reflection from a mirror.

$|m - 1| \ll 1$  and  $|m - 1| \cdot q \ll 1$ : **The Rayleigh-Gans Approximation.** This theory is applied to small particles with a refractive index close to unity. Moreover, it can be applied to differently shaped particles. The approximation only accounts for the first order of the Mie theory solution and ignores higher orders. This implies that the resultant scattering is a superposition of the scattered fields produced by different parts of the particle, while the interaction between the scattered fields is ignored. The resultant scattering function is more complex than the Rayleigh approximation implies. The scattering function is not monotonic, but has a number of extrema. Examples include coiled polymer molecules and organic particles suspended in water. The same approximation is used for studying polydisperse systems under small angle X-ray scattering.

$q \approx 1$ : **General case.** If the size of the scattering particle is comparable to the wavelength of scattered light, the full Mie theory needs to be applied. Current usage of Mie theory refers to any particles of any size. The solution can be implemented in a number of programming languages such as MatLab [83], Mathematica and Fortran [84, 85], etc. A MatLab code has been developed [83] which calculates the scattering parameters of a spherical particle with different magnetic permeabilities compared to that of its surroundings. This code was modified and then used to generate the outputs presented in this chapter. These include the angular distribution of the intensity of the scattered light, the cross section, the absorption, and the scattering efficiency. The intensity of the scattered light is proportional to the size of the particles. However, the intensity of the scattered light strongly depends on the angle, and even small variations of size lead to a significant change of the intensity of the scattered light. Examples of particles include milk fat globules which have a typical size of around 1 - 10  $\mu\text{m}$ , and red blood cells which are around 10  $\mu\text{m}$  in size.

In general, the index of refraction is a complex quantity. Hence the total extinction cross section for the particle is comprised of energy lost from the incident beam, both by scattering (*sca*) and by absorption (*abs*):

$$\sigma_{ext} = \sigma_{sca} + \sigma_{abs}, \quad (2.3)$$

$$\sigma_{sca} = \frac{W_{sca}}{I_{inc}}, \quad (2.4)$$

$$\sigma_{ext} = \frac{W_{ext}}{I_{inc}}. \quad (2.5)$$

Here  $I_{inc}$  is the intensity of the incident light illuminating the surface of the particle, while  $W_{sca}$  and  $W_{ext}$  represent the scattered and extinction energies respectively, which can be found using Maxwell's equations.  $\sigma_{sca}$  represents the intensity of light scattered in all directions for an incident wave of unit intensity. This can also be presented as  $C_{sca}$  [86]. The key parameters for Mie scattering calculations, following van de Hulst [82], are the Mie coefficients  $a_n$  and  $b_n$  for obtaining the amplitudes of the scattered field, and  $c_n$  and  $d_n$  for calculating the amplitudes of the internal field, respectively [82]. The efficiency factor  $Q_{sca}$  for a particular sphere gives the ratio of the scattering cross section to geometrical cross section ( $\pi R^2$ ):

$$Q_{sca} = \frac{\sigma_{sca}}{\pi R^2} = \frac{2}{q^2} \sum_{n=1}^{\infty} (2n+1)(|a_n|^2 + |b_n|^2). \quad (2.6)$$

The extinction efficiency is derived from the Extinction Theorem or Forward-Scattering Theorem [82], and can be presented as:

$$Q_{ext} = \frac{2}{q^2} \sum_{n=1}^{\infty} (2n+1) \text{Re}(a_n + b_n). \quad (2.7)$$

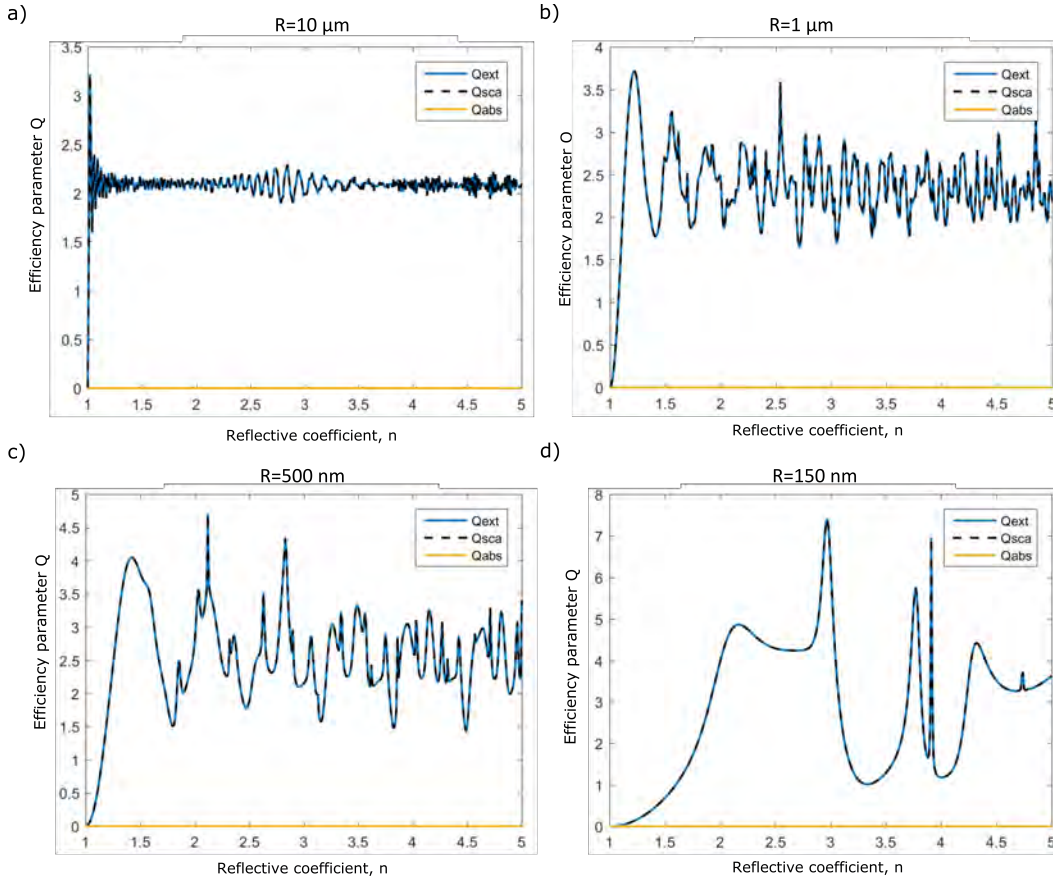


FIGURE 2.3: The Mie efficiency function for a wavelength of 650 nm for different reflective coefficients with an absorption coefficient equal to 0. The calculation is performed for the different particle sizes: a)  $R = 10 \mu\text{m}$ ; b)  $R = 1 \mu\text{m}$ ; c)  $R = 500 \text{ nm}$ ; d)  $R = 150 \text{ nm}$ .

The Mie efficiencies are calculated according to Eq. 2.6 and 2.7 and shown in Fig. 2.3. The dependencies of the efficiencies on the reflective coefficients were obtained for the particle sizes of  $10 \mu\text{m}$ ,  $1 \mu\text{m}$ ,  $500 \text{ nm}$ , and  $150 \text{ nm}$ , see Fig. 2.3. The efficiency changes dramatically for different sizes and refractive indices. The absorption coefficient is equal to zero, therefore, the extinction energy is equal to the scattered energy.

The backscattering and forward scattering efficiencies can be evaluated [82] and are given as:

$$Q_{BS} = \frac{1}{q^2} \left| \sum_{n=1}^{\infty} (2n+1)(-1)^n (a_n - b_n) \right|^2, \quad (2.8)$$

$$Q_{FS} = \frac{1}{q^2} \left| \sum_{n=1}^{\infty} (2n+1)(a_n + b_n) \right|^2. \quad (2.9)$$

Using these functions, a calculation of the scattering efficiency can be performed for particles of any size and with any optical properties. From these calculations, the amount of backscattered light can be estimated. Based on this output, the optical properties and size of the particles, which will potentially be used as seeders, can be chosen. Figure 2.4

shows the forward scattering efficiency, the backscattering efficiency, and the fraction of the two. For larger particles, the forward scattered light is dominant over the backscattered light, while for smaller particles, the level of backscattered and forward scattered light has approximately the same magnitude. The scattering process comprises of a perturbation of the electron cloud leading to a dipole moment, which, when excited by an incident wave, re-emits the EM field, see Fig 2.1. One dipole scatters waves in all directions. While in the case of two dipoles, the resultant wave, as a sum of scattered waves, depends on the separation of the dipoles and the direction of scattering [82, 87]. These radiating EM waves are scattered waves, and the superposition of all waves is what is observed [88]. In the case of forward scattering, waves produced as a result of scattering off the dipole are in phase with each other due to the direction of the incident wave. However, for any other direction this varies significantly depending on the phase difference. Particles larger compared to the wavelength of the incident wave allow more dipoles to be induced which, when re-emitted, collectively scatter in the forwards direction relative to the backward one. In the case of smaller particles the dipole separation is much smaller than the wavelength and hence the phase differences between scattered waves are small resulting in a uniform distribution of the scattering pattern. The resulting scattered intensity angular distribution is averaged over all orientation of the dipoles [82]. This effect can be seen from the angular distribution in Fig. 2.6 calculated for  $\text{TiO}_2$ .

### 2.1.2 Light Scattering: Different Seeding Particles for Self-Mixing Sensor Experiments

Different types of scattering particles used for the SM technique are shown in Table 1.3. As one of the main focuses of this work is to measure high velocities of fluids and gases, it is important to find the most efficient seeding particles or materials to obtain the required level of feedback to operate the SM sensor. The level of feedback is calculated as the ratio of the intensity of the light which is coupled back into the laser cavity to the initially emitted intensity of the laser light. A value of -123 dB is required [89] for a weak feedback regime to be obtained.

The most commonly used materials for seeding are milk, blood and polystyrene spheres of various sizes. Using information from Tables 1.4 and 1.3, hypotheses can be made about different seeding particles that can be used for testing an SM sensor.

The calculation of the scattering efficiency for different seeding particles was performed using a Mie solution in a MatLab program, modified from [83]. In order to optimise the choice of the scattering particles, the following parameters were altered: the reflective coefficient, the size of the particles, and the wavelength of the incident light. The refraction and absorption coefficients for different particles were obtained from [90].

The real part  $n$  of the complex refractive index describes the reflectivity of the material [3]. Most transparent materials in the visible range of the spectrum have a

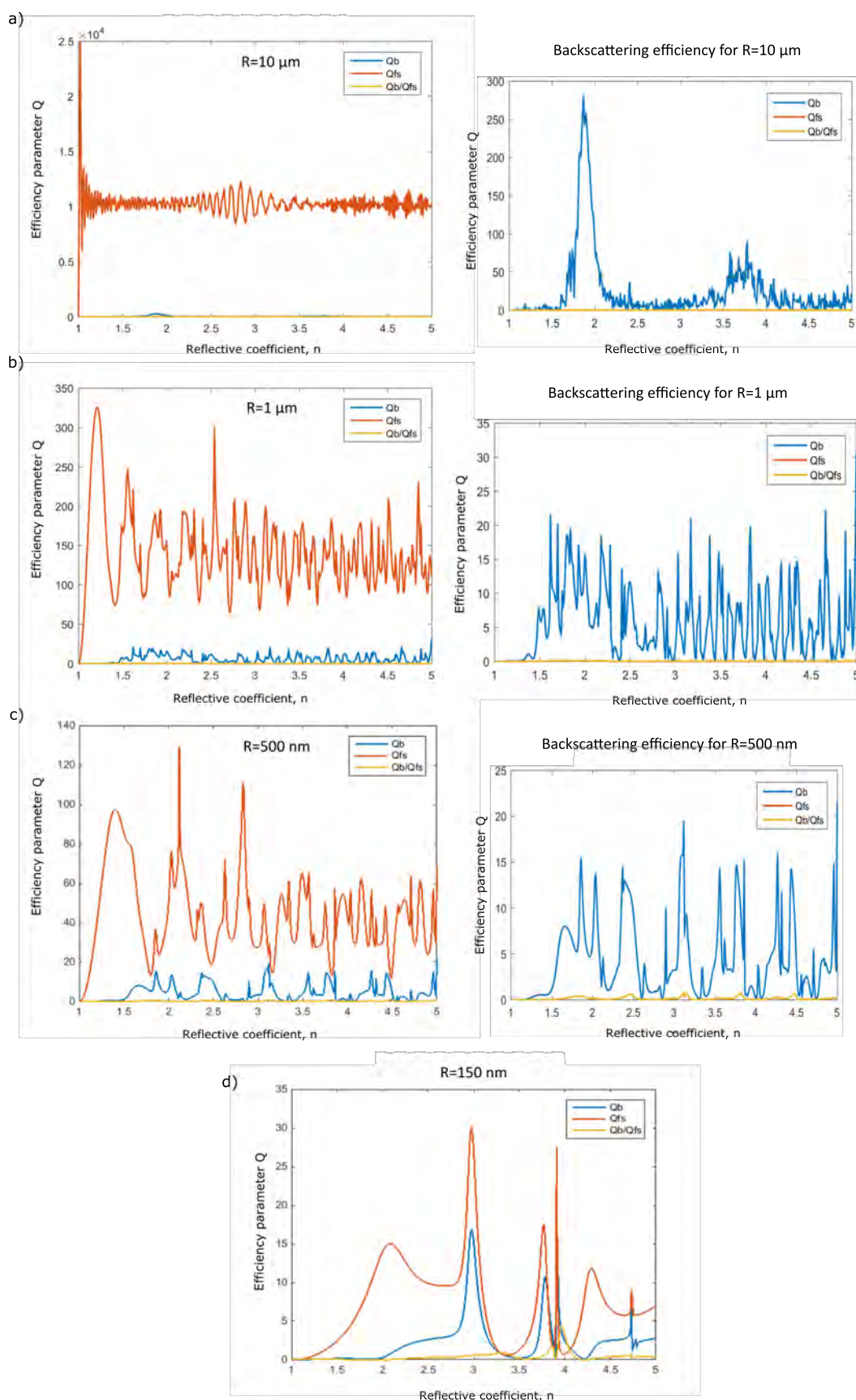


FIGURE 2.4: The backscattering efficiency (blue), the forward scattering efficiency (red), and the fraction of the two (yellow) functions for different refractive indices. The calculations were performed for a 650 nm wavelength light when scattered off particles with following different sizes: a)  $R = 10\ \mu\text{m}$ ; b)  $R = 1\ \mu\text{m}$ ; c)  $R = 500\ \text{nm}$ ; d)  $R = 150\ \text{nm}$ .

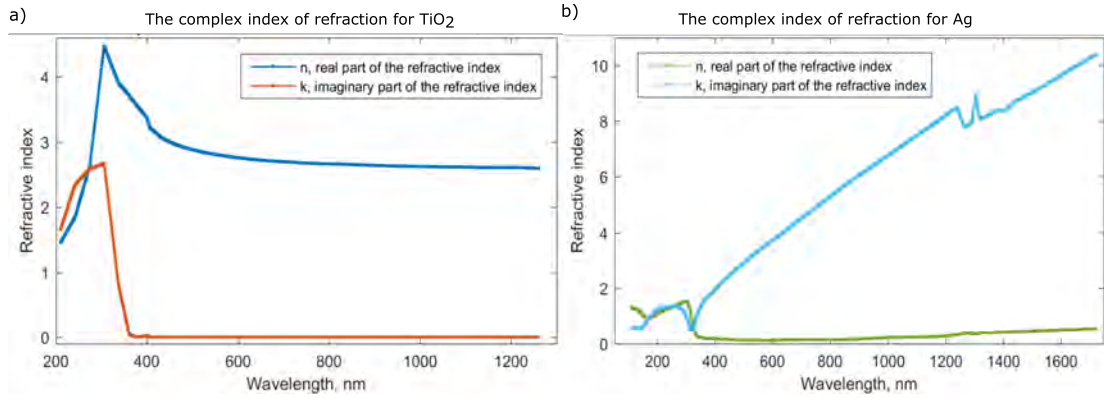


FIGURE 2.5: Complex refractive index for a)  $\text{TiO}_2$  and b) Ag as a function of the wavelength of the incident light [90].

value between 1 and 2. Most liquids and solids have a refractive index larger than 1.3. Gases at atmospheric pressure have values close to 1. Diamond has a very high refractive index of 2.42. The imaginary part,  $k$ , of the refractive index describes the attenuation of electromagnetic waves in the material. This is known as a damping constant, attenuation index, extinction coefficient, or absorption coefficient.

#### Titanium Dioxide, $\text{TiO}_2$

The geometry of an SM sensor is such that light which is coupled back into the cavity is always backscattered unless the system is modified with additional components, for example lenses, for capturing more scattered light in the SM cavity. The light is coupled within a solid angle that is defined by the focusing optics of the system.

The dependence of both the real and imaginary parts of the complex reflective index for  $\text{TiO}_2$  is presented in Fig. 2.5 (a). For a wavelength of 650 nm, the complex refractive index is  $m = 2.7152 + 0 \cdot i$  [90], where the parameter  $k = 0$  denotes that the light is not absorbed by the particle at this wavelength. Figure 2.5 (a) shows that the refractive index of  $\text{TiO}_2$  within the visible spectrum remains constant, so the material reflects or scatters all wavelengths with equal intensity. Consequently, the material has a white colour.

Figure 2.6 shows the angular distribution of the scattering efficiency obtained for  $\text{TiO}_2$  particles. The distribution is obtained for light, with a wavelength of 650 nm and a fixed angle of incidence, which scatters off the particles of different sizes. While the majority of the light scatters in the forwards direction, a proportion of the light is backscattered. For ideally spherical seeding particles, as the particle size decreases the proportion of backscattered light increases though the absolute amount of scattered light decreases.

Figure 2.7 shows the distribution of the forward scattering and backscattering efficiencies for different sized particles and different wavelengths. The distributions were calculated based on Eq. 2.8 and 2.9. The efficiency varies with the size of the seeding particle, even if the shape of the particle is spherical. Using these calculations, the

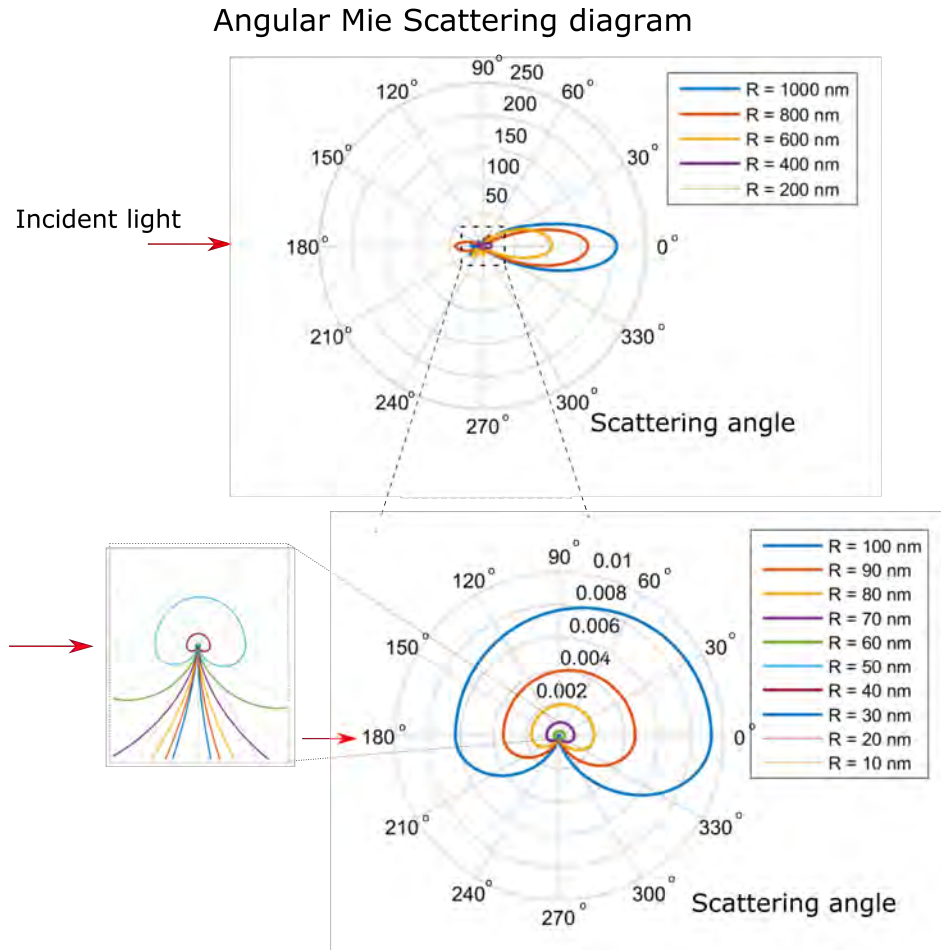


FIGURE 2.6: Angular distribution of the scattered power: angular Mie-scattering diagram for TiO<sub>2</sub> for light with a wavelength of 650 nm. Red arrows indicate the angle of incident light. The top plot shows the angular distribution for larger particles (> 200 nm), while the bottom plot shows angular distribution for smaller particles (< 100 nm). Most of the light scatters forwards, with only a small proportion of the power scattered back into the direction of incident light.

assumption on the size of the most efficiently scattering particle for a specific wavelength can be made, and vice versa. Knowing the size of the scattering particles, an approximate estimation of the scattering efficiency for the different wavelengths can be obtained. Figure 2.8 presents example calculations of the backscattering efficiency and the forward scattering efficiency for different sizes of TiO<sub>2</sub> depending on the wavelength; the plots were derived based on data from Fig. 2.7. The backscattering efficiency for different sizes of TiO<sub>2</sub> particles for 650 nm wavelength are extracted from Fig. 2.8 and are as follows:  $Q_{BS} = 0.0031$  for  $R = 21$  nm;  $Q_{BS} = 3.0$  for  $R = 150$  nm;  $Q_{BS} = 2.8$  for  $R = 1$   $\mu\text{m}$ ; and  $Q_{BS} = 1.4$  for  $R = 10$   $\mu\text{m}$ . The amount of backscattered light is not proportional to the size of the particle, and therefore has to be accounted for.

### Metal particles

Metal particles were considered as an alternative seeding material. The same parameters which were previously obtained for TiO<sub>2</sub> were calculated for metal particles such as silver (Ag) and gold (Au). The dependence of both the real and imaginary parts of

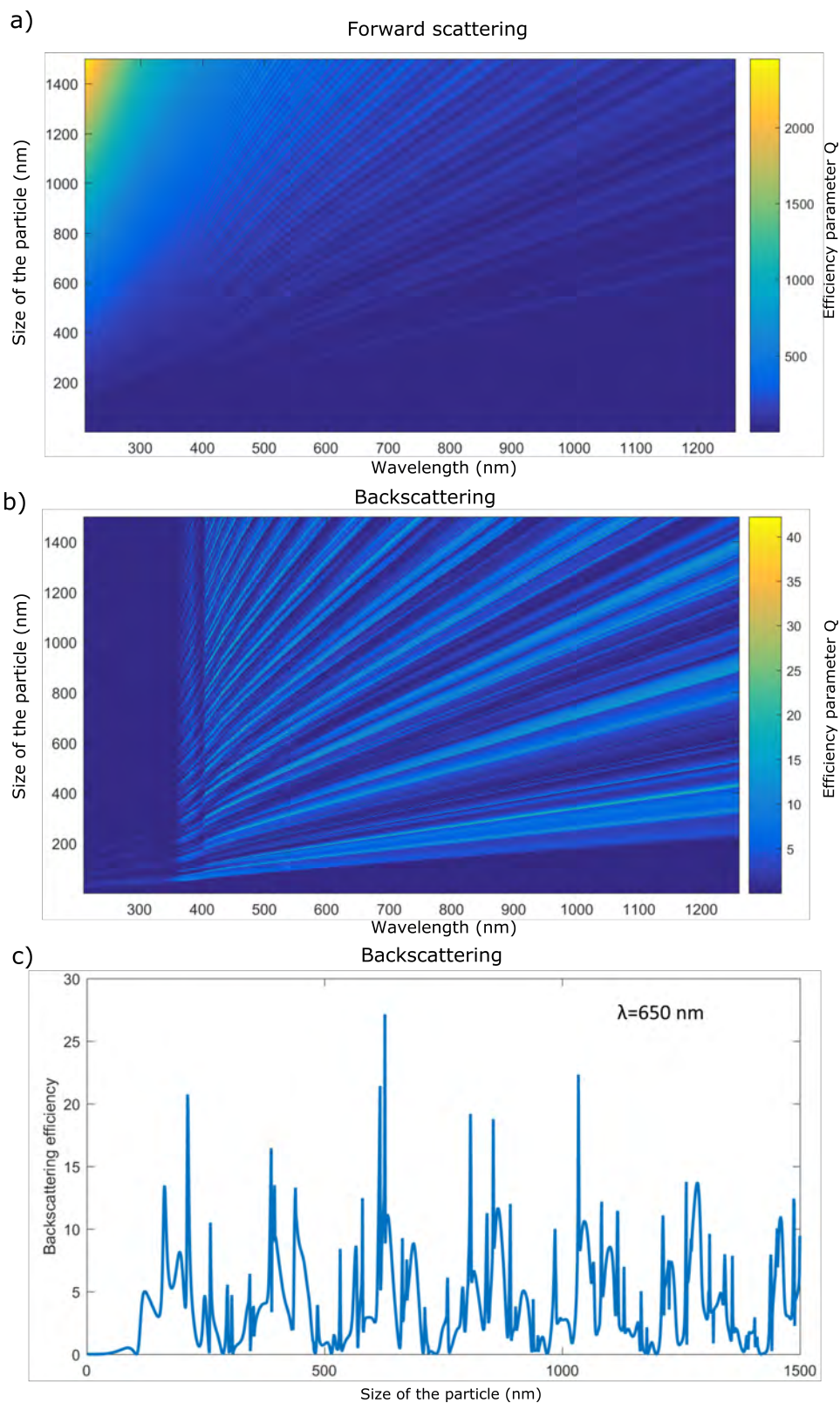


FIGURE 2.7: (a) Calculated forward scattering and (b) backscattering efficiency for  $\text{TiO}_2$  particles of different sizes and for different wavelengths. (c) Backscattering efficiency at a wavelength of 650 nm for different size of  $\text{TiO}_2$  particles derived from (b). The calculations were done based on Equations 2.8 and 2.9. The interval between the sizes of the particles is 1 nm. The distribution of the complex refractive index as a function of wavelength is shown in Fig. 2.5.

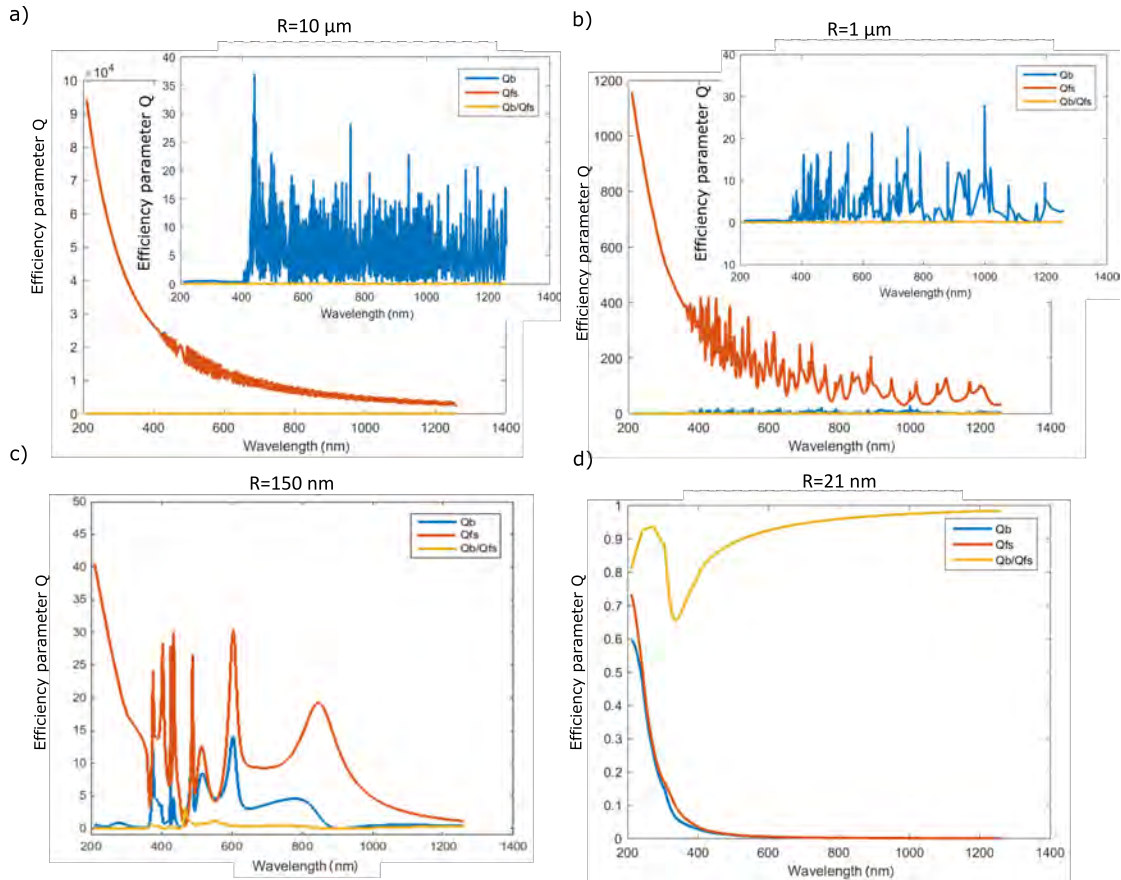


FIGURE 2.8: Mie efficiency functions dependence on wavelength for the different sizes of  $\text{TiO}_2$  particles: a)  $R = 10 \mu\text{m}$ ; b)  $R = 1 \mu\text{m}$ ; c)  $R = 150 \text{ nm}$ ; d)  $R = 21 \text{ nm}$ . Sizes were chosen to match the parameters of the experiments presented in later chapters.

The results are derived from the calculations presented in Fig. 2.7.

the complex reflective index for Ag is presented in Fig. 2.5 (b) Different sizes and shapes of both materials are readily available on the market.

The properties of metals are such that they have quasi-free electrons in the ground state that are not bound to the atom, but to the whole bulk. These free-electrons behave like a gas made of free-charge carriers, similar to a plasma. They can be excited to contain so called propagation waves. The quantum of this propagation is called a plasmon [91, 92]. A plasmon resonance is a resonance oscillation of the conduction electrons in a metal. It is caused by a displacement of electrons from their equilibrium positions under inducement by an EM wave. The lattice of positive ions is responsible for the resonance frequency. There are two types of oscillation frequency: **bulk plasmons** and **surface plasmons**. The first refers to volume plasma oscillations, and they depend only on the free electron density of the metal. Surface plasmons occur on the interface between metal and dielectric, and they are caused by surface electrons. Metal has a limited penetration depth of EM waves, which is less than 50 nm for Ag and Au. Therefore, only the plasmons associated with the surface are significant. The frequency of the surface plasmons is lower than the one associated with the bulk plasmons.

When metal nanoparticles or thin metal films are used instead of a bulk material, the plasmons behave differently and they are called **localised surface plasmons** [93]. When the size of the metal particles is smaller than the wavelength of the incident light, the electric field can move free electrons away from the metal particle. As a result of this, a dipole moment can occur. Moreover, depending on the local direction of the electric field, the dipole can have different orientations. When the frequency of the incident light is approximately equal to the frequency of a dipole plasmon, a resonance condition is reached, resulting in constructive interference. This is referred to as surface plasmon resonance or localised plasmon resonance. When the particles are bigger, a quadrupole plasmon resonance can appear due to four oppositely charged poles [91, 92].

As a result of this effect, metal nanoparticles demonstrate some abnormal scattering abilities [94] which can be used to increase the overall backscattering efficiency. Metal nanoparticles have an additional advantage of providing the opportunity to “adjust” their scattering spectrum by changing their shape and shell structure [95, 96].

The most commonly used metal nanoparticles are Ag and Au particles, which have different resonant wavelengths and sensitivities to light [96] depending on their shape, size, and shell structure. For example, Ag nanospheres of 40 - 90 nm have a resonance in the wavelength range 400 - 480 nm. Ag nanoprisms of 55 - 120 nm have a resonance in the range 600 - 700 nm. Different coatings also change the resonance wavelength.

As the SM sensor is based on the collection of backscattered light, interest is focused on the backscattering efficiency. More light scatters in the forward direction compared to backscattered light as it was described previously. The resulting scattered light is the summation of the re-emitted waves from dipoles appearing within the scattering particle exhibiting more waves in phase in the forward direction than back [82]. However, the overall behaviour of the functions can be studied from both plots, see Fig. 2.7 (a) and (b). The backscattering efficiency distribution for Ag nanoparticles of different sizes for different wavelengths is presented in Fig. 2.9. The backscattering efficiency of Ag nanoparticles is more predictable compared to the results obtained for TiO<sub>2</sub>. Figure 2.9 (b) demonstrates a smooth curve of the backscattered light distribution for various sizes of Ag nanoparticles for a 650 nm wavelength when compared to the same parameters for TiO<sub>2</sub> particles in Fig. 2.7 (c).

The resultant function of the scattered light depends on the size of the particle with a series of low-frequency maxima and minima, as a result of the inference between re-radiated and transmitted or incident waves [80, 97, 98]. These interference patterns appear for a given scattering efficiency for any kind of material, and they can be seen in Fig. 2.7 and 2.9. Their period directly depends on the phase shift, which is acquired by light passing through the centre of the sphere [98]. However, the scattering efficiency function for TiO<sub>2</sub> exhibits additional superimposed high-frequency ripples, which consist of sharp and irregular spike-like peaks, see Fig. 2.7 (c). Physically, those ripples appear when the waves propagate around the surface in a standing wave without attenuation through destructive interference, and it takes longer for this energy to be

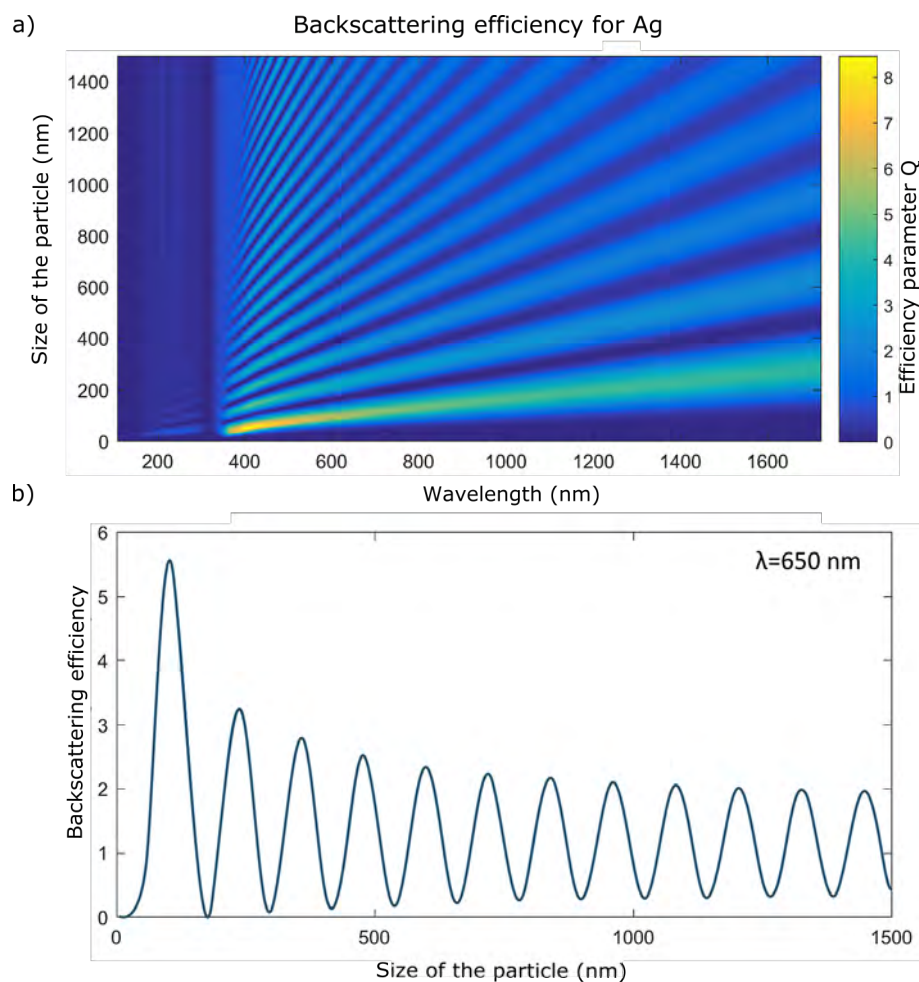


FIGURE 2.9: (a) Backscattering efficiency distribution for Ag particles of different sizes for different wavelengths. (b) Backscattering efficiency at a wavelength of 650 nm for different size of Ag particles derived from (a). The complex reflective index was obtained from [90].

removed from the sphere [99]. Hence, a large amount of energy can accumulate without leaving the sphere inside the particle, close to its surface. Since these accumulated waves are part of the incident light, when they are being emitted, they produces resonances, which appear as sharp peaks [98]. The appearance of such peaks is directly connected to the depth of the penetration or the imaginary part of the refractive index. In the case of  $\text{TiO}_2$ , the imaginary part of the refractive index  $k$  (see Fig. 2.5 (a)) is close to zero for wavelengths shorter than 400 nm meaning very low absorption of the energy and hence the waves can propagate around the surface of the sphere [82, 98]. In the case of Ag, the imaginary part of the refractive index is very high (see Fig. 2.5 (b)), and metal particles have quasi-free electrons, which participate in producing the surface plasmon resonances [91, 92]. Moreover, different plasmon modes can coexist in the same nanoparticle depending on the property of light it interacts with. The smooth character of the function appears due to the closeness of the oscillations of the excited electron cloud to the surface plasmon resonances.

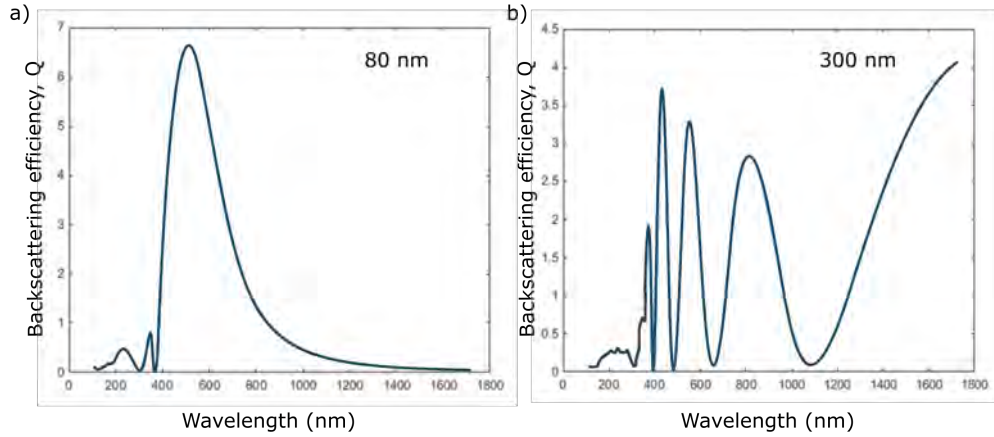


FIGURE 2.10: Distribution of the backscattered light on the wavelength of the incident light for Ag nanoparticles of size a) 80 nm and b) 300 nm, derived from Fig. 2.9.

When comparing the backscattered light distribution of  $\text{TiO}_2$  (Fig. 2.7) and Ag (Fig. 2.9), the global peak in the Ag spectrum distribution of the backscattered light is shifted in the direction of smaller particles and smaller wavelengths. It is centred around a particle in the radius range 50 - 150 nm and in the wavelength range 400 - 550 nm. Figure 2.10 shows the backscattering efficiency for both different wavelengths and for Ag particle sizes of 300 nm and 80 nm. The amount of the backscattered light which can be obtained for an 80 nm particle is higher compared with a 300 nm one. As metallic particles scatter light in a much smoother way, the best size of seeding particles for the highest scattering are much easier to select compared to the random scattering pattern for  $\text{TiO}_2$ . The wavelength of the global peak of the backscattering efficiency can be “adjusted” further by changing the shape and the structure of the nanoparticles [94, 100]. Consequently, the global peak can be obtained at the required wavelength allowing for maximum backscattered efficiency, hence higher levels of feedback for the SM sensor. The “adjustment” can be achieved by varying the shape and coatings of the metallic particles.

## 2.2 Light Scattered off Moving Particles: Expected Spectrum from an Arbitrary Moving Target

### 2.2.1 Introduction

When particles move inside a volume, the phases of the scattered waves incident on the particles are time dependent. This is due to the particles moving in relation to the light receiver. In the case of an SM sensor, the light receiver and the source of the light are the same objects. The time,  $t$ , dependence gives information about the velocity of the scatterers. The phase  $\theta_{i,w}$  of the light wave scattered off moving particle  $i$  is time-dependent [2]:

$$\theta_{i,w} = (\theta_{i,w})_0 - 2\pi\nu_w \vec{v}_i \cdot \vec{n}_w t, \quad (2.10)$$

where  $\vec{v}_i$  is the velocity of the moving particle  $i$ ,  $\vec{n}_w$  is the unit vector in the direction of light propagation, and  $\nu_w$  is the wave number. The subscript 0 indicates that the scattering particle is stationary. Moreover, the distance  $R_i$  between the scattered wave and the radiation receiver is also time-dependent due to moving scattering particle:

$$R_i = (R_i)_0 - \vec{v}_i \cdot \vec{n}_i t, \quad (2.11)$$

where  $\vec{n}_i$  is the unit vector in the direction of the scattered wave.

The theory described in Section 2.1 is valid for one particle only which interacts with light. If light is scattered off more than one particle within the illuminated area, an interferometry pattern occurs. The resulting intensity of the scattered light is a superposition of the scattered light off all particles.

The interaction of light with a scattering particle of size  $l$  leads to a diffraction pattern with an angular aperture of  $\theta \approx \lambda/l$ . In the case of a collection of independent scatterers along the path of the light, the diffraction patterns interfere with each other. This generates a far-field pattern where bright and dark areas of different sizes and shapes are distributed randomly.

The distribution function of the amplitude of the scattered EM field is expected to be Gaussian [101, 102]. It is supposed [102] to be independent of the properties of the scattering media and the character of its motion. However, in the case of 1) random phases of the diffraction patterns, and 2) large enough numbers of illuminated scatterers, the field-irradiance correlation function depends on the type of motion of the scatterers. For example, the spectrum of scattered light is a Lorentzian function when a large enough number of particles undergo Brownian motion [103, 104].

In the case of a target that is in motion, the situation is more complicated. The result depends on the nature of the target and it can be described by the following:

1. If the light scatters off the density fluctuations in the medium, there is a finite correlation between different illuminated volumes. The examples of light scattering off thermodynamical fluctuations in the medium are given in [18] and [105].

2. If the light scatters off a rotating target, the motion of the scatterers can vary from fully correlated to completely uncorrelated. It can be assumed that different parts of the rotating target are independent from each other. Different points of rotating discs have different velocities. It can be assumed that the laser light is focused into a small enough spot such that it has only one velocity value; this can be described as a delta-function. The delta-function has a unity value at the point where the laser light is focused [106].

3. If the light scatters off a flow which moves with a specific velocity, the result is similar to case 2. The scatterers are independent from each other between different scattering volumes. If the flow has different velocities, the illuminated volume within the flow can be characterised with a velocity distribution rather than one single value.

In order to obtain a spectrum of the scattered light, the velocity distribution of the scattering media or target has to be accounted for. The calculation can be first

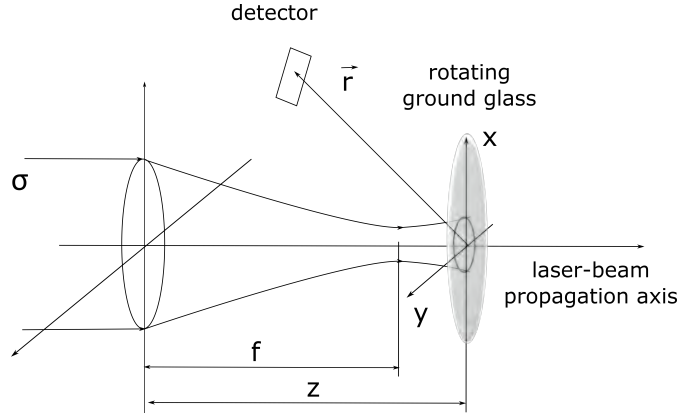


FIGURE 2.11: Geometry of the formation of the laser spot on rotating ground glass.  $\sigma$  is the radius of the incident light beam, which is focused by the lens with focal length  $f$  on the ground glass. It is located at a distance  $z$  in the plane  $(x, y)$ .  $\vec{r}$  is a radius vector from the centre of the laser spot on the ground glass to the detector.

performed for the delta-function, assuming that the target has only one specific velocity value and that the scatterers are completely uncorrelated. For the more complex case, such as moving flow, the velocity distribution function has to be used for the calculation of the spectrum of the scattered light. This calculation can be based on the previously obtained spectrum for the delta-function.

## 2.2.2 Expected Spectrum of Light Scattered off Rotating Targets

The intensity of scattered light can be estimated, assuming the following, as shown in Fig. 2.11:

- A collimated light beam has a radius  $\sigma$  before a lens.
- The light is focused by an aberration-free lens with focal length  $f$ .
- The light is focused on a rotating surface with a finite spot size.
- The rotating surface has an average roughness  $l$  which leads to a diffraction factor  $s$ .
- The light scattered off different surface areas has uncorrelated phases.
- The illuminated area  $A$  contains  $N$  scattering centres.
- The source of light is a single mode laser.

The light can be described as having a Gaussian cross section profile with emitted field amplitude  $E(\vec{r}, t)$  that varies in space and time.  $k = 2\pi/\lambda$  is a wave-vector, and  $\omega_0$  is the angular frequency of the incident light of wavelength  $\lambda$ . In the case of solid targets, the theoretical spectrum of light scattered off a rotating ground glass, see Fig. 2.11, has been analysed [107], showing that the spectrum of the signal is Gaussian.

The field-correlation function can be described by the following [107]:

$$\langle E(\vec{r}, t)E^*(\vec{r}, t + \tau) \rangle = \frac{N \langle s^2 \rangle}{A} \exp[i(\omega_0 + \vec{k} \cdot \vec{v})\tau] \int d^2\vec{r}_1 E(\vec{r}_1)E^*(\vec{r}_1 + \vec{v}\tau). \quad (2.12)$$

Here  $\vec{r}$  is a radius vector from the centre of the laser spot to the detector,  $d^2\vec{r}_1 = dx dy$ , where  $(x, y)$  is the plane of the ground glass, see Fig. 2.11. The integral extends over

the illuminated area, and  $\vec{v}$  is the velocity of the point where the light is focused. The target is located at a distance  $z$ . The emitted field  $E(\vec{r})$  passes through the lens and then towards the target. At a distance  $z$ , the incident light field can then be determined (the steps in-between are omitted):

$$E(\vec{r}) = E(x, y) = -\frac{ik}{2z} \frac{E_0 e^{ikz}}{\frac{1}{4\sigma^2} + \left(\frac{ik}{2}\right)\left(\frac{1}{f} - \frac{1}{z}\right)} \exp\left(-\frac{\left(\frac{k^2}{f} - \frac{ik}{2\sigma^2}\right)(x^2 + y^2)}{4z\left(\frac{1}{4\sigma^2} + \left(\frac{ik}{2}\right)\left(\frac{1}{f} - \frac{1}{z}\right)\right)}\right). \quad (2.13)$$

The frequency shift, described by  $\vec{k} \cdot \vec{v}$  (in the exponent in Eq. 2.12), is a Doppler shift. For a laser beam perpendicular to the rotating surface, the frequency shift is equal to 0. The field-power spectrum is the time Fourier transformation of the field-correlation function, which is given by Eq. 2.12. The field-power spectrum for the incident field from Eq. 2.13 [107] can be written as the following expression:

$$\begin{aligned} I(\omega) &= -\sqrt{2\pi} \int_{-\infty}^{+\infty} d\tau e^{-i\omega\tau} \langle E(\vec{r}, t) E^*(\vec{r}, t + \tau) \rangle = \\ &= \frac{2\pi\sigma^2}{A} \frac{N \langle s^2 \rangle E_0^2}{\sqrt{v^2 \left(\frac{k^2\omega^2}{f^2} + \frac{1}{4\sigma^2}\right)}} \exp\left(-\frac{(\omega - \omega_0)^2}{2v^2 \left(\frac{k^2\omega^2}{f^2} + \frac{1}{4\sigma^2}\right)}\right). \end{aligned} \quad (2.14)$$

Equation 2.14 can be written as

$$I(\omega) = \frac{2\pi\sigma^2}{A} \frac{N \langle s^2 \rangle E_0^2}{v/w_0} \exp\left(-\frac{(\omega - \omega_0)^2}{2v^2/w_0^2}\right), \quad (2.15)$$

where the spectrum depends on the frequency  $\omega$ , and  $w_0 = f/k\sigma$  is the waist of the laser beam. The spectrum is a Gaussian function with peaks around the angular frequency of the initial incident light. The amplitude and the full-width at half-maximum (FWHM) depend on different parameters of the system, such as the velocity of the target and the waist of the beam. These two parameters are the main variables that can be changed. The peak is broadened proportionally to the velocity of the target. Simultaneously, the FWHM of the peak is inversely proportional to the beam waist radius.

The FWHM describes a broadening of the spectrum:

$$\Delta\omega = \sqrt{2\ln 2} v \sqrt{\frac{k^2\omega^2}{f^2} + \frac{1}{4\sigma^2}}. \quad (2.16)$$

The broadening of the spectrum is directly proportional to the velocity of the illuminated area, and is inversely proportional to the focusing length of the lens. It also depends on the transverse size of the incident light. It is interesting to note that the spectrum is broadened even if the laser beam is perpendicular to the surface, i.e. when the Doppler shift is equal to 0.

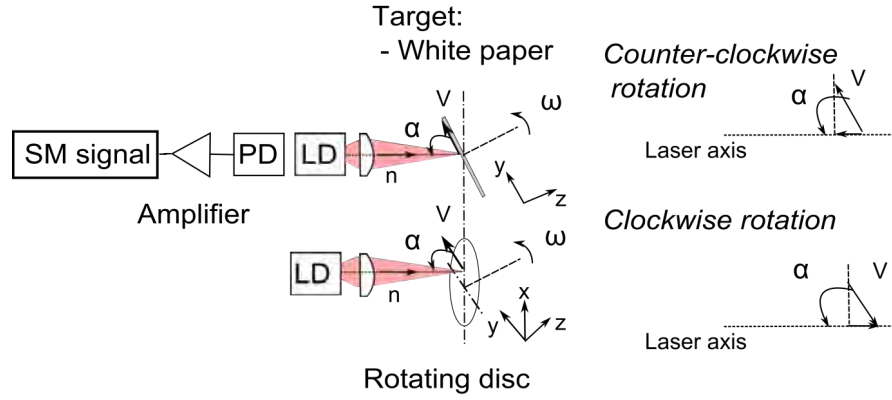


FIGURE 2.12: Geometry of the SM system for rotating disc experiments. The same geometry is used for an analysis of the light scattered off the rotating disc. The light from the laser diode is focused on the rotating disc at an angle  $\alpha$  at a point with a velocity  $v$ .

### 2.2.3 Spectrum of the Scattered Light from a Rotating Target when the Target is at an Angle

The broadening of the spectrum means that additional components are added to the spectrum. Effectively speaking, the additional frequency components are also Doppler shifted. They appear due to the roughness of the surface, i.e. due to the 3-dimensional properties of the surface.

Equation 2.15 is valid when a light beam is incident perpendicular to the target. A similar equation can be derived when accounting for a non-zero angle between  $\vec{k}$  and  $\vec{v}$ . The geometry of the self-mixing experiment in the case of a rotating target is shown in Fig. 2.12, where  $\vec{k} \cdot \vec{v} = kv \cos \alpha$  can be applied in Eq. 2.12 to calculate the field-correlated function, and then for deriving the spectrum. This leads to a shift of the main frequency  $\omega_0$  of the light. When the light is perpendicular to the target, the broadening appears due to the roughness of the surface in that plane. Hence in the case of an inclined target, the broadening is no longer proportional to the total velocity, but to the velocity component perpendicular to  $\vec{k}$ , i.e. to  $v \sin \alpha$  in Fig. 2.12. In the general case this can be defined as  $|\vec{n} \times \vec{v}|$ .

The time Fourier transformation of Eq. 2.12 then leads to a similar expression to Eq. 2.15, however, with a difference in the central frequency of the spectrum:

$$I(\omega) = \frac{2\pi\sigma^2}{A} \frac{N\langle s^2 \rangle E_0^2}{|\vec{n} \times \vec{v}|/w_0} \exp\left(-\frac{(\omega - (\omega_0 + \vec{n} \cdot \vec{v}))^2}{2(|\vec{n} \times \vec{v}|)^2/w_0^2}\right), \quad (2.17)$$

or when  $\alpha$  is the angle between vector  $\vec{n}$  and vector  $\vec{v}$ :

$$I(\omega) = \frac{2\pi\sigma^2}{A} \frac{N\langle s^2 \rangle E_0^2}{v \sin \alpha/w_0} \exp\left(-\frac{(\omega - (\omega_0 + kv \cos \alpha))^2}{2(v \sin \alpha)^2/w_0^2}\right). \quad (2.18)$$

The integral in Eq. 2.12 stays the same. The integration over the illuminated area  $A$  leads to the same dependence on the velocity, beam waist, etc. A perfect round spot

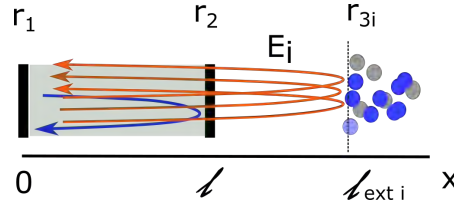


FIGURE 2.13: Schematic arrangement for the fluid interaction with an LD for an SM system, where  $r_1$  and  $r_2$  are reflection coefficients of the LD cavity, which has length of  $l$ . Each particle  $i$  can be characterised with its own parameters such as its velocity  $\vec{v}_i$ , reflectivity  $r_{3,i}$  and is located at a distance  $l_{ext\ i}$  from the LD. The light scattered off each particle can be characterised with an electromagnetic wave  $E_i$ .

corresponds to a light beam perpendicular to the target surface. When the target is located at an angle, the spot of the beam on the surface is transformed from a circle into an ellipse. This results in a different shape and size of the illuminated area  $A$ . As a result, the integration limits change. Moreover, the velocity function becomes different from a delta-function.

The spectrum of the scattered light is defined by Eq. 2.17 or 2.18. The optical power of the SM signal oscillates with a frequency proportional to the Doppler shift in the wavelength of the scattered/reflected light according to Eq. 1.42. Combining these equations, the spectrum of the SM signal is equal to:

$$I(\omega) = I_0 \frac{1}{v \sin \alpha / w_0} \exp\left(-\frac{(\omega - 2v \cos \alpha / \lambda)^2}{2(v \sin \alpha)^2 / w_0^2}\right). \quad (2.19)$$

This equation can be used for calculation of spectra of the SM sensor signal, from which the velocity can be found.

#### 2.2.4 Self-Mixing Velocimeter: Flow Measurements

In the case of fluids, the shift in the frequency of the laser light in SM is based on light scattering off discontinuities of a moving flow due to its optical properties. The scattering process for liquid and gas targets is different compared to a solid target. For a solid target the entire illuminated surface is moving whereas for liquids and gasses scattering occurs off each individual particle. The power spectrum, see Eq. 1.34 or 1.39, provides information about the scattered particles such as velocity along the laser light axis. Moreover, the same SM signal can be used for measuring other properties of the scattering particles within the liquids, such as their concentration and size [67].

Depending on the amount of particles in the scattering volume, the amount of scattered light coupled back into the laser cavity depends on: 1) the scattering cross section, and 2) the solid angle within the scattered light that can be collected by the laser system. Generally, the amount of light scattered off small particles (as targets) and the properties of that light depend on the refractive index of the seeders and surrounding area, the size, shape and orientation of particles and the observation angle [3, 82].

The equations, which were obtained for the SM signal for the general case, are valid for fluids taking into account that every particle which the light scatters off is an external cavity, see Fig. 2.13. Assuming that the measured volume contains  $i$  scattering particles which can be defined by their velocities  $\vec{v}_i$  and reflection coefficients  $r_{3,i}$ , then all parameters mentioned earlier will be different for each particle. These include such parameters as coupling coefficients  $C_i$ , the modulation functions  $m_i$ , etc. In this assumption, Eq. 1.34 and 1.36 can be re-written as:

$$\nu_F = \nu_0 - \sum_i \frac{C_i}{4\pi\tau_{D_i}} \sin(2\pi\nu_{F_i}\tau_{D_i} + \arctan(\alpha)), \quad (2.20)$$

$$P_F = P_0 \left( 1 + \sum_i m_i \cos(2\pi\nu_{F_i}\tau_{D_i}) \right). \quad (2.21)$$

The resulting SM signal can be calculated by taking into account each contribution of each scattering particle.

### 2.2.5 Signal Spectrum of Scattered Light from a Fluid

Analysis of the SM signal for velocity measurements indicates that the frequency of the SM signal is proportional to the velocity of the target. In order to obtain the frequency of the signal, it is necessary to calculate the spectrum. This is done by performing a fast Fourier transformation of the signal. The spectrum of the SM signal gives information about its frequency domain and hence the velocity of the measured target. Moreover, the resulting spectrum is directly proportional to the spectrum of the light scattered from the target.

Assuming that the Brownian motion of the moving particles can be neglected compared to the velocity of the liquid and that the scattering particles follow the carrier liquid closely, the scattered light is a superposition of the Gaussian spectrum of each independent particle the light scatters off. However, the scattered light is not distributed randomly over  $(0, \pi)$ , as for a rough surface such as a ground glass or white paper, but according to the differential scattering cross section of the scattering particles. Moreover, the spectrum of SM signal should be proportional to the integral of the scattering cross section over the illuminated area  $A$ , or illuminated volume  $V$  in the case of fluids, and over the solid angle of the light coupling optics. Hence, the spectrum of the SM signal is broadened in proportion to the maximum velocity of the fluid and to the distribution of the velocities of the fluid within the illuminated area, which are weighted proportionally to the intensity of the illuminating light. The scattering cross section function and light coupling optics influence the amount of light coupled back into the cavity and therefore the amplitude of the SM signal. The distribution of the velocities of the particles which the light scatters off also leads to a further broadening of the spectrum.

For a liquid in a tube or a flow discharging into the atmosphere, the maximum velocity is at the centre of the flow. The velocity of the particles decreases towards the edge of the flow, with the velocity equal to zero at the face of the tube, according to

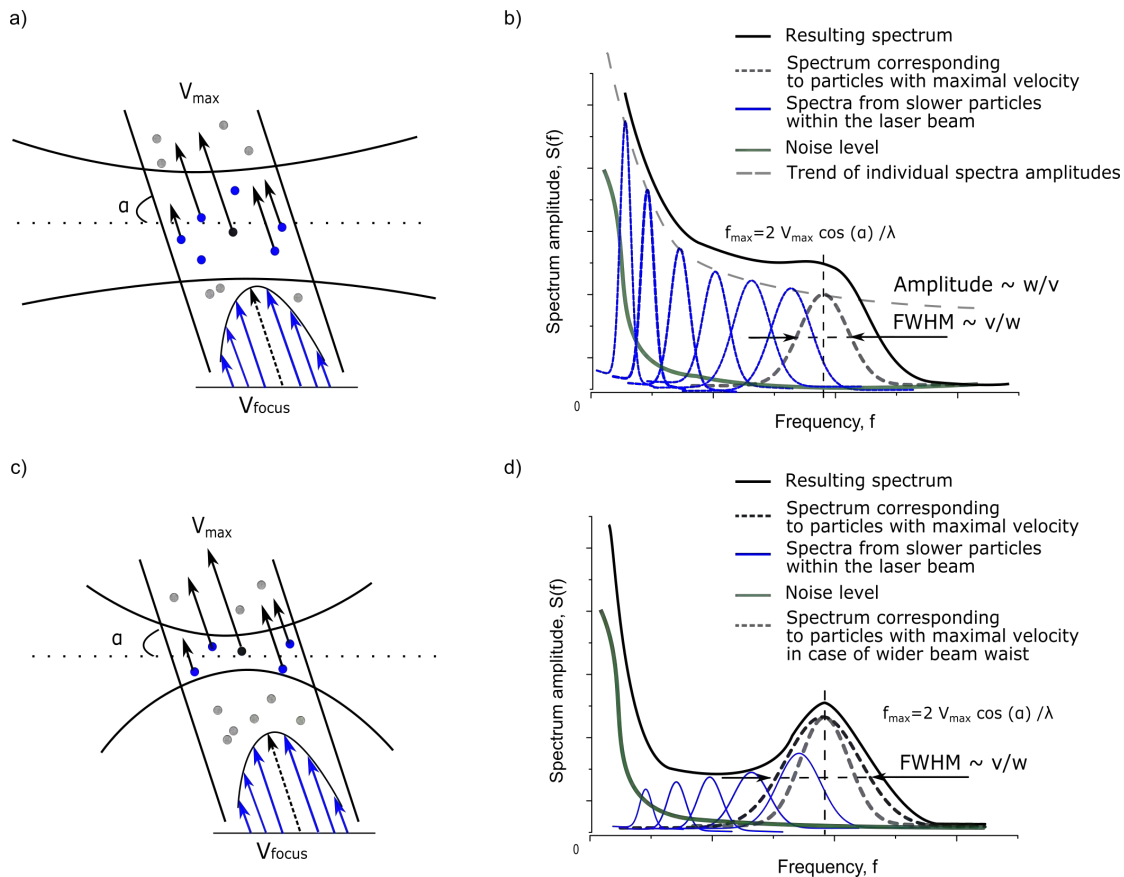


FIGURE 2.14: Schematic representation of the interaction of the laser light with fluid for two cases where the laser light is focused differently, illustrated in (a) and (c), and their schematic spectra (b) and (d) of the self-mixing signal for liquid measurements respectively. The distribution of the velocity across the fluid is shown at the bottom of the pictures (a) and (c). The laser light is focused on particles with maximum velocity. The spectrum of these components is presented by a dotted line on (b) and (d). The grey-green solid line represents the noise background. (a) The laser light has approximately an equal waist across the fluid, which means that all moving particles are illuminated with an equal intensity of light. (b) In this case, the resulting spectrum is the sum of the distribution of all velocities within the illuminated volume, which leads to a very broad spectrum with a cut-off around the peak frequency. (c) When the laser is focused onto a particular area, the highest contribution to the signal will be from that area, with a smaller contribution originating from the unfocused areas. (d) The resulting spectrum has a peak at the frequency corresponding to that velocity. The black dotted line corresponds to the spectrum of the particles with maximum velocity where the laser light is focused. It is broader compared to (b), represented by grey dotted line for comparison, due to a smaller waist of the laser beam. In the case (d), the spectrum is broadened additionally due to the contribution of nearby particles moving with different velocities.

Poiseuille's law, see Fig. 2.14. Each group of particles moving with the same velocity produces a spectrum with a dominant frequency. The resulting spectrum consists of the weighted sum of all frequency contributions within the illuminated volume. The individual components of the spectrum are broadened proportionally to the velocity of the particles they represent and inversely proportional to the waist of the laser beam at their location.

In the case that the laser light is focused onto the target in a way that the width of the laser spot is consistent across the measuring volume, see Fig. 2.14 (a), the intensity of the light from the illuminated particles moving with the same velocity is equal. However, the amplitude of the peak in the spectrum of scattered light reduces with the velocity of the target according to Eq. 2.19. Figure 2.14 (b) schematically shows the spectrum obtained in the case when moving particles contribute equally to the spectrum. The maximum velocity of the fluids is at the cut-off slope of the resulting spectrum.

If the laser light is focused in such way that the light illuminates more intensely on one particular area, see Fig. 2.14 (c), then the rest of the moving particles contribute to the overall spectrum significantly less. As a result, the spectrum will have a peak at the frequency corresponding to the velocity of the particles of the area where the light was focused. The peak of the overall spectrum is broadened more compared to the rough surface due to the contribution of the particles that move with different velocities and close to the illuminated volume, see Fig. 2.14 (d).

Assuming that the laser beam was focused at the centre of the flow, the maximum intensity will be from the particles moving with maximum velocities. If the light is focused elsewhere, the spectrum will still have a peak at the frequency corresponding to the velocity of the illuminated area. However the peak will be broadened even more due to higher frequency components, which appear from light scattered off particles with velocities higher than where the light is focused. This expands the main peak to the right. The broadening of the spectrum from the particles moving with the same velocity is shown in Fig. 2.14 (b) and Fig. 2.14 (d) according to the Gaussian distribution (Eq. 2.19).

### 2.2.6 Simulation (Model Application): the Influence of the Distribution of Velocities within the Measured Area

In the presented calculation and analysis, every photon scattered off the target was assumed to have the same Doppler shift. However, due to the finite size of the laser spot, different photons can have different Doppler shifts. The measured target can be characterised with some distribution of velocities within the area of illumination.

Figure 2.14 illustrates the spectra that can be obtained. Effectively, the mathematical equivalent of the spectra is the integration of Eq. 2.17 or 2.19 over the distribution of velocities  $\Delta v$  within the measured volume/area and over the intensity of the laser spot  $\Delta w_0$  within it:

$$I(\omega) = \int_{\Delta v \Delta w_0} I(\omega, v, w_0) dv dw_0. \quad (2.22)$$

Various targets may be characterised with different velocity distributions influencing the obtained spectra. For example, the whole surface of a mirror on a translational stage moves with the same velocity. The velocity distribution function is a delta-function. Even when the laser spot has a finite size on the surface of the disc, each scattering centre has the same velocity. Consequently, the width of the peak frequency is narrow.

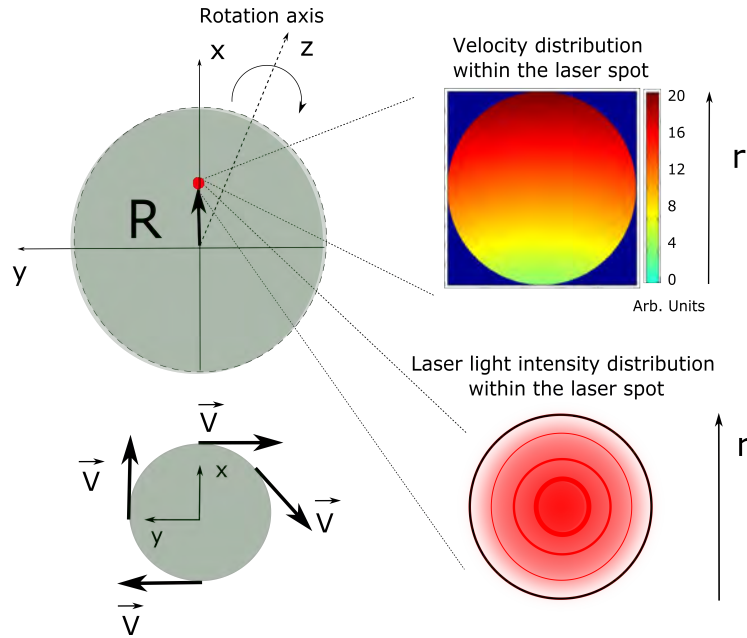


FIGURE 2.15: Schematic representation of the different velocities of the points on the disc, which rotates around the  $z$  axis. When the laser spot is non point-like, the scattering area can be characterised with a distribution of velocities. The laser spot is represented by the red circle on the disc on the top left picture. The bottom-right picture shows the distribution of the light intensity within the magnified laser spot. The top-right picture represents the distribution of the velocities within the laser spot. Green color shows the smallest value of the velocity, and dark red color indicates the maximum velocity. The velocity vector is tangential to the arc, which is shown on the bottom-right picture. The surface of the disc is located in the plane  $(x, y)$ .

In contrast, every point on a rotating disc moves at different tangential velocities, see Fig. 2.15. The motion of the rotating disc can be characterised by the rotation speed, which is given in units of revolutions per second,  $\nu$ . The tangential velocity is perpendicular to the diameter of the disc at each point and it is at a tangent to the circle. The tangential velocity  $v$  at the point of radius  $R$  is  $v = \omega R$ , where  $\omega$  is equal to  $2\pi\nu$ . Equal velocities are located on an arc of the same radius, and the velocity vector is tangential to the arc. When the laser spot has a finite size  $r$ , the illuminated area has different velocities within the laser spot leading to a distribution of the velocity, see top right picture in Fig. 2.15. Moreover, the distribution of the intensity of the light within the laser spot follows a Gaussian function with the maximum at the centre of the spot, see the bottom-left picture in Fig. 2.15. On top of that, a different number of points within the laser spot has the same velocity. That means velocities contribute to the overall spectrum differently. For example, the highest (red) and the lowest (green) velocities contribute the least to the spectrum for two reasons. Firstly, the points with such velocities are only on the edge of the laser spot; and, secondly, the intensity of the laser light is minimum at these points.

The overall spectrum can be obtained accounting for both distributions of the velocities and of the intensity in Eq. 2.19. The overall spectrum of the signal has a distribution of frequencies, which correspond to the velocity distribution.

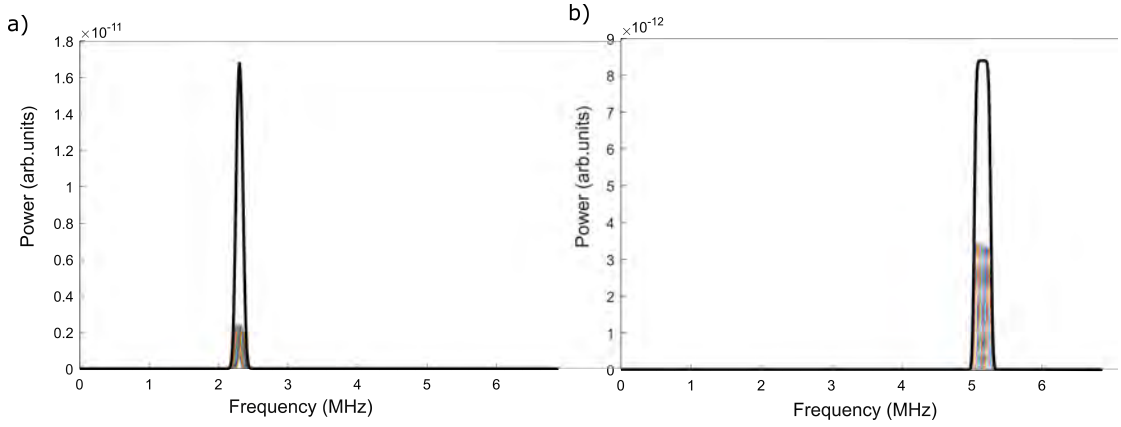


FIGURE 2.16: Simulated spectra, based on Eq. 2.19, where the distribution of the velocity within the measured area is accounted for. The black line is a superposition of the spectra obtained from light scattering off particles with different velocities, which are represented by lines under the overall spectra. The parameters used for the simulations are presented in Table 2.1: a)  $\alpha = 70^\circ$ ; b)  $\alpha = 40^\circ$ .

TABLE 2.1: Parameters used in the simulation of the spectrum in Fig. 2.16.

Parameter name	Value
Laser wavelength	$\lambda = 650$ nm
Angle between optical axis and velocity direction	$\alpha = 70^\circ$ ; $\alpha = 40^\circ$
Spot size radius	$r = 20$ $\mu\text{m}$
Velocity of the target	2.136 - 2.236 m/s

To obtain a non-zero velocity vector projection on the laser beam axis, the laser is turned by an angle  $\alpha$ . The laser light propagation vector is perpendicular to the  $y$  axis, see Figs. 2.12 and 2.15. The laser light is turned by an angle  $\alpha$  with respect to the  $z$  plane. Only the velocity vector component along  $x$  axis gives a projection on the laser axis, hence the light is focused along the  $x$  axis. All points with component on the  $y$  axis have another angle with respect to the unit vector of light propagation, see Fig. 2.15.

The simulation of the spectra can be obtained for the light scattering off the rotating disc. Assuming that the distribution of the intensity within the laser spot is constant, the resulting spectrum can be obtained by integrating Eq. 2.19 over the velocity distribution. The results of the simulations are presented in Fig. 2.16. The simulation parameters are listed in Table 2.1. The spectra on the plots are symmetrical because the distribution of the velocity within the illuminated area is equal to a delta-function.

For a laminar flow, the velocity profile in a channel is parabolic. The velocity within the fluid in a pipe varies from zero at the wall to a maximum value at the centre of the pipe, following Poiseuille's law. As the flow discharges from the nozzle, the velocity distribution follows the same law. However, the velocity at the edge has a minimum value, which can be defined by considering the properties of the system. Both cases are demonstrated in Fig. 2.14.

The simulation parameters for laminar flow are listed in Table 2.2 and the results are shown in Fig. 2.17. It is assumed that the laser beam is focused such that its

area is consistent across the measuring volume, i.e. the waist of the beam is constant for all contributions. The simulations include dark current noise on the main plots. For each case, the inserts show the resulting spectra of the simulations with the same parameters without the noise. The same results can be obtained when the frequencies that correspond to the velocities are shifted away from the noise spectrum. The spectra are scaled for better visualisation. The influence of the velocity distribution can be seen in the simulations. The shape of the spectrum varies dramatically depending on the range of the velocities included in the calculation (or experiment). The higher velocities contribute less to the amplitude since the amplitude reduces with increasing velocity.

The main conclusion from these simulations is that the frequency at the maximum amplitude of the peak does not necessarily correspond to the maximum velocity within the measured volume. Moreover, information about the velocity distribution can be obtained from the shape of the spectrum.

Figure 2.17 (a) demonstrates how a relatively small distribution of the velocity (0.5 m/s - 0.6 m/s) leads to a symmetrical shape of the spectrum. This can be fitted to a Gaussian function with the peak corresponding to the average velocity within the range of velocities. It is further evidenced from the inserts that the peak of the resulting spectrum can be shifted depending on the contributions from each velocity component.

Figure 2.17 (b) demonstrates simulation results when the velocities are within the range of 0.4 m/s - 0.6 m/s. The shape of the resulting spectrum becomes an asymmetrical Gaussian function with a steeper slope towards the minimum velocity since it contributes more to the spectrum.

For the wider distribution of the velocities within 0.3 - 0.6 m/s, the overall spectrum is disturbed such that resolving the beginning of the range of the velocities within the peak is difficult as shown in Fig. 2.18 (a). This effect appears also when the value of the frequency, which corresponds to the minimum velocity within the measured volume, is closer to the noise spectrum.

Figure 2.18 (b) is an example of when the maximum peak cannot be distinguished at all. This is due to the wider distribution of the velocities leading to an overall spectrum in the shape of a plateau with a cut-off frequency. The maximum velocity approximately corresponds to the frequency measured at half the maximum of the slope. The same principle can be applied to results from Fig. 2.14 (b,c).

The inserts in Fig 2.17 and 2.18 show the evolution of the resulting spectra when the range of the velocities within the measured volume increases. The spectrum becomes more asymmetrical and more disturbed from the Gaussian function.

### **2.2.7 Model Application: the Influence of the Waist Beam Size within the Measuring Area on the Spectrum**

The light beam profile from a laser in free space can be approximated by a Gaussian. A mathematical expression of the complex electric field amplitude can be found by solving

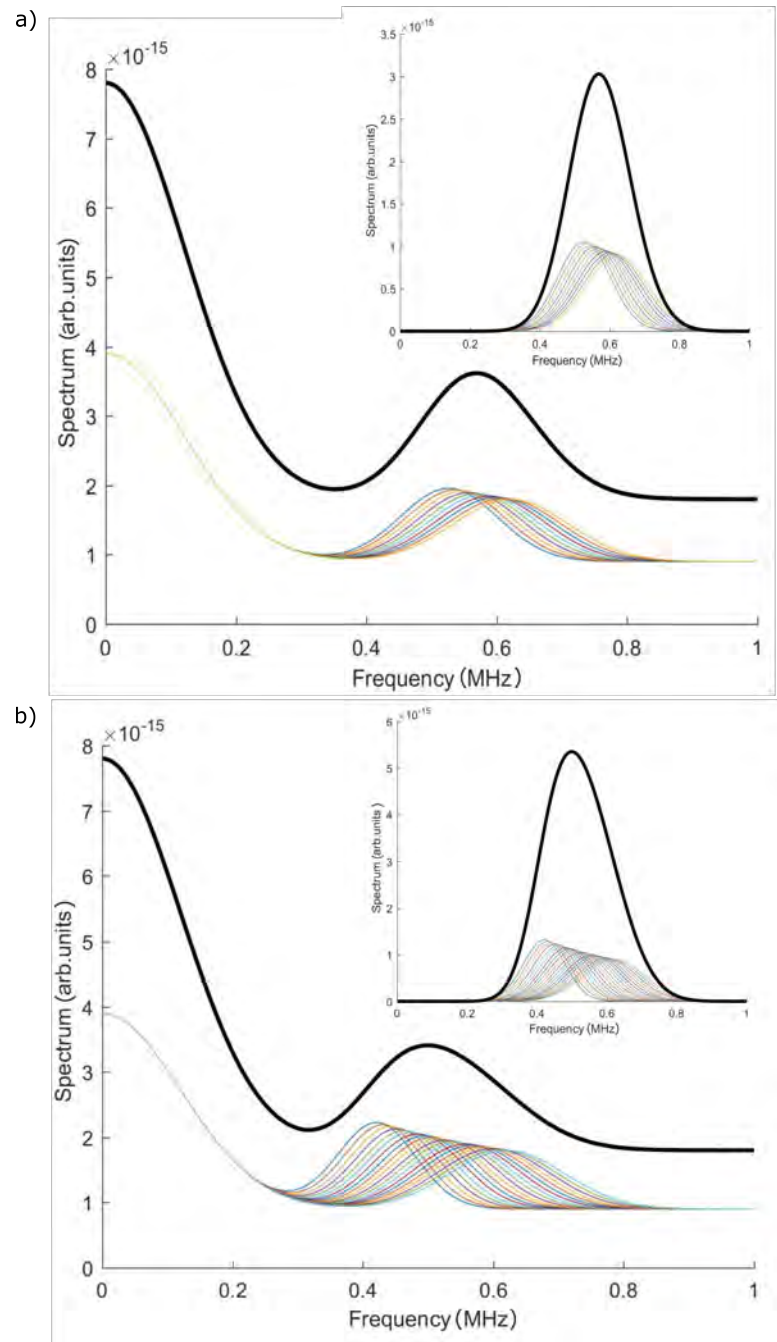


FIGURE 2.17: Calculation of the spectrum of the light scattered off the target when the velocity has a distribution, instead of being a delta-function. The parameters used in the simulation are presented in Table 2.2. The velocity is distributed as follows: a) 0.5 - 0.6 m/s, and b) 0.4 - 0.6 m/s. The results of the simulation show that the overall spectrum is influenced by all velocities. The results are shown when dark current noise was included in the main plots, and without noises in the inserts. The last results are valid for experiments when the peak frequency is shifted away from the spectrum of the noise.

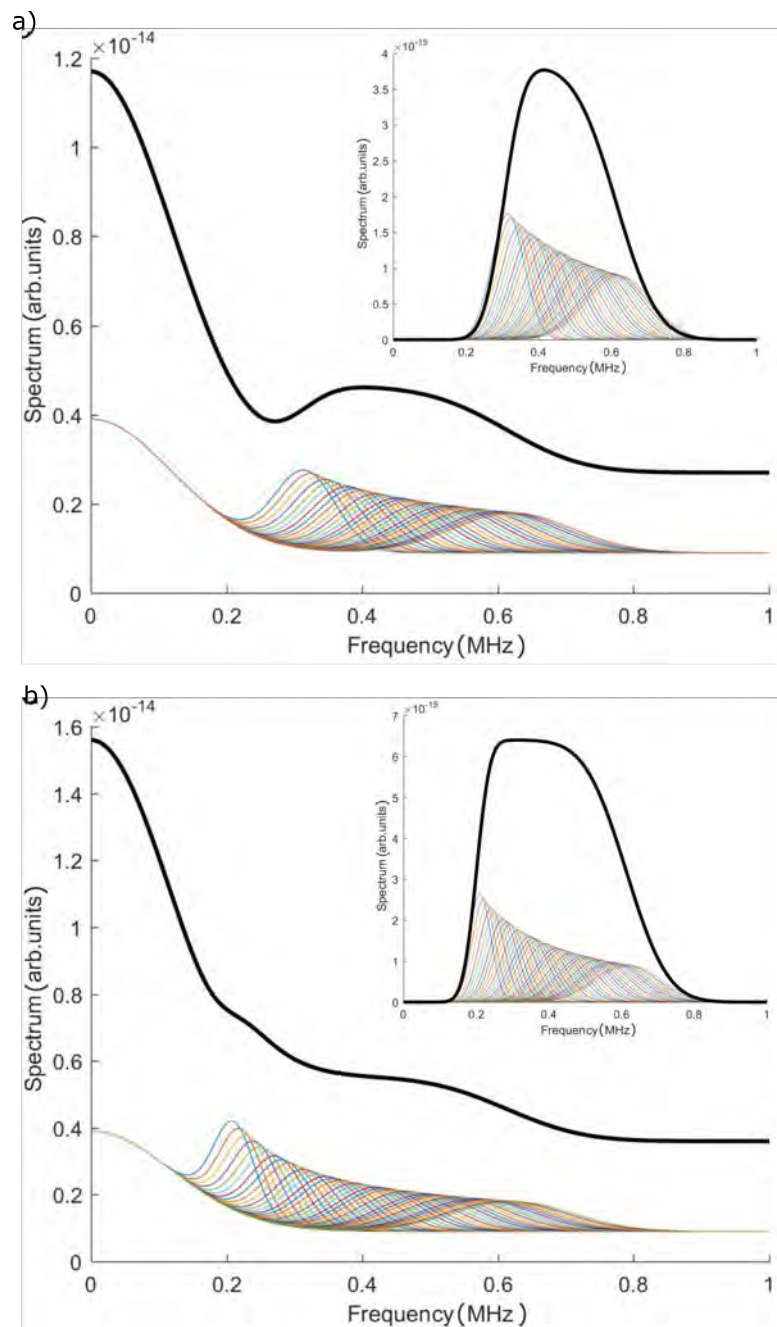


FIGURE 2.18: Calculation of the spectrum of the light scattered off the target when the velocity has a distribution, instead of being a delta-function. The parameters used in the simulation are presented in Table 2.2. The velocity is distributed as follows: a) 0.3 - 0.6 m/s, and b) 0.2 - 0.6 m/s. The results of the simulation show that the overall spectrum is influenced by all velocities. The results are shown when dark current noise was included in the main plots, and without noises in the inserts. The last results are valid for experiments when the peak frequency is shifted away from the spectrum of the noise.

TABLE 2.2: Parameters of the system used for the simulation presented in Fig. 2.17 and 2.18.

Parameter name	Value
Laser wavelength	$\lambda = 650 \text{ nm}$
Angle between optical axis and velocity direction	$\alpha = 70^\circ$
Spot size radius	$r = 2 \mu\text{m}$

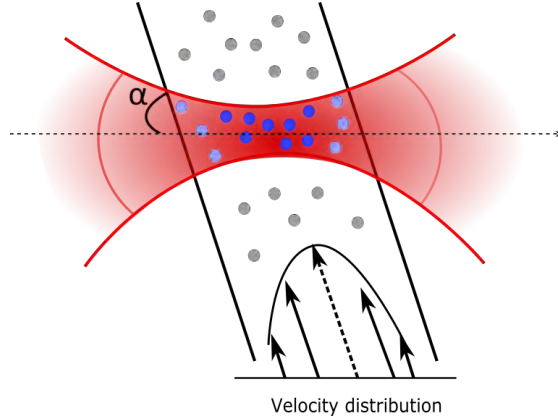


FIGURE 2.19: Schematic interpretation of the interaction of a laser beam with a Gaussian distribution incident on moving particles within a fluid, shown in red. The light is focused on the centre of the fluid channel. The blue coloured particles represent the ones which give a contribution to the SM signal. The light blue coloured particles are within the laser path, however, their contributions are assumed to be insignificant. The grey coloured particles are out of the sensing area. The particles which give a contribution are located within the depth of focus. The distribution of the velocities (bottom part of the figure) of the particles within the illuminated volume depends on the angle  $\alpha$  between the laser axis and the velocity vector. A dotted vector shows the velocity of particles where the light is focused.

the paraxial Helmholtz equation [1], yielding:

$$E(r, z) = E_0 \frac{w_0}{w(z)} \exp\left(-\frac{r^2}{w(z)} - ikz - \frac{ikr^2}{2R(z)}\right). \quad (2.23)$$

Here  $r$  is the radial distance from the centred axis of the beam,  $z$  is the axial distance from the beam's narrowest point (the "waist"),  $E_0 = |E(0, 0)|$  is the electric field amplitude at the origin at the time 0,  $w(z)$  is the radius at which the field amplitudes drop to  $1/e$  of their axial values at the plane  $z$ ,  $w_0 = w(0)$  is the beam waist size and  $R(z)$  is the radius of curvature of the beam's wavefront. The field's time dependence factor has been suppressed in the above expression.

The schematic interpretation of the interaction of the focused laser beam with a fluid channel is shown in Fig. 2.19. If the laser beam (red) is focused at the centre of the flow channel, some particles out of the laser focus (light blue colour) can still contribute to the signal since they also scatter some portion of light. The particles which are marked with a bright blue colour contribute the most to the overall spectrum.

The amplitude of the scattered spectrum is inversely proportional to the velocity of the target and proportional to the beam waist radius, see Eq. 2.19. However, it

is proportional to the cross section of the initial light beam, i.e. before the lens, and inversely proportional to the illuminated area of the target. The illuminated area can be calculated from the beam radius  $w(z)$ :

$$A = \pi w(z)^2 = \pi w_0^2 \left(1 + \left(\frac{z}{z_R}\right)^2\right), \quad (2.24)$$

where  $z_R$  is the Rayleigh length and is equal to:

$$z_R = \frac{\pi w_0^2}{\lambda}. \quad (2.25)$$

The divergence of the beam is equal to:

$$\theta_D \cong \frac{\lambda}{\pi w_0}. \quad (2.26)$$

Assuming that the target is located at a distance  $z$ , which is very close to the focus plane, i.e.  $z \ll 2z_R$  (within the depth of the focus), then the spectrum of the scattered light can be written as:

$$I(\omega) = \frac{2\pi\sigma^2}{\pi w_0^2 \left(1 + \left(\frac{z}{z_R}\right)^2\right)} \frac{N\langle s^2 \rangle E_0^2}{v/w_0} \exp\left(-\frac{(\omega - \omega_0)^2}{2v^2/w_0^2}\right) \propto \frac{1}{vw_0} \exp\left(-\frac{(\omega - \omega_0)^2}{2v^2/w_0^2}\right). \quad (2.27)$$

An important fact to note is that the Gaussian peak and its broadening are independent of the distance,  $z$ , to the object. The amplitude of the scattered light increases with decreasing size of the beam waist. The amplitude increases with an increase in the amount of scattered centres and their roughness ( $N\langle s^2 \rangle$  component). However, even though there is a clear dependence of the amplitude on the distance  $z$ , when the target is located close enough to the focus point, i.e. within the depth of the focus  $2z_R$ , the amplitude of the scattered light does not vary much. This is a promising result for the alignment and adjustment of the system for measurements.

Assuming that the illuminated volume or measured volume is within the optical density, which has an optical intensity higher than  $1/e^2$  of the peak intensity, the radius varies from  $w_0$  to  $\sqrt{2}w_0$  within the depth of focus  $2z_R$ . In this approximation, only those particles which travel within the illuminated volume contribute to the SM signal. The measured volume is centred on the focus plane of the beam. The schematic interpretation of the laser beam incident on the fluid with the particles within the fluid is presented in Fig. 2.19. Ideally, the light is focused on the central part of the flow channel, which is marked with blue scattering particles. The light blue coloured particles are still on the laser path, however, their contributions are assumed to be insignificant. The grey coloured particles are out of the sensing area and therefore do not contribute to the overall spectrum. The amount of particles, which interact with light, depends on the geometry of the system, especially on the angle  $\alpha$  between the direction of movement,

see the velocity vector in Fig. 2.19, and the laser axis. This leads to a distribution of velocities within the overall spectrum, since each particle has a different velocity.

## 2.3 Conclusion

The working principle behind an SM velocimeter is that light backscattered from a target is coupled back into the laser cavity where the initial light mixes with it. The operation of the SM sensor is strongly dependent on the level of light coupled back into the laser cavity. The amount of backscattered light can be calculated based on scattering theory leading to different results depending on the properties of the scattering object. A solid target is assumed to scatter light uniformly in all directions within the solid angle  $(0, \pi)$ . In contrast, the scattered intensity of light obtained from fluids has an angular distribution, which depends not only on the wavelength and optical properties of scattering centres, but on their size as well.

In this chapter I have presented the theoretical background which will be the basis of the rest of the work presented in this thesis. This includes a detailed study into the performance of an SM sensor, when applied to solid targets and to water flows seeded with additional particles. Firstly, theoretical studies and simulations into different seeding particles were aimed on improving the level of feedback for the SM effect in the case of flows. Secondly, since any kind of flow has particles off which light scatters, this comprehensive study can lead to a greater understanding when an SM sensor is applied to flow targets such as other liquids or gases.

To achieve these goals I needed to develop a scattering theory based on Mie theory to understand the behaviour of the SM sensor when applied to different targets. I therefore derived general formulas for scattered spectra for random geometries and for any kind of object, which had previously never been done before. Previous theories only included the case of the laser light at normal angle with respect to a rotating disc. The theory developed in this chapter has demonstrated that the light, which is backscattered from any type of target for both solid and fluid flows, is not just shifted by a frequency proportional to the target velocity, but rather the properties of the entire overall spectrum, such as its peak, the FWHM and its amplitude, are also influenced. Solid targets, such as mirrors and rotating discs, are assumed to be characterised with a velocity distribution function close to a delta function. The overall expected spectrum for this case was found to have a clear peak in the frequency domain. The expected overall spectra for fluids were calculated as well, showing the influence of different parameters on the results. These influences included parameters such as the distribution of velocities, and also the laser parameters. Moreover, assuming that fluids have a distribution of velocities within the illuminated area, this distribution strongly affects the overall spectra resulting in their different shapes. Simulations, based on this theory, have shown how the shape can vary, and one spectrum can not only provide information about the average velocity of the fluid, but leads to a full characterisation of the distribution of velocities

of the measured particles. It demonstrates the potential of the SM sensor when applied to fluids. Experimental studies of both investigations and a comparison with the theory, developed in this chapter, will be demonstrated in Chapters 3 and 4.

## Chapter 3

# Application of the Self-Mixing Technique to Solid Targets

In this chapter an overview of different parameters and the sources of possible limitations for SM sensor applications are given together with a characterisation of lasers to be used and ways to detect an SM signal. The set-up for the investigation of fast moving solid targets is shown with a discussion over the accuracy and precision which can be obtained for different geometries and solid objects. Experimental results from measurements with different solid targets, including a mirror and white paper target in different geometries, are presented for different SM regimes, followed by displacements and velocity measurements. The targets include a translational stage and a rotating disc, and application of 650 nm and 1550 nm lasers were studied, up to the limitation of the electronics used. The analysis of different parameters which can influence the performance of the sensor are also presented. These include: sources of possible limitation from the measurement set-up, bandwidth of the lasers, reflectivity of the measured targets, level of feedback from the target, velocity magnitude, and the angle between the laser axis and the target surface axis. The analysis contains both experimental results and simulations of spectra obtained for different parameters of the experiments.

### 3.1 Light Sources for Self-Mixing Measurements

#### 3.1.1 Introduction

The main advantages of the self-mixing scheme, with respect to traditional interferometry, can be listed as follows: the possibility of unambiguous measurements from a single interferometric channel; applicability to use rough surfaces instead of mirrors through diffusion rather than reflection; compactness of the set-up; much lower cost; and ease of alignment. While the first two advantages constitute a breakthrough in interferometry from a more scientific point of view, the last three are of the utmost interest for technological applications.

TABLE 3.1: Influence of different parts of an SM sensor on the limitation of measurable velocities.

<b>The parts of self-mixing sensor</b>	<b>Possible sources of limitation</b>
Laser	Oscillation frequency Emission bandwidth
SM technique	Level of feedback from the target The backscattered light spectrum
Detection items (photodiode, photoreceiver, amplifier)	Their bandwidth Quantum efficiency

An SM system consists of several parts, each of which influences its performance, and, in particular, dictates the limits on the measurable velocities. The sources of these possible limiting factors are listed in Table 3.1. Previously, only small velocities, for the case of SM velocimetry sensors applied to fluids, were studied, as previously discussed. While SM sensors have never been applied to gas jets, this thesis attempts to investigate this possibility. Velocities of gas jets are much higher than applications where SM sensors have previously been applied. Therefore, the properties of the laser sensor, and all of its parts, should be adequate to achieve the aims of the measurements.

It is important to choose a suitable laser for SM measurements. The LD employed for measurements should have a high sensitivity and small beam divergence. A discussion of different laser systems was given in Chapter 2, which includes a review of the lasers used for SM measurements (see Table 1.3).

The possible limiting factors, as listed in Table 3.1, are as follows:

1. The SM method implies that the laser itself responds to the external excitation with a frequency proportional to the velocity of the target, i.e. the frequency of the Doppler shift. The laser can respond only to a frequency which does not exceed its oscillation frequency. Additionally, the frequency can be amplified only within the bandwidth of the emission of the laser.

2. The SM technique can only work at certain levels of feedback from the target ( $I/I_0 > 10^{-12}$  [89]). Moreover, the spectrum of the backscattered light depends on the velocity of the target as well as other parameters of the target (see Chapter 2).

3. The detection items (photodiode, photoreceiver, amplifier) are crucial components of any light dependent sensor, and they only work within a certain bandwidth and with a specific quantum efficiency.

Through the experiments presented here, the effects of all these parameters are discussed in detail for specific cases. The effects from the level of feedback on the shape of the SM signal and its amplitude were presented in Chapter 1. The effects from the target velocity and laser parameters on the spectrum of the SM signal were presented in Chapter 2.

### 3.1.2 Optical Bandwidth Measurements

Optical bandwidth values may be specified in terms of frequency or wavelength. To convert a wavelength interval  $\Delta\lambda$  into a frequency interval  $\Delta\nu$ , the following equation is used:

$$\Delta\nu = \frac{c\Delta\lambda}{\lambda^2}. \quad (3.1)$$

For laser characterisation and investigations on the limiting factors, emission spectra were measured with an optical spectrum analyser (AQ6370Z). For measurements, the laser was coupled into the analyser using different fibres. A single-mode fibre with a 9  $\mu\text{m}$  diameter core and a multi-mode fibre with a 250  $\mu\text{m}$  diameter core were used. The lasers under consideration were:

1. A series of lasers with wavelengths in the range of 635 - 650 nm were characterised. These measurements demonstrated that the laser bandwidth was less than 400 MHz. The resolution of the optical spectrum analyser did not allow the bandwidth to be determined more precisely. However, velocities of up to 200 m/s can still be measured given a 400 MHz bandwidth.

2. The second type of tested lasers was a DFB (distributed feedback) laser with a wavelength of 1550 nm [108] (PL15N0021FCA-0-0-.5 laser from Laser Components). The measured spectrum is shown in Fig. 3.1 and 3.2, and the output power distribution as a function of wavelength is shown in Fig. 1.5. The wavelength bandwidth varies with injection current. In the case of emission at 10 mA, which is close to the threshold current ( $I_{th} = 9.8$  mA), the wavelength and bandwidth are 1538.88 nm and 0.13 nm respectively, which leads to a frequency bandwidth of 16.7 GHz. The central wavelength and bandwidth were found by fitting the spectrum of the laser output with a Lorentz function, see inset of Fig. 3.1. The structure of the emission spectra demonstrates that the laser is a DFB laser, which can be concluded by comparing the schematic intensity distribution in Fig. 1.6 with the experimental intensity distribution in Fig. 3.1. The measured spectrum has a clear peak, a stop bandwidth of 295.6 GHz, a separation between modes of 139 GHz, and the length of the cavity is 1.08 mm.

The emission wavelength and bandwidth of the laser change with the injection current, see Fig. 3.2 and 1.5. At high injection currents the output spectrum is no longer smooth as oscillations are observed within the bandwidth. For example as in Fig 3.1, at 30 mA the bandwidth is 60.8 GHz at a wavelength of 1539.266 nm, and the emission peak has spikes across the main peak, which is no longer Lorentzian. The resulting oscillation (or beating) of the output spectrum from an SM sensor has a well-defined frequency of the Doppler shift. When using an LD with unpredictable and non-linear oscillations in the emission spectrum, the detection of the oscillations of the output spectrum of the SM signal is difficult to achieve. For example, when the laser is operated at a current much higher than the threshold, the operation of the SM sensor is hard to predict. Conversely, at an injection current which is slightly above the threshold current, up to 15 mA in the case of this laser, the shape of the spectrum is almost Lorentzian. This allows a smooth

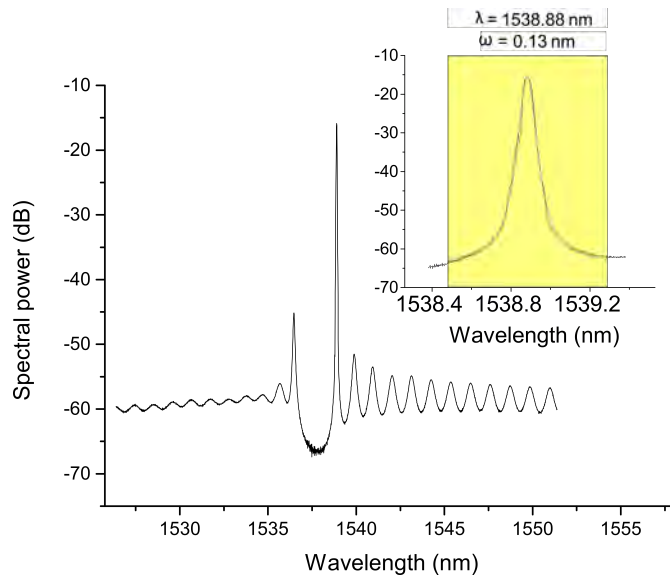


FIGURE 3.1: Measured spectrum of a DFB laser diode operating at 1538.9 nm (peak wavelength at room temperature) with operational current  $I = 10$  mA. The shape of the emission spectra demonstrates that it is a DFB laser, see Fig. 1.6, as it displays a clear stop band. The inset shows the details of the peak wavelength at which the laser operates.

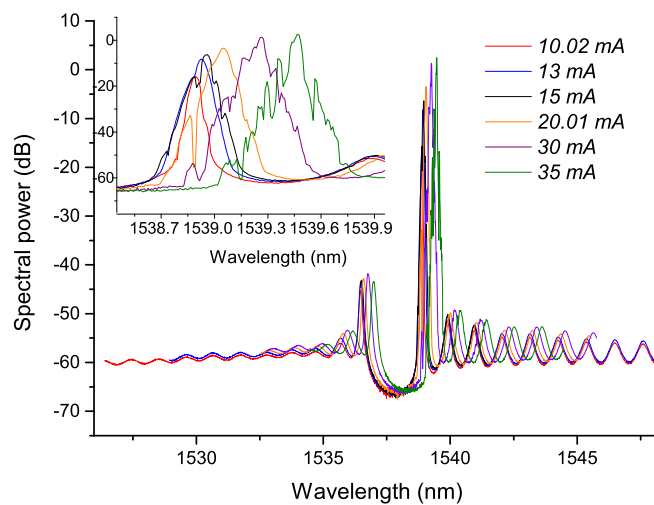


FIGURE 3.2: Measured spectrum of the diode laser at 1539 nm at different currents showing the characteristics of the DFB laser. The deformation of the shape of the laser emission line demonstrates the red-shift of the wavelength with increasing injection current. The inset shows the change of the shape of the laser line in detail as the laser injection current is varied, which is presented in different colours, see labels on the right.

response of the SM sensor to be observed. Furthermore, the relatively high bandwidth guarantees the frequency response of the laser to the external excitation with a wide range of frequencies. For example, the bandwidth of the DFB laser PL15N0021FCA-0-0.5 varies from 16.7 GHz (at 10 mA) to 31.6 GHz (at 15 mA). This laser allows a wide range of velocities, of up to 2,000 m/s, to be detected.

3. The third and final laser tested was a Multiple Quantum Well (MQW) InGaAsP

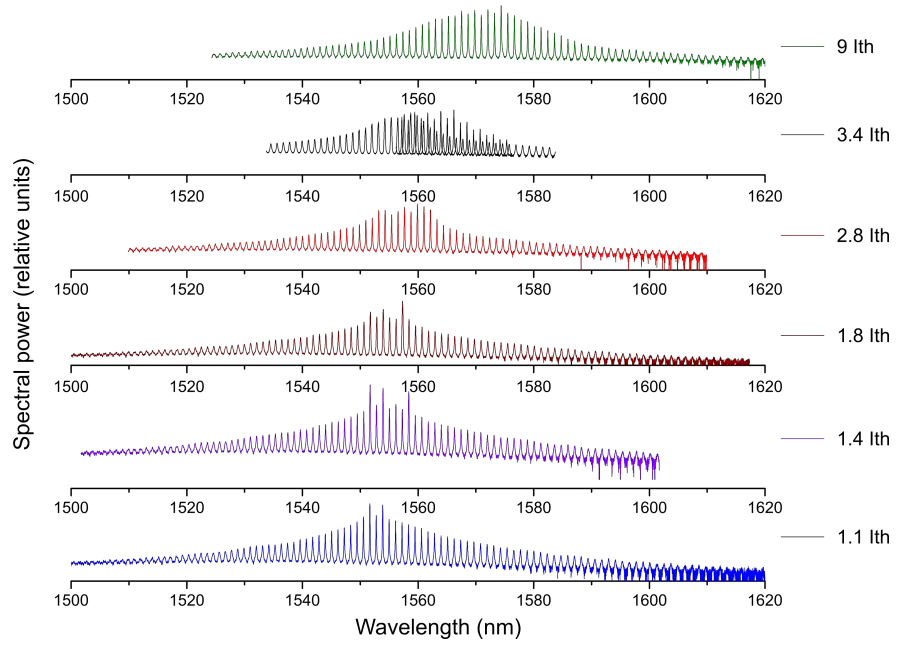


FIGURE 3.3: Measured spectra with an offset on the y-axis (curves shifted for clarity) of MQW InGaAsP LD above the threshold lasing condition ( $1.1 \cdot I_{th} - 9.0 \cdot I_{th}$ ) at room temperature. The plots demonstrate the typical behaviour of FP lasers with a number of longitudinal modes and a shift in lasing wavelength with injection current.

FP laser with a wavelength in the range of 1550 - 1580 nm which has demonstrated a potentially promising bandwidth up to 1.5 GHz. Its spectrum was measured at different currents above the threshold condition ( $1.1 \cdot I_{th} - 9.0 \cdot I_{th}$ ), using an optical spectrum analyser with a wavelength resolution of 0.05 nm. The obtained spectra are shown in Fig. 3.3, where they are presented with an offset in the y-axis to demonstrate the shift in lasing wavelength. The stepwise red-shift of approximately 15 nm of the peak wavelength with increasing injection current is typical for FP lasers. The main advantage of the MQW InGaAsP FP laser is its high bandwidth. The drawback of the laser can be seen from its emission spectra, see Fig. 3.3. The main frequency of the spectrum can hop between modes, see the schematic spectra for FP lasers in Fig. 1.6.

Figure 3.4 shows one emission spectrum of the MQW InGaAsP laser which was obtained at room temperature at  $1.8 \cdot I_{th}$ . The spectrum represents the typical characteristics of an FP cavity. During the emission, the main wavelength of the laser hops between different modes, the main three of which are highlighted in yellow in the inset of Fig. 3.4. The linewidth of the laser emission varies from 0.18 nm to 0.22 nm for 1551.75 nm and 1557.32 nm which leads to a frequency bandwidth of 22 - 27 GHz according to Eq. 3.1.

If the emission spectrum of the laser stays stable during the measurement, it can be used in an SM sensor. However, it is not certain that the laser will emit on that exact wavelength. This can lead to an inaccuracy of the measurement. The sensitivity of DFB lasers are higher than FP types of lasers for the specific coupling coefficient and cavity length values [22].

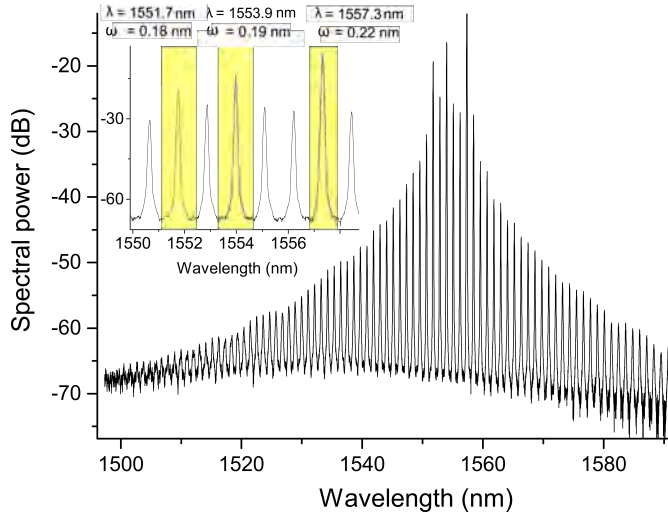


FIGURE 3.4: The emission spectrum of the laser at room temperature at  $1.8 \cdot I_{th}$ , with spikes at different wavelengths. The inset represents the lasing wavelength with three main peaks between which the laser wavelength hops. The numbers at the top give information of the wavelength  $\lambda$  and the bandwidth  $\omega$  (in nm) obtained by Lorentzian fitting.

For the majority of the results presented in this thesis, the SM experiments were performed using an LD with 650 nm wavelength (L650P007) on a single longitudinal mode with a power of less than 5 mW, and driven by a constant current just above the threshold current. This laser was chosen as it is one of the most commonly used lasers for displacement and vibration measurements, so it has proven itself to work with the SM technique [39, 42, 109, 110]. The DFB laser of  $1.55 \mu\text{m}$  was also tested as it is easier to use at accelerator-related facilities; these results are also presented in this chapter.

### 3.1.3 Detection Schemes in the Self-Mixing Technique

The SM effect influences both the power and the frequency spectrum of the laser. The external influence of the coupled-back light causes changes in the laser power and threshold gain. This is a result of the light interference, which is formed inside the active laser medium. The SM effect can be detected as a change in the power. The resulting power exhibits a beating (see Eq. 1.39) with a frequency proportional to the difference between the frequencies of the initial light and the backscattered light. This difference is effectively equal to a Doppler shift. At the same time, the laser emits light at a slightly changed wavelength (see Eq. 1.35) as a result of the SM effect. This change in the wavelength, however, is very difficult to detect without expensive equipment for high resolution wavelength measurements. The easiest way to detect the SM effect is to measure the output power oscillations. This measurements can be made in three different ways:

1. Photodiode monitoring. The variation of the output power can be detected using a photodiode (PD). Depending on the LD, the PD can be part of the laser package, otherwise the light has to be detected by an external PD. When the PD is a part of

the LD package, it is used for monitoring the laser power stability. The PD detects the reflected laser beam. As a result, the PD can also detect the SM signal oscillating at a Doppler frequency. Very weak changes in photocurrent can be amplified by a broadband transimpedance amplifier and used for the detection of output power oscillations.

2. Injection voltage detection (automatic detection). As a result of the SM effect, the driving current of the laser changes, hence the terminal voltage also changes. These variations can be directly measured [40, 45].

3. Antenna detection. This method is widely used for the detection of waves in the THz regime. It is based on the change in conductivity of a dipole antenna [111]. The same principle can be used for SM detection. The antenna can be placed outside the active medium of the laser, and the electric charge can be induced on the antenna as a result of the oscillation caused by the SM effect within the active medium. However, this technique has not previously been used for SM detection.

The automatic detection and the PD-based methods were compared, and the results were the same [45]. Therefore, preference was given to the PD detection method due to its simplicity [45]. Together with the PD-based method, the current detection should be very useful for higher velocities, when the Doppler frequency shift is far away from the spectrum corresponding to dark current noise.

As mentioned earlier, one of the main limitations on the performance of the system is the bandwidth of the detecting elements. If an LD is chosen as a light source, the built-in PD is usually part of the LD package. The built-in PD operates as a current detector to control the injection current. The PD is responsible for the power stability of the LD. The SM sensor can be designed in such a way that the current detector (PD) is used to obtain the SM signal itself. However, the limitation on the detectable frequency is dictated by the bandwidth of not only the laser and the PD, but of the transimpedance amplifier as well. The transimpedance amplifier converts the current from the PD into a voltage and then amplifies it. There are some commercially available transimpedance amplifiers, but the equipment is more expensive for bandwidths higher than 100 MHz. A photodetector with a high bandwidth can be used instead of a transimpedance amplifier. This adds some advantages, such as the possibility to use additional lasers to amplify the signal, increased flexibility in location of the system, and the possibility to use fibre optics. However, the price of these detectors is still quite high. Alternatively, custom-designed electronics can be used, and possible solutions are as follows:

1. If the beating frequency of the SM signal can be fixed to a known value, then the detection and amplification can be easier. A specially made circuit board or a transimpedance amplifier of lower than GHz bandwidth can be used for this purpose. In order to obtain an SM signal at a fixed frequency, a modification of the system using an additional laser (slave laser) as a reference point must be used.

The additional laser must have the same wavelength as the source-laser and its temperature and current must be precisely controlled. When the master laser (where the SM effect appears) is used for measurement, the beating of the voltage is proportional to

the Doppler shift. By adding a slave laser, and by adjusting the current (or temperature) of the slave laser, a beating between the slave and master laser wavelength also appears. When the SM frequency is the same as the beating frequency of the two lasers, and the system detects an increased beating due to the resonance, the shift in frequency can be determined from the wavelength of the slave laser, and not by direct measurement with an oscilloscope. The value of the current (or temperature) allows the difference in frequency with respect to the initial source-laser frequency to be calculated. A fixed frequency can be detected using filters and an integrator; the changeable and detectable factor is the frequency of the slave laser, so the exact peak will be detected as soon as there is a match between the two.

2. Another way to improve the system is to use an additional laser, if the light is delivered to an external photodetector. For example, in the case of using fibre optics, laser light can only easily be added at the last stage before the photodetector. Additional laser light of well-known frequency (wavelength) can, therefore, increase the level of the signal which is detected by the receiver.

## 3.2 Application of Self-Mixing Technique to Solid Targets

### 3.2.1 Set-up Description

The SM technique can be applied using different lasers. The properties of both the target and the laser itself need to be correctly taken into account in order to fully understand the overall signal.

Since SM is a sensitive technique, a detailed investigation into the technique had to be performed. Different targets were first studied to gain a better understanding of the working principle and how it may be applied to different targets. The following subsections will cover experiments where the SM method was applied to solid targets:

1. Study of different regimes of SM.
2. Variation of velocity and distance.
3. Investigations into scattering targets (see Fig. 3.5):
  - 3i. A mirror with a 92% reflectivity on a translational stage.
  - 3ii. White paper on a translational stage.
  - 3iii. A rotating disc.

The SM sensor is based on an LD of 650 nm wavelength (L650P007) with a power of less than 5 mW, driven by a constant current. Schematic of the experimental set-up is presented in Fig. 3.5. The light from the LD of 650 nm is focused by means of multiple lenses with a numerical aperture (NA) of 0.26 onto a target. Light then scatters off the target and is coupled back into the laser cavity, leading to an SM effect. A signal is produced by a built-in PD, amplified and converted into a voltage signal by a transimpedance amplifier by Femto, DHPCA 100 [112].

The right-hand part of Fig. 3.5 demonstrates the projection of the velocity on the laser axis in different experimental set-ups. Only the velocity component along the laser

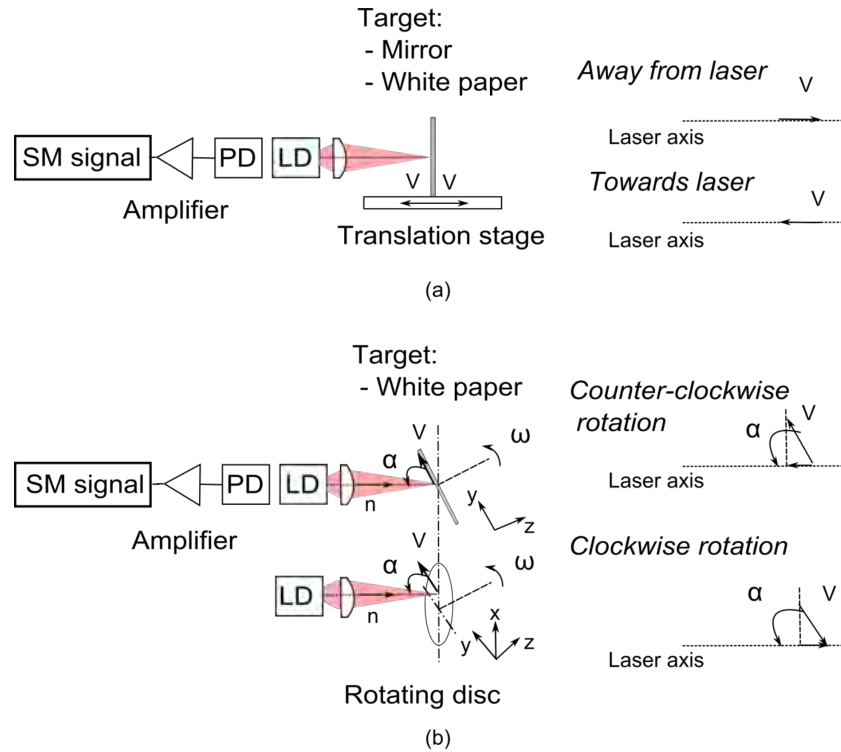


FIGURE 3.5: Illustration of the layout of the experiments on the left side, and a schematic illustration of the projection of the velocity on the laser axis for each case on the right side. Two experimental set-ups were established for testing the SM velocimetry technique: (a) a translation stage and (b) a rotating disc. The translation stage (a) moves the target (mirror or white paper) towards and away from the laser, as a result, the scattered light has a Doppler shift proportional to the velocity vector in the direction of movement. In the case of rotating disc (b) covered with white paper, the direction of the rotation defines the direction of the velocity vector relating to the laser axis. The projection of the velocity vector on the laser axis is dependant on the incident angle  $\alpha$ .

light axis interacts with the laser light. The translational stage, with a diffusive surface mounted on it, allowed additional experiments to be performed to study the effect of the angle on the signal. However, most experiments regarding angle variation were performed using the set-up with a rotating disc.

The translational stage (Fig. 3.5 (a)), which was used for experiments, allowed both the distance (up to 30 cm with a step size of 100  $\mu\text{m}$ ) and the velocity of the stage (1 mm/s - 10 cm/s) to be controlled. These parameters were known with high precision and served as a benchmark for the data obtained using the SM sensor. A rotating disc (Fig. 3.5 (b)) allows high velocities to be reached without changing the distance between the SM sensor and the target. Studies into the influence of the angle are easy to perform in such a set-up. However, this set-up resulted in some complications, which will be discussed later.

### 3.2.2 Signal Processing for Velocity Measurements

The principle of obtaining the velocity of the target from the SM signal is based on the measurement of the Doppler shift, which is the beating frequency of the signal. As

previously shown, if the target moves with a constant velocity, the spectrum of the SM signal has a peak in the frequency domain, which is proportional to the velocity. The property of the target, however, can influence the spectrum. The peak frequency might be widened and even shifted, depending on the distribution of the velocity within the measured area. The main principle of signal processing remains the same: to calculate the spectrum of the signal.

A program written in MatLab was used for data analysis and signal processing to calculate the spectrum, and then to extract the peak frequency. The basic idea is as follows. Based on the collected experimental data, a Fast Fourier Transformation (FFT) of the signal is performed, the peak of the spectrum is extracted from a fit using, for example, a Gaussian distribution. The result can then be presented by the value of the peak and the velocity, which can be calculated taking into the account the wavelength of the laser. Alternatively, the spectrum can be analysed in more detail if additional information is needed.

The spectrum of the signal is calculated by performing an FFT of the SM signal. Since the measurements are obtained from the oscilloscope, they have discrete values. The Discrete Fourier transformation (DFT) produces frequency domain components in discrete values or bins. FFT is an optimised implementation of DFT. The real signal always has a finite set of data. A Fourier Transformation (FT) is based on the assumption that the signal for the calculation is infinite, and the FT calculates the frequencies of the sine or cosine components of the signal [113]. The FFT works in a way that the infinite signal for the calculation is achieved by copying the signal itself. The actual FFT assumes there is a finite data set with a continuous spectrum that is one period of a periodic signal. For the FFT, both the time domain and the frequency domain are circular topologies, so the two endpoints of the time waveform are interpreted as though they were connected together.

As a result, two different cases can appear, see Fig. 3.6:

1. When the measured signal is periodic and has an integer number of periods within the acquisition time interval, the FFT works correctly as it matches this assumption. The spectrum has only one frequency, corresponding to the actual frequency, see Fig. 3.6 (a).

2. In any other case, the measured signal is not an integer number of periods, so the endpoints are discontinuous. These artificial discontinuities appear in an FFT as additional frequency components not present in the original signal. Therefore, the spectrum obtained using an FFT is not the actual spectrum of the original signal, but a smeared version, which leads to a spreading of the fine spectral lines into wider signals, see Fig. 3.6 (b).

Different windows (Rectangular, Hamming, Hanning, Blackman, etc. [114]) are used for smoothing the overlapping interval of neighbouring data sequences. Windowing consists of multiplying the time record by a finite-length window with an amplitude that varies smoothly and gradually toward zero at the edges. This makes the endpoints of the waveform meet and, therefore, results in a continuous waveform without sharp

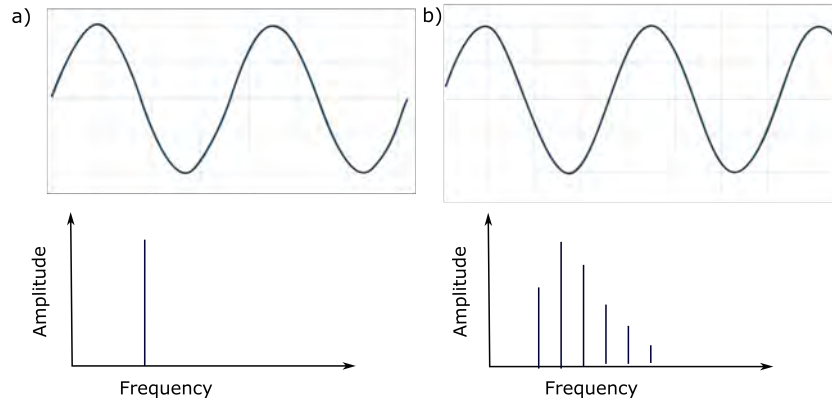


FIGURE 3.6: Two types of real signals (top plots), which can appear during experiments. An FFT can be used to obtain their spectra (bottom plots). The figure demonstrates the influence on the spectra when an FFT performed on the periodic sinusoidal signal with only one frequency in the original data. (a) When the signal has an integer number of periods within the acquisition time interval. The resulting FFT calculation gives only one true frequency in the spectrum. (b) In any other case, FFT calculation adds many frequency components due to a discontinuity at the endpoints.

The resulting spectrum is different from the true spectrum [113, 114].

transitions. This leads to two main results. Firstly, as soon as the analysed signal is not a sine or a cosine function, the additional frequencies appear in the spectrum. To overcome this effect, window functions are usually applied to the signal. Secondly, a window function disturbs the original signal, since window functions also have their own spectra. Therefore, the resulting spectrum is a multiplication of two spectra: the original one and the one from the window function. There is no universal approach for selecting a window function. In general, the Hanning window is satisfactory in 95% of cases [114], but it is advised to compare the performance of different windows for specific applications.

### 3.3 Application of the Self-Mixing Technique to a Translational Stage

#### 3.3.1 Different Regimes of the Self-Mixing Signal

The main application of the SM technique is to measure vibrations or small changes in the position of an object under study. A small displacement of the target leads to an easily identifiable signal, such as a sawtooth-like type of signal, see Chapter 1. The different regimes, which can be defined from the shape of the signal, depend on the amount of light coupled back into the laser cavity. For the first set of experiments presented in this section, different regimes of the SM signal were studied whilst investigating the influence of the distance between the laser and the object.

For the experiment, a mirror was located on a translational stage moving with a well-known velocity. The system is shown in Fig. 3.7. A plane mirror was chosen as a target since it allows a stable moderate signal without speckle effect to be obtained. The

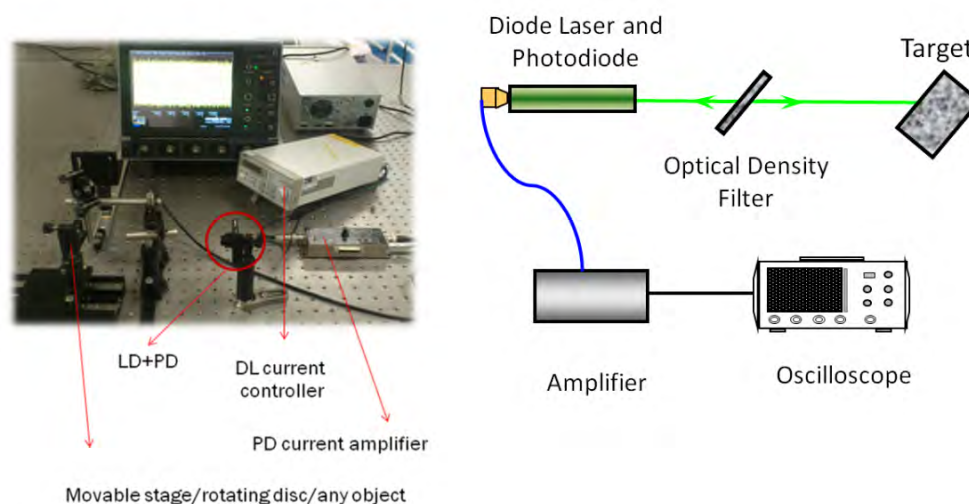


FIGURE 3.7: The SM set-up used for the first experiments with the mirror located on a translation stage as a target.

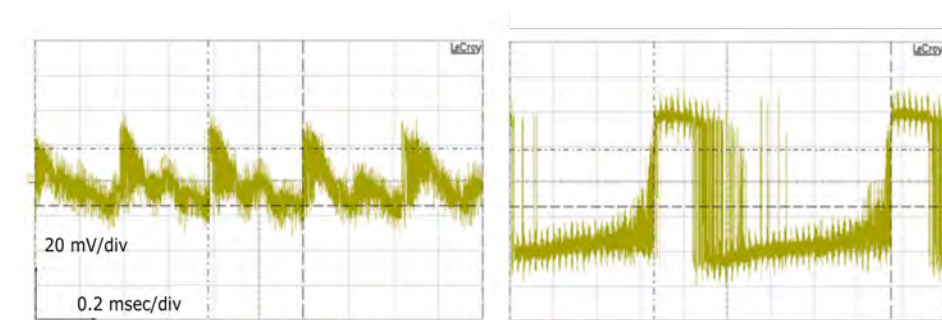


FIGURE 3.8: First experimental results obtained from the SM set-up. The signals are periodical, and their period correspond to the respective velocity of the target. However, they are far from the signals which are expected from the SM technique, i.e. sawtooth-like or sinusoidal shape. Despite the signals not looking like the theoretical ones, the frequency of the beating can still be defined with lower resolution compared to the ideal SM signals. Furthermore, those signals can be used for displacement measurement.

utilisation of the sensor was limited in this case, however, it was practical for studying the effect. Moreover, using different density filters between the laser and the target allowed the effect of the level of feedback on the shape of the SM signal to be studied.

During these experiments, the main goal was to investigate the ways to obtain the required type of signal. Examples of the first signals can be seen in Fig. 3.8. The obtained signals are completely different from what is expected from an SM signal, such as saw-tooth-like or sinusoidal shape. However, the signals are still periodical, and hence the frequency and thus velocity can be calculated. These results have lower accuracy relative to those calculated from ideal SM signals. These distorted types of signals can still be used for displacement measurements. In order to receive ideal SM signals for the velocity measurements, many factors need to be optimised such as a distance to the target, noise in the LD, noise in the amplifier and light collimation (defocusing for the mirror and focusing in the case of scattering), etc.

The next step was to study the influence of a change in the level of feedback. The measured signals are not sharp, but have a smooth increase with a subsequent decay. Strong feedback is obtained for a high level of the back coupled light, resulting in a sawtooth-like signal, which is expected to have a sharp rise (or fall) followed by a linear decay, see Fig. 1.11 (c) and (d), rather than a smooth curve, which was obtained during experiments presented in Fig. 3.8. The following changes to the set-up were made during the experiments in order to achieve a higher level of light coupled back into the laser cavity:

1. Focusing/defocusing the laser light: Defocusing is needed when an SM sensor is used for mirror-like targets due to the high reflectivity of the target. When the laser is focused on the mirror, a high level of light is coupled back into the cavity. Consequently, the laser experiences chaotic overloading, and its lasing properties become unpredictable. As a result of defocusing, feedback level decreases compared to focusing on the mirror, and the phase lock is achieved more easily;
2. Changing the distance between the laser and the target as per Chapter 1. When the target is further away from the diode laser, the amount of light which can be coupled back naturally reduces due to the beam divergence.

To study these effects, experiments with a mirror and white paper were performed using the same set-up where the target moves back and forth along the laser light axis. Figure 3.5 (a) shows the schematic set-up, and Fig. 3.9 presents the results from the experiments. The target was moved by a stage which was driven by a direct current motor controller. This allowed velocities in the range of 0.01 - 10.00 cm/s to be reached with a precision of 0.5 mm/s. The four feedback regimes, which were described in Chapter 1 (1.4.8), see Fig. 1.11, were observed and studied. Different regimes were obtained depending on how focused or defocused the light was onto the target.

Figure 3.9 demonstrates different types of SM signals and the distortion of the shape of the signal depending on the amount of light coupled back into the laser cavity when (a) a mirror and (b) a white paper were used as targets. Both plots show the obtained signal for different values of the feedback coefficient  $C$  presented by different curves with the value of  $C$  on the right side. An offset of curves along the  $y$ -axis allows signals corresponding to different level of feedback to be compared with each other. The magnitudes of the signals were not changed, so an estimation of the actual levels of the signal amplitudes could be made and an evolution of the signals corresponding to different  $C$  can be tracked.

The curves in the middle with  $C < 1$  correspond to weak feedback for which the shape of the signal is close to a sinusoid. As the amount of light coupled back into the cavity increases, the shape of the signal becomes distorted and a non-symmetrical sinusoidal signal for  $C \approx 1$ . In the case of strong feedback with  $C > 1$  the signal is sawtooth-like, which can be seen from the top and bottom curves in both Fig. 3.9 (a) and (b). These results can be compared with simulated signals, see Fig. 1.9, 1.10, and 1.11.

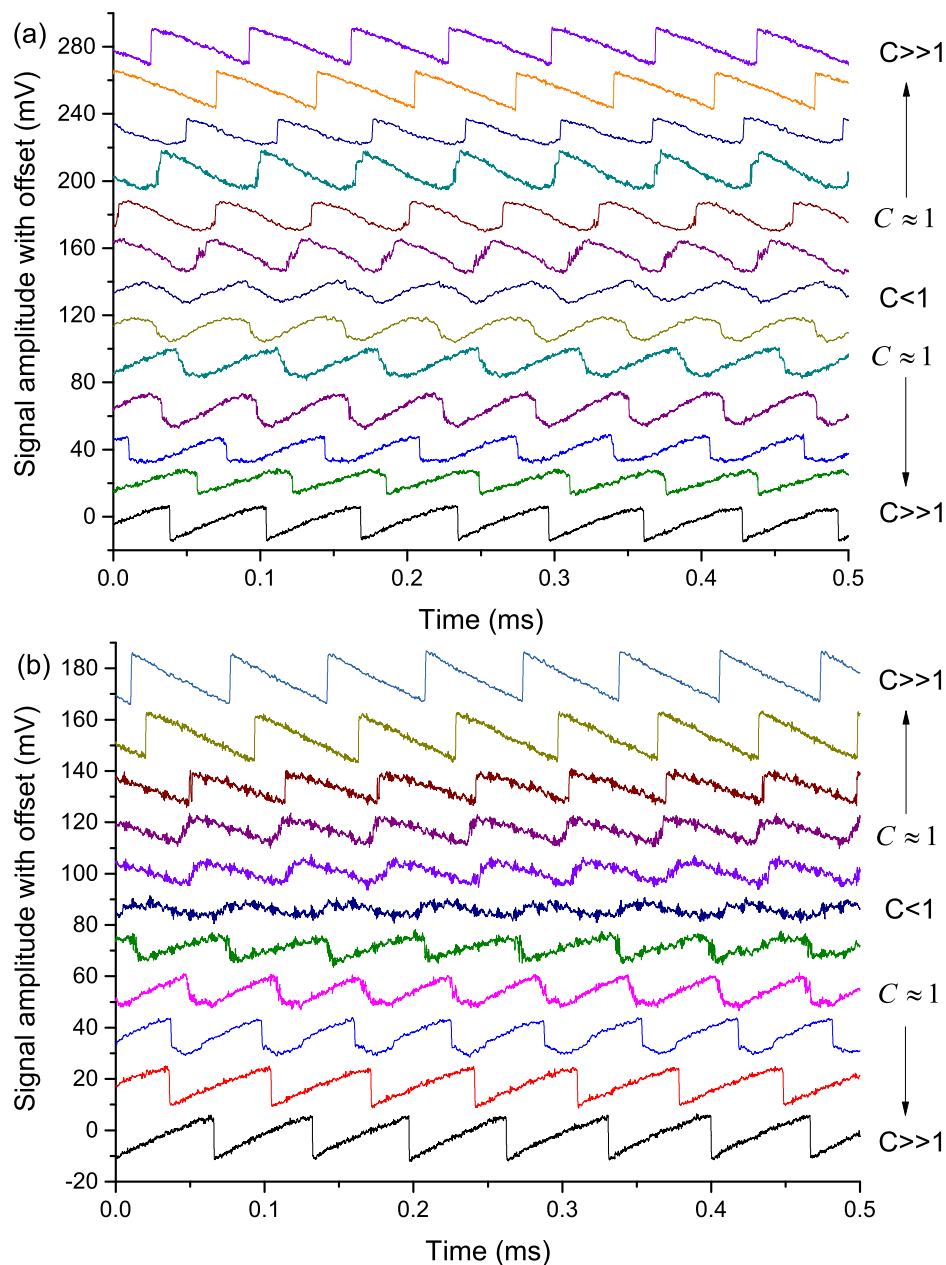


FIGURE 3.9: Experimentally obtained self-mixing signals for two different types of surface: (a) mirror and (b) white paper when the translational stage was moving with a velocity of 5.00 cm/s toward (top curves) and away (bottom curves) from the laser. The curves are shifted along the  $y$ -axis so that they can be compared with each other and as a function of the level of the feedback re-entering the cavity. The coupling efficiency is related to the coefficient  $C$ .

The direction in which the target moves can be derived from the tilt of the signal for asymmetrical signals. The evolution of the shape of the signal for different levels of feedback in Fig. 3.9 also demonstrates the changes of direction. The top signals in both, Fig. 3.9 (a) and (b), are tilted to the left which corresponds to the case where the targets move towards the LD. The bottom curves, when the signal tilts to the right, are when the target was moving away from the laser.

Experiments with a mirror, which moves across the transverse axis of the laser beam, were performed to understand the SM technique as a whole, such as the best geometry of the set-up, reduction of the noise level, the focusing/defocusing properties of the LD and the system itself. In the case of a well-adjusted set-up, the mirror target was moved up to 90 cm away from the laser without changing the shape of the signal, see Fig. 3.9 (a) where  $C > 1$ . In some cases, the laser beam was defocused in order to reduce the amount of light coupled into the laser cavity. For further reduction, density filters were tested, and applied by placing them between the target and the LD in order to avoid changes in the focusing point of the laser.

Based on the shape of the signals obtained from the SM system, some assumptions about the reflectivity of the target can be made as well. The reflectivity directly influences the feedback parameter and thus the performance of the SM technique. Reflectivity is a function of the refractive index and incident angle. The reflectivity of an aluminium mirror at a normal angle for 650 nm is around 92% [90], and it is easy to obtain a sawtooth-like signal or even to overload the laser with the amount of light coupled back resulting in a chaotic behaviour of the laser. With a rough surface target such as paper, weak or moderate feedback is expected due to a lower reflectivity equal to approximately 60% when normal to the surface for laser light of 650 nm. Typical examples of the signals received with white paper are shown in Fig. 3.9 (b).

For both targets, the signals are similar in shape, and the precision of the methods is the same. However, the amplitude of the signal is smaller when compared with the same type of signal in the mirror experiments. In the case of white paper in Fig. 3.9 (b) the signal amplitude is slightly reduced and distorted in shape as a result of speckle effects [10]. In contrast, the shape and trends are the same using the mirror as a target, see Fig. 3.9 (a). The amplitude of the signal is smaller as well, as can be seen from the offset axis. The offset gives sense of scale to the signal, which can be seen from the difference between the maximum and the minimum of each curve. The size of the laser spot on the white paper required readjustments whilst the distance between the LD and target was changed. Using the mirror as a target allowed measurements up to 90 cm away from the target to be carried out without changing anything in the set-up. However, when using white paper as a target, readjustments for additional focusing of the laser beam were required periodically up to 50 cm. No signal was detected at larger distances between the laser and the target.

The experimental results which are presented in Fig. 3.9 have demonstrated the evolution of the SM signal waveforms obtained for different values of the feedback parameter  $C$ . The experiments have also demonstrated the possibility to obtain different types of signals for both mirror and white paper targets.

### 3.3.2 Self-Mixing for Displacement Measurements

The aim of the measurements presented in the following section was to establish the accuracy with which a linear translation stage could be controlled. Displacement measurement can be achieved using a variety of different sensors applying inductive, ultrasonic, piezoelectric and optical technologies. However, the SM sensor was used due to its simplicity and sensitivity.

For measurements of displacement larger than the wavelength of the laser light, the amount of peaks within the SM signal can be calculated. Each peak corresponds to a change in position of the external cavity by half a wavelength along the laser axis. The regime of the SM sensor with strong feedback is best suited for distinguishing the fringes.

Figure 3.10 (a) demonstrates data collected during the measurements. The part of the signal enclosed by a red box corresponds to the SM signal which was used for the analysis of the displacement of the target. The part of the signal outside the enclosed region is noise from the electrical equipment. By counting the number of peaks in the signal within the red box, the absolute total distance travelled by the target can be calculated with a half-wavelength resolution (325 nm).

The displacement profile in time can be reconstructed starting from the moment when the target has advanced over half a wavelength, see Fig. 3.10 (b). Based on the leaning of the peaks with a sharp edge on the left side with a longer decay time on the right side, a conclusion on the direction of the displacement can be made as well. In this example the target was moved towards the laser. In Fig. 3.10 (a), the stage was moved by  $5.2 \mu\text{m}$ , which was confirmed by SM sensor measurements as well. As it can be seen from the part of the signal enclosed by the red box, there were 16 fringes, so the displacement was equal to  $5.2 \mu\text{m}$ .

The reconstructed displacement profile shows that the velocity of the target was not constant over time, see Fig. 3.10 (b). On the contrary, the stage was moving fast at the beginning and was slowing down towards the end. The velocity profile can be reconstructed from the displacement function, or from the spectrum of the SM signal. However, only the measurement of the displacement was within the scope of this experiment. The measurements were done for displacements of the target in the region from  $0.35 \mu\text{m}$  to  $6.5 \mu\text{m}$  with a step of 325 nm, which was sufficient for the required reference measurements. Using the SM sensor allows the distances the stage was instructed to move to be benchmarked with the distances the stage actually moved, see Fig. 3.10 (c). The expected gradient for this graph was 1; a gradient of 1.01 was found, indicating a 1% error. The error accounts for the disappearing of one of the peaks in the SM signal due to the initial phase of the wave at the start of the measurement [77]. The translational stage itself is assumed to move with a precision of 50 nm.

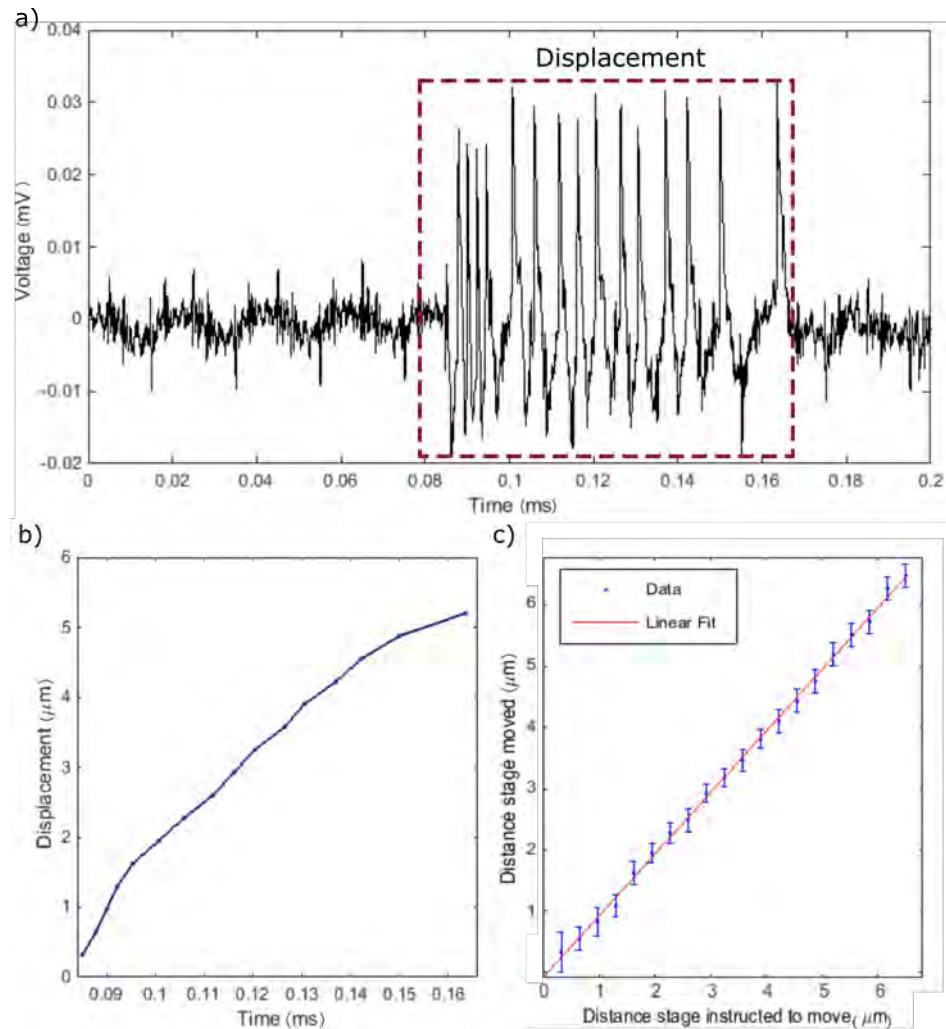


FIGURE 3.10: An SM sensor applied to displacement measurements. (a) Example of the signal obtained experimentally. The part of the signal enclosed with a red box corresponds to the SM effect in the case of moderate feedback level. Every peak within the enclosed region corresponds to a half-wavelength displacement. The information on the direction of the movements can be obtained from the leaning of the signal, which denotes that the target was moving towards the laser. (b) The absolute displacement profile in time along the laser axis was reconstructed from the signal, which is shown in (a). (c) The plot shows the relation between the reference distance ( $x$ -axis), over which the stage was supposed to move, and the displacement which was measured by the SM sensor ( $y$ -axis).

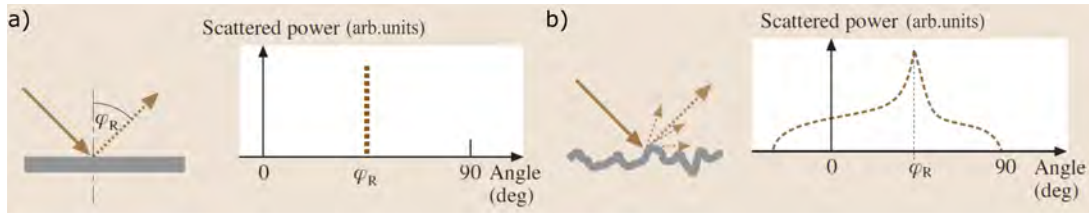


FIGURE 3.11: Depending on the roughness of the surface, the light can be reflected in different ways. (a) When the surface is perfectly smooth, or mirror-like, the scattered spectrum has one specific direction of reflection. (b) The light scatters off a rough surface over a wide angle around the specular direction. Dotted arrows and dotted lines represent scattered (reflected) light on the left hand side diagrams, with the scattered light spectrum on the right hand side plots, of both plots (a) and (b). The solid arrows shows the incident light on both diagrams and spectra [1]

### 3.3.3 Mirror and White Paper on a Translation Stage: Reflectivity Effect

Using the same experimental set-up, measurements of the velocity of a mirror and white paper were performed. The main difference between these two types of targets is the nature of the reflection they produce. In Chapter 2, the scattering theory was described which allowed the angular distribution of the light scattered off particles to be calculated. In addition, the light interacts with the target in terms of directionality in two different ways: specular reflection and diffuse reflection [1], see Fig. 3.11.

1. Mirror-like reflection, or specular reflection, can be described according to the law of reflection, i.e. the reflection angle equals the incident angle, see Fig. 3.11 (a).

2. Diffuse reflection occurs at surfaces where light is reflected at many angles rather than only one, see Fig. 3.11 (b). An ideal diffusive surface has equal luminance in all directions, this is referred to as Lambertian reflection. A non-ideal surface should be described using Mie scattering theory to find the amplitude of scattered light as a function of the incident angle.

Examples of SM signals which can be obtained using these two different types of surfaces can be seen in Fig. 3.9 and Fig. 3.12. After obtaining satisfactory results with the mirror as a target, the same experiments were performed with white paper. White paper is a target which scatters light as a diffuse reflector. In this case, alignment is not such a critical issue as misalignment would not lead to a disturbed peak (splitting) as it was the with the mirror. The amount of light which goes back into the laser cavity depends on focusing/defocusing of light onto the target. Strong feedback can be obtained for sharp light focusing onto the target, see Fig. 3.9. A similar evolution of the SM signal can be obtained by using attenuating filters in front of the target or by changing the focusing properties of the laser beam. It needs to be pointed out that even when the signal is noisy and disturbed, most of the time the frequency can be easily calculated for relatively small velocities of the target. The examples presented in Fig. 3.8 are far from SM-like signals. However, the period of the oscillations can be found and the velocity can be estimated, even though with a 10% lower accuracy.

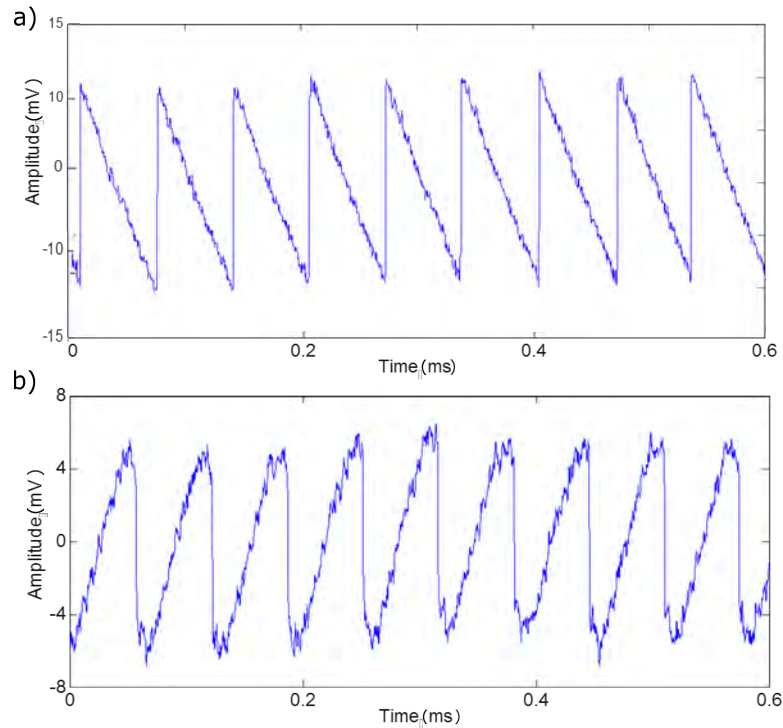


FIGURE 3.12: Examples of signals received from SM when the feedback parameter is  $C \gg 1$ : (a) with a mirror as target, and (b) with white paper as target. The target moves at the same speed, but in opposite directions.

### 3.3.4 Mirror and White Paper on a Translation Stage: Velocity and Distance Variation

During subsequent experiments, the accuracy of the velocity measurements of the targets moving with well-defined and well-referenced velocity was assessed. The translational stage (Fig. 3.5 (a)), which was used in the experiments, allowed for the velocity change within the range 1 mm/s - 10 cm/s with a precision of 0.1 mm/s. The measured velocities of the targets were calculated (see Section 3.2.2) by performing an FFT of the voltage signal, and applying Hamming and Blackman-Harris windows. The spectra were processed using a smoothing filter, and the peaks of the spectra were found by fitting a Gaussian distribution in the frequency domain. This fitting function was chosen according to the investigation demonstrated in Chapter 2.

Examples of different types of the SM signals are shown in Fig. 3.9. Any of which can be used to calculate the frequency, and hence the velocity of the target. The influence of the distance on the accuracy with which the velocity can be calculated was then studied. The velocity of the translational stage was fixed at different values and a set of measurements was performed. The starting point from which the target moved was fixed at a different distance, enabling the investigation of the influence of this distance on the accuracy and precision of the measurements.

The results of the measurements are presented in Fig. 3.13, which shows both the accuracy and precision of the measurements. The thin red straight solid line is the

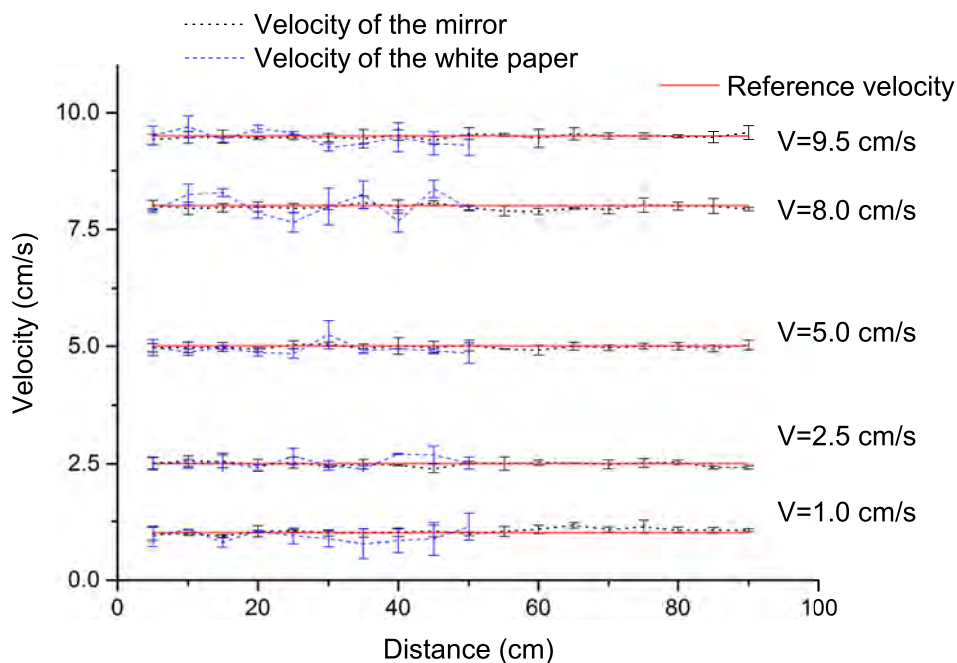


FIGURE 3.13: Examples of measurements using a movable stage which allowed precise velocity measurements of a mirror (black dotted lines) and white paper (blue dotted lines) to be taken in the range of 0.01 - 10.00 cm/s at different distances between the laser and the target. The reference velocities are shown by straight red solid lines. Velocity measurements were carried out up to 90 cm for the mirror and 50 cm for the white paper and showed a better than 1% accuracy and 1.5%, respectively. The error bars indicate the range of the measured velocity obtained in different independent sets of the experiments. The reference velocity error is assumed to be negligible at this plot since the manufacture claims the velocity precision to be 0.1 mm/s.

reference velocity, which was defined by the velocity of the translational stage assumed to be moving with a precision of 0.1 mm/s. The measured velocities are shown by black and blue dotted lines for mirror and white paper as targets, respectively. Each curve is presented with associated error bars, which give the range within which the measured velocities were obtained over multiple readings. The measurements are presented at the different distances where they were obtained.

Accurate measurements with a precision better than 1.5% of the velocity were obtained in the range of 0.01 - 10.00 cm/s at a distance of up to 50 cm between the LD and white paper target; and up to 90 cm with a mirror as a target.

It should be mentioned that the roughness of the paper is about 40 - 50  $\mu\text{m}$  whereas the laser light wavelength is 0.63  $\mu\text{m}$ . As a consequence of this, the so-called speckle effect occurs and the coherence decreases. Moreover, whereas the mirror target in the case of a well-adjusted set-up was moved up to 90 cm from the laser without changing the shape of the signal, the white paper target needed constant readjustment to have strong feedback. The set-up was modified, so the distance between the target and the laser was fixed. This allows measurements of velocities up to the limit of the set-up, which was determined to be 10 cm/s, with high precision, see Fig. 3.13.

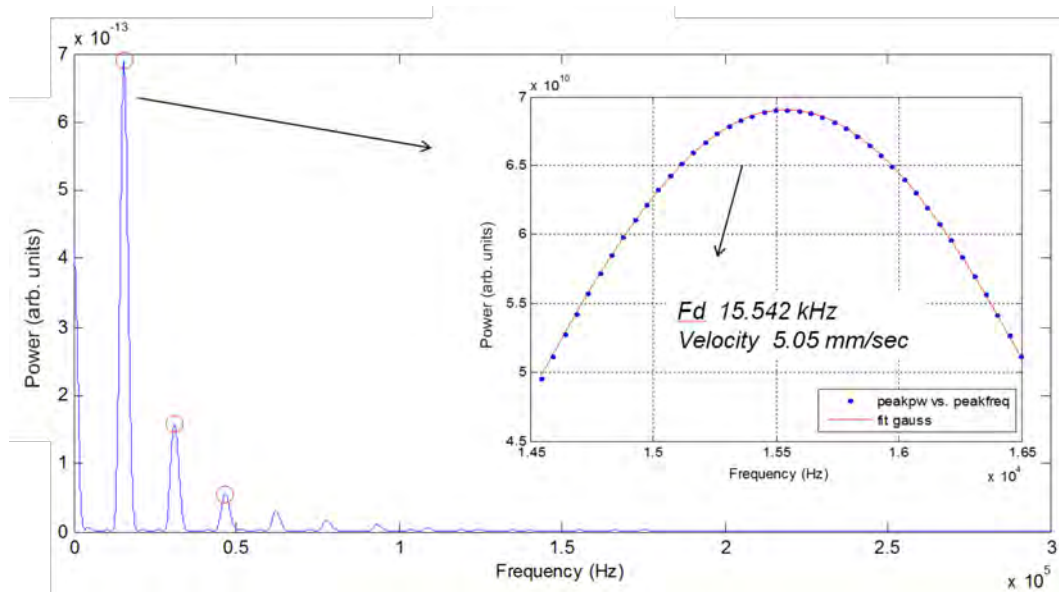


FIGURE 3.14: The spectrum of a typical signal, when a mirror is used as a target for velocity measurements demonstrates the effect which appears in the case of strong feedback with parameter  $C \gg 1$ . The sawtooth-like signal leads to multiple frequencies in the power spectrum. The insert shows the fitting algorithm for extracting the exact peak of the spectrum.

### 3.3.5 The Influence of Different Levels of Feedback on the Spectra

In the case of the SM effect, the measurement of different targets can lead to various spectra. Different levels of feedback cause the shape of the signal to deviate from a sinusoid, and hence the change in the shape of its spectrum. For example, for the SM signal with feedback parameter  $C \gg 1$ , its spectrum has additional frequencies caused by an FFT analysis of the function which differs from a sinusoid. An example of a spectrum obtained after data analysis for a signal similar to the ones in Fig. 3.9 is shown in Fig. 3.14. The reference velocity of the target was 5 mm/s. Together with the main peak, additional multiple peaks appear because of the type of SM signal used for measurements, i.e. a sawtooth-like signal leads to the appearance of additional peaks on the spectrum calculated by FFT.

Strong feedback from the target in the SM effect can not only lead to additional multiple peaks in the spectra, but also to a splitting of these peaks. This effect is illustrated in Fig. 3.15. Two cases are presented: the aligned case and a slightly misaligned one (inset). Since the target was a mirror, the system was very sensitive to misalignment. Only the light which was reflected under exactly  $0^\circ$  angle contains a non-disturbed shift in the frequency. The light which was misaligned even for a few minutes of an angle was still coupled back into the cavity, and any diode laser has a beam divergence of several minutes. As a result, the frequency of this additionally coupled light was shifted due to the error in the angle leading to a broadened spectrum in addition to splitting the peaks, see inset in Fig. 3.15. In the case of moderate feedback, the effect is limited to a broadening of the peak. If the SM sensor works under strong feedback, it demonstrates

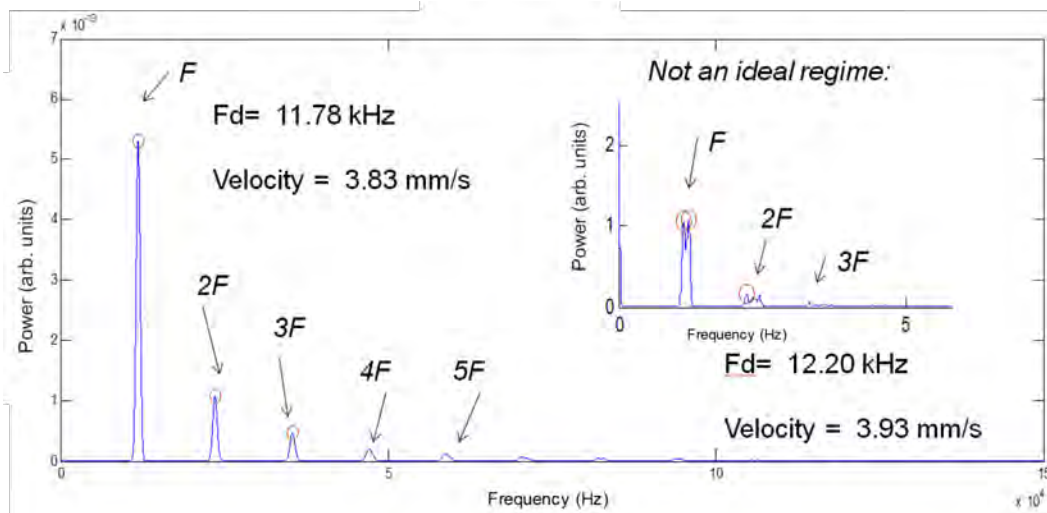


FIGURE 3.15: The spectrum of a typical signal in the case of a mirror used as target for velocity measurements which demonstrates the effect of misalignment in the case of strong feedback or  $C \gg 1$ . The sawtooth-like signal leads not only to multiple frequencies in the power spectrum, but to a splitting of the peaks as well. The plot shows the spectrum corresponding to the aligned case, and the inset illustrates the effect from misalignment.

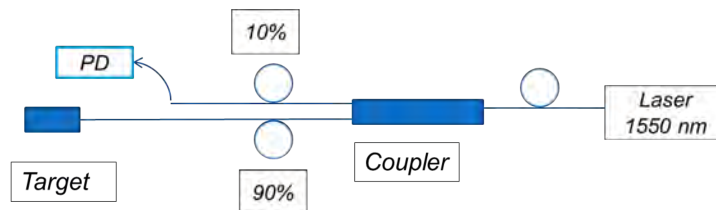


FIGURE 3.16: The set-up used for testing the 1550 nm fibre-based laser. The coupler allows two different detection systems to be tested and used: one built-into the laser photodiode and one external to the system photodiode.

an extreme sensitivity and immediate response even to a small change in the system. Any misalignment then leads to a lower amplitude of the spectrum as well, as it can be seen in both spectra.

### 3.3.6 Self-mixing Velocimeter Based on 1550 nm Laser

A DFB laser with a wavelength of 1550 nm and with a power of less than 2 mW delivered using fibre optics was used for testing its potential use. Fibre optics can improve the level of the signal and the delivery system. The set-up for the 1550 nm laser was similar to those used before in the experiments, see Fig. 3.16. Using a coupler, a fraction of 90% of the emitted light is directed towards the moving target where it is scattered and then coupled back into the fibre. The coupler allows light to be sent back into the laser, where the SM effect occurs. The remaining 10% of the laser light is sent to the photodiode by the coupler, which allows the testing of two schemes for signal detection: using the built-in PD and the external PD. Using the external PD allows for extending the bandwidth if it is needed.

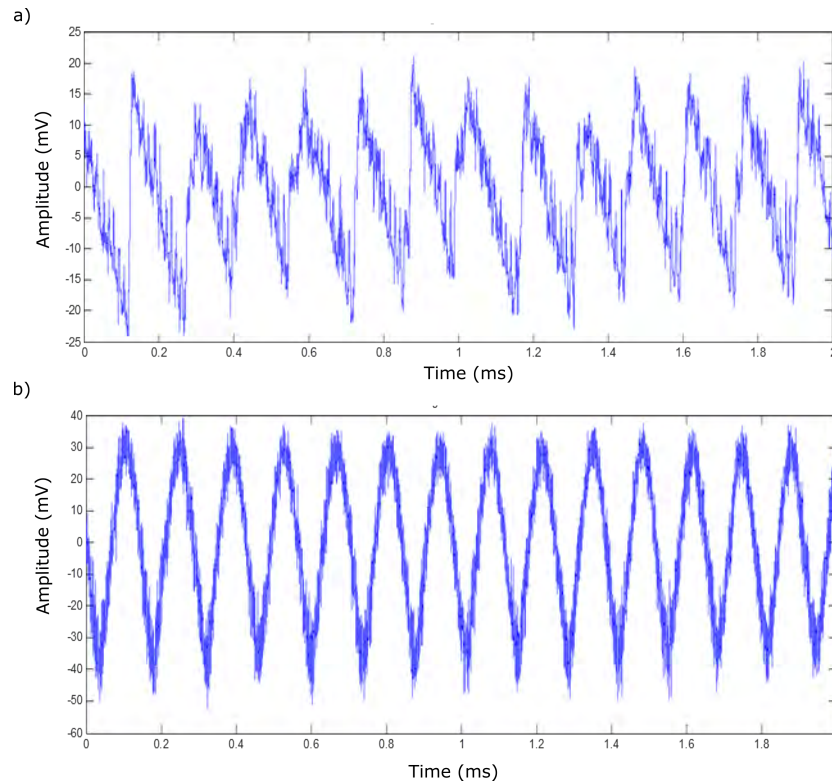


FIGURE 3.17: Examples of signals obtained for different types of fibres for transporting light: a) single-mode fibre ( $9 \mu\text{m}$  diameter core); and b) multi-modes fibre ( $250 \mu\text{m}$  diameter core).

Fibres exist in two types, single-mode and multi-mode. They differ in the size of the core with  $9 \mu\text{m}$  (single-mode) and  $250 \mu\text{m}$  (multi-mode) diameters, used in the experiments. The larger diameter fibre allows more light to be transported and coupled into the fibre. However, multi-mode fibre supports more than one propagation mode leading to a distortion in the light propagating within the fibre. Examples of obtained signals using different fibres are presented in Fig. 3.17 with (a) single-mode and (b) multi-mode fibres. It can be seen, that in the case of the single-mode fibre, the amplitude of the signal is lower compared to the multi-mode one. However, the signal for the multi-mode fibre is noisier compared to the single-mode fibre, which was expected.

The translational stage was again used to study signals off a mirror, and after, a white paper. Verifications of the results were done based on the reference velocities obtained from the translational stage. The corresponding spectra of the signals, which were collected during the experiments with white paper, with the velocities ranging from  $2 \text{ mm/s}$  to  $7 \text{ mm/s}$ , can be seen in Fig. 3.18. Different colours relate to the signal originating from various velocities of the target. The precision of the measurements were better than 1%, and the fibre optics demonstrated the potential of the application, however it had much lower signal levels.

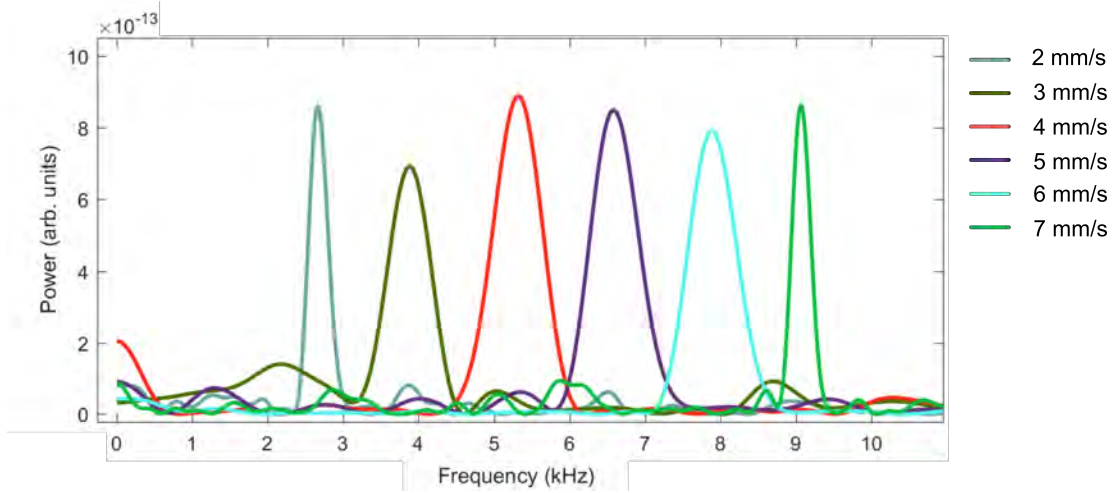


FIGURE 3.18: Examples of the spectra of signals related to the signals obtained from targets moving with velocities ranging from 2 mm/s to 7 mm/s. Different colours of spectra are related to various velocities.

### 3.4 The Self-Mixing Technique with a Rotating Target of Low Reflectivity

#### 3.4.1 Set-up Description

A rotating disc covered with white paper allowed the limitations of the SM set-up to be investigated at high velocities. The distance between the target and the laser was fixed to 10 cm in the geometry shown in Fig. 3.5 (b) and 3.19. The rotational speed of the disc can vary from  $2\pi$  rad/s to  $300\pi$  rad/s which translates into tangential velocities from 1 cm/s to 100 m/s. The power spectrum of the light scattered off rough surfaces is anticipated to be Gaussian with a frequency corresponding to the Doppler shift typical for the SM system (see Chapter 2, Section 2.2). The Doppler shift for the SM system is equal to

$$f = 2 \frac{\vec{n} \cdot \vec{v}}{\lambda}, \quad (3.2)$$

where the velocity vector  $\vec{v}$  and the unit vector  $\vec{n}$  changes according to the position of the laser spot.

The co-ordinate system is defined to be  $(x, y)$  on the surface of the disc with the origin at the centre, and  $z$  is parallel to the normal vector of the disc surface. In Fig. 3.13 (a), for vectors  $\vec{v} = v(0, 1, 0)$  and  $\vec{n} = (0, \cos \alpha, \sin \alpha)$  the Doppler shift is equal to  $f = 2\omega R \cos \alpha / \lambda$ . In the case when the laser is shining on any point on the disc surface (see Fig. 3.13 (b)), the vector  $\vec{v}$  is given by  $\vec{v} = v(\sin \beta, \cos \beta, 0)$ . Thus, the Doppler shift in the most general case is equal to

$$f = \frac{2\omega R \cos \alpha \cos \beta}{\lambda}. \quad (3.3)$$

The reflectivity properties of the white paper are that 60% of the light is expected to scatter at a wavelength of 650 nm. The amount of light scattered in different directions

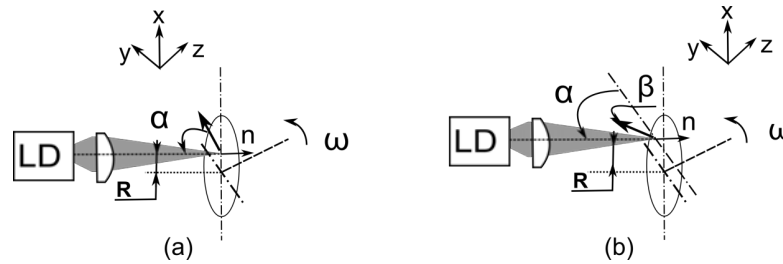


FIGURE 3.19: The laser light from the LD is focused by means of multiple lenses onto a point on a rotating disc located a distance  $R$  from the point of rotation. The origin of the  $(x, y, z)$  coordinate system is defined to be at the point of rotation of the disc.  $\vec{n}$  is a unit vector in the direction of propagation of light, and  $\omega$  is the rotational speed of the disc. (a) In the case of the laser shining onto any point on the  $x$  axis, the Doppler shift depends only on the angle  $\alpha$  between laser light direction and the disc surface ( $y$  axis). (b) At any other point, the Doppler shift depends on the angle  $\beta$  between the velocity vector and  $y$  axis.

depends on the incident light angle with a maximum at  $90^\circ$ . At the same time, the angle has to be different from  $90^\circ$  since  $\cos 90^\circ = 0$  and the Doppler shift is equal to zero here as well.

In order to validate the results of the measurements obtained by using the SM system, a photo-interrupter circuit based on a OPT101 photodiode amplifier from Texas instruments [115] and a microcontroller board (ATMega 328 [116]) were used for measuring the rotational speed of the motor. The system therefore comprises of a photodiode coupled with an amplifier in saturation mode of operation. When it detects light it produces a pulse equal to the power supply voltage which is 5 V. On the same perforated board an LED was placed to produce the light signal. The signal of the photodiode provides the input to a microcontroller board where the pulses are measured within a fixed time and the rotation speed is calculated. For every value of the velocity defined in such a way, the rotation speed can only be measured with a certain accuracy, which affects the precision of the velocity calculated from the experiment.

### 3.4.2 Rotating Target with Low Reflectivity: Spectra

The calculated velocity is found from the frequency extracted from the signal spectrum. The different parameters influence both the signal itself as well as its spectrum. A typical example of the collected results is presented in Fig. 3.20 and 3.21.

The behaviour of the signals, see Fig. 3.20, 3.21 (a), demonstrates the modulation of the intensity which is much higher compared to the signals obtained in the experiments with a translational stage (see Fig. 3.9). The modulation appears due to the speckle effect, since the signal is collected over time while the laser light is reflected or scattered off the independent areas of the disc. An additional reason for a high modulation of the signal is that the laser spot is a non-point-like, hence the laser light is scattered off the points with different velocities, as opposed to the translational stage, where all points had exactly the same velocity.

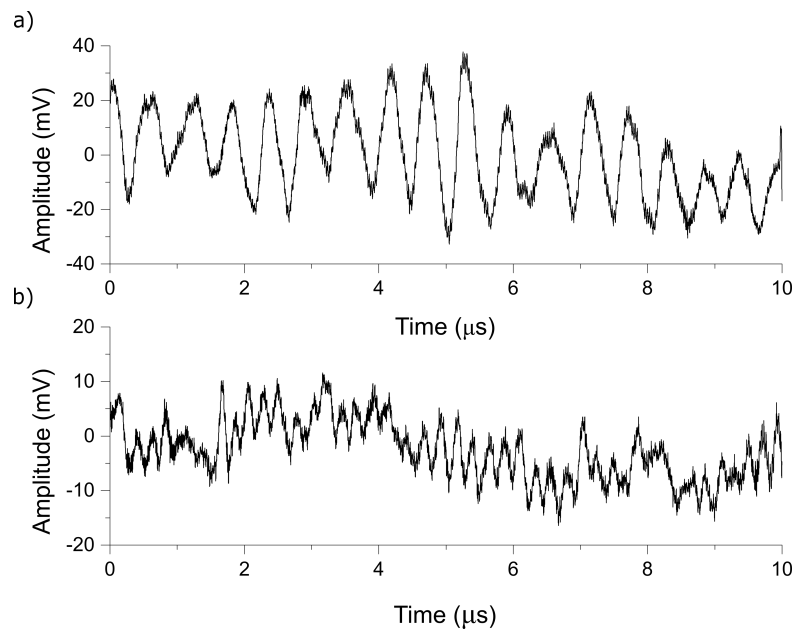


FIGURE 3.20: Example signal received from set-up with a rotating disc. The reference and measured velocity were 4.6 m/s and 15.3 m/s. The angle between the velocity vector and laser axis was  $83^\circ$ . The direction of the moving target is backward with respect to the laser, as it can be seen from the curve leaning to the right. It demonstrates the intensity modulation effect due to a non-point-like laser spot and speckle effects.

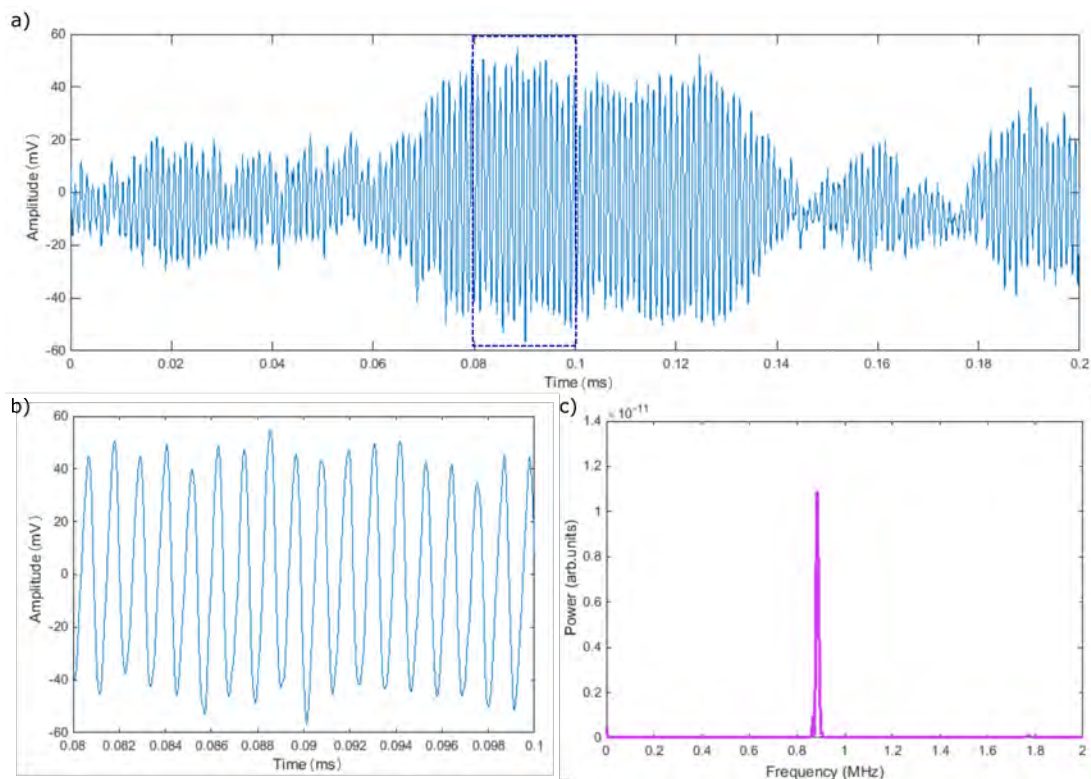


FIGURE 3.21: The experimental results for velocity measurements of the rotating disc are presented: (a) the SM signal; (b) the enlarged part of the signal from 0.08 ms to 0.1 ms; and (c) calculated spectra of the signal, the frequency from which can be used for the velocity calculation. The velocity of the measured point was 64.4 cm/s ( $\nu = 6$ ,  $R = 2.05$  cm) and the angle  $\alpha$  of  $65^\circ$ . The measured frequency is 0.85 MHz, and the expected frequency shift is 0.84 MHz.

Figure 3.20 shows the signals at two different velocities, 4.6 m/s and 15.3 m/s at the same angle of  $83^\circ$ . Here, the typical profile of the signal can be clearly seen at different times. The intensity modulation due to the speckle effects can be seen from the plots of the signal in Fig. 3.20, where the signals have shapes typical of weak feedback. For the top plot, the direction of the movement can be defined from the signal leaning to the right denoting a backward movement with respect to the laser. The bottom plot has less distinguishable leaning therefore the direction of the moving cannot be determined.

Figure 3.21 (a) shows the acquired signal for velocity measurement during 0.2 ms with high modulation of the amplitude do to speckles. Figure 3.21 (b) demonstrates that within a small period of acquisition, of around 0.02 ms, the amplitude of a signal varies little. The signal corresponds to the SM signal for weak feedback. The frequency of the fluctuation can be found by FFT, and Fig. 3.21 (c) shows the spectrum of this signal with a relatively narrow and clear peak at 0.85 MHz. The value agrees well with a reference frequency corresponding to the parameters of this experiment: 0.84 MHz for 64.4 cm/s velocity ( $\nu = 6$ ,  $R = 2.05$  cm, and  $\alpha = 65^\circ$ ).

Additional effects, other than those due to speckles, in this experiment were from a non-point-like laser spot, resulting in spreading of the spectrum. The laser spot has a finite size (see Fig. 2.15), i.e. it is non-point-like, which means that for each point on the disc, a different tangential velocity is measured which results in a distribution of velocities with different weights in the measured signal. In the case of a translational stage with a mirror on it, the whole surface moves with the same velocity. As a result, the resonant peak of the spectrum is quite narrow, even if the spot of the laser light is non-point like. In contrast, each point on the disc has a different velocity causing the broadening of the peak when the size of the laser spot is even slightly different from point-like.

On top of broadening due to speckle effects, the fundamental broadening of the spectrum of the scattered light appears as an effect from the values of the velocity of the target, the angle between target and the laser axis, and the waist size of the light, as shown in Chapter 2.

As the theoretical discussion has demonstrated, different parameters, such as the velocity,  $v$ , the angle,  $\alpha$ , and the size of the laser spot,  $w_0$ , can influence the spectra and hence the performance of the sensor and impose limitations on the measurable velocities. The results of different experiments were compared with simulations of the Doppler spectra, which were obtained for fixed parameters using the previously obtained Eq. 2.19:

$$I(\omega) = I_0 \frac{1}{v \sin \alpha w_0} \exp \left( - \frac{(\omega - 2v \cos \alpha / \lambda)^2}{2(v \sin \alpha)^2 / w_0^2} \right). \quad (3.4)$$

That means that the obtained spectrum has a peak corresponding to the Doppler shift in the frequency domain equal to  $2v \cos \alpha / \lambda$ . A measure of the FWHM describes a

broadening of the spectrum; this was calculated and found to be equal to

$$\Delta f = 2\sqrt{2 \ln 2} \frac{v \sin \alpha}{w_0}. \quad (3.5)$$

The amplitude of the peak is proportional to the following:

$$I \propto \frac{1}{w_0 v \sin \alpha}. \quad (3.6)$$

Hence, the spectrum has a peak at the frequency centred around the frequency of the Doppler shift and is broadened proportionally to the velocity  $v$  of the target and to the sine of the incident angle  $\alpha$  and inversely proportional to the beam waist radius  $w_0$ . The Gaussian peak and its broadening are independent of the distance to the object. The amplitude of the scattered spectrum is inversely proportional to the velocity of the target, to the sine of the incident angle  $\alpha$  and to the beam waist radius  $w_0$ .

The results presented in the following subsections contain data obtained through both experiments and simulations. Since large data sets were collected, only the important results are presented here, with each subsection dedicated to the influence of a particular parameter.

### 3.4.3 Variation of the Target Angular Velocity with a Fixed Position of the Laser Spot

The variation of the velocity was achieved by changing two parameters separately: the rotational speed of the disc ( $\nu$ ) and the position of the laser spot on the disc which changes the radius  $R$ .

The following experiments were performed to measure the influence of the magnitude of the velocity on the signal by varying the angular velocity of the disc. For each case, the laser spot position on the disc was fixed, as was the angle between the disc and the laser beam axis. The angular velocity was increased by varying the speed of the motor, hence the linear velocity was different as well. Measurements were performed for various combinations of fixed parameters allowing for a broader analysis. According to Eq. 3.5 and 3.6, the peak of the spectra is expected to be widened and its amplitude to be lowered with increasing velocity.

Figure 3.22 (a) shows the Doppler spectra of the resulting signals for the measurements obtained when the laser light was shining onto the disc under an angle of  $65^\circ$ , and the laser spot was located on the disk at 1.7 cm from the rotation centre for different rotational speeds ranging from 4 to 15 revolutions per second (rps). The results can be compared with simulated Doppler spectra in Fig. 3.22 (b) with the same parameters.

Additional experiments were performed for higher velocities in the range of 3.3 m/s to 7.7 m/s which lead to a larger Doppler shift in the frequency spectrum. Figure 3.23 demonstrates the spectra obtained in the experiments and in the simulation. Measurements were performed at a fixed angle of  $72^\circ$  between the laser axis and the disc surface

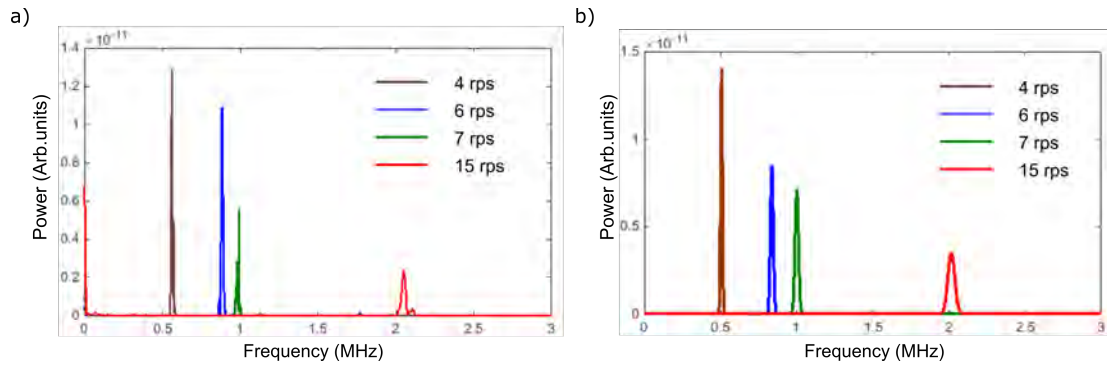


FIGURE 3.22: The result of variation of the angular velocity by changing the rotation speed on the Doppler spectra obtained (a) experimentally and by (b) simulation. The angle between the laser axis and the surface of the disc was fixed at  $65^\circ$  and the laser spot was fixed at a radius of 1.7 cm from the center of the disc. The rotation speed here is 4, 6, 7, and 15 rps. The corresponding velocities were varied from 0.43 m/s up to 1.6 m/s.

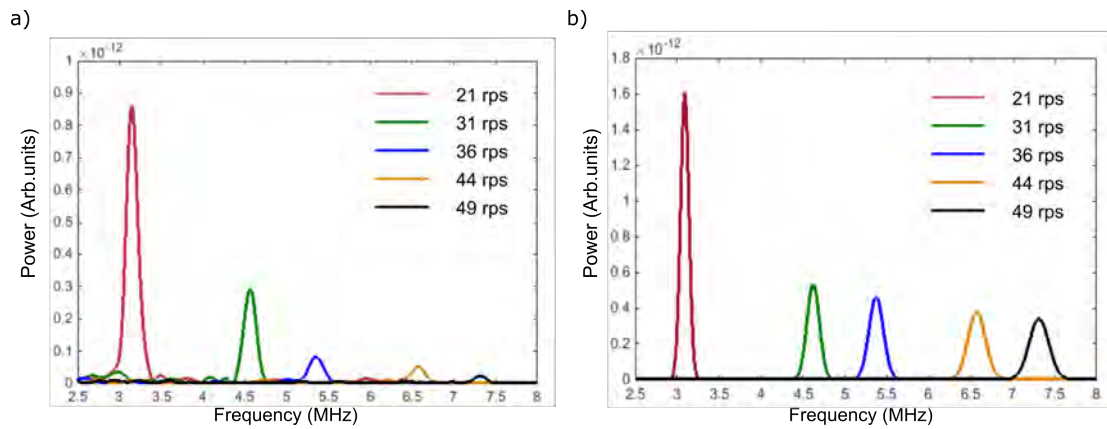


FIGURE 3.23: The result of variation of the angular velocity by variation of the rotating speed on the Doppler spectra obtained (a) experimentally and by (b) simulation. The angle between the laser axis and the surface of the disc was fixed at  $72^\circ$  and the laser spot was fixed at a radius of 2.5 cm from the center of the disc. The rotation speeds here were 21, 31, 36, 44, and 49 rps. The corresponding velocities were varied from 3.3 m/s up to 7.7 m/s.

and when the laser beam was focused at a distance of 2.5 cm from the centre of the disc. The tangential velocity was varied by changing the angular speed of the disc, to 21, 31, 36, 44, and 49 rps.

The experimental and simulated results agree well. The resonance frequency and its FWHM increase linearly with the disc's angular velocity. The amplitude of the peak decreases with increasing velocity. For both sets of experiments, shown in Fig. 3.22 and 3.23, however, the amplitudes, which correspond to the larger, more than 5 MHz frequencies, decrease much faster than expected. This is possibly due to the response of the amplifier used in the experiment. On top of the influence of the value of the velocity itself on the width and on the amplitude of the peak, the imperfection of the laser spot within the measured area of the disc leads to a reduction in amplitude and also widening of the FWHM of the peak, see Fig. 2.15.

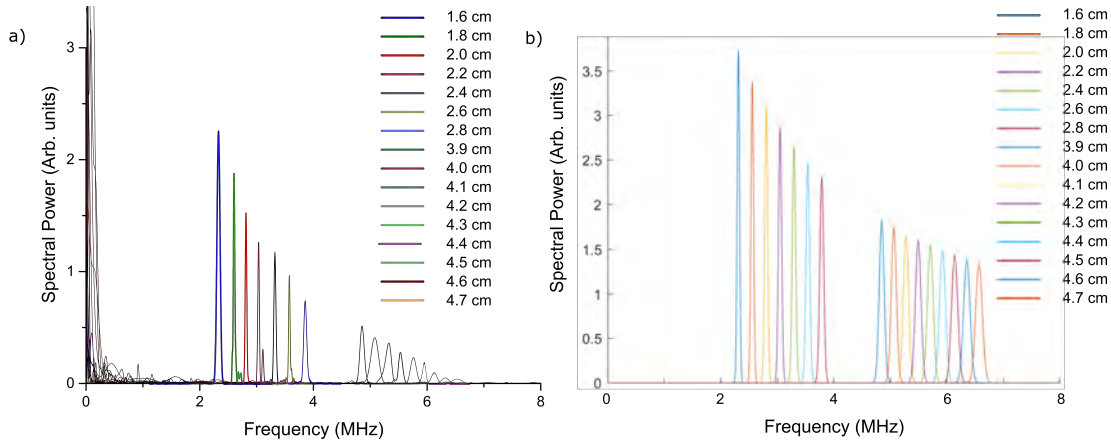


FIGURE 3.24: The result of variation of the measured velocity by changing location of the laser spot on the disc. The Doppler spectra were obtained (a) experimentally and (b) by simulation. The angle between the laser axis and the surface of the disc was fixed to  $60^\circ$  and the rotation speed was 15 rps. The laser spot was moved along the diameter of the disc and the radius was varied from 1.6 cm to 4.7 cm. The corresponding velocities were varied from 1.5 m/s up to 4.4 m/s.

### 3.4.4 Variation of the Position of the Laser Spot with a Fixed Angular Velocity

The variation of the velocity was achieved not only by changing the angular velocity, but also by varying the laser spot position on the surface of the disc. The theoretical trend should be the same as was discussed in the previous subsection due to the fact that the velocity of the spot is defined as  $v = \omega R$ , where  $R$  is the radial distance between the center of the rotating center and the laser spot, and  $\omega$  is a rotational speed, see Fig. 3.19 (a).

The laser spot position plays the same role as it did with the rotational speed, i.e. it should have the same effect on the Doppler spectra. The results of the experiments and of the simulation for the parameters used are presented in Fig. 3.24. The angle was fixed at  $60^\circ$ , and the rotation speed at 15 rps. The laser spot was moved along the  $x$ -axis of the disc surface, see Fig. 2.15 for explanation, therefore the projection of the velocity on the laser axis depends only on the angle  $\alpha$  and not on the angle  $\beta$ , see Fig. 3.19. The radius was varied from 1.6 cm to 4.7 cm leading to a variation of the velocity from 1.5 m/s to 4.4 m/s. The experiments and the simulations, shown in Fig. 3.24 (a) and Fig. 3.24 (b) respectively, agree well in terms of the Doppler shift and hence the velocity. The amplitude of the peak reduces with the velocity growth. In case of the experimental results, the peak's amplitude decreases much faster compared to the simulation results. The peak widens when the velocity is increased, which is to be expected.

### 3.4.5 Variation of the Angle between Laser Axis and Velocity Vector

The behaviour of the spectrum function depending on the angle between the laser light axis and the velocity vector is important to study since it defines the geometry in which

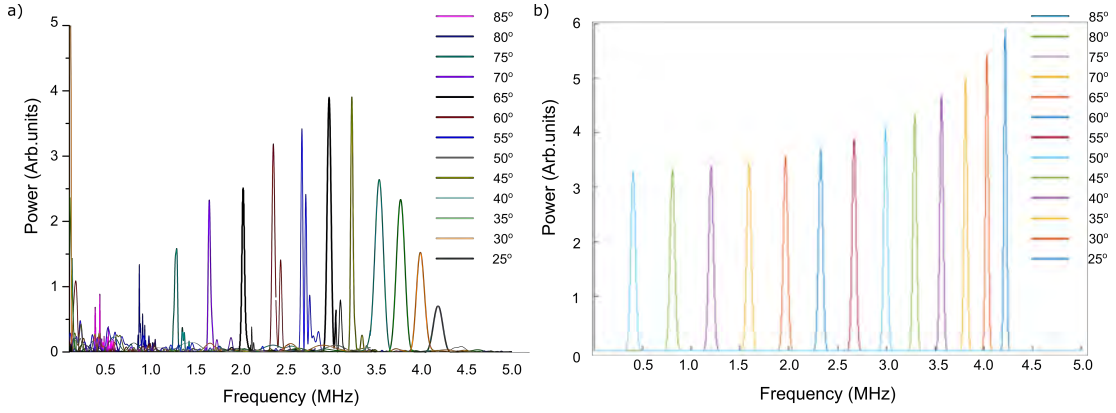


FIGURE 3.25: The result of variation of the angle between the laser axis and the velocity vector on the Doppler spectra obtained (a) experimentally and (b) by simulation, when the linear velocity was fixed at 1.5 m/s. The angle was varied from  $85^\circ$  to  $25^\circ$  in steps of  $5^\circ$ , allowing the effect of the angle on the spectra to be studied and hence the performance of the sensor.

the sensor can be applied. The angle is one of the main parameters which can be changed in the experiments for the velocity characterisation of different targets, and vice versa.

According to Eq. 3.4, the peak of the spectrum should be centred on a frequency equal to  $kv \cos \alpha$ . This means that when the angle  $\alpha$  is close to  $0^\circ$ , the Doppler shift will have a maximum value, and when  $\alpha$  approaches to  $90^\circ$  the Doppler shift will approach zero. Based on Eq. 3.5, the peak should be narrow when  $\alpha$  is close to  $0^\circ$ , and it broadens when  $\alpha$  approaches  $90^\circ$ . At the same time, Eq. 3.6 shows that the amplitude of the peak is maximum when  $\alpha$  is close to  $0^\circ$ , and a minimum when  $\alpha$  is close to  $90^\circ$ .

The angle between the laser light axis and the velocity vector (see Fig. 3.19) was varied to verify the theoretical prediction. The angle was varied from  $85^\circ$  to  $25^\circ$  in  $5^\circ$  steps. The rotational speed of the disc and the position of the laser spot were fixed such that the tangential velocity was equal to 1.5 m/s.

The experimental and simulated results of the Doppler spectra for different angles are presented in Fig. 3.25 (a) and (b) respectively. When the angle approaches  $90^\circ$ , the velocity projection decreases, hence the Doppler shifted frequency is small and easy to detect using photodetectors with lower bandwidth. The amount of light coupled back is also reduced. Moreover, as it can be seen from the simulations, for angles close to  $90^\circ$  the bandwidth of the peak is wider and the amplitude of the peak is smaller. As the angle decreases, the peak in each power spectrum becomes sharper and should have a larger amplitude. However, the bandwidth of the amplifier is limited (10 MHz), and the amplification coefficient of the amplifier reduces, so in the experimental results the amplitude of the peak decreases.

The frequencies of the peaks, obtained experimentally and by simulations, agreed well and were within an error of less than 5%. The experimental spectra had a broader FWHM and additional peaks around the main peaks compared to the simulations.

According to Eq. 3.5, the FWHM should decrease with decreasing angle while other parameters remain fixed. Interestingly, during the experiment, this was the case up until

the angle reached  $50^\circ$ . After that when the angle became smaller than  $50^\circ$ , not only did the amplitude of the peak decrease, but the peak also broadened dramatically.

Each of the presented spectra was obtained based on signals, which were collected in a relatively short period of time, see examples in Fig. 3.21, 3.20. However, for the full assessment and estimation of the velocities, data collected within longer periods of time gave smoother spectra with one clear peak.

The theoretical analysis is unexpected since a smaller angle between the laser light axis and the velocity vector should be more desirable, i.e. when the light is shining exactly towards the moving target, as in the case of a gas jet or any other flow. At the same time, this means that the Doppler shift frequency is at its maximum, hence the detection system must have a very high bandwidth for high velocities. In the case of gas jet measurements, the angle is the only parameter of the system which can be changed. When applied to the disc, the geometry with a small angle between the laser light axis and the velocity vector affects the size of the laser spot on the surface causing it to spread over a larger area. This meant the light was scattered off the area of the disc with a wider distribution of velocities ultimately leading to a widened overall spectrum.

### 3.4.6 Other Contribution to the Spectra

In all experiments, the focusing of the beam was adjusted to have a maximum level of signal. One of the parameters of influence on the spectra is the size of the laser spot. An attempt was made to make this spot as small as possible, which would lead to a maximum scattering signal. However, a smaller laser light spot means a slightly lower amplitude and wider peak. This effect can be clearly seen when comparing the signals and corresponding spectra for the mirror and the disc experiments. In the first case, the peaks were indeed more narrow when the laser spot on the target was relatively large. However, it was crucial to have a small laser spot on the disc, since a larger spot leads to a greater spread in velocities and results in multiple Doppler shifts in the frequencies, hence a wider peak as a whole.

Another additional effect was the instability of the rotational speed and surface roughness of the disc, which was unavoidable during the experiments. These factors lead to the variation of the velocities hence to the wider spectrum with lower peak in the amplitude as well. Hence, the balance between the influence of the different parameters is an important thing to consider for the velocity measurements using the SM technique.

### 3.4.7 Studies into the Accuracy of Velocity Measurements

From every measured signal a corresponding frequency spectrum was found from which the velocity was calculated. In the case of the rotating disc, a reference velocity can be found based on Eq. 3.3. The relative error of the reference velocity can be calculated by differentiating Eq. 3.3 with the angle variation between the laser and the disc giving the most significant uncertainty. The uncertainty of the radius  $\Delta R$  is defined as the

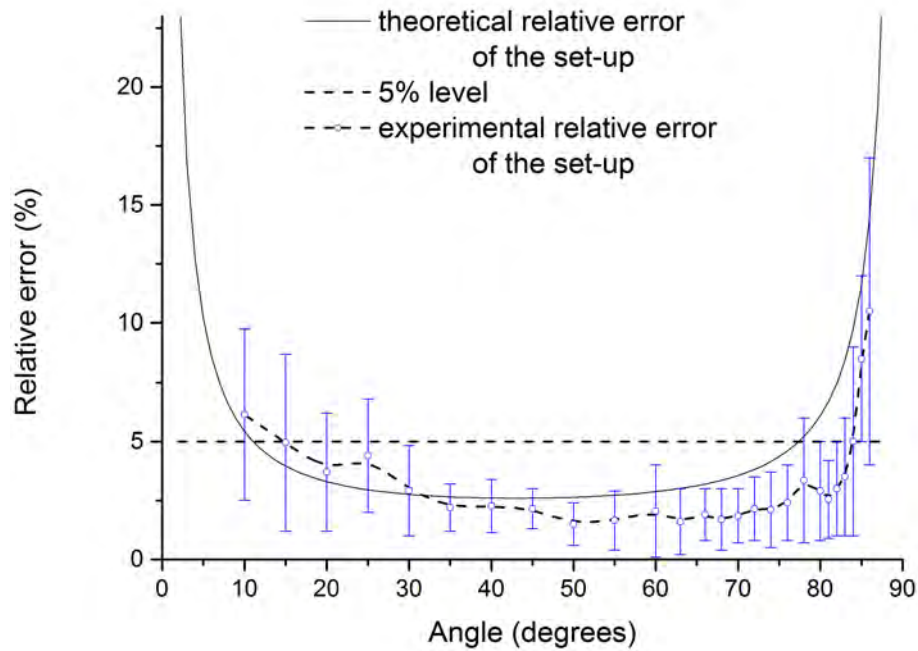


FIGURE 3.26: The theoretical and experimental relative error dependence on the angle between the disc covered with white paper and the laser. The theoretical error was calculated based on uncertainties in the experimentally measured quantities and shown by the solid line. The experimental accuracy is shown by the dashed line with round dots, which represent the mean accuracy calculated from multiple readings over a range of velocities. The error bars on the experimental plot represent the range of the measured velocities obtained after a set of independent experiments and demonstrate the precision of the results. The experimental results follow the same trend as the theoretical one. In the range of  $15^\circ$  -  $85^\circ$  relative errors were better than 5%, and the most precise measurements were received in the range of  $30^\circ$  -  $75^\circ$ .

size of the laser spot on the paper; all other errors are limited by the instrumentation. The experimental uncertainty of the velocity, based on the uncertainties in the measured quantities, was calculated according to  $\delta v_{laser} = \sqrt{(\delta R)^2 + (\delta \nu)^2 + (\delta \alpha)^2}$ , where  $\delta R = \Delta R/R$ ,  $\delta \nu = \Delta \nu/\nu$ , and  $\delta \alpha = \tan(\alpha)\Delta \alpha$ .

The calculated dependency of the velocity uncertainty on the angle from the set-up is shown by a solid black line in Fig. 3.26, where the dashed line represents the 5% level of accuracy. For calculations, it was assumed that the angle could be measured with a  $0.5^\circ$  precision. The rotational velocity was measured with an accuracy of 1%. The size of the laser spot on the paper depends on the angle  $\alpha$  as it is proportional to the cosine of this angle. This leads to an increasing relative error of the measurements at small, less than  $10^\circ$ , angles due to a broadening of the frequency spectrum. Speckle modulation increases dramatically at angles larger than  $80^\circ$  which also results in frequency spectrum broadening [44, 56]. Considering the trend of the calculated experimental uncertainties, presented in Fig. 3.26 by a black solid line, the optimal range of angles from an accuracy point of view is between  $13^\circ$  -  $77^\circ$  which gives an error of less than 5% and between  $25^\circ$  -  $63^\circ$  less than 3%.

Figure 3.26 demonstrates the results of the accuracy which was achieved during the experiments for different angles, which are shown by a dashed line. The accuracy of the measurements was defined as the relative error in relation to the reference velocity. For each angle shown on the plot, multiple measurements were taken over a velocity range of 0.5 m/s to 30 m/s with at least 10 measurements for each velocity. The points in Fig. 3.26 represent the average of the uncertainty over the velocity range for each angle. Along with the accuracy of the measurements, the error bars are shown for each point, These are equivalent to the precision of the independent measurement within the total accuracy of the results.

The experimental accuracy follows the same trend as the theoretical one in Fig. 3.26 with sharp improvements of the accuracy starting from an angle of  $15^\circ$  with a plateau of 3 - 4% of the accuracy in the range of  $25^\circ$  -  $80^\circ$  and with a rise of inaccuracy above  $85^\circ$ . The error bars for each point in the plot show that the precision of the measurements improves within the range of  $25^\circ$  -  $75^\circ$ .

Figure 3.27 demonstrates typical waveforms and their FFTs in the case of an accuracy below and above 5%, see Fig. 3.27 (a) for 1.4% accuracy and Fig. 3.27 (b) for 6.7%. The signals were chosen such that the peaks of the FFTs were relatively close to each other for comparison. The Doppler shifts in the frequency are 3.41 MHz for Fig. 3.27 (a) and 3.23 MHz for Fig. 3.27 (b), which correspond to tangential velocities of 1.76 m/s and 1.06 m/s respectively whilst the angle between the laser axis and the surface of the disc was  $51^\circ$  and  $9^\circ$  respectively, see Fig. 3.12. The signals in Fig. 3.27 have a shape typical for weak feedback. The set-up allows calculation and verification of the self-mixing method with velocities of up to 50 m/s. The only limitation of the experiment found so far is from the electrical circuit parameters (bandwidth of the amplifier/detection system). As a result, the high velocities were measured only when an angle  $\alpha$  of close to  $90^\circ$  was applied, so the corresponding resonant frequency is within the bandwidth of the detection system. As a consequence, the measurements were performed with reduced accuracy.

### 3.4.8 Discussion

The experimental results of the velocity measurements with the white paper target are shown in Fig. 3.28. Using a disc as a target allows the self-mixing velocimeter to be validated. During the experiment, the following parameters were varied: the position of the laser spot on the disc, the angle  $\alpha$  and the rotational speed of the disc. As the experimental and theoretical calculations have shown, different parameters influence the performance and the accuracy of the SM sensor. The major effects arise from the magnitude of the velocity, the velocity range, and the geometry of the set-up. The central Doppler frequency is defined by the velocity of the target at the centre of the laser spot and the angle between the laser light axis and the velocity vector. Its amplitude and FWHM are influenced by the velocity magnitude and the angle, and those parameters have a major influence on the result.

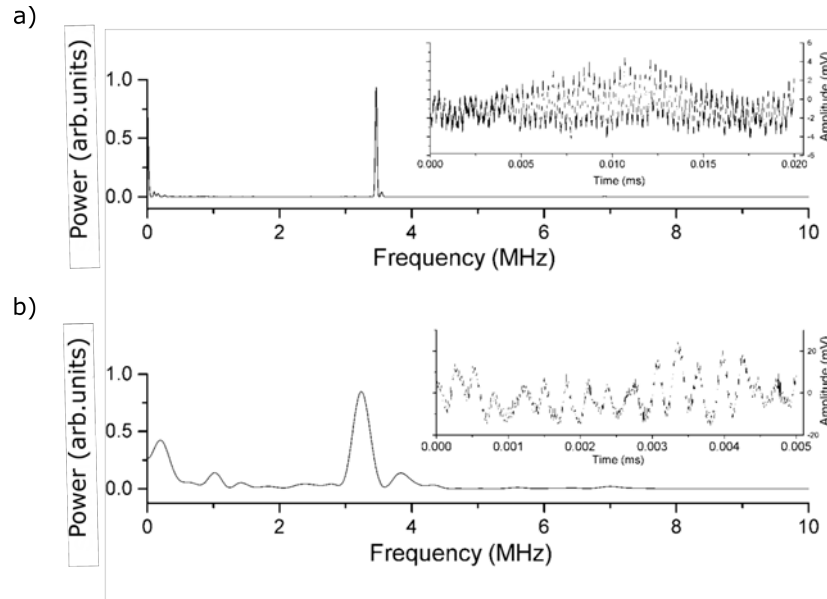


FIGURE 3.27: Examples of typical SM signals and their FFTs in the case of a rotating disc for the case of a relative error (a) below 5% and equal to 1.4%, and (b) above 5% and equal to 6.7%. The reference and measured velocities were (a) 1.76 m/s and (b) 1.06 m/s respectively. The angles between the velocity vector and laser axis were (a)  $51^\circ$  and (b)  $9^\circ$  leading to Doppler frequencies of 3.4 MHz and 3.23 MHz, respectively. The waveforms demonstrate the intensity modulation effect due to non-point-like laser spot and speckle effects leading to a broadening of the frequency spectrum. In case (b), the spectrum is expected to be broader due to the changing of the size of the laser spot on the disc.

Accuracy studies of the SM sensor for the disc measurements were performed. The accuracy is dominated by the angle between the target and the laser, see Fig. 3.26. The accuracy of the reference velocity was obtained based on the uncertainties of the variables used for calculations. The measured velocity shown in Fig. 3.28 is an average of repeated measurements with a combined error. Starting from 20 m/s, only large values of  $\alpha$  were used, close to the normal of the disc surface, due to the low bandwidth of the transimpedance amplifier (10 MHz) in the readout electronics. The precision of the results are, on average, better than 6%. Typical measurements of the signals for the case of a disc rotating at 15 revolutions per second with an incident laser angle of  $29.5^\circ$ , and a laser spot size on the disk of 1.65 cm are shown in Fig. 3.20. The corresponding velocity is 0.77 m/s with 0.3% accuracy. Here, the typical profile of the signal can be clearly seen through different times, so it can be seen that the SM signal has a shape typical for weak feedback.

### 3.5 Application of Self-Mixing Sensors for Accelerators

Applications of the SM sensor for measurements of solid targets in accelerators can be widely extended for monitoring the displacements of test equipment, such as, for example, translational stages for delivering collimators, scrapers, laser light, etc., and

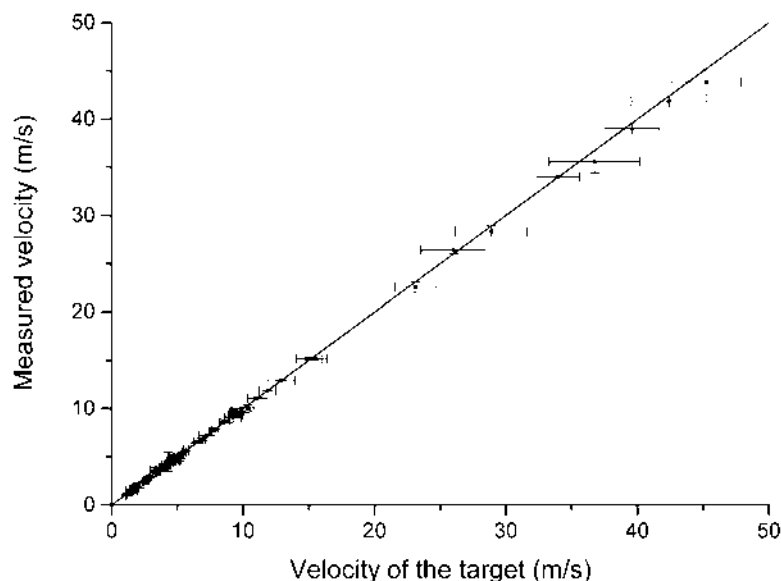


FIGURE 3.28: Experimental results from measurements of a rotating disc covered with white paper. The difference in the measured and estimated velocity is within the limits of uncertainty. The upper limitation of the velocity was due to the bandwidth of the amplifier used for the SM velocimeter. The increasing uncertainty at high speeds, equal to and higher than 20 m/s, is caused by the angle, close to  $90^\circ$ , used for the measurement.

measuring the speeds of various objects such as the speed of moving screens used for many diagnostics (for example mechanical shutters) and including rotating components, such as choppers and rotating wheel targets, which are used as neutron sources. The SM sensor can be used for characterising any kind of object which has changed its position, and the measurements can be performed efficiently and with a high degree of accuracy, which is desirable for diagnostics and for the correct operation of the particle accelerator equipment.

SM sensors are well-suited for detecting small movements and lateral, as well as angular displacements. In beam diagnostics, screens are widely used which include moving things in and out. For example, scrapers for beam diagnostics are effectively blades located in the direction of the particle beam which are moved across the beam aperture. The information of the displacements of scrapers and the time profile of their movement are essential for the correct beam positioning [117]. Cameras, with any types of shutters, would give a profile from the exposure which would allow more information about the obtained image to be gathered and hence the diagnostics itself to be improved. Most equipment is delivered using a translational stage and in some cases, as it is with laser knife movements, which was measured and shown in this chapter, an independent assessment of such displacement is required. This is the case with the delivery of collimators, scrapers, lasers, optical components, lens, etc. An SM sensor can also be used for angular measurements, which can be used for defining the angle of screens and mirrors when a high precision is essential.

Moreover, a displacement measurement from just one set of measurements, performed with an SM sensor, allows a profile of the change in the position of measured object to be built which is useful for careful studying of the process of thermal distortion of the measured object. The thermal expansion-contraction cycle of the material remains constant in time, unless the structural modification of the material occurs which inevitably leads to the change of the material properties. Some materials behave differently when their structure changes which is usually an indicator of a possible break in the material, which leads to the breakdown of the equipment. Based on this expansion-contraction profile, breakdown of equipment under tension can be predicted. This makes SM sensors incredibly useful devices for real time monitoring of changes in position, for example of accelerator components during the cool-down [118, 119] the phase within a cryostat, which are widely used in accelerators [117, 120] in superconducting radio-frequency cavities and superconducting magnets [121] and in the study of expansion due to heat and hence detection of stress and strain factors in harsh environments, such as a reactor, or for space applications as a potential application.

Mechanical or electro-mechanical chopper devices are used in proton therapy to control the radiation level being delivered to the patient. Mechanical choppers are also used for producing pulsed beams of particles for timing. The rotational speed of choppers can be measured using the SM set-up in the way described and applied in this chapter. A 4-tonne helium-cooled tungsten wheel, a target [122] for producing the neutron particle for European Spallation Sources, is designed to rotate in order to spread a heat load around the wheel, and its rotational speed provides the information for the most energy-efficient design.

### 3.6 Conclusion

This chapter addresses a design and characterisation of the sensor based on the SM effect in laser diodes and its application to solid targets. An LD SM velocimeter was developed as an easy-to-build and compact solution when compared to alternative measurement techniques. The measuring system includes a laser, a photodiode, a current controller, a transimpedance amplifier with a specially developed current delivery system to it, and an oscilloscope. The data analysis system consists of a dedicated MatLab code which includes velocity calculations based on collected signals and spectra. The SM sensors in this chapter were designed utilising commercially available laser diodes of 650 nm operated at a power of 5 mW, and of 1550 nm at a power of 2 mW. The majority of the experiments, presented in this thesis, were performed using 650 nm LD. Several experiments were performed with 1550 nm laser using fibre optics to deliver the light to the target and back to the laser. The 1550 nm lasers, embedded with fibre optics, were also used to test different detection schemes of the SM effect. It has been demonstrated in this chapter that each of the components of the SM sensor affects the performance of the sensor and limits the measurable velocity. Measurements of the laser parameters

have shown that the most suitable laser, as well as detectors of light and amplifiers, requires a bandwidth which corresponds to the range of velocities, which the sensor is aimed at. The system can address different needs as it can be applied to different types of measurements for multiple purposes, e.g. velocimetry and displacement, both with a high sensitivity. An initial calibration and verification of the method as well as SM sensor accuracy was performed on a set-up which permitted velocities up to 50 m/s to be studied. A detailed analysis of different parameters which can influence the performance of the sensor was conducted. These include: sources of possible limitations from the measurement set-up; bandwidth of the lasers; reflectivity of the measured targets; level of feedback from the target; velocity magnitude; and the angle between the laser axis and the velocity vector.

In order to understand and estimate the limitation of the SM method, the theory, which was developed in Chapter 2, of the expected spectrum of light after scattering in the case of an SM sensor was tested. Experimental and simulation studies, performed by myself, into the influence from the magnitude of the target velocity, the geometry of the SM sensor and different reflectivities of solid targets on the overall spectrum, were found to be parameters having the strongest affect on the results. The experiments demonstrated an agreement with the theory of the scattered spectra developed in Chapter 2. For example, the FWHM of the peak of the calculated spectra widened with increasing velocity magnitude, while the amplitude of the peak decreased. It has been demonstrated that for the best performance of the sensor, a balance between different parameters is required. An angle close to  $90^\circ$  leads to a smaller shift in the frequency, which allows amplifiers with a lower bandwidth to be used, but, at the same time, it means less amount of backscattered light. Moreover, the accuracy of the measurement reduces as well. The best precision and accuracy was achieved in the range of  $13^\circ$ - $77^\circ$ . The experimental results showed that the velocity of a white paper target can be measured with an accuracy of better than 2% and micrometer spatial resolution over a velocity range from 0.5 mm/s to 50 m/s. The studies presented in this chapter, and performed by myself, allow a limitation on the maximum velocity which can be measured by an SM sensor to be improved upon by an order of magnitude. This is a very significant enhancement of this technology which had not previously been applied in the context of particle accelerators. The studies have also yielded the capability of being applied to the measurement of much higher velocities than ever before.

## Chapter 4

# Self-Mixing Technique Applied to Fluids

This chapter covers experimental measurements of the velocities of fluids and the spectra obtained from the SM effect. This includes studies into the velocity of the particles which make up the fluid, the distribution of velocities of these particles, the concentration of seeding particles added to the fluid to increase the signal, particle size and their optical properties as well as the laser focusing properties. The results are linked to the theoretical investigations into the spectra which were obtained and discussed in Chapter 2. The application of the sensor for such purposes at particle accelerators is also presented.

### 4.1 Introduction

SM sensors have demonstrated excellent performance when working with solid targets. Velocities of up to 50 m/s were measured with different geometries for mirror and paper targets. However, in the case of flows light is scattered and reflected differently compared to hard surfaces. In particular, instead of scattering off the whole surface, light interacts with separate particles or with some inhomogeneity within the illuminated volume. Additional investigations into this subject have to be conducted to assess the performance of the sensor in the case of flows. As the designed SM set-up was able to measure the velocities of solid targets up to 50 m/s, the same set-up was used with fluids. A gas jet differs from a solid in terms of several parameters, such as its high velocity and its low level of reflectivity. Tests on fluids allow the SM sensor to be assessed by changing only one parameter: the nature of the scattering process. Since the velocities of liquids are easier to control, the influence of different parameters on the SM measurement can be studied.

The theoretical review and investigation into spectra which can be obtained from the moving particles within the fluid was presented in Chapter 2. The simulations which are presented in this chapter are based on the theory developed there.

## 4.2 Fluid as a Target

During subsequent experiments, the application of the SM sensor to fluids was studied. The nature of light scattering off liquids is different from solid targets. In particular, it involves scattering off particles within the fluid, which can be natural particles within the fluid or artificially seeded ones. When applied to water, the level of the amount of scattered light is low, so the initial studies were performed using different seeding particles.

The seeding material for velocimetry, in case of laser interferometry generally and for the SM sensor itself, varies a lot. Since a number of experiments of a similar character have previously been performed for Particle Imaging Velocimetry, the first choice of material can be taken directly from there, see Table 1.4. Moreover, SM sensors have previously been applied to measure the dynamics of seeded water. The types of seeders used for SM experiments were chosen mostly in order to imitate the biological targets, such as blood and viruses [59, 65]. The table with all seeders and the properties of applied SM sensors from different experiments were presented in Table 1.3. The main easy-to-use seeder is milk. The velocity measurements demonstrated in literature did not exceed 15 cm/s for milk as a target [43]. Different seeders demonstrated the following results: measured velocities of up to 17 cm/s with polystyrene spheres as seeders of 1.23  $\mu\text{m}$  size [66], and with lower velocities in case of the smaller sizes of the seeders, and up to 30 cm/s [66] for the blood measurements for very high concentration and without reference verification of the experimental results.

### 4.2.1 Set-up Description

An experimental set-up was designed to measure the velocity of liquids, and the set-up is presented in Fig. 4.1. An LD with 650 nm wavelength with 5 mW power as a source of light and built in photodiode for monitoring the current bias was used for the velocity measurements. The light from the LD was focused using a lens onto the fluid target at different angles  $\alpha$ , see the schematic set-up of the SM sensor in Fig. 4.1 (a). Different angles allow a wider range of velocities for the measurements to be investigated. The backscattered light from the target was coupled back into the cavity using the same lens. The data analysis based on an FFT allows the spectra of the signal to be calculated, which can be compared with spectra obtained theoretically.

The liquid was discharged into the atmosphere using a nozzle at the end of the tube, see Fig. 4.1 (b). Steady laminar flow with a constant velocity was achieved using a pump allowing control of the pump speed. The laser light was focused on the centre of the liquid flow at a distance of 0.4 cm from the nozzle outlet at  $28^\circ$ .

The transition between laminar and turbulent states can be predicted from the Reynold's number, which is equal to the ratio of inertial to viscous forces [19]. The laminar regime is achieved when the Reynold's number is less than 2,300. The range of

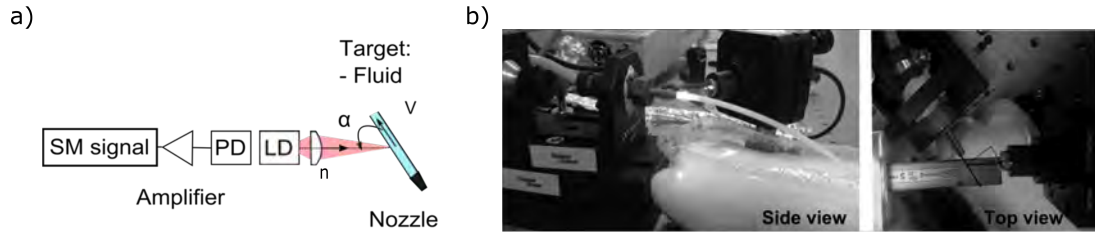


FIGURE 4.1: Set-up of the SM sensor used for velocity measurements with a fluid as a target. (a) The SM set-up contains an LD with light focused onto a target at an angle  $\alpha$  from the normal of the target surface. A PD takes the role of a detector of the SM modulated light, the signal from which is converted into the voltage signal by a transimpedance amplifier. (b) The liquid flow discharges from the nozzle into the atmosphere using a controlled pump system, which allows a reference velocity to be defined.

applied pump rates supported the laminar flow allowing a stable and measurable reference velocity of the water stream. For the presented set-up, a laminar flow is predicted up to a fluid velocity of 3 m/s. The variation of the diameter of the nozzle and viscosity of the liquid allows for higher velocities to be reached without entering the turbulent regime flow.

The experimental set-up was constructed in such a way that different parameters can be varied. The seeding material parameters, such as the material itself and the size of the seeders, were changed without changing the viscosity of the fluid. Based on the information from Tables 1.4 and 1.3, the experiments were performed with the following seeders:

- Milk: 3 - 6  $\mu\text{m}$ ;
- Titanium dioxide: 1  $\mu\text{m}$  ; 150 nm; 21 nm.

All solutions and powders used in the experiments have a white colour. The white colour of the fluid meant that all wavelengths within the visible spectrum of light scattered equally. Light scatters off the moving particles with some angular distribution of scattering efficiencies corresponding to the properties of the scattered particles.

#### 4.2.2 Milk and Titanium Dioxide as Seeders: Verification of the Measurements

A mixture of water with milk was used for fluid velocity measurements at first. Milk is an emulsion of fat globules in water, where 87% of the milk is water, and only 4% is fat globules. The refractive index for the milk at 650 nm wavelength is 1.45 and the light absorption coefficient is less than  $10^{-5}$  [123], which results in a reflectivity of approximately 3.5%.

In the first set of experiments the velocity of the diluted milk was measured in the range between 1 and 20 cm/s. The distance between the LD and the target was fixed to 4 cm. The measurements were performed for different concentrations of milk in the water: 10%, 5%, and 1%. The shape of the fat globules is close to spherical. The average

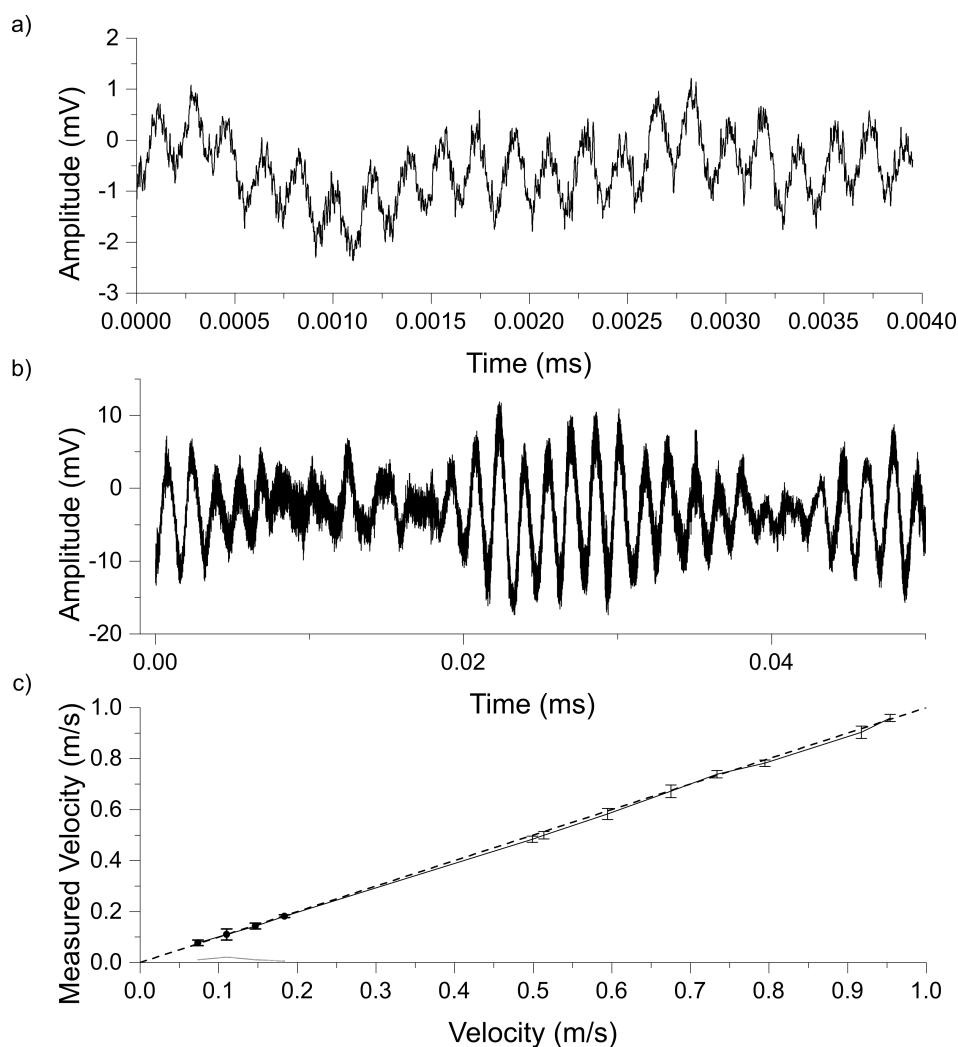


FIGURE 4.2: Experimental results from measuring the velocity of fluids. Examples of the signal received from the set-up with (a) milk and (b) a titanium oxide water solution as the target. The reference and measured velocity was 0.55 m/s in case of titanium dioxide. (c) The results of the measurements of the velocity up to 1 m/s were measured with an accuracy better than 4%. Velocities in the range of 1 to 20 cm/s were carried out for milk diluted in water to a 5% concentration, shown by round dots. Higher velocities, up to 1 m/s, shown in the graph are obtained from measurements of the titanium oxide in water solution with less than 1% concentration in volume and were also measured with accuracy greater than 4%.

size of the fat globules is 3 - 6  $\mu\text{m}$  [123]. The approximate amount of particles is  $10^6$  per volume for undiluted milk [124]. This results in  $10^5$ ,  $0.5 \times 10^5$ , and  $10^4$  particles for the 10%, 5%, and 1% concentrations of the diluted mixtures respectively. An example of the SM signal obtained during the experiment with milk can be seen in Fig. 4.2 (a). The errors in the velocities of the fluid were within the limits of uncertainty of measurements and calculations. Figure 4.2 (c) shows the measurements of the velocities, where the velocities of up to 20 cm/s correspond to the case of milk being used as a seeder.

In the second set of experiments, the velocity of water seeded with titanium dioxide ( $\text{TiO}_2$ ) was measured using the same set-up with a laser of wavelength 650 nm. The size

of seeders was less than  $1\ \mu\text{m}$ . The concentrations of less than 1% of the volume were investigated. The value of the refractive index (1.49) of the  $\text{TiO}_2$  solution was calculated based on a measurement of the critical angle from a measurement of the angle of total internal reflection.

An example of the SM signal obtained during the experiment with  $\text{TiO}_2$  can be seen in Fig. 4.2 (b). The signal can be characterised as a signal with weak feedback. The velocities of fluids up to 1 m/s were successfully measured with high accuracy, as shown in Fig. 4.2 (c). The reference velocity of the fluids (the dashed line) was calculated based on the pump rate and the diameter of the nozzle. The differences in the resulting and estimated velocity of the fluid were within the limits of uncertainty of measurement and calculations.

The measured velocity was found from the averaged spectrum of 50 power spectra for each velocity on the plot. The acquisition time was of the order of 10 ms, therefore the sensor can be regarded as an on-line monitor.  $\text{TiO}_2$  seeders allowed better signal with higher velocities of up to 1 m/s to be achieved even though the size of the seeders was smaller, when compared to the milk solution with the maximum measured velocity of 20 cm/s.

### 4.3 Effects of Variation of Different Parameters of the Flow

The influence of different parameters on the spectra was studied analytically in Chapter 2. The experimental set-up was used to verify the effect from these parameters in experimentally obtained spectra.

The influences of different parameters on the spectrum of the SM signal were studied while measuring the velocity of the liquid. This included varying the pump speed of the liquid which allowed the laminar flow velocity to be changed. The concentration of the seeding particles was also varied which allowed the amount of scattered light to be controlled.  $\text{TiO}_2$  particles of different size were used for the experiments and analysis.

The measured velocity of the fluid was calculated by performing an FFT of the SM signal. The peak of the spectrum corresponding to the frequency shift was found by fitting a Gaussian distribution. The FWHM of the Gaussian distribution should be proportional not only to the velocity of the target and the inclining angle, but also to the distribution of the velocities of the moving targets within the interaction or illuminated volume, see Fig. 2.19.

In order to validate the results which were obtained by the SM system, the pump rate of the flow was used to calculate the maximum reference velocity which could be achieved within the fluid channel. The experimental uncertainties of the velocity are based on the uncertainties of experimentally measured quantities. These include: the pump speed, the diameter and shape of the nozzle, the inclination angle  $\alpha$ , and the assumption that laminar flow was achieved when the fluid discharged from the nozzle. The influence on the accuracy of the velocity measurement on the angle  $\alpha$  has been

studied and demonstrated, and it was shown that at an angle of  $70^\circ$ , the relative error is lower than 3%. From every measured signal and spectrum obtained from it, the velocity can be calculated from the Doppler shift. However, the fitting of the spectrum brings its own uncertainty on the measurement, in particular on the precision of the determined value of the peak.

### 4.3.1 Velocity of the Laminar Flow

Sets of experiments were undertaken to study the influence of the velocity of the target on the spectrum of the SM signal. The velocity of the fluid was steadily increased from 0.5 to 1.5 m/s for each experiment. The spectra of the SM signals measured with increasing velocities are presented in Fig. 4.3 (a). Different colours represent different flow pump rates. The liquid was seeded with  $\text{TiO}_2$  with an average diameter of  $1 \mu\text{m}$ . Their concentration was fixed at 0.6%. The concentration was calculated as the ratio of the mass of the solute over the mass of solution. Such a low concentration guarantees the negligible change of the viscosity of the seeded water.

The influence of the pump speed on the peak frequency (squares) and the amplitude of the peak (circles) are presented in Fig. 4.3 (b). The peak frequency coincides with the peak of a fit to the FFT coefficients, and the amplitude of the peak is the maximum value of this fit for the spectra. The frequencies corresponding to the peaks, which are proportional to the velocity of the fluid, follow a linear trend (blue dashed line). Whilst the amplitude of the peak is inversely proportional to the fluid velocity (green dashed line). The inverse of the amplitude for the peak frequency is shown by the green line in the figure on the right side of the Fig. 4.3 (b). For reference, the measured velocity of the fluid is presented on the top  $x$ -axis.

The experimental results agree with theory regarding the velocity influence on the spectra. The characteristics of the spectrum of the SM signal strongly depend on the velocity of the target. The frequency corresponding to the peak of the spectrum is proportional to the velocity. The FWHM of the peak also increases with increasing velocity. The amplitude of the peak decreases at the same time, see Fig. 4.3.

As expected from Eq. 2.19, the amplitude of the peak of the spectrum is inversely proportional to the fluid velocity. The amplitude of the peak decreases such that there is a maximum velocity which can be measured. Figure 4.3 (b) can be used for the prediction of the level of expected signal for higher velocities, based on which and using additional algorithms can allow the signal analysis to be improved.

### 4.3.2 The Shape of the Spectrum

If the laser light is focused on the centre of the fluid discharging from the nozzle, each spectrum should have a clear peak which corresponds to the case illustrated in Fig. 2.14 (d). When the laser light is focused on particles moving with the maximum velocity, the spectrum is broadened due to the particles moving with lower velocities, hence it is shifted into the blue frequency domain. This means that the spectrum is

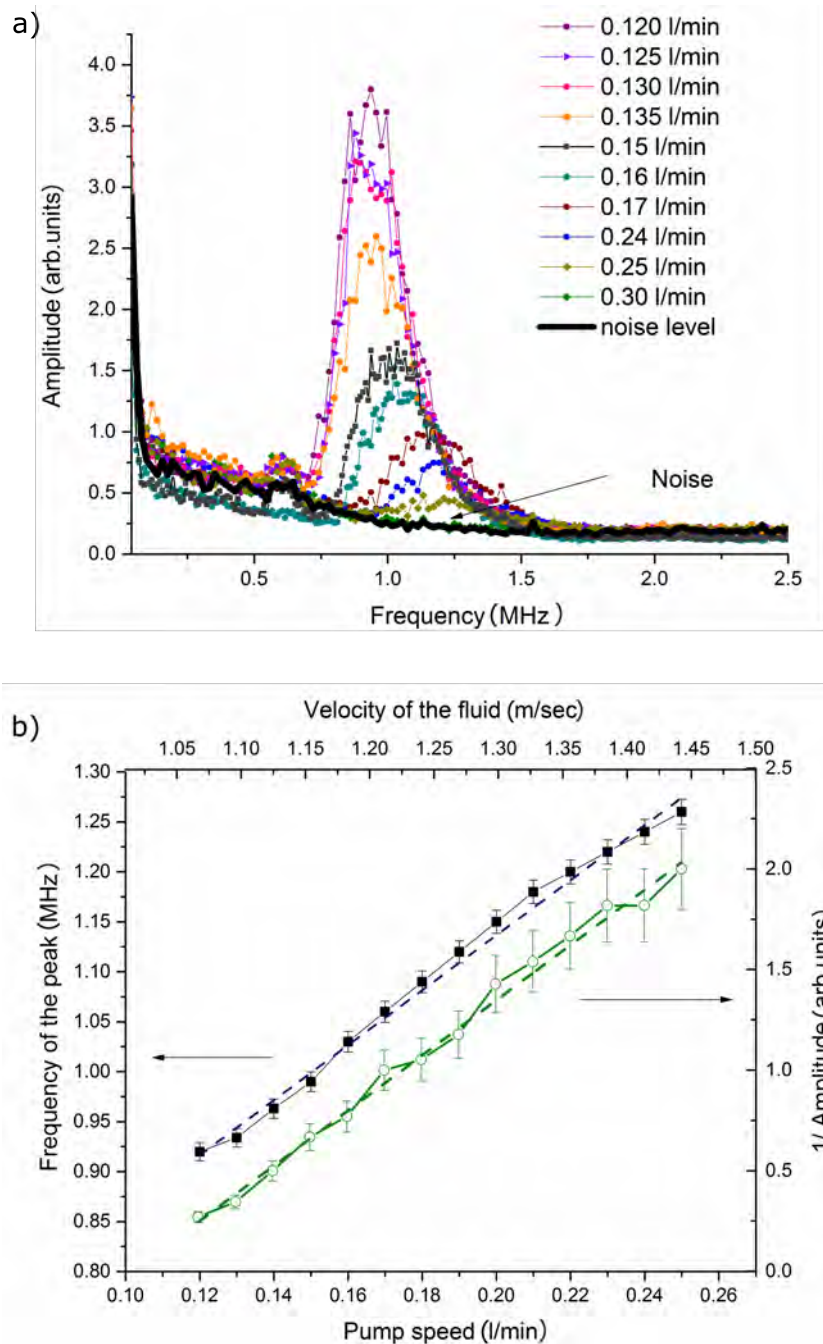


FIGURE 4.3: The spectrum of typical SM signals received whilst measuring the velocity of the laminar flow with different experimental variables fixed. The seeding material,  $\text{TiO}_2$ , had an average diameter of  $1 \mu\text{m}$  with a concentration of no more than 1%. (a) The velocity of the liquid was increased in each experiment. Each spectrum corresponds to an experiment with a different laminar velocity of the flow in the range of 0.12 l/min to 0.25 l/min. (b) The processed results of the experiments. The measured velocity linearly increases with the pump speed, as expected. The experimental results of the amplitude of the spectrum peak measurements are presented by green dots.

broadened towards lower velocities (see Fig. 2.14 (b) and (d)). The simulations were shown in Chapter 2.

Figure 4.3 (a) shows the spectra obtained for different velocities of the fluid using the SM sensor. The spectra are not symmetrical in relation to the maximum frequency (Fig. 2.14 (c) and (d)), neither do they have a plateau (Fig. 2.14 (a) and (b)), both cases correspond to the light being focused on the particles moving with maximum velocity. Instead, each spectrum, represented by different colours, has a sharp rise of the curve and a following gradual slope. The noise level (a thick black solid line) is not high enough to influence the shape of the spectra in that regard. A possible explanation of the asymmetry of the spectra obtained in the experiments is shown in Fig. 4.4, where both symmetrical (a, b) and asymmetrical (c, d) overall spectra are shown. Figure 4.4 shows the interaction of the light with fluid when the light is focused at the centre of the fluid (a) and at the point which is shifted from the centre (b). The overall spectra for these cases are shown on the right part of the picture. The velocity of the particle where the light was focused and correspondent components of the spectra are shown by dotted black lines. The additional components are shown by blue lines. When the light is focused on particles moving with velocities lower than the maximum, see the red vector for the maximum and black dotted line for the focus point in Fig. 4.4 (c), a part of light still scatters off the particles moving with higher velocities compared to the velocity of those on which the light is focused. Those particles and their velocities contribute significantly to the overall spectrum so it changes the symmetry. The colours of spectral components are correspondent to the colours of the velocity vectors themselves. Figure 4.4 (d) demonstrates the overall spectrum for the shifted focus point, and how it leads to a shift of the symmetry of the peak of the spectrum towards a higher frequency, thus higher velocities, see red colour, compared to the plot (b) of the symmetrical overall spectrum.

The overall spectrum in Fig. 4.4 (d) demonstrates how light scattering off particles with higher velocities can shift the spectrum and change the symmetry of it. The maximum amplitude of the overall spectrum corresponds to the frequency proportional to the velocity of the area on which the light was focused. However, light scattering off particles which move faster than those on which the light is focused leads to a broadening of the spectrum and changes the type of spectrum symmetry. Since the overall resulting spectrum is a superposition of all spectra of scattered light, it undergoes a broadening from the components corresponding to the particles moving with higher velocities, see Fig. 4.4 (d). The spectrum which can be obtained from the particles with higher velocities is represented by a red thin line in Fig. 4.4 (d). The spectrum obtained from the focus point is shown by a black dotted line. Even though the light beam is focused at a specific point in the fluid, the light still scatters off all particles the light beam illuminates before the focus point. The spectra, which are obtained from the particles outside the focus point, are represented by blue lines. The overall spectrum is shown by a black solid line, demonstrating a sharp rise towards the peak followed by a gradual slope away from it as a consequence of additional particles which the light

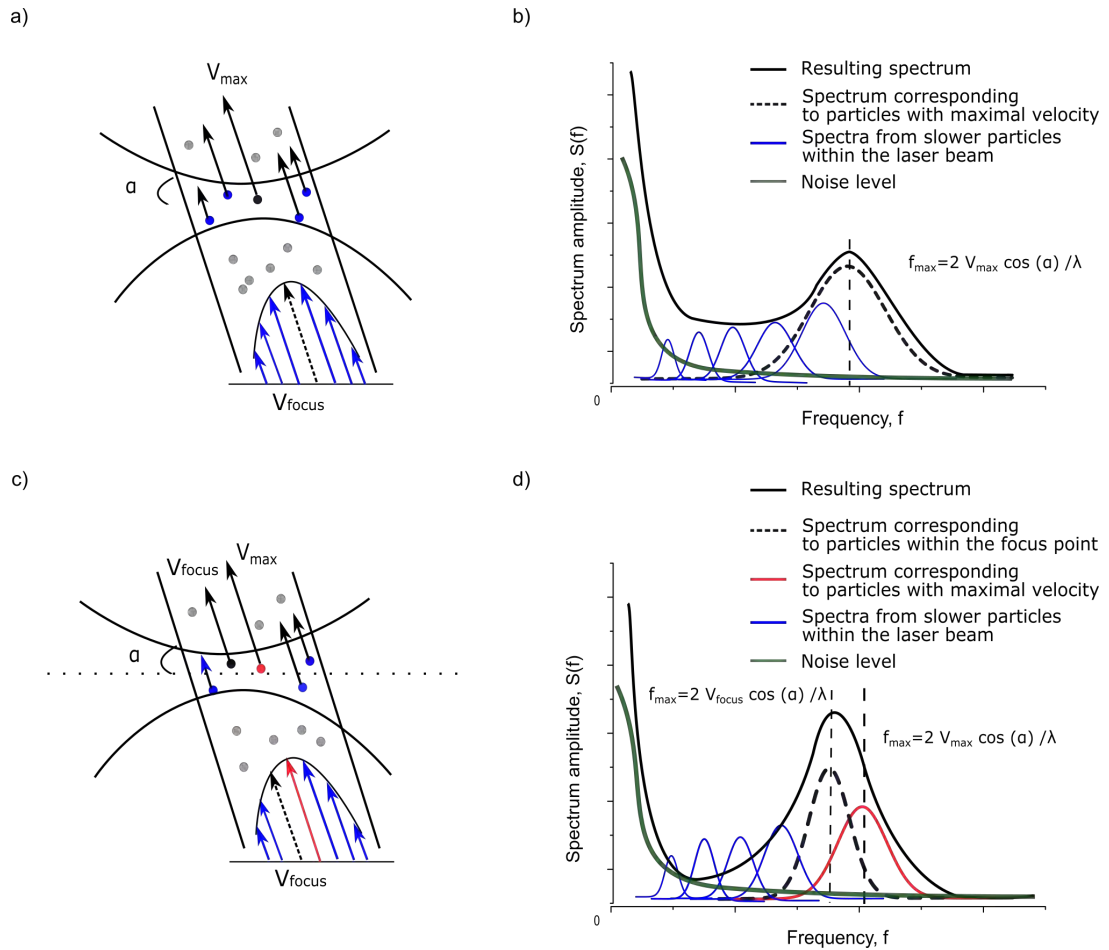


FIGURE 4.4: Schematic explanation of the spectrum obtained in the experiments with different velocities. The laser beam focus is (a) at the centre of the fluid and (c) shifted from the area of maximum velocity. The distribution of the velocity across the fluid is shown on the bottom of the pictures (a) and (c) where the dotted vector corresponds to the velocity of particles on which the laser light is focused. In case of (a), it is the centre of the fluid. In case of (c), the maximum velocity is shown by red colour. Comparing with (a), the point which the laser light was focused (c) on was shifted from the area of the maximum velocity within the fluid. (b) and (d) The overall spectra of the signal for 2 cases, where the individual contribution from the velocities are marked with the same colours. The grey-green thick solid line represents the noise background. The solid black line shows the overall spectra.

scatters off.

The spectrum, which is broadened towards higher frequencies, can be seen from the results of the experiments presented in Fig. 4.3 (a) where each of the spectra is broadened asymmetrically towards the right.

### 4.3.3 Concentration of the Seeding Materials

One of the biggest advantages of the SM sensor is its sensitivity, as even a small amount of moving particles within the sensing volume can produce a detectable signal. The limitation on the minimum detectable concentration depends on the size of the particles, the refractive index and cross section together with the level of noise. The effect from

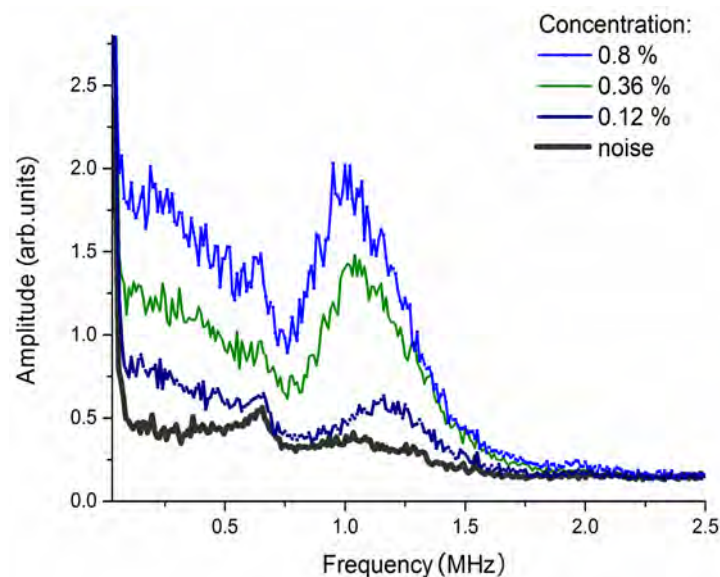


FIGURE 4.5: The experimental influence of the concentration of seeders ( $\text{TiO}_2$ ,  $1 \mu\text{m}$  diameter) in the flow of water on the spectrum of the self-mixing signal with fixed peak velocity at  $1.2 \text{ m/s}$ . The spectra obtained in experiments with different amount of seeding particles in water:  $0.8\%$ ,  $0.36\%$  and  $0.12\%$  demonstrate the effect of differences in concentration on the spectra.

the size of the particles is presented later in this chapter. The variation of concentration of the seeding particles and its effect on the overall spectrum will be presented in this section with details for one specific size of particles, namely  $1 \mu\text{m}$ .

The amplitude of the self-mixing signal is proportional to the amount of scattered light, and so is proportional to the concentration of particles the light scatters off. The same set-up was used to study the effect of varying the seeder concentrations while keeping the velocity fixed.

Figure 4.5 shows an example of three representative average spectra for water seeded with titanium dioxide particles with an average diameter of  $1 \mu\text{m}$ . The plots show the results of the experiments when the peak velocity of the liquid was fixed at  $1.2 \text{ m/s}$ . The concentration of the seeders was varied from  $0.8\%$  to  $0.03\%$  with increasingly small steps after  $0.3\%$ . The concentration was calculated as ratio of the mass of solute to the mass of solution. The noise level is obtained when the laser light did not interact with the water. Figure 4.6 (a) shows the processed result of all experiments with variation of the concentration of the seeders in water. The results of the measurement such as the dependence of the amplitude (left side) and of the frequency of the peak (right side) are shown for each tested concentration. The frequency of the peak was constant in two regions: at a concentration above  $0.5\%$  and below  $0.22\%$ . Figure 4.5 shows the spectra for the concentration of  $0.8\%$  (above  $0.5\%$ ),  $0.36\%$  (in the region between  $0.5\%$  and  $0.22\%$ ) and  $0.12\%$  (below  $0.22\%$ ). These three concentrations were chosen to represent three ranges of the spectra where their behaviour and hence obtained results were different.

At higher concentrations starting from 0.2% and up to 0.8% the spectrum has an asymmetrical shape, see Fig. 4.5. It shows that the light was focused on particles moving with a velocity less than the maximum, as it was discussed in the previous subsection. The spectrum looks like the one in Fig. 4.4 (d). The distribution of the velocities within the measured area, which is illuminated by the laser light, is shown in Fig. 4.4 (c). The distorted shape of the spectra may be a result of additional higher frequency components which occur due to light scattering off particles with higher velocities. Moreover, this leads to a shift of the peak of the spectrum toward the maximum velocity.

At concentrations of above 0.5%, the frequency of the spectra is constant and equal to 1.02 MHz. In the range of 0.5% and 0.22% the frequency of the peak shifts towards higher values, and at low concentrations, below 0.22%, it is constant again and equal to 1.11 MHz. This means that when light scatters off particles at a high concentration, the light does not interact with particles moving with velocities that are higher than those where the light is focused. When the concentration decreases, the light scatters off particles with higher velocities which hence contribute more to the overall spectrum.

At lower concentrations the spectrum becomes more symmetrical at which point the frequency of the peak value remains constant, see the dark-blue spectrum in Fig. 4.5 for a typical spectrum for lower concentrations and Fig. 4.6 for the results. This means that at lower concentrations more light is scattering off particles moving with the maximum velocity. The spectra which relate to concentrations higher than 0.5% correspond to the velocities of particles on which the light was focused. At concentrations lower than 0.22% the peak of the spectra corresponds to the maximum velocity of the fluid. The gradual change of the peak of the frequency from 1.02 MHz to 1.11 MHz demonstrates the effect of scattering off the particles with higher velocity with more of the single particle scattering processes involved.

After an analysis of the shape of the spectra obtained for the different experiments was completed, the interaction point between the laser beam and the fluid was studied closely. It appeared that the focus point of the laser light was shifted from the centre of the fluid by 10% of the fluid channel width, which meant that the light was not focussed on the maximal velocity and that the spectrum was broadened for reasons just discussed. The frequency peak of the spectrum corresponds to the maximum velocity of the liquid after the concentration of seeders was reduced to 0.25%.

The amplitude of the spectrum decreases gradually when the concentration is decreased, see Fig. 4.6 (a). It was still possible to observe the SM signal to obtain information of the velocities at the lowest concentration of 0.03% of seeders in the water. The trend of the peak amplitude of the spectrum is shown in Fig. 4.6 (a) on the left side of the plot. The amplitude is proportional to the square root of the concentration of the seeders. Figure 4.6 (b) shows an enlarged part of plot (a) for the amplitude dependence for the concentration in the range of 0.3% to 0.03%. This relationship is valid up to the concentration of 0.17%. The data was split into two sets and interpolated using a square root function:  $y = k\sqrt{x}$  with two different values of  $k$  (green and orange lines in

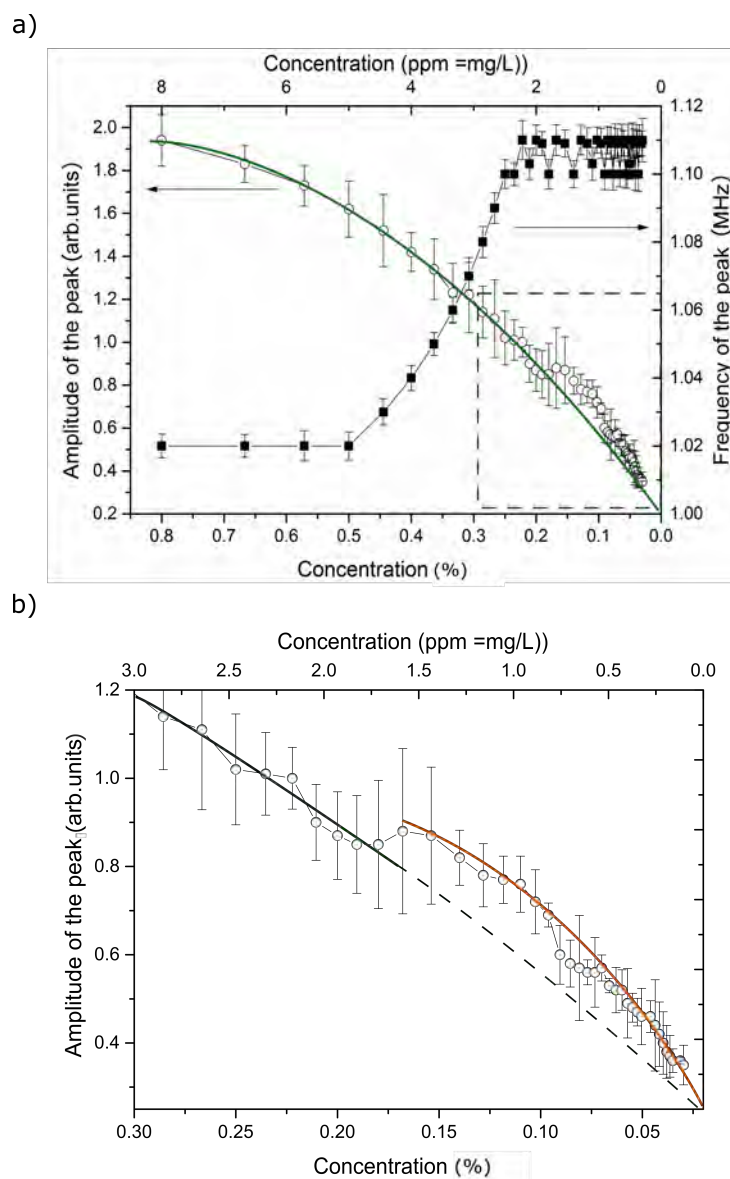


FIGURE 4.6: The experimental influence of the concentration of seeders ( $\text{TiO}_2$  of a  $1\ \mu\text{m}$  diameter) in the flow of water on the spectra of the self-mixing signal with fixed flow velocity ( $1.2\ \text{m/s}$ ). (a) Experimental dependence, after subtracting the noise, of the amplitude of the spectrum peak on the concentration of the seeders on the left axis of the plot, and the extracted peak frequency depending on the concentration of the seeders on the right axis of the plot. The concentration of seeders was decreased in each experiment from  $0.8\%$  to  $0.03\%$ . (b) A detailed amplitude dependence, see embedded square in plot (a), in the concentration range of:  $0.3\% - 0.03\%$ . The green and orange lines represent interpolation using a square root function,  $y = k\sqrt{x}$ , of the data with different values of  $k$  respectively, which represented splitting the data into two sets.

Fig. 4.6 (b)). The data for concentrations higher than 0.17% can be interpolated using  $k \approx 2.1$ , and for lower concentrations with an interpolation coefficient of  $k \approx 2.25$ .

Figure 4.7 shows spectra for different concentration of the seeding particle of 150 nm and 21 nm in more details. The spectra behave in the same way as described before.

#### 4.3.4 Size of Seeding Materials

According to the theory developed in Section 2.2, the amplitude of the peak of the spectrum should be proportional to the number of seeders in the flow, i.e. to the concentration. The size of the scattering particles influences the level of the signal, which can be obtained applying the SM technique. Sets of spectra were obtained during experiments for a certain size of the seeding particles and their concentration, which was gradually varied from a starting value towards pure water. Figure 4.7 shows the representative spectra obtained for particles of size of 150 nm with a concentration range of 2% to 0.03% and 21 nm with a concentration range of 3.7 % to 0.04 %. The green colour on all plots represents the spectra with maximum concentration for the experiments. The grey coloured spectra show the noise level spectra which were obtained by measuring at a time when the laser light did not interact with fluid. The obtained noise spectrum varied dramatically over different sets of experiments due to conditions beyond control: temperature variations, electrical mains fluctuations, etc.

The effect of the asymmetrical spectra, which was previously discusses, was also observed in the results presented here. Figure 4.8 shows all processed data of results obtained for the experiments, presented in Fig. 4.7, with various size seeders. The plots show the dependence of the concentration on the amplitude of the peak for the same type of seeders ( $\text{TiO}_2$ ) of different diameters: 1  $\mu\text{m}$ , 150 nm, and 21 nm. The pump speed was fixed such that the maximum velocity inside the flow was 1.3 m/s. The amplitude is presented with error bars which were based on the error in the fitting of the peak. The interpolations of the dependence for each different set of particles are shown by thin green lines.

The spectra obtained from the experiments were influenced by different parameters of the performed experiments, such as the size of seeders, their optical properties and concentration, the distribution of velocities, and an additional analysis and verifications were required prior to drawing any conclusions about the measured velocity of the fluid. The results of the experiments have shown effects such as, for example, the shift of the frequency with the concentration, or the change of amplitude behaviour, all of which were studied in details. When analysing the amplitude dependence on the concentration from Fig. 4.8 (a), they were fitted to a square root function within error bars for each diameter. However, the data changes trends at certain values, see enlarged section in Fig. 4.8 (b), and a polynomial function fits the data more precisely, while a square root function for fitting allows the analysis of physics behind the effect to be explained. The points, or regions, where the trends change are deemed of special interest and are marked by inflection points similar to those shown in Fig. 4.6. For the data, corresponding to

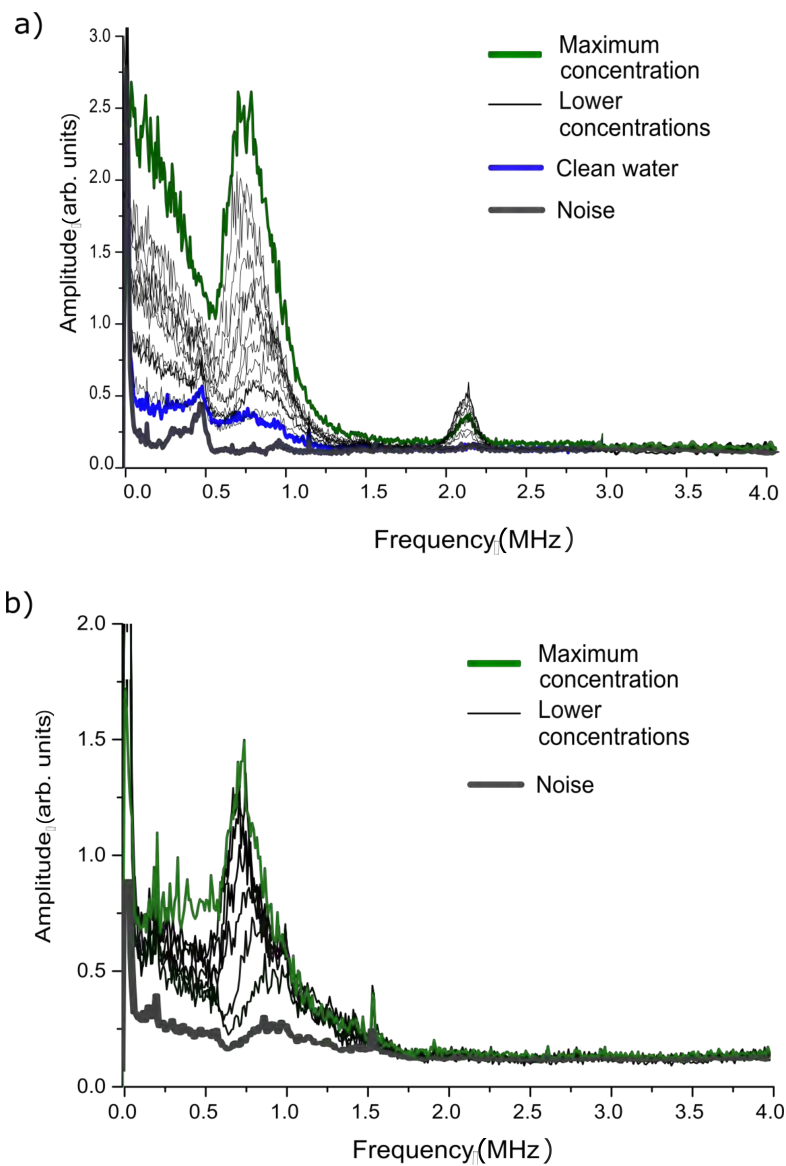


FIGURE 4.7: The experimental influence of the concentration of  $\text{TiO}_2$  seeders in the flow of water on the spectrum of the self-mixing signal when the size of the seeders is different: (a) 150 nm, and (b) 21 nm when the concentration was decreasing from maximum to pure water (no seeders). The amplitude of the spectrum peak decreases steadily with decreasing concentration.

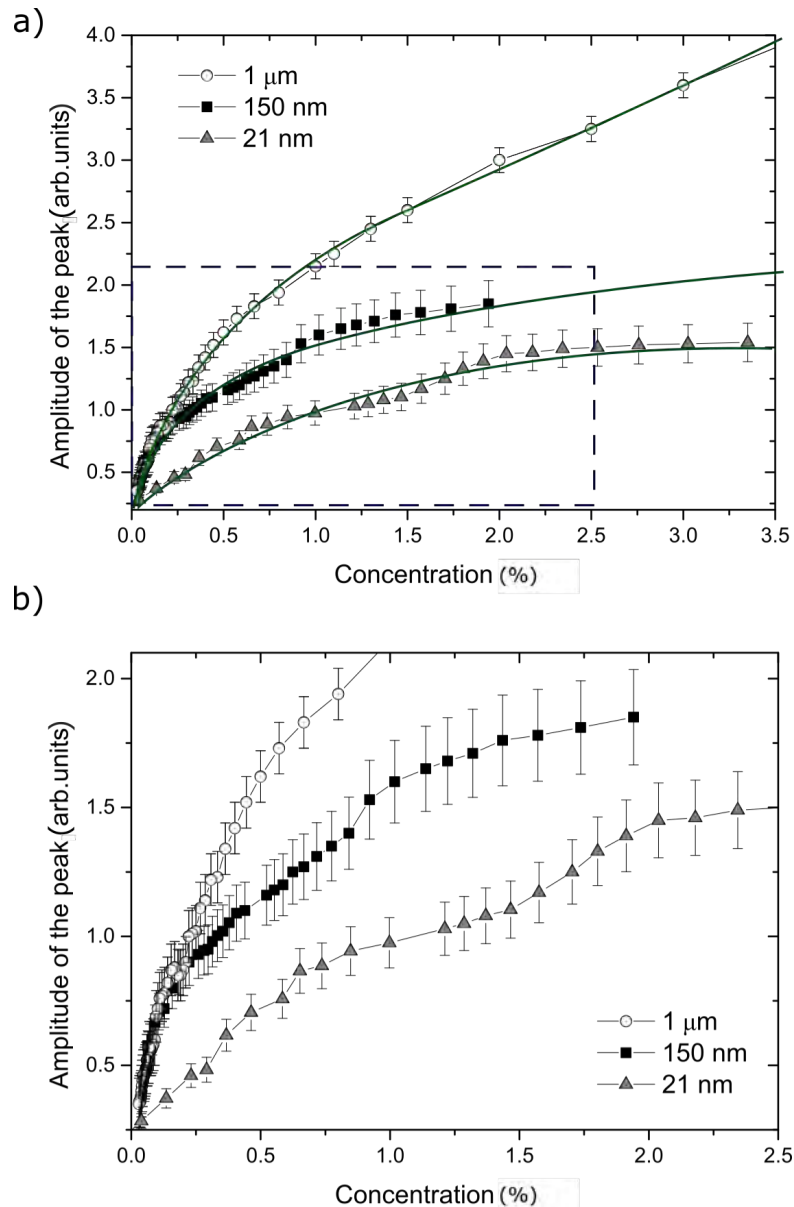


FIGURE 4.8: (a) The experimental influence of the concentration of TiO<sub>2</sub> seeders in the flow of water on the spectrum of the self-mixing signal with a fixed flow velocity (at 1.3 m/s). The obtained result for seeders with 1 μm diameter are shown by round white dots, 150 nm diameter by black square dots, and 21 nm by grey triangular dots. The interpolations of the dependence for each different set of particles are shown by thin green lines. The amplitude of the spectrum peak decreases steadily with decreasing concentration. The part of the amplitude-concentration dependence within the enclosed region is shown in plot (b) demonstrating more details of the behaviour the functions.

the 21 nm seeding particles, the fitting function changes its behaviour at a concentration approximately equal to 1.7%, for 150 nm the change is at around 0.75%, and for seeders of size 1  $\mu\text{m}$ , the critical or inflection point is located at approximately 0.17% concentration. Figure 4.6 shows a detailed representation of the last function corresponding to the particles of a 1  $\mu\text{m}$  diameter seeders. The general behaviour of the fitting functions does not change; however, it shows small steps at the various critical or inflection points before resuming the overall square root trend. A reason for this is the change of scattering process from multiple to single or vice versa at the concentrations corresponding to the infection points. When the particles are separated by a large distance compared to their sizes, it is considered as single scattering. These particles contribute to the scattered light equally, and the overall scattered field is the sum of all the individual components. As the particles approach each other, i.e. the concentration of the scatterers grows, the Maxwell equations must be solved by satisfying boundary conditions for all particles. In this case, the simplified analytical solutions cannot be used, and numerical methods have to be applied. One of the computational modelling methods is density functional theory [125] which is used for the investigation of the electronic structure of many-body systems. The finite-element approach is an alternative method which is usually adapted to solve Maxwells equation under many conditions, and this method is implemented into different commercially-available software, for example EMFLEX from Weidlinger Associates Inc. Another approach for studying the multiple-scattering effects is radiative transfer techniques [126]. All of these methods require additional information about many parameters of the system.

The amount of backscattered light strongly depends on the size of the particles, particularly if the size of the scattering particles is of the order of the wavelength of the incident light. In Fig. 4.8, the peak amplitude of the spectrum is higher for the 1  $\mu\text{m}$  diameter seeding particles compared to 150 nm and to 21 nm. However, when the size of the seeding particles was 5  $\mu\text{m}$ , the amplitudes of the peaks were observed to be also lower compared to the amplitudes correspondent to the 1  $\mu\text{m}$  diameter seeders. The peak amplitudes reach saturation level at the certain concentration which means the level of SM signal spectra cannot be raised higher by increasing the concentration.

#### 4.3.5 Focus Point of the Laser Light

The shapes of the spectra obtained from the experiments with fluids are different when compared with results from the experiments with solid targets. In particular, the SM spectra obtained for fluids are broadened and non-symmetrical. This occurs as a result of the way the light scatters off moving particles and the properties of these particles. Firstly, when the scattering particles are characterised by a velocity distribution different from a delta function, the superposition of all spectra leads to various possible shapes of the overall spectrum. As a result, it cannot necessarily be fitted by a Gaussian function. Secondly, the majority of light scatters off the area of fluid where the laser light is focused, hence the predominant contribution to the overall spectrum corresponds exactly to the

velocities of the particles in this area. However, other contributions from the particles which are not in the focus of light also influence the shape of the overall spectrum with minor effects mostly resulting in its broadening. Thirdly, the contribution from other particles in the fluid depends on the concentration of the scattering particles and this influences the intensity of the scattered light. A higher concentration of particles scattering the light leads to a higher amplitude of the scattered signal. However, Fig. 4.8 demonstrates that amplitudes of the spectra reach a saturation at certain levels of seeder concentrations with the exception of the particles of  $1\ \mu\text{m}$  diameter for which they can reach higher values for bigger concentrations. Moreover, depending on the character of the scattering process, i.e. it is either multiple or single, additional unwanted components can appear in the overall spectrum.

When the laser light is focused onto different points of a fluid, the overall spectrum is expected to vary. Experiments for the verification of the theory of the overall spectrum, which was developed in Section 2.2, were designed and performed as a part of this thesis. Using the same experimental set-up, the laser was gradually moved along the light axis, and the obtained spectra were collected. The displacement of the laser along the laser light axis allowed the laser focus point to be moved. Figure 4.9 (a) shows a picture of the set-up being used. The angle between the laser axis and the fluid's velocity vector was varied from  $80^\circ$  to  $55^\circ$  in the experiments, and the obtained results for different angles are presented later in Section 4.3.6.  $\text{TiO}_2$  particles of  $150\ \text{nm}$  diameter were used as seeders, and their concentration was fixed at  $0.5\%$ . Figure 4.10 shows the schematic representation of the experiment when the laser focus point was studied. The obtained spectra at an angle of  $80^\circ$  are shown along the laser axis at different points, where the data were collected from. A schematic picture of the laser light and fluid and approximate location of the interaction point are shown on the left side of Fig. 4.10. Each presented spectrum corresponds to different interaction points when the light focus was moved with a step of  $100\ \mu\text{m}$ . The first measurement was taken when the laser light was focused on the farthest point from the laser with respect to the fluid (i.e. behind it). The rest of the data were obtained while moving the laser with a fixed step so that the focus goes through the centre of the fluid. The particles within the centre of the fluid were expected to have a maximum velocity of approximately  $1.65\ \text{m/s}$ , see Fig. 4.9 (b). The processed data obtained during the experiments are presented in Fig. 4.11, while the right part of Fig. 4.10 presents the same results in a schematic way to demonstrate the coordinates the spectra were obtained at.

Figure 4.11 (a) shows several spectra obtained when the laser light focus was within the centre of the fluid. The light-blue thick line represents the noise inherent to the SM system. The brown spectrum was the first obtained data. Every successive spectrum has a higher peak amplitude when compared to the previous spectrum moving toward the centre of the fluid, see the red spectrum shown above the line representing the fluid centre. Each peak in these spectra can be fitted with a simulated function according to Eq. 2.19. The spectra are centred at a frequency of approximately  $600\ \text{kHz}$ , which

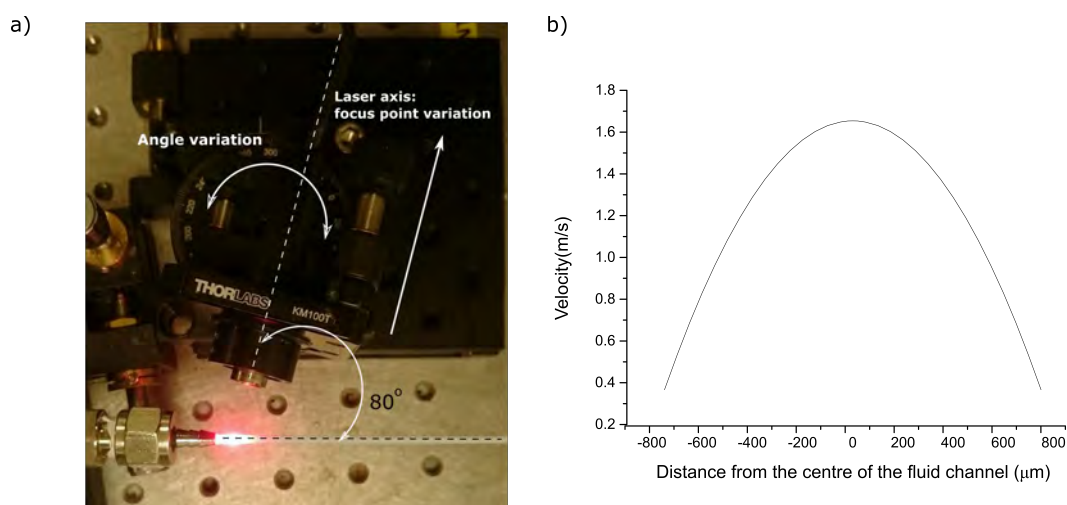


FIGURE 4.9: (a) Set-up of the focus point study, where the laser was moved along the laser axis when the light was fixed at  $80^\circ$ . The variation of the angle and the direction of the movements of the laser are shown by the white lines. The dotted line represents the laser light axis. (b) Fluid velocities distribution within the fluid channel for different points from the centre of the fluid channel. It was calculated assuming the pump speed of  $0.22 \text{ mL/min}$  and the radius of the nozzle of  $0.84 \text{ mm}$  radius based on Poiseuille's law.

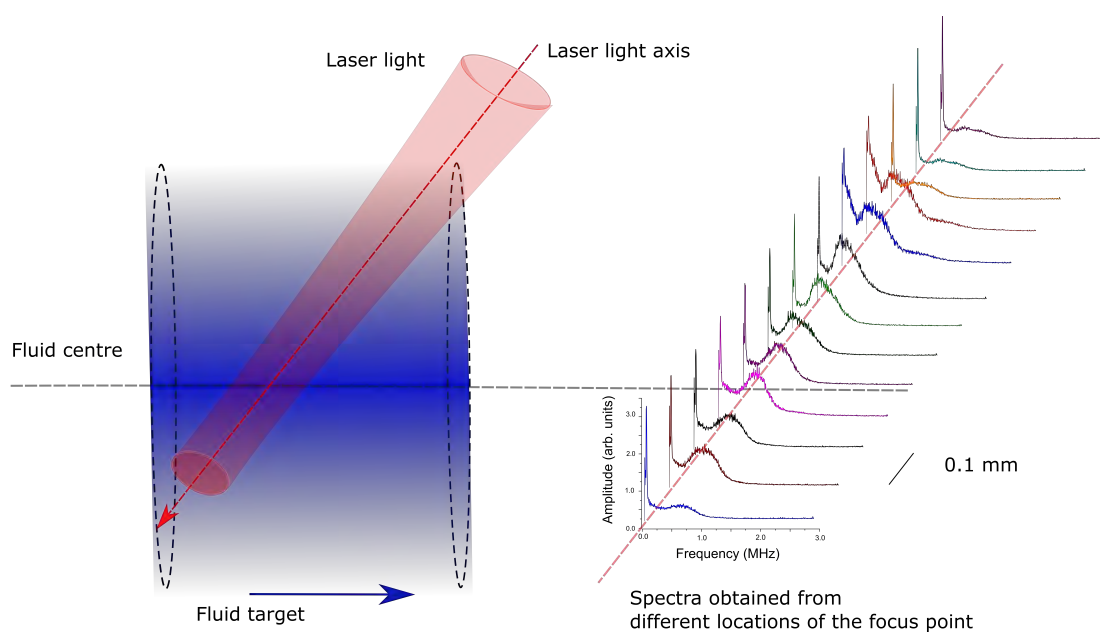


FIGURE 4.10: Schematic representation of the set-up for focus point study is shown on the left side of the picture. The spectra, which were obtained during the SM experiments, are presented on the right, along with the laser light axis with an approximate location of where they were obtained from. The evolution of the spectra along the laser axis demonstrates the difference in shape of the spectra when the focus point is shifted. For a fixed angle, the spectra were obtained at each fixed position of the laser as it was moved along the laser light axis in small steps of  $100 \mu\text{m}$ . The experimental data obtained is presented in Fig. 4.11.

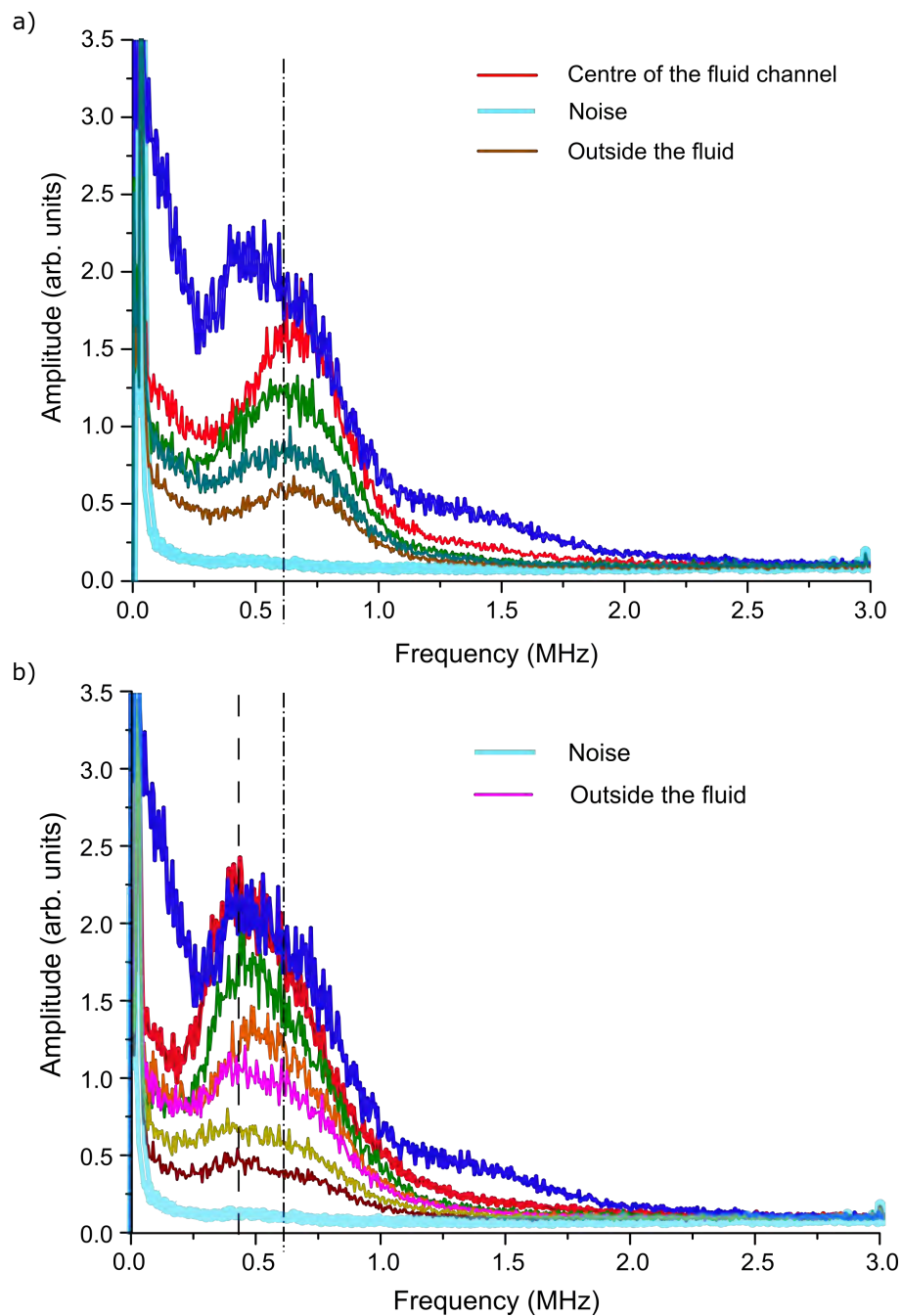


FIGURE 4.11: The obtained spectra for studying the focus point while measuring the velocity of the fluid. Thin black lines show the fitting of the spectra. Different colours of the data correspond to results from different focus points. a) The laser was focused behind (first curve, brown colour) the fluid centre and moving towards it in steps of  $100 \mu\text{m}$ ; and a red coloured symmetrical data for the centre point. The blue spectrum corresponds to the next step of  $100 \mu\text{m}$  and is shown for the comparison on both plots. b) The laser was focused very close to the centre of the fluid, but, in front of it. While the focus point moves along the laser axis away from the centre, the amplitudes of the spectra decrease with each step, and their shapes are not symmetrical (towards the brown curve). The spectra represents the obtained results from the interaction of the fluid with the laser light, shown in Fig. 4.10 in the region above and below the dotted line representing the centre of the fluid channel in plots (a) and (b), respectively.

is shown by the dotted line. The shapes of the spectra are symmetrical, and their amplitudes increase while moving the focus point closer to the centre of the fluid channel. The next  $100\ \mu\text{m}$  step along the laser axis led to a complete change of the shape of spectra, see the blue spectrum in Fig. 4.11 (a).

Figure 4.11 (b) shows the next set of data, which were obtained for the light focus point moving further away from the centre of the fluid along the laser axis. The blue spectrum is shown here as well, having the maximum amplitude when compared with other spectra. Starting from it, shapes of the obtained spectra are asymmetrical. Moreover, the amplitude decreases with every step along the axis as well. Several spectra, collected last, were obtained when the focus point was outside the fluid.

Figure 4.12 (a) shows several spectra from Fig. 4.11 (b) which were obtained when the laser light focus was outside the fluid channel together with two spectra (green and orange) from the inside the fluid for comparison. On two representative spectra black lines demonstrate how the data can be fitted with two different types of functions with different peak frequencies. The spectrum obtained from the fluid when the laser focus point is shifted from the centre leads to the asymmetrical spectra. The theory, which was developed in Chapter 2, was used for the simulation of spectra utilising various experimental conditions, such as the laser wavelength, the waist of the beam, the angle, the velocities distribution, in order to fit the results from the simulations to the experimental data. Figure 4.12 (b) demonstrated the simulations of spectra when applying Eq. 2.19, where the distribution of velocities within the measured area has been accounted for. The experimental data for a green curve corresponds to the simulations performed for the range of the velocities of  $0.6\ \text{m/s}$  to  $1.55\ \text{m/s}$ , which corresponds to the range of frequencies  $320 - 830\ \text{kHz}$  with a peak at  $460\ \text{kHz}$ . As it was demonstrated in Section 2.2.6 during simulations, the shape of the overall spectra provides information about the distribution of the velocities within the measured area. The red experimental spectra were fitted with results from simulations performed for the distribution of velocities within  $0.9\ \text{m/s}$  to  $1.65\ \text{m/s}$ , the orange spectrum corresponds to velocities in the range of  $0.65\ \text{m/s}$  to  $0.85\ \text{m/s}$ , and the turquoise spectrum corresponds to velocities within  $1.1\ \text{m/s}$  to  $1.4\ \text{m/s}$ . These spectra were chosen for demonstration as they represent the spectra collected from the centre of the fluid channel (red), from the point after the centre of the fluid close to the laser (green and orange) and from the point before the centre of the fluid further from the laser (turquoise). All simulations were obtained for velocities range with the precision of  $0.05\ \text{m/s}$  for the presented spectra.

As soon as the laser light focus point was shifted outside the fluid the behaviour of the spectra changed, see spectra starting from the pink one in Fig. 4.12 (a). All presented spectra still have a peak at a frequency of  $600\ \text{kHz}$ . However, the second peak has a higher amplitude. This can be extracted from the data by fitting it to a Gaussian function, centred around  $450\ \text{kHz}$ . Both frequencies are shown by dotted lines to help display the results. All the obtained data have peaks at around both frequencies, given that a majority of the light was scattered off particles with a velocity corresponding

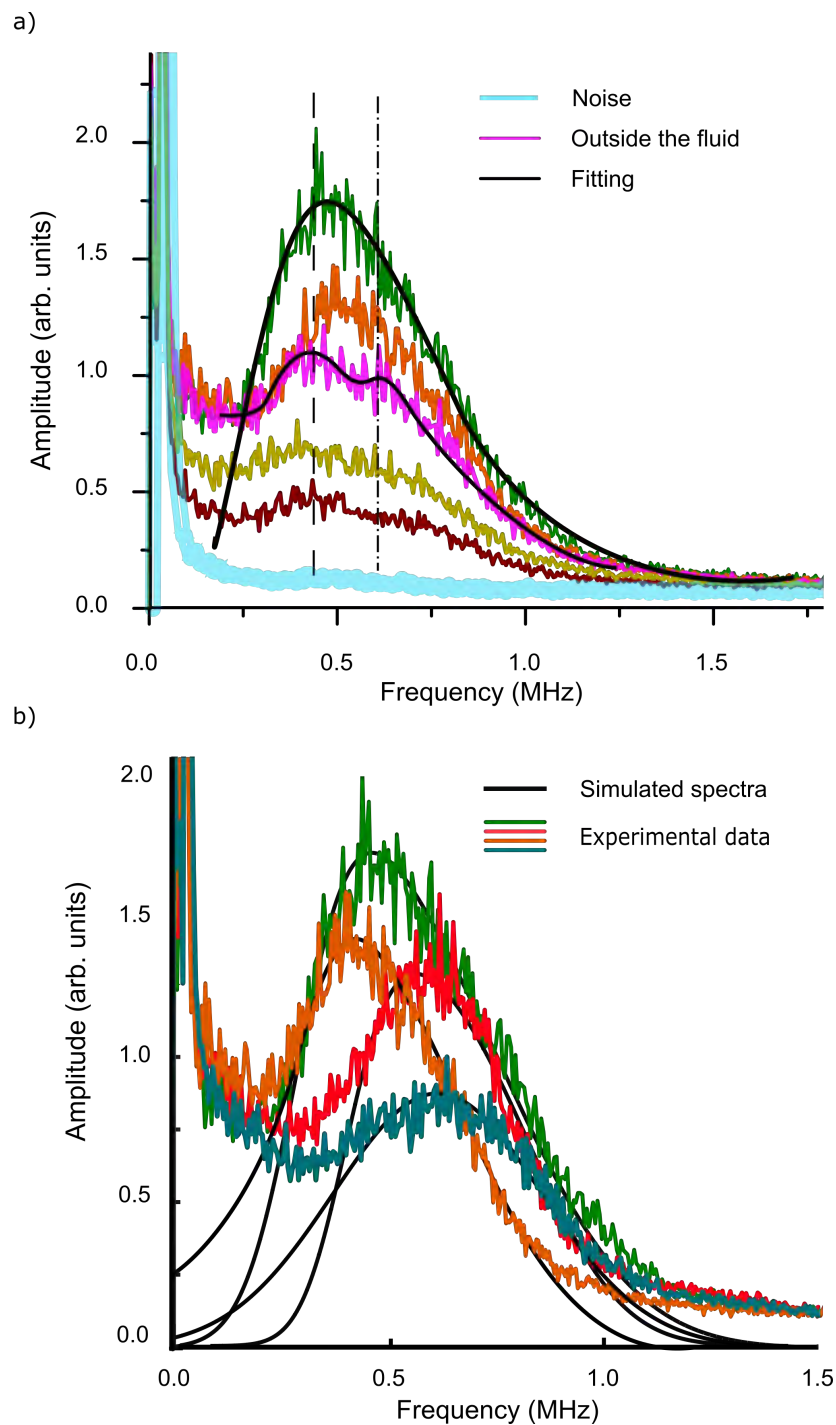


FIGURE 4.12: (a) Enlarged overall spectra for studying the focus point while measuring the velocity of the fluid when the laser was focused a fractionally before the centre of the channel, see Fig. 4.11 (b), the colours of curves have been preserved from the previous figure. The first black fitting line of the green spectrum shows the asymmetry of the obtained spectra when the light is focused outside the centre of the fluid channel. The second black line of the pink spectrum shows that spectra have more than two peaks after being shifted outside the fluid channel. (b) The simulation of the spectrum to match the asymmetrical spectrum obtained during experiments.

to the 450 kHz frequency. Since smaller velocities produce higher amplitude spectra when all other conditions are identical, the conclusion may be drawn that the minimum velocity within the fluid corresponds to a peak of 450 kHz. At the same time, part of the laser light scatters off particles with the maximum velocity and these correspond to 600 kHz. The emergence of two peaks occurs because the majority of the light scatters off the edge of the fluid and the nature of the scattering process changes, which leads to the presence of two independent spectra from inside and outside the fluid channel added together.

Figure 4.10 shows the evolution of the spectra along the laser axis for a graphic representation of the experimental data. The explanations, which were given before, can be observed from the change of all spectra. When the focus point of the light moves along the fluid from the edge of the channel to the centre, the amplitude of the spectra increases and then decreases from the centre to the opposite edge. The experimental spectra obtained from the centre of the fluid channel are symmetrical. It is still possible to extract the velocity of the fluid even when the laser is not properly aligned with the centre of the fluid channel. The data were more easily retrieved when the laser light was focused in front of the fluid centre rather than behind it.

### 4.3.6 Angle Variation

The same set of experiments was performed when the laser was fixed at different angles: 70°, 60°, and 55°. The laser was shifted along the laser axis in 500  $\mu\text{m}$  steps. Figure 4.13 shows all spectra obtained during the experiments with angles of 70° and 60°; Fig. 4.14 is for an angle of 55°. The numbers demonstrate how far the laser focus point was moved from the centre of the fluid with the number 1 corresponding to the farthest point. The diagrams on the right side of each plot show the approximate locations of the focus point (red) for each number within the fluid core (blue). The colour intensity within the fluid shows the change in the magnitude of the velocity of the particles. The deformations of the circles demonstrate that the optical path for the laser light varies when it is turned at different angles. As it was with previous experiments, the laser was firstly focused behind the centre of the fluid, and then the laser focus point was moved towards the centre and, subsequently, in front of it. The amplitude of the spectra increases with each step up to the point where the laser was focused onto the centre of the fluid, and it decreases henceforth. Taking into account the previously shown results for an angle of 80°, the following conclusions can be made. The amplitudes of the spectra, which correspond to focusing the light at the centre of the fluid, decreases with the angle. Moreover, the range within which the laser focus point can be moved decreases as well. When the angle was fixed at 80°, the laser was moved all together within more than 2 cm. In the case of 70°, 60°, and 55°, the laser could be moved within a range of 4 mm, 3 mm, and 1 mm respectively.

A possible explanation for this is the following. When the angle is smaller than 90°, the smaller this angle the longer the light path becomes along which light scattering

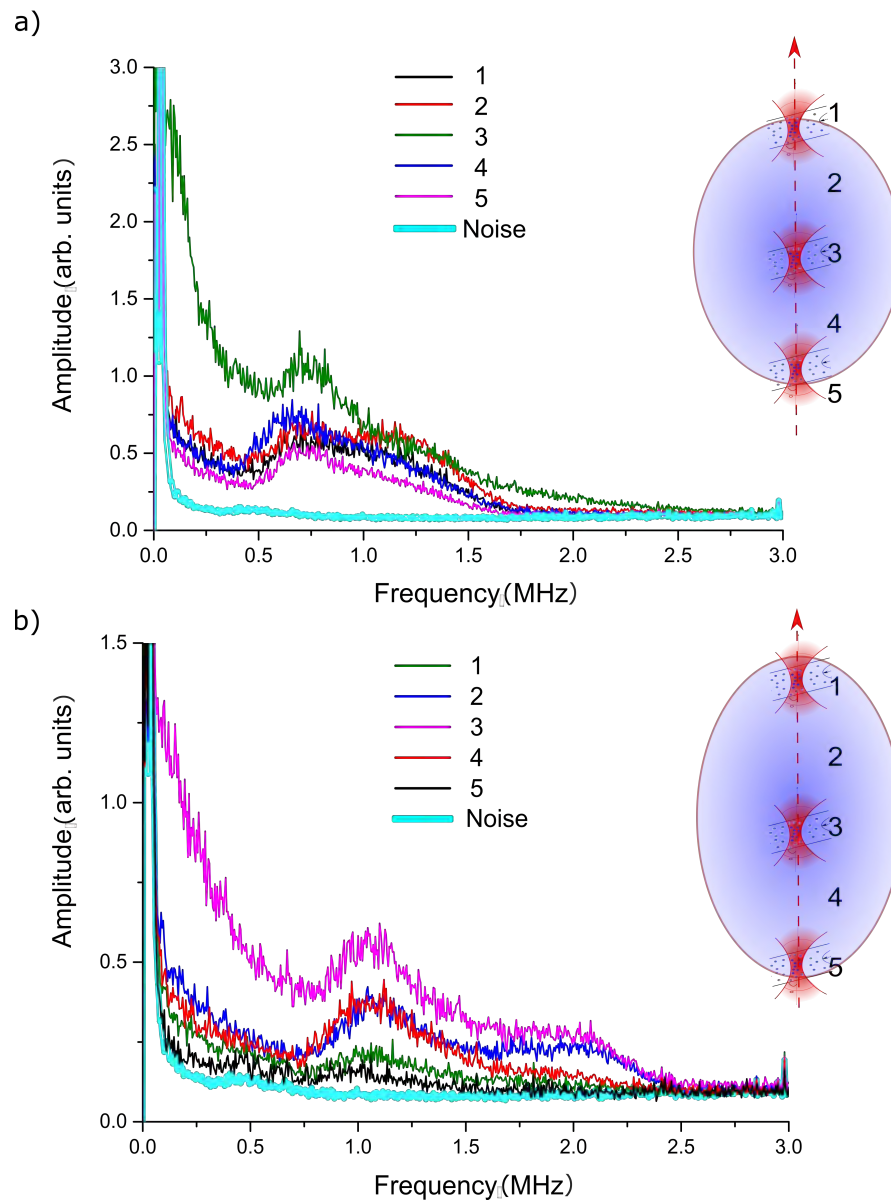


FIGURE 4.13: The obtained spectra when varying the point of the laser light focus for different angles a)  $70^\circ$ , b)  $60^\circ$ . For both cases, the first point where the laser light was focused lies behind the centre of the fluid channel, and after it was moved along the laser axis towards the centre and in front of it. The light-blue thick line represents the noise within the SM system. The numbering of the data corresponds to the areas of focus (red) on the diagrams of the fluid (blue) on the right side of the figures. It allows the evolution of the spectra to be observed in details. The spectrum number 3 should be approximately at the centre of the fluid channel.

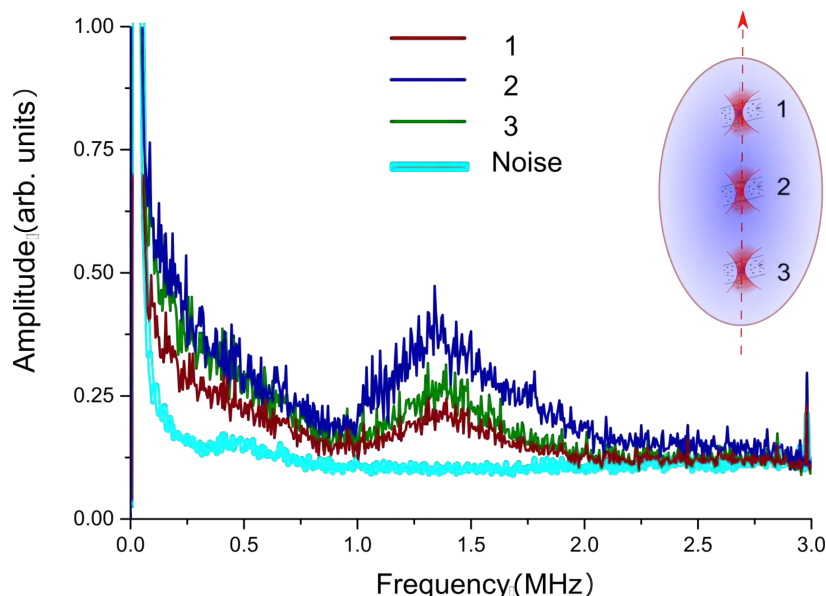


FIGURE 4.14: The obtained spectra for a fixed angle of  $55^\circ$  when varying the point of the laser light focus are presented by different colours. The light-blue thick line represents the noise within the SM system. The numbers demonstrate how far the laser focus point was moved from the centre of the fluid. The diagram demonstrates the approximate locations of the focus point (red) for each number within the fluid core (blue) with the number 1 located at farthest point from the laser. The colour intensity within the fluid shows the change in the magnitude of the velocity of the particles. The arrow shows the direction of the laser light. The spectrum number 2 should be approximately at the centre of the fluid.

TABLE 4.1: Results of the theoretically calculated frequency and measured frequency based on the velocity value of 1.654 m/s.

Angle	$0^\circ$	$80^\circ$	$70^\circ$	$60^\circ$	$55^\circ$
Maximum calculated frequency, MHz	5.1	0.9	1.7	2.5	2.9
Obtained maximum frequency, MHz	–	0.6	1.1	1.8	1.9
Second peak, MHz	–	0.45	0.7	1.1	1.4

occurs. As a result, less light scatters off the centre of the fluid and the peak broadens. The spectra appear to have a plateau towards higher frequencies, see Fig. 4.13 and 4.14. It was only possible to obtain a significant data-set at an angle of  $80^\circ$ . However, all spectra can be fitted with spectra functions. Table 4.1 presents the results. It includes the calculated frequency, which is based on the pump rate (0.22 mL/min) and the size of the nozzle (0.84 mm radius) for different angles. The maximum velocity was expected to be equal to 1.654 m/s, see the distribution of the fluid velocities within the fluid channel for different distance from the centre in Fig. 4.9 (b). The second part of the table provides two peak frequencies that are obtained through fitting for each angle. The measured frequencies are found to be within 5% of the calculated frequencies.

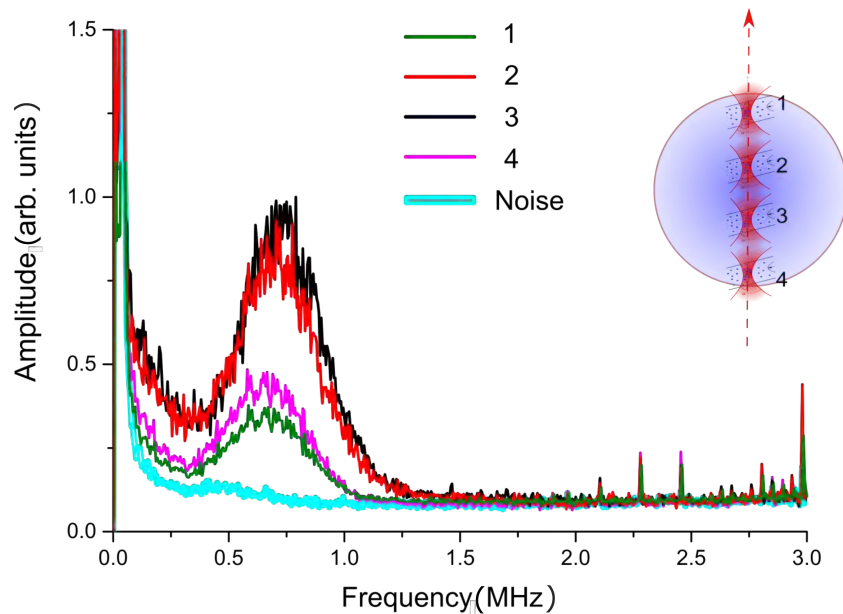


FIGURE 4.15: The obtained spectra when varying the point of the laser light focus for water without seeders at an angle of  $80^\circ$ . The light-blue thick line represents the noise coming from the laser. The numbers demonstrate how far the laser focus point was moved from the centre of the fluid. Focus point number 1 was located at the farthest point from the laser. The diagrams on the right side shows the approximate locations of the focus point (red) for each number within the fluid core (blue). The colour intensity within the fluid shows the change in magnitude of the velocity of the particles. The arrow shows the direction of the laser light. The deformations of the circles demonstrates that the optical path of the laser light varies when it turned at different angle. The spectra number 2 and 3 are obtained near the centre of the fluid.

#### 4.3.7 Water without Seeders

After adjusting the set-up to the best possible location, i.e. with highest amplitude spectra, measurements with clean water were also performed. The angle between the laser light and the fluid was fixed at  $80^\circ$ . Figure 4.15 shows the spectra, which were obtained along the axis in 200 nm steps. They can be compared with spectra obtained in the same geometry for the seeded water, see Fig. 4.11. The obtained spectra can be fit with a Gaussian functions, and the peaks are in the range of 680 - 710 kHz. Even small variations of the angle between  $79^\circ$  and  $80^\circ$  lead to the expected frequency in the range of 660 - 720 kHz.

#### 4.3.8 Flow Velocity Profile Measurements and Resolution Discussion

Based on the obtained results from the experiments, the velocity profile can be obtained with  $\mu\text{m}$  resolution. To measure the velocity profile, the scanning was done across the water channel and the laser focus point was moved in 100  $\mu\text{m}$  steps. The depth of the focus can give an estimation of the sensing volume, and can be calculated according to Eq. 2.25, and for the experimental condition, it is equal to approximately 6 mm, which is much larger than the flow channel width. That means all velocities within the flow channel should exist in the frequency domain of the SM signal. However, the moving

of the focus point with 100  $\mu\text{m}$  steps changed the profile of the spectra. Moreover, none of the profiles exhibited the flat profile which is expected to be obtained in the case of the velocity values changing from zero towards the maximum. Signals collected from the centre of the fluid channel produce spectra with a Gaussian peak, while other points within and outside of the fluid channel exhibit asymmetrical spectra of signals, i.e. signals have different shapes when collected from different points. This indicated that signal processing has to be adapted for each point where the signal is collected from. Taking into account that the sensing length in the direction of the laser axis is much higher than the fluid channel, the effective signal, which changes the shape of the SM spectra, appears from a laser light beam waist of 35  $\mu\text{m}$ . Moreover, when the light propagates inside the fluid, the path is less compared to the laser light in the air due to refraction according to  $d_{water} = n_{water} \cdot d_{air} / (2 \cos(n_{water}\alpha)) \approx 0.67 \cdot d_{air}$ . The following conclusions can be drawn:

- The point of collection of the signal should be used for analysing the signals. The shape of the SM spectra defines the distribution of the velocity and has to be taken into account for the calculation.
- The particles on the path of the laser light can be backscattered and cause the change of the signal spectra even if they are not in the focus.
- The SM spectra shapes vary for different points of data collection hence not all particles are participating in the production of the spectra with the biggest amount of backscattered light appearing from the focus point.
- When the signal was collected close to the fluid edges, it had a wider velocity distribution compared to the centre point, where the velocity profile is symmetrical, see Fig. 4.4 (a).
- The spatial resolution of the obtained results is lower than the step of the laser movement or the size of the focus point due to influence from different particles.
- With decreased angle, the laser light is focused on the particles with a larger distribution of velocities. Moreover, the light has a longer path inside the flow causing a higher contribution from the sensing area hence further reducing the resolution of the result as well.

The distribution of the velocity within the same light path is bigger for points which are close to the edge and smaller when the light is focused in the centre of the fluid. However, the simulation has shown that the obtained spectra correspond to higher velocities distribution than expected if the light scatters off only the particles within the focus point. For example, the green and red spectra from Fig. 4.12 correspond to the light path of 400  $\mu\text{m}$ , while the orange and turquoise spectra were obtained for the velocity distribution which fits within 100  $\mu\text{m}$ . The overlapping of the measured velocity distribution obtained from the simulation results using Eq. 2.19 allows the velocity profile to be reconstructed based on the experiments presented in previous sections with high resolution.

## 4.4 On the Properties of Spectra from an SM Sensor

When the experiments with solid targets were performed, the obtained spectra of the SM signals allowed the velocity to be calculated from the Doppler shift, which appeared as a clear peak in the spectra. Experimental results demonstrated the influence of different parameters of the experiments, such as the broadening of the spectra and the changing of the amplitude of the spectra depending on angle, the focus point and the velocity value. The peak was still easy to identify and to verify with a reference value. When the target was changed to fluids, the experimental results were far from what was obtained for solid targets. The initial goal of the thesis was to study the limitation of the SM method with the aim to achieve it and to improve the maximum velocity which can be obtained using the SM sensor. From a theoretical point of view, the SM sensor should allow high velocity measurements to be measured. The limitations of which were found in this thesis to be coming from the electronics and from the bandwidth of the detecting system, see Chapter 3 for details. However, the experiments with fluids showed new challenges first in getting enough signal, and then with analysing the results. The literature review on the fluid characterisation using the SM sensor has revealed the confusion when explaining the spectra obtained from fluids. In particular, 1) the spectra did not have a clear peak and instead it was a wide peak; 2) the peak was not correlated to the reference velocity and had some shift; 3) the shapes of the spectra were not symmetrical anymore, and they varied a lot depending on the condition of the experiments.

It was found that the SM sensor performance when applied to fluids was studied by several groups all over the world, and generally there were three approaches to explain the results:

1. The groups from Japan [70, 127] used the SM sensor for studying the dynamics of small particles aiming at a biological object. When the fluid spectra were obtained, they were assumed to be Gaussian with a peak related to the Doppler shifts. However, the group found that the reference frequency was larger than the one obtained in the experiments. They found the correlation parameter to be the same for the same set of experiments, so they used it as a calibration coefficient. The explanation [70, 127] of the shift of the spectra was that the observed spectra is the summation of the spectra corresponding to different velocities within the fluid channel.

2. The group from Italy calculated [64] the Doppler spectra specifically for the parabolic velocity profile when the velocity varies from zero to the maximal value. They calculated the impinging power on the PD assuming one ray of light passing through the optical laser system (leading to scatters behaving as a medium with linear scatter density). The resulting calculated spectra demonstrated a reduction and broadening with increasing pump speed. Their experimental result for velocities of 22 mm/s and 100 mm/s corresponded to the symmetrical shapes of the calculated spectra. They presented [64] several experimentally obtained spectra for fluid velocities of 110 m/s and 165 mm/s, which agreed with reference velocities, however, the shapes of the spectra

were asymmetrical and there was no study of the influence of the angle on the broadening of the spectra.

3. An Australian group published their study [56] of the SM sensor spectra applying studies, which were performed in 1971 by Estes [107], on the scattering of light from a rough rotating target when the laser light was shone perpendicular to the surface. Estes [107] has shown the influence of the velocity on the spectra and found them to broaden with increasing velocity. Prior to the theoretical investigation, experiments were performed to study the broadening of the spectra depending on the angle for the rotating disc. It was found [56] that the peak of the frequency shift is proportional to the sine of the incident angle while the broadening of the peak is proportional to the cosine in the geometry presented in the paper. The appearance of the cosine dependence has been explained based on the shift of the random phase variation due to the roughness of the surface.

In Chapter 2 for developing the theory, a generalisation of the work done by Estes [107] was obtained without the assumption of perpendicularity of the laser light beam with respect to the target. Afterwards, the idea of the Japanese group about summation of all spectra was used on the result (see discussion in Chapter 2 on that matter), and the integral was written. As it was shown, the mathematical equivalent of the summation of spectra is the integration of Eq. 3.4 over the distribution of velocities  $\Delta v$  within the measured area and over the intensity of the laser spot  $\Delta w_0$  within it. If the velocity is changing from  $v_1$  to  $v_2$ , and the waist of the beam is assumed to be constant, the integral can be written as:

$$I(\omega) = \int_{v_1}^{v_2} I(\omega, v) dv,$$

where:

$$I(\omega, v) = I_0 \frac{1}{v \sin \alpha w_0} \exp \left( - \frac{(\omega - 2v \cos \alpha / \lambda)^2}{2(v \sin \alpha)^2 / w_0^2} \right). \quad (4.1)$$

This integral can be solved, however, the analytical expression contains the error function, and hence is difficult to evaluate. When the target can be characterised with a velocity distribution, the mathematical model shows that the maximal point does not correspond to the maximal velocity. The experimental results which are presented in this thesis and by other groups have demonstrated the same effect. According to Fermat's theorem [128], the local extremum of a differentiable function occurs where its first derivative is equal to zero:

$$I'_\omega(\omega_{max}) = \frac{d}{d\omega} \int_{v_1}^{v_2} I(\omega, v) dv = 0.$$

According to the Leibniz integral rule [128], the function can be differentiated under the integral sign as:

$$\frac{d}{dx} \int_{u(x)}^{v(x)} f(x, t) dt = f(x, v(x)) \frac{dv}{dx} - f(x, u(x)) \frac{du}{dx} + \int_{u(x)}^{v(x)} \frac{\partial f(x, t)}{\partial x} dt.$$

In this case, the integral limits  $v_1$  and  $v_2$  of the spectrum integral are independent of frequency, hence first and second terms are equal to zero, leading to:

$$\frac{d}{d\omega} \int_{v_1}^{v_2} I(\omega, v) dv = \int_{v_1}^{v_2} \frac{\partial I(\omega, v)}{\partial \omega} dv.$$

Let function  $I(\omega, v)$  from Eq. 4.1 be written as:

$$I(\omega, v) = \frac{a}{v} \exp\left(-\left(\frac{\omega - bv}{cv}\right)^2\right).$$

Let  $1/x = v$ , then  $dv = -1/x^2 dx$  and

$$I(\omega, v) = ax \exp\left(-\left(\frac{\omega x}{c} - \frac{b}{c}\right)^2\right).$$

Then the differentiation of the function is as follows:

$$\begin{aligned} \int_{v_1}^{v_2} \frac{\partial I(\omega, v)}{\partial \omega} dv &= \int_{x_1}^{x_2} 2ax \left(\frac{\omega x}{c} - \frac{b}{c}\right) \frac{x}{c} \frac{1}{x^2} \exp\left(-\left(\frac{\omega x}{c} - \frac{b}{c}\right)^2\right) dx = \\ &= \int_{x_1}^{x_2} \frac{2a}{c} \left(\frac{\omega x}{c} - \frac{b}{c}\right) \exp\left(-\left(\frac{\omega x}{c} - \frac{b}{c}\right)^2\right) dx. \end{aligned} \quad (4.2)$$

This integral has a solution, which is:

$$\begin{aligned} \int_{x_1}^{x_2} \frac{2a}{c} \left(\frac{\omega x}{c} - \frac{b}{c}\right) \exp\left(-\left(\frac{\omega x}{c} - \frac{b}{c}\right)^2\right) dx &= \frac{c}{\omega} \exp\left(-\left(\frac{\omega x}{c} - \frac{b}{c}\right)^2\right) \Big|_{x_1}^{x_2} = \\ &= \frac{c}{\omega} \left[ \exp\left(-\left(\frac{\omega x_2}{c} - \frac{b}{c}\right)^2\right) - \exp\left(-\left(\frac{\omega x_1}{c} - \frac{b}{c}\right)^2\right) \right]. \end{aligned} \quad (4.3)$$

Then for  $I'(\omega_{max}) = 0$  and for  $v_1$  and  $v_2$ :

$$0 = \frac{c}{\omega_{max}} \left[ \exp\left(-\left(\frac{\omega_{max} \frac{1}{v_2}}{c} - \frac{b}{c}\right)^2\right) - \exp\left(-\left(\frac{\omega_{max} \frac{1}{v_1}}{c} - \frac{b}{c}\right)^2\right) \right].$$

This leads to:

$$\left| \frac{\omega_{max} \frac{1}{v_2}}{c} - \frac{b}{c} \right| = \left| \frac{\omega_{max} \frac{1}{v_1}}{c} - \frac{b}{c} \right|.$$

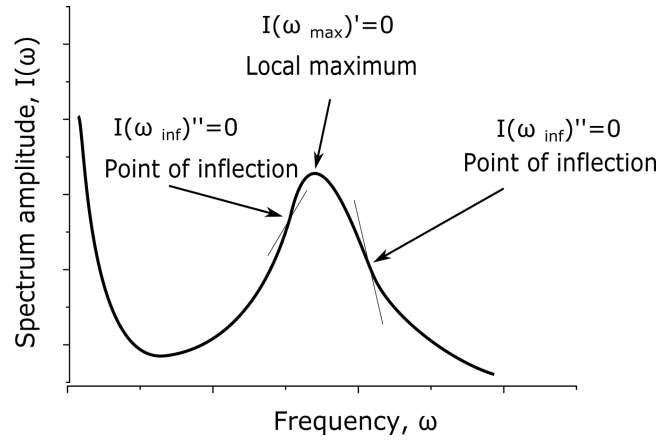


FIGURE 4.16: The points of maximum and inflection on the function similar to one obtained from SM sensor

The first solution is trivial and is  $v_1 = v_2$ , and the second one is:

$$\frac{\omega_{max} \frac{1}{v_2} - \frac{b}{c}}{c} = - \left( \frac{\omega_{max} \frac{1}{v_1} - \frac{b}{c}}{c} \right),$$

$$\omega_{max} \left( \frac{1}{v_1} + \frac{1}{v_2} \right) = 2b,$$

$$\omega_{max} = \frac{2bv_1v_2}{v_1 + v_2}. \quad (4.4)$$

If the velocity distribution is close to a delta function, then Eq. 4.4 leads to the peak of the spectrum at the point  $bv$ , which is as expected. In the general case, Eq. 4.4 allows the maximum velocity to be found if the minimal velocity is known and the spectra is obtained, and vice versa.

The additional equation for the solving the velocity distribution can be found from the point of inflection of a differentiable function which can be found where its second derivative is equal to zero [128]. The point of inflection of the function is the point where the curvature of the function changes, see Fig. 4.16.

The same equation can be used for the analytical solution, applying the Leibniz rule:

$$I''_{\omega}(\omega_{inf}) = 0,$$

$$\frac{d^2}{d\omega^2} \int_{v_1}^{v_2} I(\omega, v) dv = \frac{d}{d\omega} \int_{v_1}^{v_2} \frac{\partial I(\omega, v)}{\partial \omega} dv.$$

Using the answer to the solution of the integral according to Eq. 4.3, and differentiating it by  $\omega$ , the result can be written as:

$$\frac{d}{d\omega} \left( \frac{c}{\omega} \left[ \exp \left( - \left( \frac{\omega}{v_2 c} - \frac{b}{c} \right)^2 \right) - \exp \left( - \left( \frac{\omega}{v_1 c} - \frac{b}{c} \right)^2 \right) \right] \right) =$$

$$\begin{aligned}
&= \exp\left(-\left(\frac{\omega}{v_2 c} - \frac{b}{c}\right)^2\right) \left[-\frac{c}{\omega^2} - \frac{c}{\omega} \frac{2}{c v_2} \left(\frac{\omega}{v_2 c} - \frac{b}{c}\right)\right] - \\
&- \exp\left(-\left(\frac{\omega}{v_1 c} - \frac{b}{c}\right)^2\right) \left[-\frac{c}{\omega^2} - \frac{c}{\omega} \frac{2}{c v_1} \left(\frac{\omega}{v_1 c} - \frac{b}{c}\right)\right].
\end{aligned}$$

This function in the point of inflection is equal to zero. Assuming that the experimental data can easily provide the two frequencies: the frequency of the peak,  $\omega_{max}$ , and the frequency at which the direction of the curvature changes,  $\omega_{inf}$ , on the right slope of spectrum function, then the system of two unknowns can be solved and  $v_1$  and  $v_2$  to be found:

$$\begin{cases} \omega_{max} = \frac{2bv_1v_2}{v_1 + v_2}, \\ \exp\left(-\left(\frac{\omega_{inf}}{v_1 c} - \frac{b}{c}\right)^2\right) \left[-\frac{c}{\omega_{inf}^2} - \frac{c}{\omega_{inf}} \frac{2}{c v_1} \left(\frac{\omega_{inf}}{v_1 c} - \frac{b}{c}\right)\right] - \\ - \exp\left(-\left(\frac{\omega_{inf}}{v_2 c} - \frac{b}{c}\right)^2\right) \left[-\frac{c}{\omega_{inf}^2} - \frac{c}{\omega_{inf}} \frac{2}{c v_2} \left(\frac{\omega_{inf}}{v_2 c} - \frac{b}{c}\right)\right] = 0. \end{cases} \quad (4.5)$$

This system allows the values of  $v_1$  and  $v_2$  to be found. Since the values  $v_1$  and  $v_2$  are positive and  $v_2$  is larger than  $v_1$ , from the first equation it can be found that the initial velocity belongs to the interval of  $\left[\frac{\omega_{max}}{2b}; \frac{\omega_{max}}{b}\right]$ , which allows the numerical solution of the second equation from the system 4.5 to be obtained faster and in the correct range. Generally, the second equation can have multiple solutions depending on the parameter  $\omega_{inf}$ . This system of equations was tested on simulated spectra and on experimental data. This system can be solved with one  $\omega_{inf}$  corresponding to the right side of the spectrum, see Fig 4.16. However, this value can be found only with a certain accuracy, and it is much more ambiguous compared to  $\omega_{max}$ . The second point of inflection allows the initial and maximal velocity to be checked and to be defined more accurately.

An example of a solution is presented for one of the functions from Fig. 4.12 presented by the green curve. This example is shown as a typical way of how the system can be solved and as a demonstration of the developed theory. This function can be characterised with the following parameters:  $\omega_{max} = 460$  kHz,  $\omega_{inf} = 700$  kHz and 250 kHz, though the point of inflection for frequencies bigger than the frequency of the peak is more straightforward to define. The second equation can be solved analytically. The left part of the second equation can be presented as the function with  $v_1$  as a variable. The value of  $v_2$  can be calculated from the first equation of the system 4.5, and values of other parameters,  $b$  and  $c$ , of the function can be found from the known parameters of the experiment (an angle, a wavelength, a waist of the beam, etc.). The function from the second equation is plotted for known parameters with  $v_1$  as a variable and then value of  $v_1$  is found when the function crosses the zero axis. Figure 4.17 shows two functions for  $\omega_{inf} > \omega_{max}$ , 700 kHz, and  $\omega_{inf} < \omega_{max}$ , 250 kHz, shown by green and blue lines respectively, each of which has more than one solution (six and four solutions respectively) which can be found from functions crossing the zero axis shown by an orange

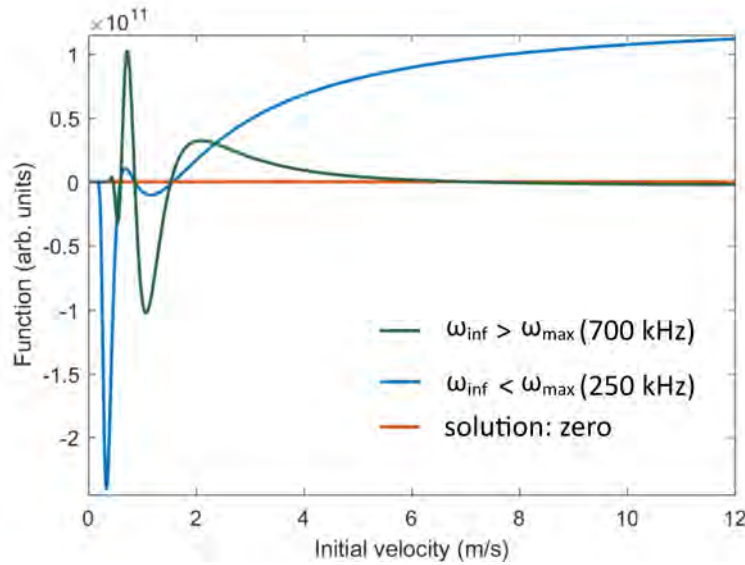


FIGURE 4.17: The numerical solution of the system of the equations 4.5 for experimental data when two point of inflection were used for verifying the solutions, which are presented by blue ( $\omega_{inf} > \omega_{max}$ ) and green ( $\omega_{inf} < \omega_{max}$ ) lines. The orange line represents the solution of the equation, i.e. when the function crosses zero. The limitation of the possible values of the velocities were not included in order to demonstrate the behaviour of the function.

line. Figure 4.18 demonstrates the behaviour of these functions for the initial velocity within the interval of  $[\frac{\omega_{max}}{2b}; \frac{\omega_{max}}{b}]$ . Both functions cross the zero axis in two points where both of them corresponds to the same velocities. As it was mentioned before, only one of the solution is enough for the defining of  $v_1$  and  $v_2$ . However, the numerical solution for both points of inflection is shown with a green line for  $\omega_{inf}$  = of 700 kHz and a blue line for 250 kHz. When the solutions were studied more closely, the solution at point A, see Fig. 4.18, is a trivial one  $v_1 = v_2$  and it always exists. The function, which corresponds to the inflection point at the frequency less than  $\omega_{max}$ , crosses the zero axis in only two points, and hence the point B is the only solution of the equation. However, it might be easier to find another inflection point, which corresponds to  $\omega_{inf} > \omega_{max}$ . In such a case, point C is the solution as well. This point corresponds to  $v_1$  and  $v_2$  being equal to 0.56 m/s and 7.05 m/s, respectively. In the case presented here, the second function (blue line) demonstrates that the true solution for this system of equations is at the point C. Figure 4.18 (b) shows the enlarged plots around point C. The solution for  $v_1$  and  $v_2$  is around 0.595 m/s and 1.53 m/s, respectively, which was the case for the experiments. The solution for the point C could be the true solution when the spectrum looks like a plateau due to its wide range of velocities.

The solution of this equations has been used for analysing the experimental data, and has demonstrated an excellent performance with independent referencing using additional properties of the obtained overall spectra of SM signal. The system of equations 4.5 allows the velocity range to be calculated with a high precision.

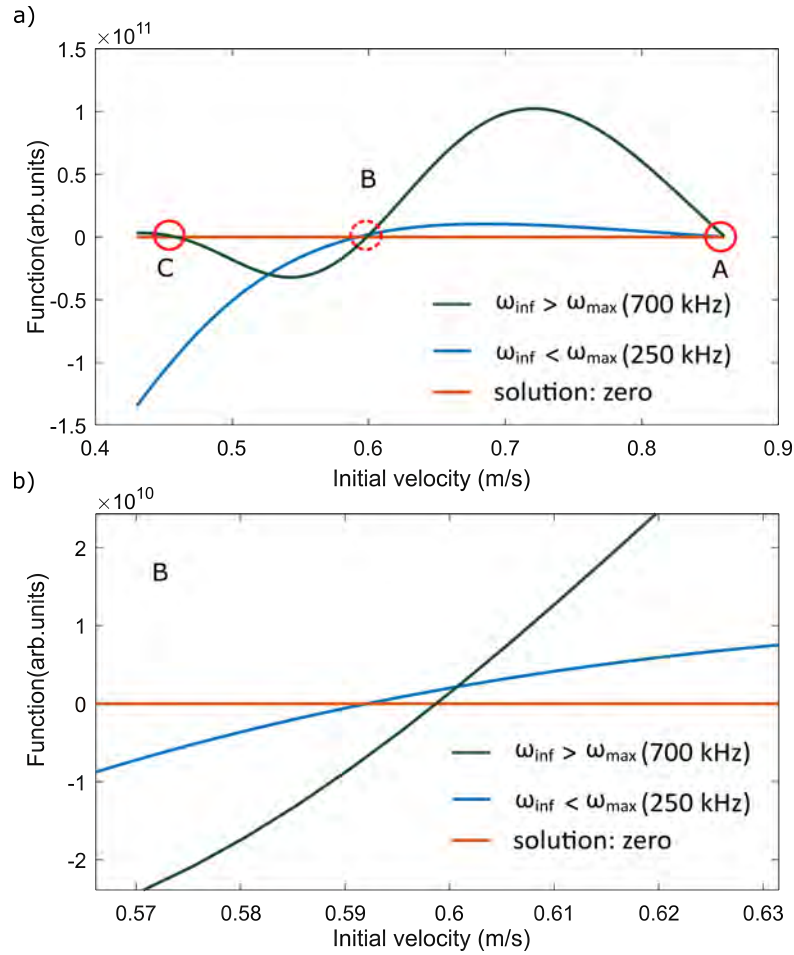


FIGURE 4.18: (a) The numerical solution of the system of the equations 4.5 for one of the experiments within the minimal velocity interval of  $[\frac{\omega_{max}}{2b}; \frac{\omega_{max}}{b}]$  for the experimental data. Two point of inflection were used for verifying the solutions (crossing with orange line representing zero), which are presented by blue ( $\omega_{inf} > \omega_{max}$ ) and green ( $\omega_{inf} < \omega_{max}$ ) lines. Points A, B and C represent the solution of the equations, i.e. the point of function crossing the zero axis. (b) The enlarged function around point B is showing the true solution for the presented case.

## 4.5 Application in Accelerators

Measurements, presented in this chapter, have demonstrated the potential of the SM sensor when it is applied to fluids. The SM sensor allows for accurate rate measurements with the resolution that the laser can be moved at along the laser axis. From one measurement by SM sensor, the velocity range can be defined based on the overall collected spectrum of the signal. The task can be reversed, and the angle between the laser axis and the fluid can be identified.

Accurate and precise measurements of fluid rates by using a compact device can be useful for the flow rate characterisation of cooling water, which is used for heat removal from accelerator components, including accelerator structures [129], waveguide networks [130], klystron collectors and electrical towers [130, 131], Radio Frequency (RF) cavities [132, 133] and RF guns [134], solenoid coils [129] and bending magnets [130],

the injector cavity walls and RF couplers [135]. The cooling is essential for the main heater exchange towers [129], which are responsible for all cooling subsystems, as well as for electric heaters and power supplies [129–131]. The main challenge for currently used flow meters is their limited life-time and the requirement that they be installed inside coolant tubes, leading to difficulties in changing them when they break.

SM sensors can be used for measuring the velocities of liquid in an electrospray ion source which is produced by allowing liquid [136] to flow through a small needle at the tip of which is a high voltage gradient which disperses the liquid into electrically charged droplets. These droplets are then used as a mass analyser and for the mass spectroscopy of solids [137], liquids, and biomolecules [138]. The planar electrospray array of a liquid ion source [139] can be used for coating, printing and nanosatellite propulsion. The flow rate of liquids and droplets is important for the geometry of the resulting arrays and hence for the performance of the ion source itself. At present, the characterisation of velocities is based on indirect calculations [139].

Helium nanodroplet spectroscopy is widely used for bio-molecules spectroscopy and vibrational spectroscopy of metal clusters in water clusters at free electron Lasers [140]. The velocity of the fluid is crucial for its production as it defines not only the size of the droplets, but the collision energy, which is important for the spectroscopy [141]. The conventional velocity measurements are too complicated so the only way the information about the helium droplets velocity is found by solving the differential equations describing their behaviour or by additional photo-dissociation of the droplets using femto-second laser pulses [141]. An SM sensor is sensitive enough to detect the velocity of such droplets.

## 4.6 Conclusion

In this chapter, the application of an SM sensor for the measurements of fluid velocities was demonstrated and studied in detail. This includes the influence of different parameters on the experimentally obtained spectra of the measured SM signal. It was theoretically studied in Chapter 2 and experimentally for solid targets in Chapter 3. An experimental set-up was developed which allowed measurements to be compared with analytical and numerical solutions to verify and benchmark the SM velocimeter. The velocity of the fluid in the set-up can reach up to 3 m/s without entering the chaotic regime. The spectra were studied for different fluid velocities, scattering particles concentration, scattering particles size, particle types, laser focusing properties and angles between the laser axis and velocity vector. I have demonstrated that increasing the target velocity reduces the peak amplitude of the spectrum and at the same time broadens the frequency distribution. The concentration of the seeder particles allows the amount of scattered light to be controlled, and hence the amount of light coupled back into the laser cavity. The concentrations of scattering particles were tested in the range from 4% to clean water with small steps, as low as 0.03%, in order to study the parameters which

allow sufficient feedback and output signal to be achieved. Velocity measurements of clean water were obtained once the set-up was adjusted and all parameters are taken into account carefully. A range of particles of different sizes was studied: 10  $\mu\text{m}$ , 1  $\mu\text{m}$ , 150 nm, and 21 nm, and different particles such as milk and  $\text{TiO}_2$ . Even though the reflectivity properties of these two types of particles are similar, it has been shown that smaller  $\text{TiO}_2$  particles provide less feedback. Depending on the size, the amplitudes of the peak reach saturation level for certain concentrations. The spectral dependence on the location of the focus point within the fluid was found to be in agreement with the theory which was proposed in Chapter 2 regarding the shape of the obtained spectra depending on: 1) the focal point of the laser light; 2) the velocity distribution function; and 3) a number of seeders. It has been shown that, in the case of a fluid, the sensor works better for angles close to  $90^\circ$  due to the distribution of the velocities. Fluids, which were measured in this chapter, have a broader velocity distribution compared to solid targets (see Chapter 3) with a distribution close to a delta-function. The measured SM spectra contain frequencies from all velocities of particles the light scattered off, which leads to broader and non-symmetrical spectral shapes. The model of spectra, which I developed in Chapter 2, allows the precise distribution of the velocities to be included and simulated when fitting the experimental data, and hence the velocity distribution can be found based on this. The velocity measurements from the overlap of different fluid regions allow the velocity range to be found based on one single measurement with a precision of better than 0.05 m/s for the measurements of high velocities presented in this chapter. The SM sensor has demonstrated the ability to measure the velocities of pure water, however, a better and clearer signal was obtained for high seeder concentrations. In this chapter, the laser velocimeter has provided detailed information about the velocity and density of liquids, with a spatial resolution of less than 35  $\mu\text{m}$  (the waist size of the laser used in this chapter). The experiments allowed the velocities of fluids up to 1.65 m/s to be measured, compared to only 30 cm/s achieved elsewhere [66].

In this chapter, I have derived the analytical solutions for matching the parameters of the experiments, which allow independent calculations of the range of velocities to be performed based on two points of the overall spectra obtained during the experiments: the frequencies corresponding to 1) the peak of the spectrum, and 2) the point of inflection. The system of equations, linking these two frequencies with the velocity range, has been obtained, and its numerical solution provides accurate values of the velocities. This solution has never been obtained before. Previously, the empirical fitting was done for each separate experimental data leading to a rather difficult analysis of experiments. The studies and measurements in this chapter have demonstrated the application and usage of the SM sensor for velocities with a much higher range and magnitude compared with results currently presented in the literature. Finally, some potential applications of the technique to the field of accelerator physics were introduced. The verification of the SM sensor for the fluid case was essential before considering the application of the technique to other targets such as gases or plasmas.



## Chapter 5

# Gas Jets in Accelerators and Their Characterisation

The application of gas jets in accelerators is presented in this chapter. Possible existing methods for gas jets characterisation demonstrate that new compact sensors are required for non-invasive velocity and density measurements of gas jets. The application of the gas jet to beam instrumentation is one of the areas where such sensors can be beneficial. This chapter includes possible SM system integration into a gas jet set-up together with calculation of the expected level of backscattered light for the SM sensor when it is applied to gases. The application of the SM sensor for gas characterisation in accelerators concludes the chapter.

### 5.1 Gas Jets

#### 5.1.1 Gas Jets: Basic Definitions

A gas jet is formed when a gas flows from a region with a high pressure to a region with a lower pressure through an aperture. This aperture is usually referred to as a *nozzle*. The process of forming the gas jet is called *gas expansion*. The gas jet has a number of properties which makes it suitable for various applications. Basic quantities used in this chapter are as follows [142].

*Type of flow.* In fluid dynamics, a flow can be formed in two main regimes. The *continuous regime* of the flow consists of relatively high densities of particles, collisions between which occur frequently enough for the flow to have a collective pressure and temperature. In the case of a *molecular flow*, each molecule is isolated, and all molecules within the flow are treated individually. In both cases, the elementary constituent of the flow is referred to as a *particle*, which is a volume element of a flow for a continuous regime and an individual molecule for a molecular flow.

*Mach Number  $M$ .* A pressure perturbation, or a sound wave, within a fluid travels at the speed of sound. For ideal gases, the speed of sound within the flow can be derived from kinetic theory. For real gases, the pressure and density of the gas also influence the

speed of sound. Particle velocity of a gas jet is usually characterised by the dimensionless Mach number  $M$ , which is a ratio of the velocity of a particle to the speed of sound for a specific gas at the local temperature. The dynamics of the flow varies for the different geometries in which it is formed, which are usually defined by the nozzle. The behaviour of the flow varies when it is subsonic  $M < 1$  or supersonic  $M > 1$ . A supercritical gas jet has a pressure and a temperature higher than its critical pressure and temperature.

*Gas jet shaping.* The property of the gas jet includes its density, which defines its shape. Depending on the difference in pressure when a gas jet is formed, the jet can achieve various densities while expanding. Various types of nozzles can be used for the collimation of the gas jets to achieve certain speeds and density profiles, which can then be used in a number of applications. For example, when a gas expands from a conical-shape nozzle, it forms with a “pencil-like” distribution of gas density, and such gas jets are used for atomic physics and for beam instrumentation. The “sheet-like” gas jet is extracted by means of nozzles comprised of several slits; such jets can be used for beam instrumentation as well as for laser-plasma acceleration. Gas cells are usually closed volumes which contain a gas and the experiments are done inside that cell. The products of the experiments are then studied, by looking into the gas jet expanding from this cell via a nozzle. An example of the formation of a sheet-like gas jet as well as how the gas jets are in use in accelerator-related facilities are presented later.

*Gas jet characterisation.* Gas jets as gaseous targets with special characteristics of density and speed have been widely used in science and technology. The unique properties of gas jets, such as low internal temperature and high directionality allow for gas jets to be used in molecular spectroscopy [143], nuclear fusion [144] and atomic physics [145, 146]. In these areas, the constant velocity and density distribution of the gaseous target is a vital parameter for the best research performance and results. The characterisation of gas jets is crucial for their implementation at accelerator facilities. The properties of gas jets can be measured using different techniques or sensors to provide required information. Gas jets in particle accelerators have very special demanding conditions on the diagnostics (low density and non invasiveness) which massive, high density jets for aircraft, for example, do not have. For the optimal usage and verification of the properties of the gas jets, they should be characterised with high accuracy, in particular with regards to their velocity and density profile. In these applications, gas jet velocities can be up to 2,000 m/s and inhomogeneously distributed across the jet. It is desirable to have a technique or a sensor which can be easily integrated into an existing set-up with minimum additional optical components.

Many techniques for measuring supersonic flows have been proposed ranging from mechanical [147–152], acoustic [153] and optical [2, 4, 6, 9, 154–162] ones, see Appendix A for the complete description and the review on currently used methods. When judging a method its range of application (low or high pressure), its precision, the complexity of the set-up, and the level of flow disruption (invasive or non-destructive methods) have to be considered. However, all currently used methods for such a characterisation are

either not reliable or require a powerful laser system. For this, all sorts of expensive, complicated, and large mechanical apparatuses are used, which cannot be installed in accelerators (especially future very small laser-based accelerators), therefore research into the area of new and compact methods has yet to be done. Even though, within the available optical techniques many different tools for visualisation and characterisation of the gas flows exist, accelerator facilities require techniques which can be used in a harsh environment, so it is not simply a matter of using any of the techniques mentioned earlier. Typical ways of observing and visualising gas flows are rather complicated and usually demand additional equipment and substantial changes to the set-up where the gas jet is used or produced. As a result, at accelerator facilities where gas jets are used, the combination of various techniques have been applied to measure the properties of gas jets, instead of only one sensor.

### 5.1.2 Application of Gas Jets in Accelerators

The areas where gas jets can have applications range from laser acceleration to airplane jet engines. What follows is a review of some of the applications more relevant to low density jet (less than one bar), with a defined density profile. Gas targets are an important tool with unique properties, such as low internal temperatures with high directionality, which make them beneficial for a number of accelerator based experiments. Gas jets are used for many purposes at accelerator facilities. Prior to using gas jets shaped into a thin sheet as a non-destructive beam profile monitor for various types of particle beams [163], gas jets operate in reaction microscopes for atomic physics [146]. Supersonic gas jets in various configurations are used for the production and spectroscopy of radioactive isotopes [164]. Gas jets produce a laser induced plasma for laser-plasma acceleration experiments [165]. The utilisation of gas jets for nano-scale surface treatment can be beneficial for Radio Frequency (RF) cavities to increase the voltage breakdown strength [166].

**The Reaction Microscope (ReMi) for Atomic Physics** experiments was initially designed and developed at the Max Planck Institute for Nuclear Physics [146] for the full characterisation of atomic and molecular reactions. ReMi uses a cold supersonic (800 m/s) gas jet shaped into a thin sheet or a cylinder to study the point of collision between the accelerator beam and the target. ReMi allows the distribution of the moments of the charged particles to be obtained. The reaction itself takes place between the projectile ions and the gas target. The collimation of the gas jet to submillimeter cross sections and focusing of the accelerated beam can give information on the absolute position of where the reaction takes place [167]. ReMi allows to investigate full differential cross section of a number of interactions from medium to high projectile energies.

**The Production and Spectroscopy of Radioactive Isotopes (In-Gas Laser Ionisation and Spectroscopy)** is important on-going research for the nuclear spectroscopy which is aimed at a production of exotic radioactive isotopes and their investigation using the resonance laser ionisation in gases. For the nuclear reaction products, an accelerator beam is focused onto a target inside the gas, from which the isotopes are obtained [168, 169]. A high pressure noble gas is used for thermalising and neutralising the nuclear reaction products in their ground or low-lying metastable atomic states, and they are transported by gas flow to the exit orifice. After the laser ionisation, it is analysed by mass separators. The spectral resolution of the resonance ionisation has been improved by using supersonic gas jets instead of gas cells [169], when the laser beam is crossed with a supersonic gas jet for the resonant ionisation. The ions can be obtained from thick targets combined with hot cavities, and from the thin targets in combination with gases, which can be gas cells or gas jets [168].

**Laser-Plasma Accelerators** are regarded as a next generation of compact accelerators [165] which can allow high accelerating electric fields of more than  $100 \text{ GV m}^{-1}$  to be sustained in a short acceleration length. Accelerators based on normal conducting radio-frequency cavities have an accelerating gradient up to  $120 \text{ MV m}^{-1}$  [117, 170] past which breakdown appears. To reach TeV in a linear configuration in conventional accelerator, the accelerator needs to be the order of 10s of km long. The accelerating structure for laser-plasma acceleration consists of plasma, which is excited by a laser pulse or an ultra-relativistic electron pulse [171]. While the pulse propagates through the plasma, it excites a running longitudinal charge separation wave. The electrons are pushed away from the front and the back of the pulse thereby forming a trailing longitudinal density [165]. A supersonic gas jet is used as a target to provide the plasma medium for the laser-plasma acceleration [172]. The gas jet is ionised by the front of the laser pulses, and for the best performance [165], a flat-top gas jet density profile with a steep gradient at the edges is required. Another very important criterion is reproducibility of the same properties of the gas targets, and, hence, of the plasma. The monochromaticity of the gas jets gives a huge advantage by producing a well defined profile of plasma with the same properties each time. The various configurations of the gas jets and different gases, such as helium [173–175], nitrogen [175, 176], neon [175] and argon [175, 177], are being tested to achieve the best accelerating gradient.

The increasing demand of gas jets means that their characterisation is essential, and the characterisation of the gas jet's velocity profile is required for their correct operation at many applications and for their optimisation. Sensors are required to obtain accurate information about the velocity, the density and the temperature, especially based on the fact that all existing methods are not fully fulfilling all requirements. The SM sensor is an excellent alternative for such purposes.

## 5.2 Gas Jets for Beam Diagnostic

### 5.2.1 Beam Diagnostics: Gas Jet Set-up

Beam diagnostics play a vital role in the study of beam dynamics, enabling beam operation and machine optimisation. Even though many diagnostics have been developed, they all have limitations and requirements on conditions under which they can be used. When applied to accelerators with a high energy beam, well-established techniques such as interceptive foils and scintillating screens can be utilised for beam diagnostics only if a small fraction of the beam is used for the diagnostic purpose. In the case of low energy beams, the challenge is not to destroy the beam in the process of using the beam diagnostic sensors. Another important demand is to maintain the required vacuum conditions. Non-interceptive and non-destructive monitors are highly desirable as they can be used as on-line monitors without interfering with the operation of the beam. The interaction of a beam and a gas allows gas-based diagnostics to be successfully applied for beam diagnostics, which include Ionisation Profile Monitor (IPM) and Beam Induced Fluorescence (BIF). IPM is a non-invasive method based on the detection of the ions produced as the main beam ionises the residual gas. Another commonly used BIF monitor detects the light emitted during the de-excitation of the same residual gas [178]. Both of these methods, though, require a long signal acquisition time when they are used in non-destructive and non-invasive regime because that implies a low gas density and ultra-high vacuum.

As an alternative technique for beam diagnostics, an ionisation beam profile monitor utilising a supersonic gas jet was developed at the Cockcroft Institute [179–182]. The monitor is based on a neutral gas, shaped into a thin sheet. The jet travels perpendicularly to the particle beam propagation axis with its plane tilted at  $45^\circ$  with respect to the horizontal plane and crosses the beam. The ionisation products are extracted and used to determine a beam profile. A schematic drawing of the gas jet monitor is presented in Fig. 5.1.

The experimental setup of the gas jet monitor is composed of seven main sections. In the direction that the jet travels, see Fig. 5.1 from left to right, these are: a nozzle chamber, an outer chamber, a differential pumping chamber, an interaction section, and three damping sections [180, 182, 183]. The first three chambers evacuate the jet, and the three differential pumping sections prevent overloading of the turbo-pumps with the high gas flows in the first expansion stage, see Fig. 5.1.

In the nozzle chamber a neutral gas is injected through an aperture with a  $30\ \mu\text{m}$  diameter with initial pressure between 1 - 10 bars. The first collimator with a diameter of  $180\ \mu\text{m}$  is located after the aperture within a distance of less than 2 cm. More than 99.9% of the gas is evacuated from the nozzle chamber, by intense pumping. Without efficient evacuation, turbulences would occur in the gas flow around the nozzle, disrupting the supersonic flow. Further collimation is done by the second circular collimator with a diameter of  $400\ \mu\text{m}$ . At this stage the density of the jet is reduced to less than  $10^{16}\ \text{m}^{-3}$ .

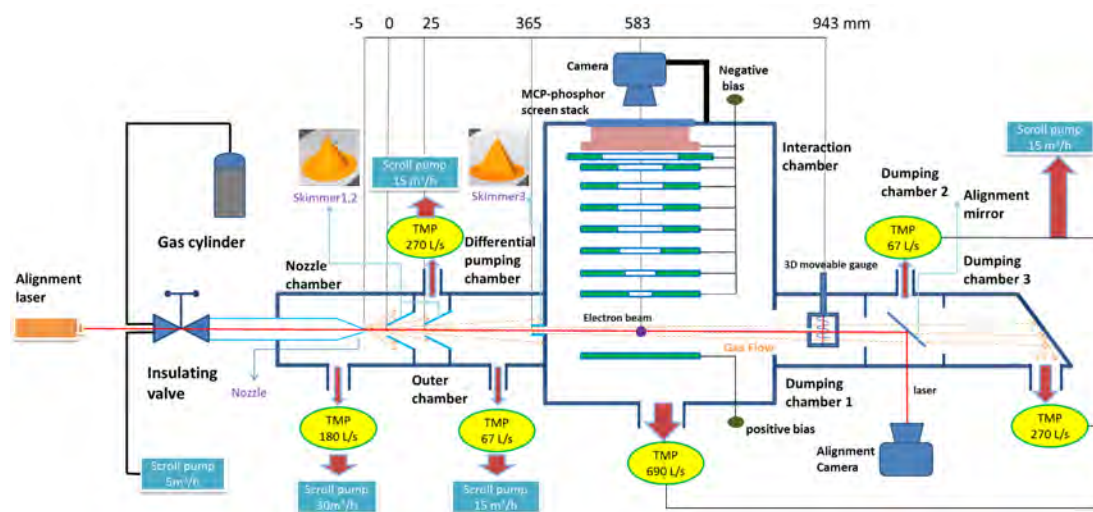


FIGURE 5.1: Schematic representation of a beam monitor based on a gas jet setup including vacuum system layout [181–183].

The third collimator with a rectangular slit of 4 mm by 0.4 mm is located 30 cm away from the second aperture. It is rotated by  $45^\circ$  around the jet propagation axis and shapes the jet into a thin sheet.

After the jet enters the interaction chamber, at the centre of the chamber it crosses the beam. Ionisation occurs at the point of the interaction of the electron beam with a gas jet, see an illustration of the set-up in the interaction chamber in Fig. 5.1. An external electric field accelerates the produced ions toward a microchannel plate (MCP) detector. Inside the MCP, every ion produces a cascade of electrons, which are then incident on a phosphor screen. As a result, the phosphor screen emits light which is then detected by a camera, allowing the two-dimensional beam profile to be imaged.

The gas jet consists of high density of  $10^{15} - 10^{18} \text{ m}^{-3}$  neutral molecules, which can be molecular nitrogen, argon, or helium. The gas jet sheet is estimated to have a velocity in the range of 500 - 1,500 m/s. It has an approximate width of 1.5 mm and an approximate thickness of 0.15 mm at its interaction point with the beam. The characterisation of the gas jet sheet is important for further calibration of the beam monitor, so a sensor for obtaining this information is needed. The sensor is required to measure the velocity and the density in these ranges. Moreover, it is desirable to have a sensor which can be easily integrated into an existing set-up with minimum additional optics components due to complexity of the set-up itself. For example, methods such as PTV, PIV, LSV are impossible to use, and interferometric or absorbing techniques are difficult to install and calibrate properly.

### 5.2.2 Currently Used Methods for Characterisation of the Gas Jet

The gas jet beam profile monitor itself can be used for the estimation of some gas jet properties. This alternative technique for calculating the velocity of the gas jet is based on the pictures of the beam profiles obtained from the interaction of the gas jet with

the electron beam. Figure 5.2 shows the profile of the beam, which was imaged by the residual gas and by the gas jet. The gas molecules were ionised and then accelerated by an electric field towards the MCP. The velocity was derived from the offset of the beam profile on the MCP. Examples of such measurements are presented in Fig. 5.2. The images were obtained from the ionisation of the residual gas, see horizontal line on pictures in Fig. 5.2, and from the gas jet, see the spot on pictures in Fig. 5.2. When the beam ionises the atoms or molecules of the gas jet, the shift of an image in the direction of the jet can clearly be seen, and the velocity of the gas jet can be calculated from this offset. The bottom pictures in Fig. 5.2 show the experimentally obtained image of the electron beam from both gas jet and residual gas on the left hand side, and the simulated beam image on the right hand side. The ions from the gas jet have initial mean velocity along the gas flow which causes the ions to drift along the  $x$ -axis. During the simulations, different presumed initial velocities were scanned to match the separation between two beam profiles from the offset of the images. The bottom plots in Fig. 5.2 were found to correlate with a velocity of around 860 m/s. The simulations were obtained for molecular nitrogen at room temperature for a separation of 2.63 mm [183]. For the reference value, the terminal velocity of the gas jet can be calculated as [142]:

$$v_{jet} = \sqrt{\frac{2\gamma kT}{(\gamma - 1)m}},$$

where  $k$  is the Boltzmann constant,  $m$  is the molar mass,  $\gamma$  is the heat capacity ratio, and  $T$  is the stagnation temperature. For mono-atomic gases,  $\gamma$  is presumed to be 5/3, and for polyatomic gases it is approximately 1.4. For molecular nitrogen, the theoretical jet velocity is around 800 m/s at room temperature. The difference between the velocity values obtained in the experiment and those calculated for an ideal gas is caused by the accuracy of the measurement of the separation in the experiment and by the fact that the gas in the chamber might have impurities so it differs from an ideal gas.

### 5.2.3 Installation of the Self-Mixing Sensor into the Existing Set-up

An SM sensor can be potentially used for independent measurements of the gas jet velocity for following reasons. SM sensors, being self-aligning, do not require additional changes of the set-up they are applied to, which is the case for any other technique [184]. It allows direct measurements to be obtained rather than indirect calculations and simulations currently required for velocity measurements.

As it was demonstrated in the previous chapters, the SM sensor provided information about the Doppler shift, which occurs after the interaction of laser light with a target. In the case of a gas jet, its velocity vector has the direction of the gas jet expansion. The best performance of the SM sensor was found to be when the angle between the laser light axis and the velocity vector was in the range of 13° to 77°. An SM sensor requirement is to have access to a gas jet to provide for such an angle. The SM sensor can be installed into the gas jet in the following two alternative ways: 1) through a viewport or a window

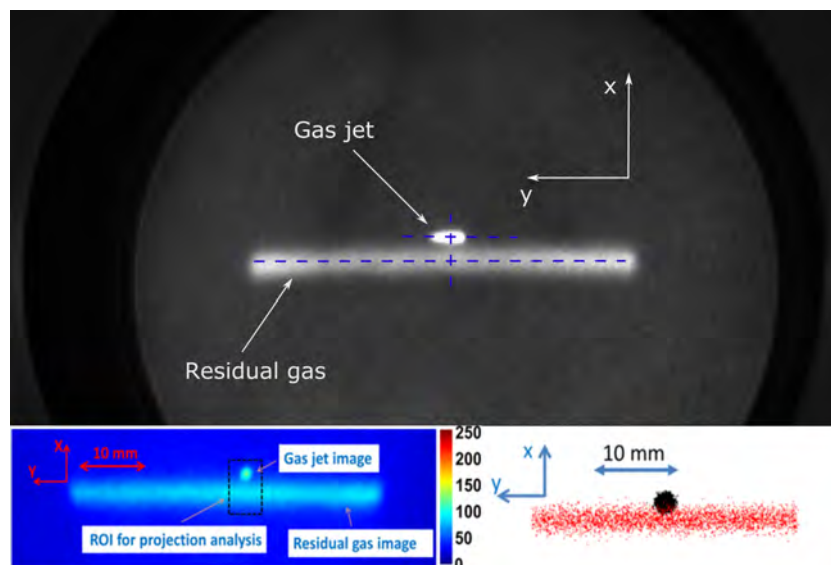


FIGURE 5.2: An example of estimation of the gas jet velocity by studying the pictures obtained from the MCP, which captured the beam profile as a result of interaction of the electron beam with gases. The top picture shows typical image obtained from the MCP, demonstrating two beam profiles: from the residual gas and from the gas jet. The bottom left side picture and right hand side picture show the experimental image and simulated beam image, which was obtained at the location of the MCP result using experimental parameters, for calculation of the velocity of the gas jet from the separation [183].

in one of the chamber ports and 2) through an optical feedthrough located at the flange of one of the chamber ports. As described before, the beam profile set-up consists of seven main sections. Several sections have vacuum chambers with ports, however, most of these ports are occupied with equipment and other sensors. As a result, these ports cannot be equipped with an SM sensor. The interaction chamber has several ports, however, some of them are also occupied or they have obstructions on the path from the port to the gas, so the light of the SM sensor cannot be delivered to the gas jet. The first dumping chamber, however, has several free ports, and the properties of the gas jet in this chamber are considered to be the same as in the interaction chamber.

A 3D model of the beam profile monitor is shown in Fig. 5.3 (a), which was presented earlier in Fig. 5.1. The first way to install and apply the SM sensor to gas jet measurements is to use a view-port or a window to shine the laser light through, see Fig. 5.3 (b). This allows the laser axis to be positioned in relation to the gas jet at any angle, which fits into the geometry of the port, in the required range for the best performance of the sensor. The viewport or the window of the chamber is transparent to the wavelength of the laser of the SM sensor. In the case of the transparent window, the flexibility of the angle is a big advantage. In this case, the SM sensor, which is going to be used for testing this method of velocity characterisation, consists of 650 nm LD, where the SM effect appears. Another laser, which is planned to be tested on the gas jet is 450 nm LD, similar to the 650 nm laser series. The signal from the built-in PD is to be delivered using the custom-built system to the transimpedance amplifier

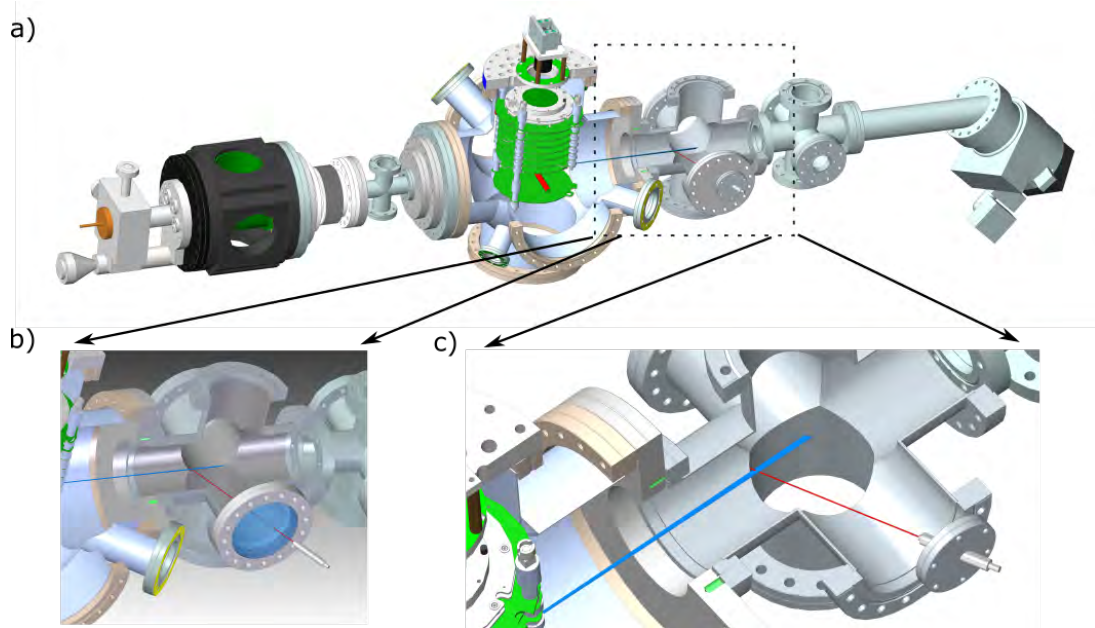


FIGURE 5.3: The gas jet monitor set-up for beam diagnostic with the ways to implement the SM sensor into it. The gas jet propagates from left to right, and it can be seen by the blue line. The light from the SM sensor is presented by the red line assuming the 650 nm wavelength. (a) the gas jet monitor from Fig. 5.1 is presented in the 3D model. The installation of the SM sensor in the first damping chamber, which is enclosed in the dashed box, can be realised using: (b) the view port with a window transparent to the wavelength of the SM sensor laser, which allows the laser to be used at any angle, or c) the optical feedthrough with the SM laser, which has a fixed angle between the laser and the gaseous target.

with a bandwidth of up 2 GHz. The signal is going to be collected for several minutes to provide a higher intensity and better statistics. The viewport allows the angle and distance to the gas jet to be varied, and the light focus point can be easily adjusted, to provide the best level of signal. However, the window reduces the amount of light going toward the target, and also the backscattered light and, therefore, the light coupled back into the laser cavity. This method can be applied assuming the amount of backscattered light is enough for the SM effect.

In order to improve the level of the signal, the investigation into the seeding of the gas jet with additional particles was considered (see following subsections) and showed that particles as small as 10 nm can be used for increasing the level of the SM signal in the case of a low intensity gas jet. The seeding system is frequently used for multiple purposes in gas jets, however it would not be desirable due to the possible contamination of the chambers and/or vacuum.

As an alternative approach, one of the ports of the first damping chamber can be replaced with a flange that has an optical feedthrough, see Fig. 5.3 (c). To have a Doppler shift, the angle between the vector of the velocity and the laser axis should be non-zero. For that, the optical feedthrough, see Fig. 5.3 and 5.4, is tilted at  $65^\circ$  in relation to the surface of the port, which leads to the angle of  $65^\circ$  between the laser axis and the velocity vector of the gas jet. This optical feedthrough has



FIGURE 5.4: Pictures of the optical feedthrough, which was designed to use for gas jet velocity measurements. The optical feedthrough is going to be coupled with the light from the laser, and as a result the light axis has a fixed angle between the laser and the gaseous target.

a fibre of 200  $\mu\text{m}$ , which is hermetically sealed into the stainless steel shell and can sustain a vacuum range of 760 Torr (1 atm) to  $1 \times 10^{-10}$  Torr [185]. It has a numerical aperture of 0.22, which is equal to a whole acceptance angle of  $24.8^\circ$ . The optical fibre operates at wavelengths in the range from 400 nm to 2200 nm with some absorption at 1400 nm. The optical feedthrough allows several lasers to be applied as a part of the SM sensor, including 1550 nm LD, which was previously tested for velocity measurements, see Chapter 3(3.3.6). In Section 3.3.6 the application of the 1550 nm fibre-based laser has demonstrated that the SM sensor can be built using fibre optics, which allows the sensor to be used in an environment where the access to the target might be restricted. Using feedthrough and the focusing lens inside the vacuum, the light to the gaseous target is easily delivered. Outside the feedthrough, the light is easy to couple, and then, using the coupler, the SM signal can be enhanced and detected by an external PD with a high bandwidth of 1.5 GHz. Alternative methods of the enhancement of the backscattered light are presented in Chapter 3, and can be used on this set-up. Since the optical feedthrough operates at a wide range of wavelengths, the 650 nm LD can also be used. It has to be coupled directly into the feedthrough, using the coupling lens.

#### 5.2.4 Self-mixing Technique: Expected Backscattered Light in Gas jets

Assuming an SM technique is used for the gas jet, an estimation of the expected backscatter can be found using Rayleigh scattering theory. The optical power collected by the detector can be found [4] using the following expression:

$$P_{DET} = \eta I_I N V \int_{\Delta\Omega} \frac{9\pi^2}{N^2 \lambda^4} \left( \frac{n^2 - 1}{n^2 + 2} \right)^2 \sin^2 \phi d\Omega, \quad (5.1)$$

where  $P_{DET}$  is the power collected by the detector,  $\eta$  is a collection efficiency,  $I_I$  is an intensity of the incident light,  $N$  is the number density of the gas (molecules/ $\text{cm}^3$ ),  $V$  is the volume of the gas illuminated by the incident light,  $n$  is the index of the refraction of the illuminated gas, and  $\Omega$  is the angle of integration, measured from the direction parallel to the incident light electric field oscillation. A light collection efficiency can

be calculated using Eq. 1.45 presented earlier. The refraction index  $n$  is linked to the density by the Lorentz-Lorenz equation [186, 187], which is valid for a dilute gas and molecular flow:

$$n \approx \sqrt{1 + 3A \frac{P}{RT}}, \quad (5.2)$$

where  $A$  is a volume occupied by a mole of scatterers. The volume of a single scatterer  $A_{single}$  (atom or molecule) can be calculated as  $A$  divided by the Avogadro's number:  $A_{single} = A/A_{av}$ . The ideal gas equation can be used for substituting the pressure and temperature with the density:

$$n \approx \sqrt{1 + 3A \frac{P}{RT}} = \sqrt{1 + 3A \frac{n}{V}} = \sqrt{1 + 3A_{single}N}. \quad (5.3)$$

Substituting Eq. 5.3 in Eq. 5.1:

$$P_{DET} = \eta I_I N V \int_{\Delta\Omega} \frac{9\pi^2}{\lambda^4} \left( \frac{A_{single}}{A_{single}N + 1} \right)^2 \sin^2 \phi d\Omega, \quad (5.4)$$

where  $A_{single}N$  is dimensionless and represents the fraction of the gaseous volume occupied by molecules. In a dilute gas, the distance between molecules is much bigger than the diameter of the molecules, leading to a value of  $A_{single}N \ll 1$ . Hence, the effect of  $N$  on reducing the coupled power is overcome by the effect of increasing it by the  $N$  in the numerator of Eq. 5.4.

The minimum level, required for the performance of the SM sensor, of the coupled back power in ratio to the incident light power is found to be equal to -123 dB [89] of attenuation. The incident power  $P_I$  of the light can be calculated by multiplying  $I_I$  with the area of the measured volume, which is assumed to have a constant cross sectional area. Assuming that  $d$  is the depth of the measured volume, Eq. 5.4 can be written as:

$$\frac{P_{DET}}{P_I} = \eta N d \int_{\Delta\Omega} \frac{9\pi^2}{\lambda^4} \left( \frac{A_{single}}{A_{single}N + 1} \right)^2 \sin^2 \phi d\Omega. \quad (5.5)$$

The importance of the geometry and size of the depth  $d$  of the measurement volume is highlighted in different works [188, 189], however no precise formula has been provided for its computation. The depth of the measured volume is a crucial factor in the evaluation of the expected backscattered radiation as well as of the received signal, and it is strongly dependent on the particular geometry of the optics. The depth of the measurement volume influences on the finesse of the velocity mapping, and the simulation should be done to obtain the measured depth in every specific case. In the geometry of the gas jet set-up for the beam instrumentation, such a depth is equal to approximately 1.5 mm. It was assumed as well that working in the geometry of backscattering light means working at an angle  $\phi$  of around  $65^\circ$ . Assuming the detector lens, which is the same as the collimating lens in the case of an SM sensor, has a diameter of roughly 2 cm and the measurements are done at a distance of roughly 15 cm from the investigation

volume, the maximum achievable  $\phi$  will be roughly in the range:

$$\frac{\pi \cdot 65^\circ}{180^\circ} - \arctan\left(\frac{1}{15}\right) < \phi < \frac{\pi \cdot 65^\circ}{180^\circ} + \arctan\left(\frac{1}{15}\right) \Rightarrow 61^\circ < \phi < 69^\circ, \quad (5.6)$$

which means that  $0.85 < \sin \phi < 0.93$ . The solid angle covered by the detector in the geometry considered above can be considered as subtended by a small facet of a flat surface  $d\Sigma$  at the distance  $r$  from a viewer as:

$$d\Omega = 4\pi \left( \frac{d\Sigma}{4\pi r^2} \right) = 4\pi \frac{\pi \cdot 0.01^2}{4\pi \cdot 0.15^2} \approx 1.4 \cdot 10^{-2}. \quad (5.7)$$

Making the approximation that  $A_{single}N + 1 \approx 1$ ,  $A_{single}$  is calculated by taking the cube of the diameter of the particle:  $A_{single} \approx D^3$ . Hence:

$$\frac{P_{DET}}{P_I} = \eta N d \Delta\Omega \frac{9\pi^2}{\lambda^4} A_{single}^2 = \eta N d \Delta\Omega \frac{9\pi^2}{\lambda^4} D^6. \quad (5.8)$$

This formula also demonstrates the expected Rayleigh scattering dependence, namely that it is proportional to the sixth power of the diameter of the scatterers and inversely proportional to the fourth power of the wavelength.

To calculate the level of the signal, the following parameters were assumed to be used in the experiments [163, 181]: a perfect collection efficiency of  $\eta = 1$ ;  $N = 4 \cdot 10^{15}$  (corresponding to a pressure of  $10^{-8}$  mbar at 20 K);  $d = 1.5$  mm;  $\Delta\Omega = 0.014$ ;  $\lambda = 650$  nm;  $D = 0.1$  nm. The result of the calculation is an attenuation of -220 dB, which is far higher than tolerated by the self-mixing technique. This means that one photon for each  $10^{24}$  is backscattered. To bring the solution closer to the needed attenuation value of -123 dB [89] for the SM sensor to work, seeding of the gas with particles as small as 10 nm is required. Using the optics with bigger lenses can improve the attenuation by one order of magnitude. The laser wavelength of 450 nm can also increase the signal level by one order of magnitude. This implies that seeding with 10 nm particles is necessary and they will follow the flow quite closely. For example,  $\text{TiO}_2$  particles of about 500 nm are reported [7] to fulfil this condition. Seeding particles do not disturb the gas, however, major differences in gas dynamics can occur only in regions of high velocity gradients. As a result, the different regions of the gas jets with lower velocities can be targeted instead of the high velocities for characterisation of the gas flow.

The laser velocimeter is a self-aligning device, based on the self-mixing method where the laser is both a transmitter and receiver of the signal. It should be pointed out that laser self-mixing is usually used for measurements of low velocities and vibrations. The theoretical analysis presented here shows the possibility to extend these measurement capabilities also to high velocities by altering the design.

The experiments with a 1550 nm laser based on fibre optics have demonstrated the possibility to utilise such type of lasers for velocity measurements with the potential feasibility to use it for gas jet experiments where it may be more practical.

### 5.3 Conclusion

Gas targets are used for a number of applications in particle accelerators and accelerator-based experiments. This includes beam diagnostic purposes where supersonic gas jets, which combine low internal temperatures with high directionality, show great promise as a tool to characterise beams of charged particles in least invasive ways. These gas jets typically have velocities of up to 1,500 m/s and feature an inhomogeneous density distribution across the jet.

All currently used methods for the characterisation of the jet itself are either not very reliable or require a powerful laser system. A specific challenge lies in the measurement of the gas jet density and velocity as these almost fully characterise the jet behaviour. A possible way to obtain this important information was shown in this chapter.

A feasibility study on using an SM sensor for velocity measurements of gas jets was presented. It was shown that such a compact sensor can be easily integrated into an existing set-up without significant changes to the installation nor the need of major additional equipment. Different geometries for such a sensor, as well as its fundamental properties and ways to integrate it into a gas jet set-up have been discussed.

It was shown that an SM sensor can be installed at the location of an existing viewport or by using an inclined optical feedthrough. A vacuum window on the one hand allows an optimisation of sensor performance by varying the angle between the target and the laser light axis during the actual measurement. On the other hand, an optical feedthrough gives access to higher light intensities at the location of the target. This in turn means that more scattered light can be coupled back into the laser cavity.

It had been shown in the earlier Chapters 3 and 4 that a wide range of velocities can be determined with an SM sensor. Also, options to extend the accessible velocity range and achievable accuracy with which velocities can be measured were discussed. The biggest challenge of the SM sensor remains the measurement of very high velocities, up to several times the speed of sound and this will be an interesting future challenge. The work within this thesis provides a reliable estimate of achievable signal levels, presents different options of sensor integration, and has established a comprehensive theory and simulation basis for this particular application.



## Chapter 6

# Conclusion and Outlook

### 6.1 Conclusion

This thesis has focused on the development of a semiconductor laser based velocimeter that has been developed for an application in the field of accelerator physics. It utilises the self-mixing effect in lasers, resulting in a compact and self-aligned system. A range of important data can be acquired including vibrations, small displacements, and velocities. Prior to this project the main usage of self-mixing sensors was to measure relatively small changes in a target position, and the measurement of small velocities due to the high sensitivity of the sensor. It was not fully determined whether the sensor could be used also for the measurement of a range of different targets and for higher velocities.

The main focus of this thesis was the study into the advancement of this sensor technology and the underpinning theory to pave the way for a whole range of new applications. This included both, theoretical and experimental studies. A general theoretical model was successfully developed for the SM sensor. This allowed an expected SM signal to be calculated, the sensor fundamental limitations to be estimated, and hence allowed the sensor performance to be pushed to its limits. Important progress was also made in measuring velocities of solid and fluid targets, with at least a factor of ten higher precision than previously achieved. This was made possible by advancements in detection and data collection, together with improved data analysis algorithms.

Chapter 1 gave an introduction to the general principles of optical diagnostics and the theory behind the self-mixing effect. Examples of self-mixing applications and the state-of-the-art of this method were also given. It was shown that the self-mixing technique can be used to detect small changes in target position, roughness or vibration. As a result, sensors using this phenomenon have been mainly applied to the measurement of vibrations, small displacements and slow movements, with measured velocities rarely exceeding 5 m/s. Examples were given of measurements using solid targets detecting velocities of up to 25 m/s, and fluids in the range of 0.1 mm/s to 10 cm/s. It was also shown that the majority of earlier works had focused on the precision of such measurement, in particular a high spatial resolution.

Chapter 2 introduced the scattering theory. On this basis a theory of the spectra which can be expected for the self-mixing sensor was developed. The effect from the absolute velocity, the velocity distribution, as well as the laser properties were all included in the theory. This was shown to provide a precise calculation of the expected overall spectra in particular experimental setups. This theory was then used to model the results of experiments and studying the reasons behind limitations discovered in the frame of this thesis. This model was then benchmarked against experimental data in order to establish a realistic velocity distribution. This new theory was shown to allow the reconstruction of the velocity distribution on the basis of a single measurement, and was also key to identifying the intrinsic limitations of the self-mixing technique.

Chapters 3 and 4 presented experimental results obtained as part of this PhD project. All experimental set-ups were described in detail. These were developed specifically for this project to fully understand all aspects of the sensor and its response to a range of different targets. Self-mixing is a non-linear phenomenon which occurs inside the laser cavity, and hence a comprehensive study into the different regimes in which the sensor can be operated was required.

Chapter 3 focused on studies into the influence of velocity variations and of distance between the laser and the target on the performance of the sensor. It also presented an experimental study into the impact of reflectivity of the measured target on the self-mixing signal; specifically on the types of feedback in different regimes (weak, moderate, strong) [71]. Theoretical and experimental investigations into the achievable accuracy and precision of the sensor were then performed for various angles and velocities. These experiments included the following objects: a remote-controlled translation stage as a movable target with a mirror with 99% reflectivity; white paper target mounted on the same translation stage; and a rotating disc covered with white paper [184]. The mirror and white paper on the translational stage allowed further understanding of how different types feedback impact on the final signal in the sensor. It was found that the white paper mounted on a rotating disc gave access to detailed information about the variation of the velocity. It was also the ideal target to study the impact from changes to the geometry of the entire system. Such as how accuracy and precision of the system varies with the angle of incidence/reflection under a fixed distance between target and laser. It also allowed the current limits of the method to be determined for a given sensor system. It was found that velocities higher than 50 m/s could be precisely measured. The accuracy of the sensor was also studied and it was found that a relative error of better than 3% could be achieved [72]. Finally, a theoretical analysis showed the possibility to extend the measurement capabilities of the sensor to much higher velocities by altering the design and electronics.

Compared to solid targets, fluids exhibit fundamentally different scattering processes leading to a lower backscattered intensity. In Chapter 4, the application of the SM sensor to fluids was studied, with emphasis on the investigation of seeding particles for the improvement of the resulting signal [190]. It was shown that seeding particles can be

used as a means to improve signal level and quality for both, fluid and gaseous targets. Variables that influence the resulting spectrum were investigated to better understand the individual contributions to the final signal. This included primarily the velocity of the target and the concentration of the seeders. It was shown that the spectrum of the signal directly depends on all these factors [191]. Experiments demonstrated the possibility of using the SM technique to measure the velocity of fluids up to 1.7 m/s for the case of pure water. This proved that even pure water provides sufficient backscattered light for the SM effect to occur. Seeding particles can be used to increase the amount of backscattered light, leading to an enhanced signal level. This means seeding particles can be used to measure higher velocities. Theoretical investigations into the overall spectrum and its dependence on different parameters as previously introduced in Chapter 2, were used to fully understand experimental results and carry out a detailed data analysis. It was found that increasing the target velocity reduces the amplitude of the peak of the spectrum whilst also broadening its peak. Analysis of the spectrum allows information on the distribution of the velocities within the volume of the flow illuminated by laser light to be obtained. The limitation of the maximum measured velocity of 1.7 m/s could be overcome with improvements to the optical system, benefiting from the reflective properties of specific scattering particles, as well as optimising laser parameters such as wavelength and beam waist. This chapter concluded with an analytical solution for the analysis of the experimental spectra, based on two frequency points. It was shown that by simply using the spectrum peak and the point of inflection, the velocity distribution can be obtained with good precision. This new approach not only simplifies the experimental analysis considerably, it also provides more precise information about the velocities.

Chapter 5 addressed the investigation into the application of the self-mixing sensor on gaseous targets. This had not previously been studied. Calculations of the estimated signal level from gaseous targets showed even lower expected levels of scattered light. Using results from Chapters 2 and 4, it was shown how the sensor could be used and integrated into a setup using a gas jet for the purpose of beam monitoring. This is an area of high importance, as gas jets are used for a number of fundamental and applied research applications. The chapter indicated possible ways of designing, integrating and operating a self-mixing sensor in such a demanding environment. Theoretical and simulation studies indicate likely signal levels which will be carefully assessed as part of future studies.

This thesis has studied the application of a laser-based self-mixing sensor in an accelerator environment. This is the first time that this has been studied in detail. A comprehensive study into the velocity limitations of the SM sensor was also performed [190]. This thesis presents measurements of velocities which are one order of magnitude higher than reported anywhere before, for the case of both solids and fluids. This significantly expands the range of applications for this type of sensor. A new theory was also developed which enhances data analysis and improves the overall understanding of the

self-mixing phenomenon. It also provides comprehensive information about the profile of the velocities within a measured area from a single measurement. This opens up additional opportunities for data analysis and application of the sensor.

## 6.2 Outlook

The projects and ideas presented in this thesis have advanced the science of the SM sensor and its potential applications beyond what had been previously presented in literature. As stated in Chapter 5, the application of the sensor to the characterisation of the gas jet will allow for not only simple benchmarking of already existing methods of gas jets characterisation, but also potentially new and easier to implement approaches, which can be utilised and advance many particle accelerators. Additional experiments are planned for tests of the sensor on at least two gas jets: a gas jet for beam diagnostics and a gas jet as a source for a laser-plasma driven accelerator (see Chapter 5). This will open a unique opportunity to benchmark the sensor with various simulations and to advance the monitoring of gas jets within the accelerator community. This work provides the basis for further studies such as the characterisation of different gas jets; studies into 3D position and motion detection in an ultra-high vacuum environment, using different lasers and benchmarking of numerical studies; SM sensor optimisation; and studies into different applications.

As a part of SM sensor optimisation, the method, as proposed in Chapter 3, of enhancement of the data acquisition system to improve the overall performance of the sensor can be studied in detail. This will include designing and building the optimised electronics for use at 50 or 100 MHz, supported by the already available transimpedance amplifier. Using an additional laser will serve as a reference point for a higher precision. It will have the same wavelength as the primary laser, however, its frequency will be measured through temperature control. This will allow any shift in frequency to be measured not directly via the oscilloscope but with the additional laser and resulting current changes that will be detected by the electronics. This will advance the SM sensor in a completely new way in order to develop the detector into a stand-alone solution where all components are housed in a single casing.

The experimental results obtained in Chapter 4 demonstrated scientifically interesting effects, which were beyond the scope of the development of the SM sensor itself, such as mapping the region of the concentrations for various seeding particles where the border of the processes between the single particle scattering and multi-scattering lies. Additional simulations and benchmarking with the SM sensor measurements can significantly extend the research around this sensor.

Theoretical studies into the influence of the velocity distribution on the overall spectra, which were verified with experiments, open the platform for a completely new approach for analysing data for many applications of SM sensors for the first time. This goes beyond particle accelerators and can be applied to the whole complex of various

self-mixing sensors aimed at different applications. This thesis demonstrated the very first verification of this theory. However, more extended research including experiments for various fluids will advance the application of the theory for SM sensors. As a result of such research, the additional information, which can be obtained from one measurement will allow the 3D characterisation of the velocity profile of flows without the need for an additional scanning system.



# Appendix A

## Characterisation of Gas Jets

### A.0.1 Characterisation of Gas Jets

An optimised gas jet with specific parameters is a highly important tool which is used in a number of applications in many fields of physics including aerodynamic, machining, spectroscopy, and many other fields [192, 193]. Many techniques for measuring supersonic flows have hence been proposed for the gas jets characterisation. The method for measuring velocities of flows (gases and liquids), spray and particle characterisation, and combustion diagnostics are interchangeable from one field to another. When using these techniques, it is important to understand the measurement principle, and its limitations, such as maximum velocities and the conditions under which the different methods can be used. It is also very important to find a compromise between the required parameters and the financial cost of the set-up. The different methods used for classification can be divided into three main groups: mechanical, acoustic, and optical techniques, all of which differ depending on the application goal.

**Mechanical techniques** are based on the dynamic interaction of a gas jet with a probe. These methods utilise one or several of the following processes: the variation of some properties or a dynamical behaviour of the probe inside the flow, for example an object flowing with the gas jet; the penetration of the flow into the probe such as a Pitot pressure probe; and the tracking of the volume going through a certain area. Mechanical devices can be based on the thermal characteristics of the gas jet and they can measure the thermal conduction and heat transfer within the flow, for example Hot-Wire Anemometry (HWA) [147]. A Pitot pressure probe is a tube, which is placed into the flow. As the flow penetrates the tube, the pressure within the tube is measured. The pressure within the flow is then calculated using the Bernoulli equation. The scan can be performed by varying the position of the gas jet or the position of the tube itself where possible, and from the pressure the velocity can also be calculated. This method is intrusive, i.e. the probe changes the dynamic of the gas flow, therefore, additional simulations are required. Figure A.1 demonstrates the obtained result and the perturbation of the gas dynamic due to the probe. However, at most facilities, an additional measurement of the gas jet also was required in order to verify the obtained

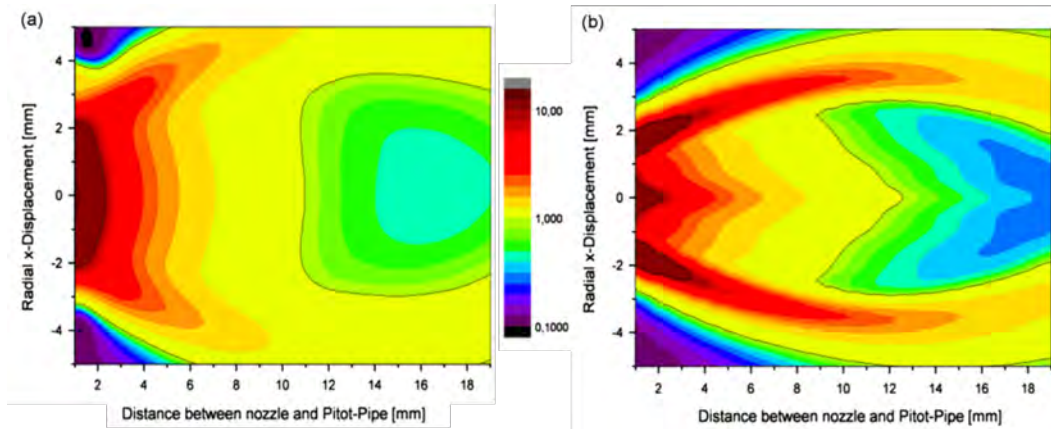


FIGURE A.1: (a) Measurements of the impact-pressure flow field of the supersonic gas jet displacing the supersonic nozzle relative to the Pitot probe and (b) computer simulation of the impact from the Pitot probe for the gas jet [148]

results. This technique was applied for the characterisation of the gas jet, which was used for spectroscopy at the HITRAP facility at GSI [148] and at the facility at Jyvaskyla, Finland for IGISOL [149].

Another group of mechanical sensors are based on magnetohydrodynamics and electrohydrodynamics phenomena, and they include measurements of ionisation level or discharge tracking. The dielectric barrier discharge effect was suggested [150] for the visualisation of gas flows. Another more recent technique of visualisation of the jet by measuring the glow discharge under pressure was proposed for use at GCIB accelerators. These methods do not require difficult equipment [151], but they have not revealed the cross-section of the jet [152].

Mechanical methods are reliable and relatively simple to build. For supersonic flows, though, mechanical techniques are too intrusive and they are only occasionally suitable for low densities. Any modification to the free expansion is bound to result in major perturbation of the investigated system. It leads to erroneous measurements, and it is also disruptive of the jet itself, which loses its homogeneous velocity distribution and its high density and then will be unusable for the application it is designed for.

**The acoustic methods** are mostly based on the formation of the acoustic wave within the flow using different equipment and then measuring its changed properties. The main principle for such technique is to produce a high frequency signal, up to  $10^{14}$  Hz, within the measured area of the gas jet, using, for example, a piezoelectric transducer. If such a wave reflects from the other side of the gas jet, a standing wave can be produced, which properties (amplitude and/or phase shift) will depend on the reflection coefficient of the medium [153]. This allows the change of the temperature of the gas jet, its pressure or its density to be traced, since the reflectivity is a function of these parameters. Acoustic techniques are preferable for high densities, they provide only limited information about the flow with a low resolution.

**The optical methods** are represented by a broad spectrum of different methods with the majority of techniques based on scattering of light off the gas, and they also

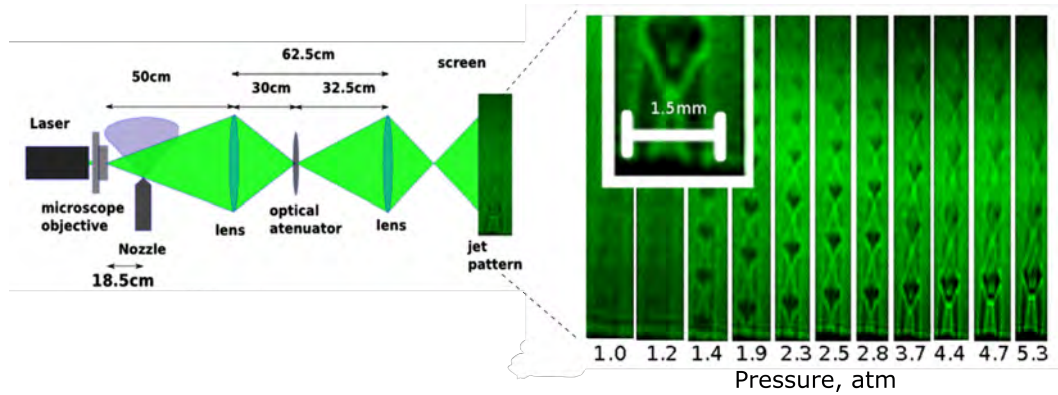


FIGURE A.2: The example of the Schlieren photograph of the gas expansion [157]. The optical set-up is shown on the left side of the figure, and the right part demonstrates the Schlieren images of the jet at different pressures, which are indicated under each image

include such phenomena as luminescence and fluorescence. The scattering processes allow the measurements of various parameters such as velocity, density, reflectivity, temperature, and absorption coefficient to be performed. The most commonly used optical methods are PIVs [6, 9] and various LDVs techniques [2, 154, 155], described earlier. Optical methods are usually non invasive and allow the velocities to be measured with high precision. However, some of them are not suitable for low densities, e.g. Schlieren photographs. The most common optical methods used in the area of gas flow visualisation are: Schlieren photographs; Particle Image Velocimetry; Absorption Sensors; Interferometry; and Laser Doppler Velocimetry.

*Schlieren photography* is a technique [156] based on the variation of refractive index as a function of the density of a flow. The region of interest in the flow is illuminated with bright collimated light (flash lamps, LED panel, pulsed laser), and a knife edge is placed behind the flow. As a result it intercepts roughly half the transmitted light, when the flow is stationary. The picture made using such a set-up is compared to a picture taken without the knife edge which results in a photograph half as bright. If the fluid moves, density gradients give rise to a varying index of refraction, which deviates light at an increasing angle in the direction of the density gradient. Part of the light is blocked by the knife edge, and the illumination of the corresponding area varies on the image capture device. This way, an image can be obtained in points of different density which can be identified by the colour intensity of the image. Figure A.2 shows an example of the Schlieren photographs obtained for the characterisation of a gas jet used for low energy nuclear reaction studies [157]. Different densities of the jet are shown by the variation from black to green colour. The main advantage of this technique is its simplicity and the reliability of the set-up. The drawbacks of such a system are its low resolution and that only one, perpendicular to the knife-edge, component of the gradient per photograph can be measured. Such a system requires a very high gas density of up to several bars to work properly in comparison with the gas density of a typical gas jet application (lower than  $10^{-5}$  mbar) for particle accelerators.

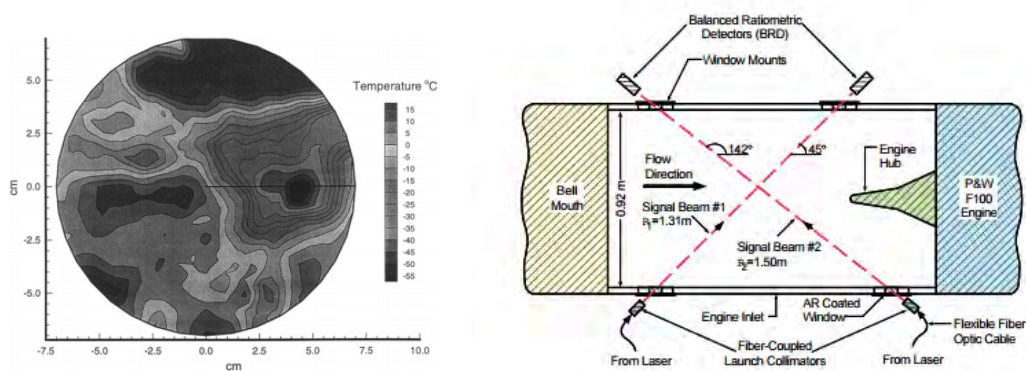


FIGURE A.3: Examples of the absorption sensors: a reconstruction of the temperature field distribution in a turbulent jet flow of  $O_2/N_2$  on the left plot and the sensor configuration using a laser diode for studying a mass flow for a full-scale aeroengine inlet on the right figure [158].

*Particle Imaging Velocimetry (PIV)* was described in Chapter 1. When applied to gas jets, a typical set-up consists of the same equipment described earlier: a visualisation camera, a high power laser, an optical system for receiving a light sheet from laser, tracer particles and a synchronizer. However, in the case of gas jets the particles do not always follow the flow. The velocity of a seeding particle is proportional to the mass. The tracer particles are usually big and have large mass. According to the Rayleigh scattering equation, for the correct working of the PIV in order to trace the reflected light, the tracing particles are required to be much bigger in size than the gas molecules, which are usually contained in the gas jets ( $O_2$ , Ar, etc.). Moreover, seeding the jet is not only complicated and requires complex set-ups, but has also negative effects on the jet, disrupting its velocity and density distribution to some extent, by slowing it down and even wearing down the vacuum pumps, decreasing the lifetime of equipment. Furthermore, the numerical algorithms, which are required to extrapolate the actual jet velocity from the movement of seeding particles, are not only complex, but also carry large uncertainties.

*Absorption sensors* are based on the absorption of the laser light while it propagates through the medium and can provide information about temperature or density depending on which parameters are known. Two absorption transition probes can give the pure function of the temperature of the media as well. An example of the results obtained using the absorption sensor for the temperature field reconstruction for the characterisation of the gas jet is presented in Fig. A.3 on the left hand side of the plot. Using the same absorption sensor in different configurations, measurements of different gas jet parameters are possible. As shown in Fig. A.3 on the right hand side, the same sensor was used for measurements of the mass flow, particles concentration, gas temperature, and its velocity [158]. The challenge is to choose the correct diode sensor in order to obtain a sufficient level of the signal [159].

*Interferometry* (see Chapter 1 for details) can be employed [194] for measuring the density by using the variation of the index of refraction with density, which occurs in a

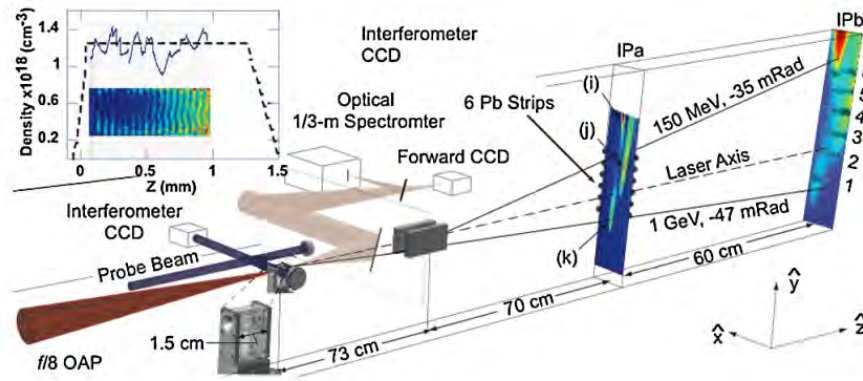


FIGURE A.4: An example of a Michelson interferometer installed into the set-up for the gas cell characterisation, which is used in the laser wakefield accelerator [161]. As it can be seen, the complexity of the interferometry makes it unsuitable for its use at many facilities.

gas. The measurements are achieved by locating one of the arms of the interferometer within the gas. Computational fluid dynamics simulations can provide a wealth of information about velocity if the density is given. Interferometry does not provide a direct measurement of velocity and it is best suited for studying high density gases so that variation of refractive index is high.

Interferometric and absorbing techniques [160] usually require an installation of a complex additional set-up into an existing system and are hardly applicable for use in gas jet set-ups. An example of such an installation of the Michelson interferometer is shown in Fig. A.4. This set-up was used for the characterisation of the gas inside the gas cell for the laser wakefield acceleration [161].

*Laser Doppler Velocimetry (LDV) and Spectroscopy* work on the same basic principle: the Doppler shift experienced by the radiation incident on a moving particle. The only difference between these two approaches is the method of visualisation of the Doppler shift. Rayleigh scattering is the principle which lies behind the very basis of LDV, see Chapters 1 and 2 for details. Based on common principles of LDV and scattering, many different techniques have been developed. When applying LDV to flows, the Doppler shift can be detected using interferometry. For example, if the scattered light with the Doppler shift is superposed with a reference beam to produce the interference pattern, the difference in frequency between the two light beams results in a beating signal with a frequency of the Doppler shift. Spectroscopy allows the spectrum of the Doppler-shifted light to be detected directly. For example, Spectrally Resolved Rayleigh Scattering (SRRS) reconstructs the spectrum of the scattered light for the flow visualisation [4, 162]. The Doppler broadening of the light after the interaction with moving flows gives direct information on the Doppler shift. SRRS exploits standard spectrometry techniques such as interferometric filters like a scanning Fabry-Perot interferometer [1, 162] or molecular filters [195], which use the narrow absorption bands of gases. LDV, spectroscopy and interferometry techniques overlap almost completely

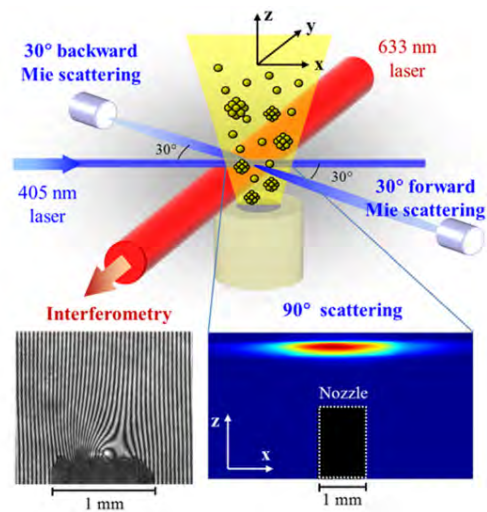


FIGURE A.5: An example of an experimental set-up which has three optical diagnostics (scattering under different angles and neutral gas interferometry) for the characterisation of a gas flow [196].

when they are applied. One example of the combined experimental set-up which exploits the scattering phenomenon for a gas flow characterisation is presented in Fig. A.5.

# Bibliography

- [1] F. Träger. *Springer Handbook of Lasers and Optics*. Springer Handbook of Lasers and Optics. Springer New York, 2007. ISBN 9780387304205.
- [2] V.P. Klochkov, L.F. Kozlov, and I.V. Putykevich. *Laser Anemometry, Remote Spectroscopy and Interferometry*. Nauka, Kiev, 1985.
- [3] M. Born, E. Wolf, A.B. Bhatia, D. Gabor, A.R. Stokes, A.M. Taylor, P.A. Wayman, and W.L. Wilcock. *Principles of Optics: Electromagnetic Theory of Propagation, Interference and Diffraction of Light*. Cambridge University Press, 2000. ISBN 9780521784498.
- [4] R.B. Miles, W.R. Lempert, and J.N. Forkey. Laser Rayleigh scattering. *Measurement Science and Technology*, 12(5):R33, 2001. URL <http://stacks.iop.org/0957-0233/12/i=5/a=201>.
- [5] M. Zhang, M. Xu, Y. Zhang, G. Zhang, and D.J. Cleary. Flow-field investigation of multihole superheated sprays using high-speed PIV. part ii. axial direction. *Atomization and Sprays*, 23(2), 2013.
- [6] P.H. Biwole. *Large Scale Particle Tracking Velocimetry for 3-dimensional Indoor Airflow Study*. 2009.
- [7] D. Mitchell, D. Honnery, and J. Soria. Study of underexpanded supersonic jets with optical techniques. In *16th Australasian Fluid Mechanics Conference (AFMC)*, pages 217–224. School of Engineering, The University of Queensland, 2007.
- [8] R. D. Keane, R. J. Adrian, and Y. Zhang. Super-resolution particle imaging velocimetry. *Measurement Science and Technology*, 6(6):754, 1995. URL <http://stacks.iop.org/0957-0233/6/i=6/a=013>.
- [9] M. Raffel, C.E. Willert, S.T. Wereley, and J. Kompenhans. *Particle Image Velocimetry: A Practical Guide*. Experimental Fluid Mechanics. Springer, 2007. ISBN 9783540723080.
- [10] J.W. Goodman. *Speckle phenomena in optics: theory and applications*. Roberts and Company Publishers, 2007.

- 
- [11] N.A. Fomin. *Speckle Photography for Fluid Mechanics Measurements*. Experimental Fluid Mechanics. Springer, 1998. ISBN 9783540637677.
- [12] R.J. Adrian and J. Westerweel. *Particle Image Velocimetry*. Cambridge Aerospace Series. Cambridge University Press, 2011. ISBN 9780521440080.
- [13] A. Schroeder and C.E. Willert. *Particle image velocimetry: new developments and recent applications*, volume 112. Springer Science & Business Media, 2008.
- [14] Z. Zhang. *LDA application methods: laser Doppler anemometry for fluid dynamics*. Springer Science & Business Media, 2010.
- [15] A. Donges and R. Noll. Laser measurement technology. *Springer Series in Optical Sciences, Springer, Berlin, Heidelberg*, 2015.
- [16] O. Svelto. *Principles of Lasers*. Springer US, 2010. ISBN 9781441913029.
- [17] J. Ohtsubo. *Semiconductor Lasers: Stability, Instability and Chaos*. Springer Series in Optical Sciences. Springer Berlin Heidelberg, 2012. ISBN 9783642301476.
- [18] I.L. Fabelinskii. *Molecular scattering of light*. Springer Science & Business Media, 2012.
- [19] F. Durst. *Fluid Mechanics: An Introduction to the Theory of Fluid Flows*. Graduate Texts in Physics Series. Springer Berlin Heidelberg, 2008. ISBN 9783540713425.
- [20] M. Yamada. *Theory of Semiconductor Lasers: From Basis of Quantum Electronics to Analyses of the Mode Competition Phenomena and Noise*. Springer Series in Optical Sciences. Springer Japan, 2014. ISBN 9784431548898.
- [21] R. N. Hall, G. E. Fenner, J. D. Kingsley, T. J. Soltys, and R. O. Carlson. Coherent light emission from GaAs junctions. *Physical Review Letters*, 9:366–368, Nov 1962. doi: 10.1103/PhysRevLett.9.366. URL <http://link.aps.org/doi/10.1103/PhysRevLett.9.366>.
- [22] D.M. Kane and K.A. Shore. *Unlocking dynamical diversity: optical feedback effects on semiconductor lasers*. John Wiley & Sons, 2005.
- [23] H. Haken. Analogy between higher instabilities in fluids and lasers. *Physics Letters A*, 53(1):77 – 78, 1975. ISSN 0375-9601. doi: [http://dx.doi.org/10.1016/0375-9601\(75\)90353-9](http://dx.doi.org/10.1016/0375-9601(75)90353-9). URL <http://www.sciencedirect.com/science/article/pii/0375960175903539>.
- [24] R. Lang and K. Kobayashi. External optical feedback effects on semiconductor injection laser properties. *Quantum Electronics, IEEE Journal of*, 16(3):347–355, Mar 1980. ISSN 0018-9197. doi: 10.1109/JQE.1980.1070479.

- [25] J.H. Churnside. Laser doppler velocimetry by modulating a CO<sub>2</sub> laser with backscattered light. *Appl. Opt.*, 23(1):61–66, Jan 1984. doi: 10.1364/AO.23.000061. URL <http://ao.osa.org/abstract.cfm?URI=ao-23-1-61>.
- [26] M.J. Rudd. A laser doppler velocimeter employing the laser as a mixer-oscillator. *Journal of Physics E: Scientific Instruments*, 1(7):723, 1968. URL <http://stacks.iop.org/0022-3735/1/i=7/a=305>.
- [27] M.J. Rudd. A laser Doppler velocimeter employing the laser as a mixer-oscillator. *Journal of Physics E: Scientific Instruments*, 1(7):723, 1968.
- [28] F. Sporleder. Travelling wave line model for laser diodes with external optical feedback. In *Proc. URSI Int. Symp. Electromagnet. Theory*, pages 585–588, 1983.
- [29] J. Mork. *Nonlinear dynamics and stochastic behaviour of semiconductor lasers*. PhD thesis, 1989.
- [30] A. Ritter and H. Haug. Theory of laser diodes with weak optical feedback. ii. limit-cycle behavior, quasi-periodicity, frequency locking, and route to chaos. *JOSA B*, 10(1):145–154, 1993.
- [31] I. Pierce, P. Rees, and P.S. Spencer. Multimode dynamics in laser diodes with optical feedback. *Physical Review A*, 61(5):053801, 2000.
- [32] G.A. Acket, D. Lenstra, A. Den Boef, and B. Verbeek. The influence of feedback intensity on longitudinal mode properties and optical noise in index-guided semiconductor lasers. *Quantum Electronics, IEEE Journal of*, 20(10):1163–1169, Oct 1984. ISSN 0018-9197. doi: 10.1109/JQE.1984.1072281.
- [33] T. Bosch, N. Servagent, and S. Donati. Optical feedback interferometry for sensing application. *Optical Engineering*, 40(1):20–27, 2001. doi: 10.1117/1.1330701. URL <http://dx.doi.org/10.1117/1.1330701>.
- [34] W.M. Wang, K.T.V. Grattan, A.W. Palmer, and W.J.O. Boyle. Self-mixing interference inside a single-mode diode laser for optical sensing applications. *Light-wave Technology, Journal of*, 12(9):1577–1587, Sep 1994. ISSN 0733-8724. doi: 10.1109/50.320940.
- [35] E.T. Shimizu. Directional discrimination in the self-mixing type laser Doppler velocimeter. *Applied optics*, 26(21):4541–4544, 1987.
- [36] Ş.K. Özdemir, S. Takamiya, S. Ito, S. Shinohara, and H. Yoshida. Self-mixing laser speckle velocimeter for blood flow measurement. *Instrumentation and Measurement, IEEE Transactions on*, 49(5):1029–1035, 2000.
- [37] Y. Fan, Y. Yu, J. Xi, and J.F. Chicharo. Improving the measurement performance for a self-mixing interferometry-based displacement sensing system. *Applied Optics*, 50(26):5064–5072, 2011.

- [38] S. Ottonelli, M. Dabbicco, F. De Lucia, M. Di Vietro, and G. Scamarcio. Laser-self-mixing interferometry for mechatronics applications. *Sensors*, 9(5):3527–3548, 2009.
- [39] M. Liess, G. Weijers, C. Heinks, A. van der Horst, A. Rommers, R. Duijve, and G. Mimmagh. A miniaturized multidirectional optical motion sensor and input device based on laser self-mixing. *Measurement Science and Technology*, 13(12):2001, 2002.
- [40] R. Kliese, Y.L. Lim, K. Bertling, A. Bakar, T. Bosch, and A.D. Rakić. Self-mixing displacement sensing using the junction voltage variation in a GaN laser. In *Optoelectronic and Microelectronic Materials and Devices.*, pages 23–25. IEEE, 2008.
- [41] S. Ottonelli, F. De Lucia, M. di Vietro, M. Dabbicco, G. Scamarcio, and F.P. Mezzapesa. A compact three degrees-of-freedom motion sensor based on the laser-self-mixing effect. *Photonics Technology Letters, IEEE*, 20(16):1360–1362, Aug 2008. ISSN 1041-1135. doi: 10.1109/LPT.2008.926569.
- [42] L. Krehut, J. Hast, E. Alarousu, and R. Myllyla. Low cost velocity sensor based on the self-mixing effect in a laser diode. *Optoelectronics review*, (4):313–320, 2003.
- [43] F.F.M. De Mul, L. Scalise, A.L. Petoukhova, M. Van Herwijnen, P. Moes, and W. Steenbergen. Glass-fiber self-mixing intra-arterial laser Doppler velocimetry: signal stability and feedback analysis. *Applied optics*, 41(4):658–667, 2002.
- [44] W. Huang, H. Gui, L. Lu, J. Xie, H. Ming, D. He, H. Wang, and T. Zhao. Effect of angle of incidence on self-mixing laser Doppler velocimeter and optimization of the system. *Optics Communications*, 281(6):1662–1667, 2008. doi: <http://dx.doi.org/10.1016/j.optcom.2007.11.029>. URL <http://www.sciencedirect.com/science/article/pii/S0030401807012230>.
- [45] S. Shinohara, A. Mochizuki, H. Yoshida, and M. Sumi. Laser doppler velocimeter using the self-mixing effect of a semiconductor laser diode. *Applied Optics*, 25(9):1417–1419, 1986.
- [46] T. Taimre, K. Bertling, Y.L. Lim, P. Dean, D. Indjin, and A.D. Rakić. Methodology for materials analysis using swept-frequency feedback interferometry with terahertz frequency quantum cascade lasers. *Optics express*, 22(15):18633–18647, 2014.
- [47] M.C. Phillips, I.M. Craig, and T.A. Blake. Reflection-absorption infrared spectroscopy of thin films using an external cavity quantum cascade laser. In *SPIE OPTO*, pages 86310C–86310C. International Society for Optics and Photonics, 2013.

- [48] E. Gagnon and J.F. Rivest. Laser range imaging using the self-mixing effect in a laser diode. *IEEE Transactions on Instrumentation and Measurement*, 48(3):693–699, 1999.
- [49] R. Day, E. Lacot, F. Stoeckel, and B. Berge. Three-dimensional sensing based on a dynamically focused laser optical feedback imaging technique. *Applied optics*, 40(12):1921–1924, 2001.
- [50] M.T. Fathi and S. Donati. Thickness measurement of transparent plates by a self-mixing interferometer. *Optics letters*, 35(11):1844–1846, 2010.
- [51] G. Giuliani, S. Bozzi-Pietra, and S. Donati. Self-mixing laser diode vibrometer. *Measurement Science and Technology*, 14(1):24, 2002.
- [52] S. Donati. Developing self-mixing interferometry for instrumentation and measurements. *Laser & Photonics Reviews*, 6(3):393–417, 2012.
- [53] A.N. Lukashkin, M.E. Bashtanov, and I.J. Russell. A self-mixing laser-diode interferometer for measuring basilar membrane vibrations without opening the cochlea. *Journal of neuroscience methods*, 148(2):122–129, 2005.
- [54] L. Scalise, Y. Yanguang, G. Giuliani, G. Plantier, and T. Bosch. Self-mixing laser diode velocimetry: application to vibration and velocity measurement. *Instrumentation and Measurement, IEEE Transactions on*, 53(1):223–232, Feb 2004. ISSN 0018-9456. doi: 10.1109/TIM.2003.822194.
- [55] A. Magnani and M. Norgia. Spectral analysis for velocity measurement through self-mixing interferometry. *Quantum Electronics, IEEE Journal of*, 49(9):765–769, 2013.
- [56] R. Kliese and A.D. Rakić. Spectral broadening caused by dynamic speckle in self-mixing velocimetry sensors. *Optics Express*, 20(17):18757–18771, 2012.
- [57] M. Norgia, S. Donati, and D.D. Alessandro. Interferometric measurements of displacement on a diffusing target by a speckle tracking technique. *Quantum Electronics, IEEE Journal of*, 37(6):800–806, 2001.
- [58] S. Shinohara, S. Ito, S. Takamiya, H. Yoshida, et al. Compact optical instrument for surface classification using self-mixing interference in a laser diode. *Optical Engineering*, 40(1):38–43, 2001.
- [59] Ş.K. Özdemir, T. Takasu, S. Shinohara, H. Yoshida, and M. Sumi. Simultaneous measurement of velocity and length of moving surfaces by a speckle velocimeter with two self-mixing laser diodes. *Applied optics*, 38(10):1968–1974, 1999.
- [60] G. Plantier, C. Bes, and T. Bosch. Behavioral model of a self-mixing laser diode sensor. *Quantum Electronics, IEEE Journal of*, 41(9):1157–1167, 2005.

- [61] X. Raoul, T. Bosch, G. Plantier, and N. Servagent. A double-laser diode on-board sensor for velocity measurements. *Instrumentation and Measurement, IEEE Transactions on*, 53(1):95–101, Feb 2004. ISSN 0018-9456. doi: 10.1109/TIM.2003.821483.
- [62] L. Campagnolo, M. Nikolić, J. Perchoux, Y.L. Lim, K. Bertling, K. Loubiere, L. Prat, A.D. Rakić, and T. Bosch. Flow profile measurement in microchannel using the optical feedback interferometry sensing technique. *Microfluidics and nanofluidics*, 14(1-2):113–119, 2013. doi: 10.1007/s10404-012-1029-0. URL <http://dx.doi.org/10.1007/s10404-012-1029-0>.
- [63] M. Nikolić, E. Hicks, Y.L. Lim, K. Bertling, and A.D. Rakić. Self-mixing laser Doppler flow sensor: an optofluidic implementation. *Applied optics*, 52(33):8128–8133, 2013. doi: 10.1364/AO.52.008128. URL <http://ao.osa.org/abstract.cfm?URI=ao-52-33-8128>.
- [64] L. Rovati, S. Cattini, and N. Palanisamy. Measurement of the fluid-velocity profile using a self-mixing superluminescent diode. *Measurement Science and Technology*, 22(2):025402, 2011. URL <http://stacks.iop.org/0957-0233/22/i=2/a=025402>.
- [65] M. Norgia, A. Pesatori, and L. Rovati. Self-mixing laser Doppler spectra of extracorporeal blood flow: A theoretical and experimental study. *Sensors Journal, IEEE*, 12(3):552–557, March 2012. ISSN 1530-437X. doi: 10.1109/JSEN.2011.2131646.
- [66] M.H. Koelink, F.F.M. De Mul, A.L. Weijers, J. Greve, R. Graaff, A.C.M. Dassel, and J.G. Aarnoudse. Fiber-coupled self-mixing diode-laser doppler velocimeter: technical aspects and flow velocity profile disturbances in water and blood flows. *Applied optics*, 33(24):5628–5641, 1994.
- [67] C. Zakian, M. Dickinson, and T. King. Particle sizing and flow measurement using self-mixing interferometry with a laser diode. *Journal of Optics A: Pure and Applied Optics*, 7(6):S445, 2005. URL <http://stacks.iop.org/1464-4258/7/i=6/a=029>.
- [68] Ş.K. Özdemir, S. Shinohara, S. Takamiya, and H. Yoshida. Noninvasive blood flow measurement using speckle signals from a self-mixing laser diode: in vitro and in vivo experiments. *Optical Engineering*, 39(9):2574–2580, 2000. doi: 10.1117/1.1287262. URL <http://dx.doi.org/10.1117/1.1287262>.
- [69] S. Cattini and L. Rovati. A simple and robust optical scheme for self-mixing low-coherence flowmeters. In *SPIE BiOS*, pages 895102–895102. International Society for Optics and Photonics, 2014.

- [70] K. Otsuka. Self-mixing thin-slice solid-state laser metrology. *Sensors*, 11(2):2195–2245, 2011.
- [71] A.S. Alexandrova, V. Tzoganis, and C.P. Welsch. Self-mixing diode laser interferometry for velocity measurements of different targets. In *SPIE Photonics Europe*, pages 91412C–91412C. International Society for Optics and Photonics, 2014.
- [72] A.S. Alexandrova, V. Tzoganis, and C.P. Welsch. Laser diode self-mixing interferometry for velocity measurements. *Optical Engineering*, 54(3):034104, 2015. doi: 10.1117/1.OE.54.3.034104. URL <http://dx.doi.org/10.1117/1.OE.54.3.034104>.
- [73] S. Burgmann, N. Van der Schoot, C. Asbach, J. Wartmann, and R. Lindken. Analysis of tracer particle characteristics for micro piv in wall-bounded gas flows. *La houille blanche*, (4):55–61, 2011.
- [74] A. Melling. Tracer particles and seeding for particle image velocimetry. *Measurement Science and Technology*, 8(12):1406, 1997.
- [75] N. Schunk and K. Petermann. Stability analysis for laser diodes with short external cavities. *Photonics Technology Letters, IEEE*, 1(3):49–51, March 1989. ISSN 1041-1135. doi: 10.1109/68.87893.
- [76] R.P. Green, J.-H. Xu, L. Mahler, A. Tredicucci, F. Beltram, G. Giuliani, H.E. Beere, and D.A. Ritchie. Linewidth enhancement factor of terahertz quantum cascade lasers. *Applied Physics Letters*, 92(7):071106, 2008. doi: <http://dx.doi.org/10.1063/1.2883950>. URL <http://scitation.aip.org/content/aip/journal/apl/92/7/10.1063/1.2883950>.
- [77] T. Taimre, M. Nikolić, K. Bertling, Y.L. Lim, T. Bosch, and A.D. Rakić. Laser feedback interferometry: a tutorial on the self-mixing effect for coherent sensing. *Advances in Optics and Photonics*, 7(3):570–631, 2015.
- [78] J.W. Strutt. On the transmission of light through an atmosphere containing small particles in suspension, and on the origin of the blue of the sky. In *Scientific Papers*, volume 4, pages 397–405. Cambridge University Press, 2009. ISBN 9780511703997. URL <http://dx.doi.org/10.1017/CB09780511703997.052>. Cambridge Books Online.
- [79] G. Mie. Beitrge zur optik trber medien, speziell kolloidaler metallungen. *Annalen der Physik*, 330(3):377–445, 1908. ISSN 1521-3889. doi: 10.1002/andp.19083300302. URL <http://dx.doi.org/10.1002/andp.19083300302>.
- [80] H.C. Hulst and H.C. van de Hulst. *Light Scattering by Small Particles*. Dover Books on Physics. Dover Publications, 1957. ISBN 9780486642284. URL <https://books.google.co.uk/books?id=PlHfPMVAFRcC>.

- [81] P.A. Webb. A primer on particle sizing by static laser light scattering. In *Micro-metrics: Technical workshop series*, 2000.
- [82] C.F. Bohren and D.R. Huffman. *Absorption and scattering of light by small particles*. John Wiley & Sons, 2008.
- [83] C. Mätzler. MatLab functions for Mie scattering and absorption, version 2. *IAP Res. Rep*, 8, 2002.
- [84] M.E. Milham. Electromagnetic scattering by magnetic spheres: Theory and algorithms. Technical report, DTIC Document, 1994.
- [85] R.J. Tarento, K.H. Bennemann, P. Joyes, and J. Van de Walle. Mie scattering of magnetic spheres. *Physical Review E*, 69(2):026606, 2004.
- [86] Milton Kerker. *The scattering of light and other electromagnetic radiation: physical chemistry: a series of monographs*, volume 16. Academic press, 2013.
- [87] Shermila Brito Singham and Craig F Bohren. Light scattering by an arbitrary particle: a physical reformulation of the coupled dipole method. *Optics Letters*, 12(1):10–12, 1987.
- [88] M. Bass and Optical Society of America. *Handbook of Optics: Fundamentals, techniques, and design*. Number v. 1 in Handbook of Optics. McGraw-Hill, 1995. ISBN 9780070477407. URL <https://books.google.co.uk/books?id=igNLAQAATAAJ>.
- [89] K. Otsuka. Self-mixing thin-slice solid-state laser Doppler velocimetry with much less than one feedback photon per Doppler cycle. *Optics letters*, 40(20):4603–4606, 2015.
- [90] W. L. David and W.R. Hunter. Comments on the optical constants of metals and an introduction to the data for several metals. In E.D. Palik, editor, *Handbook of Optical Constants of Solids*, pages 275 – 367. Academic Press, Boston, 1985. ISBN 978-0-08-054721-3. doi: <http://dx.doi.org/10.1016/B978-0-08-054721-3.50017-4>. URL <http://www.sciencedirect.com/science/article/pii/B9780080547213500174>.
- [91] M. Pelton and G.W. Bryant. *Introduction to Metal-Nanoparticle Plasmonics*. A Wiley-Science Wise Co-Publication. Wiley, 2013. ISBN 9781118583043. URL <https://books.google.co.uk/books?id=Df-1t3eqo-kC>.
- [92] Xiaofeng Fan, Weitao Zheng, and David J Singh. Light scattering and surface plasmons on small spherical particles. *Light: Science & Applications*, 3(6):e179, 2014.
- [93] M.L. Brongersma and P.G. Kik. *Surface plasmon nanophotonics*. Springer, 2007.

- [94] B. Luk'yanchuk, N.I. Zheludev, S.A. Maier, N.J. Halas, P. Nordlander, H. Giessen, and C.T. Chong. The Fano resonance in plasmonic nanostructures and metamaterials. *Nature materials*, 9(9):707–715, 2010.
- [95] H. Kuwata, H. Tamaru, K. Esumi, and K. Miyano. Resonant light scattering from metal nanoparticles: Practical analysis beyond Rayleigh approximation. *Applied physics letters*, 83(22):4625–4627, 2003.
- [96] E. Petryayeva and U.J. Krull. Localized surface plasmon resonance: Nanostructures, bioassays and biosensing. *Analytica chimica acta*, 706(1):8–24, 2011.
- [97] A.A. Kokhanovsky. *Light Scattering Reviews 8: Radiative transfer and light scattering*. Springer Praxis Books. Springer Berlin Heidelberg, 2013. ISBN 9783642321061. URL <https://books.google.co.uk/books?id=SR5EAAAAQBAJ>.
- [98] M.I. Mishchenko, L.D. Travis, and A.A. Lacis. *Scattering, Absorption, and Emission of Light by Small Particles*. Cambridge University Press, 2002. ISBN 9780521782524. URL [https://books.google.co.uk/books?id=i6r1YFyK\\_g8C](https://books.google.co.uk/books?id=i6r1YFyK_g8C).
- [99] Steven C Hill and Robert E Benner. Morphology-dependent resonances. *Optical Effects Associated with Small Particles. Edited by CHANG RK ET AL. Published by World Scientific Publishing Co. Pte. Ltd., 1988. ISBN# 9789814415804, pp. 1-61*, pages 1–61, 1988.
- [100] Y.H. Fu, A.I. Kuznetsov, A.E. Miroshnichenko, Y.F. Yu, and B. Lukyanchuk. Directional visible light scattering by silicon nanoparticles. *Nature communications*, 4:1527, 2013.
- [101] W. Martienssen and E. Spiller. Coherence and fluctuations in light beams. *American Journal of Physics*, 32:919–926, 1964.
- [102] F.T. Arecchi. Measurement of the statistical distribution of Gaussian and laser sources. *Physical Review Letters*, 15(24):912, 1965.
- [103] F.T. Arecchi, M. Giglio, and U. Tartari. Scattering of coherent light by a statistical medium. *Physical Review*, 163(1):186, 1967.
- [104] N.A. Clark, J.H. Lunacek, and G.B. Benedek. A study of Brownian motion using light scattering. *Am. J. Phys*, 38(5):575–585, 1970.
- [105] G.B. Benedek. Brandeis university summer institute in theoretical physics. 1968.
- [106] F.T. Arecchi. Quantum optics, 1969.
- [107] L.E. Estes, L.M. Narducci, and R.A. Tuft. Scattering of light from a rotating ground glass. *JOSA*, 61(10):1301–1306, 1971.

- [108] Laser Components. Laser diode datasheet, 2012. URL [http://www.lasercomponents.com/fileadmin/user\\_upload/home/Datasheets/pd\\_ld/cwdm13-16.pdf](http://www.lasercomponents.com/fileadmin/user_upload/home/Datasheets/pd_ld/cwdm13-16.pdf). original document from laser components on photodiodes.
- [109] F. De Lucia, M. Putignano, S. Ottonelli, M. Di Vietro, M. Dabbicco, and G. Scarmario. Laser-self-mixing interferometry in the Gaussian beam approximation: experiments and theory. *Optics express*, 18(10):10323–10333, 2010.
- [110] C. Li, Z. Huang, and X. Sun. Infrasonic detection by laser diode self-mixing interferometry. *Chinese Optics Letters*, 11(2):021201, 2013.
- [111] S. Matsuura, M. Tani, and K. Sakai. Generation of coherent terahertz radiation by photomixing in dipole photoconductive antennas. *Applied Physics Letters*, 70(5):559–561, 1997.
- [112] FEMTO. Variable gain high speed current amplifier datasheet dhpca-100, 2015. URL [https://www1.aps.anl.gov/files/download/DET/Detector-Pool/Electronics/Amplifiers/dhpca-100\\_r9\\_Datasheet.pdf](https://www1.aps.anl.gov/files/download/DET/Detector-Pool/Electronics/Amplifiers/dhpca-100_r9_Datasheet.pdf).
- [113] M. Hoffmann. Digital signal processing mathematics. 2008.
- [114] K.M.M. Prabhu. *Window Functions and Their Applications in Signal Processing*. CRC Press, 2013. ISBN 9781466515840.
- [115] Texas Instruments. Opt101 monolithic photodiode and single-supply transimpedance amplifier, 2016. URL <http://www.ti.com/lit/ds/symlink/opt101.pdf>.
- [116] Arduino. Arduino/genuino uno microcontroller board based on the atmega328p, 2016. URL <https://www.arduino.cc/en/Main/ArduinoBoardUno>.
- [117] A. Chao and M. Tigner. *Handbook of Accelerator Physics and Engineering*. Handbook of Accelerator Physics and Engineering. World Scientific, 1999. ISBN 9789810235000.
- [118] R. Nagimov, P. Harmer, D. Kishi, A. Koveshnikov, R. Laxdal, H. Liu, and N. Muller. The cryogenic infrastructure for srf testing at triumph. In *17th International Conference on RF Superconductivity (SRF2015), Whistler, BC, Canada, Sept. 13-18, 2015*, pages 919–922. JACOW, Geneva, Switzerland, 2015.
- [119] W. Liao, S. Chang, W. Chiou, P. Chuang, F. Hsiao, H. Li, T. Lin, and H. Tsai. Development of separator cooling system for helium. In *7th International Particle Accelerator Conference (IPAC'16), Busan, Korea, May 8-13, 2016*, pages 1209–1211. JACOW, Geneva, Switzerland, 2016.

- [120] S. Ghosh, R. Mehta, G.K. Chowdhury, A. Rai, P. Patra, B.K. Sahu, A. Pandey, D.S. Mathuria, J. Chacko, A. Chowdhury, et al. Superconducting LINAC at inter-university accelerator centre: operational challenges and solutions. *Physical Review Special Topics-Accelerators and Beams*, 12(4):040101, 2009.
- [121] T.M. Page, J. DiMarco, Y. Huang, D.F. Orris, M.A. Tartaglia, I. Terechkin, and J.C. Tompkins. HINS superconducting lens and cryostat performance. *IEEE Transactions on Applied Superconductivity*, 19(3):1356–1359, 2009.
- [122] ESS. Target for ess neutrons source, 2016. URL <https://europeanspallationsource.se/target>. European Spallation Source technology information.
- [123] M.-C. Michalski, V. Briard, and F. Michel. Optical parameters of milk fat globules for laser light scattering measurements. *Le Lait*, 81(6):787–796, 2001.
- [124] P. Walstra. *Dairy Technology: Principles of Milk Properties and Processes*. Food Science and Technology. Taylor & Francis, 2013. ISBN 9780824746414.
- [125] D. Sholl and J.A. Steckel. *Density Functional Theory: A Practical Introduction*. Wiley, 2011. ISBN 9781118211045. URL [https://books.google.co.uk/books?id=\\_f994dmAdv0C](https://books.google.co.uk/books?id=_f994dmAdv0C).
- [126] Jacqueline Lenoble et al. *Radiative transfer in scattering and absorbing atmospheres: standard computational procedures*, volume 1. A. Deepak Hampton, VA, 1985.
- [127] S. Sudo, Y. Miyasaka, K. Nemoto, K. Kamikariya, and K. Otsuka. Detection of small particles in fluid flow using a self-mixing laser. *Optics express*, 15(13):8135–8145, 2007.
- [128] A.M. Wazwaz. *A First Course in Integral Equations*. World Scientific, 1997. ISBN 9789810231019.
- [129] A.W. Chao, K.H. Mess, M. Tigner, and F. Zimmermann. *Handbook of accelerator physics and engineering*. World scientific, 2013.
- [130] K.R. Kim, H.G. Kim, B.H. Lee, H.S. Han, C.W. Chung, Y.C. Kim, and I.S. Ko. Operational experience of cooling water systems for accelerator components at PLS. In *Proceedings of the 2005 Particle Accelerator Conference*, pages 850–852. IEEE, 2005.
- [131] R. Kato, S. Isaka, H. Sakaki, S. Kashiwagi, and G. Isoyama. Stability analysis of the rf linac based on an ar model. *Nuclear Instruments and Methods in Physics Research Section A: Accelerators, Spectrometers, Detectors and Associated Equipment*, 528(1):244–248, 2004.

- [132] E.J. Minehara, M. Sawamura, and R. Hajima. *Free Electron Lasers 2003: Proceedings of the 25th International Free Electron Laser Conference and the 10th FEL Users Workshop, Tsukuba, Ibaraki, Japan, 8-12 September 2003*. Newnes, 2012.
- [133] A. Kasugai, K. Sakamoto, R. Minami, K. Takahashi, and T. Imai. Study of millimeter wave high-power gyrotron for long pulse operation. *Nuclear Instruments and Methods in Physics Research Section A: Accelerators, Spectrometers, Detectors and Associated Equipment*, 528(1):110–114, 2004.
- [134] K. Floettmann, V. Paramonov, A. Skasyrskaya, and F. Stephan. Rf gun cavities cooling regime study. *TESLA-FEL Report*, 2, 2008.
- [135] D.C. Nguyen, P.L. Colestock, S.S. Kurennoy, D.E. Rees, A.H. Regan, S. Russell, D.L. Schrage, R.L. Wood, L.M. Young, and T. Schultheiss. Overview of the 100ma average-current rf photoinjector. *Nuclear Instruments and Methods in Physics Research Section A: Accelerators, Spectrometers, Detectors and Associated Equipment*, 528(1):71–77, 2004.
- [136] A. Jaworek. Micro-and nanoparticle production by electrospaying. *Powder technology*, 176(1):18–35, 2007.
- [137] J. Shiea, M. Huang, H. HSu, C. Lee, C. Yuan, I. Beech, and J. Sunner. Electrospay-assisted laser desorption/ionization mass spectrometry for direct ambient analysis of solids. *Rapid Communications in Mass Spectrometry*, 19(24):3701–3704, 2005.
- [138] C.N. McEwen, R.G. McKay, and B.S. Larsen. Analysis of solids, liquids, and biological tissues using solids probe introduction at atmospheric pressure on commercial LC/MS instruments. *Analytical Chemistry*, 77(23):7826–7831, 2005.
- [139] B. Gassend, L.F. Velasquez-Garcia, A.I. Akinwande, and M. Martinez-Sanchez. A microfabricated planar electrospay array ionic liquid ion source with integrated extractor. *Journal of Microelectromechanical Systems*, 18(3):679–694, 2009.
- [140] W. Schöllkopf, S. Gewinner, H. Junkes, A. Paarmann, G. von Helden, H. Bluem, and A. Todd. The new ir and thz fel facility at the fritz haber institute in berlin. In *SPIE Optics+ Optoelectronics*, pages 95121L–95121L. International Society for Optics and Photonics, 2015.
- [141] F. Stienkemeier and K.K. Lehmann. Spectroscopy and dynamics in helium nanodroplets. *Journal of Physics B: Atomic, Molecular and Optical Physics*, 39(8):R127, 2006.
- [142] G. Scoles et al. *Atomic and molecular beam methods*, volume 1. Oxford university press New York, 1988.

- [143] R.E. Smalley, L. Wharton, and D.H. Levy. Molecular optical spectroscopy with supersonic beams and jets. *Accounts of Chemical Research*, 10(4):139–145, 1977.
- [144] V. Rozhansky, I. Senichenkov, I. Veselova, D. Morozov, and R. Schneider. Penetration of supersonic gas jets into a tokamak. *Nuclear fusion*, 46(2):367, 2006.
- [145] J. Ullrich, R. Moshhammer, R. Dörner, O. Jagutzki, V. Mergel, H. Schmidt-Böcking, and L. Spielberger. Recoil-ion momentum spectroscopy. *Journal of Physics B: Atomic, Molecular and Optical Physics*, 30(13):2917, 1997.
- [146] J. Ullrich, R. Moshhammer, A. Dorn, R. Dörner, L.P.H. Schmidt, and H. Schmidt-Böcking. Recoil-ion and electron momentum spectroscopy: reaction-microscopes. *Reports on Progress in Physics*, 66(9):1463, 2003. URL <http://stacks.iop.org/0034-4885/66/i=9/a=203>.
- [147] S.C. Morris and J.F. Foss. Transient thermal response of a hot-wire anemometer. *Measurement science and technology*, 14(3):251, 2003.
- [148] D. Tiedemann, K.E. Stiebing, D.F.A. Winters, W. Quint, V. Varentsov, A. Warczak, A. Malarz, and T. Stöhlker. A pulsed supersonic gas jet target for precision spectroscopy at the HITRAP facility at GSI. *Nuclear Instruments and Methods in Physics Research Section A: Accelerators, Spectrometers, Detectors and Associated Equipment*, 764:387–393, 2014.
- [149] M. Reponen, I.D. Moore, I. Pohjalainen, T. Kessler, P. Karvonen, J. Kurpeta, B. Marsh, S. Piszczek, V. Sonnenschein, and J. Äystö. Gas jet studies towards an optimization of the IGISOL LIST method. *Nuclear Instruments and Methods in Physics Research Section A: Accelerators, Spectrometers, Detectors and Associated Equipment*, 635(1):24–34, 2011.
- [150] K. Luria, N. Lavie, and U. Even. Dielectric barrier discharge source for supersonic beams. *Review of Scientific Instruments*, 80(10):104102, 2009.
- [151] A. Ieshkin, Y. Ermakov, V. Chernysh, I. Ivanov, I. Kryukov, K. Alekseev, N. Kargin, and Z. Insepov. Computer simulation and visualization of supersonic jet for gas cluster equipment. *Nuclear Instruments and Methods in Physics Research Section A: Accelerators, Spectrometers, Detectors and Associated Equipment*, 795:395–398, 2015.
- [152] K. Luria, W. Christen, and U. Even. Generation and propagation of intense supersonic beams. *The Journal of Physical Chemistry A*, 115(25):7362–7367, 2011.
- [153] R.A. Smith, T. Ditmire, and J.W.G. Tisch. Characterization of a cryogenically cooled high-pressure gas jet for laser/cluster interaction experiments. *Review of scientific instruments*, 69(11):3798–3804, 1998.

- [154] A. Donges and R. Noll. *Laser Measurement Technology: Fundamentals and Applications*. Springer Series in Optical Sciences. Springer Berlin Heidelberg, 2014. ISBN 9783662436349.
- [155] Z. Zhang. *LDA Application Methods: Laser Doppler Anemometry for Fluid Dynamics*. Experimental Fluid Mechanics. Springer, 2010. ISBN 9783642135149.
- [156] G.S. Settles. *Schlieren and shadowgraph techniques: visualizing phenomena in transparent media*. Springer Science & Business Media, 2012.
- [157] F. Favela, L. Acosta, E. Andrade, V. Araujo, A. Huerta, O.G. de Lucio, G. Murillo, M.E. Ortiz, R. Policroniades, P. Santa Rita, et al. New supersonic gas jet target for low energy nuclear reaction studies. *Physical Review Special Topics-Accelerators and Beams*, 18(12):123502, 2015.
- [158] M.G. Allen. Diode laser absorption sensors for gas-dynamic and combustion flows. *Measurement Science and Technology*, 9(4):545, 1998.
- [159] H. Li, A. Farooq, J.B. Jeffries, and R.K. Hanson. Near-infrared diode laser absorption sensor for rapid measurements of temperature and water vapor in a shock tube. *Applied Physics B*, 89(2-3):407–416, 2007.
- [160] G. Giuliani, M. Norgia, S. Donati, and T. Bosch. Laser diode self-mixing technique for sensing applications. *Journal of optics. A, Pure and applied optics*, 4(6):S283–S294, 2002.
- [161] C.E. Clayton, J.E. Ralph, F. Albert, R.A. Fonseca, S.H. Glenzer, C. Joshi, W. Lu, K.A. Marsh, S.F. Martins, W.B. Mori, et al. Self-guided laser wakefield acceleration beyond 1 GeV using ionization-induced injection. *Physical review letters*, 105(10):105003, 2010.
- [162] J. Panda and R.G. Seasholtz. Velocity and temperature measurement ins supersonic free jets using spectrally resolved rayleigh scattering. 1999.
- [163] V. Tzoganis and C.P. Welsch. A non-invasive beam profile monitor for charged particle beams. *Applied Physics Letters*, 104(20):204104, 2014.
- [164] Y. Kudryavtsev, R. Ferrer, M. Huyse, P. Van den Bergh, and P. Van Duppen. The in-gas-jet laser ion source: Resonance ionization spectroscopy of radioactive atoms in supersonic gas jets. *Nuclear Instruments and Methods in Physics Research Section B: Beam Interactions with Materials and Atoms*, 297:7–22, 2013.
- [165] K. Schmid. *Laser Wakefield Electron Acceleration: A Novel Approach Employing Supersonic Microjets and Few-Cycle Laser Pulses*. Springer Theses. Springer Berlin Heidelberg, 2011. ISBN 9783642199509.

- [166] D.R. Swenson, E. Degenkolb, and Z. Insepov. Study of gas cluster ion beam surface treatments for mitigating rf breakdown. *Physica C: Superconductivity*, 441(1):75–78, 2006.
- [167] R. Dörner, V. Mergel, O. Jagutzki, L. Spielberger, J. Ullrich, R. Moshhammer, and H. Schmidt-Böcking. Cold target recoil ion momentum spectroscopy: a momentum microscope to view atomic collision dynamics. *Physics Reports*, 330(2):95–192, 2000.
- [168] B.A. Marsh. Resonance ionization laser ion sources for on-line isotope separators. *Review of Scientific Instruments*, 85(2):02B923, 2014.
- [169] Y. Kudryavtsev, T.E. Cocolios, J. Gentens, M. Huyse, O. Ivanov, D. Pauwels, T. Sonoda, P. Van den Bergh, and P. Van Duppen. Dual chamber laser ion source at LISOL. *Nuclear Instruments and Methods in Physics Research Section B: Beam Interactions with Materials and Atoms*, 267(17):2908–2917, 2009.
- [170] A. Grudiev, S. Calatroni, and W. Wuensch. New local field quantity describing the high gradient limit of accelerating structures. *Phys. Rev. ST Accel. Beams*, 12:102001, Oct 2009. doi: 10.1103/PhysRevSTAB.12.102001. URL <http://link.aps.org/doi/10.1103/PhysRevSTAB.12.102001>.
- [171] J. Faure, Y. Glinec, A. Pukhov, S. Kiselev, S. Gordienko, E. Lefebvre, J.-P. Rousseau, F. Burgy, and V. Malka. A laser-plasma accelerator producing monoenergetic electron beams. *Nature*, 431(7008):541–544, September 2004. ISSN 0028-0836. URL <http://dx.doi.org/10.1038/nature02963>.
- [172] C. Rechatin, J. Faure, A. Ben-Ismaïl, J. Lim, R. Fitour, A. Specka, H. Videau, A. Tafzi, F. Burgy, and V. Malka. Controlling the phase-space volume of injected electrons in a laser-plasma accelerator. *Phys. Rev. Lett.*, 102:164801, Apr 2009. doi: 10.1103/PhysRevLett.102.164801. URL <http://link.aps.org/doi/10.1103/PhysRevLett.102.164801>.
- [173] T. Hosokai, K. Kinoshita, A. Zhidkov, K. Nakamura, T. Watanabe, T. Ueda, H. Kotaki, M. Kando, K. Nakajima, and M. Uesaka. Effect of a laser prepulse on a narrow-cone ejection of MeV electrons from a gas jet irradiated by an ultrashort laser pulse. *Phys. Rev. E*, 67:036407, Mar 2003. doi: 10.1103/PhysRevE.67.036407. URL <http://link.aps.org/doi/10.1103/PhysRevE.67.036407>.
- [174] K. Nakajima, D. Fisher, T. Kawakubo, H. Nakanishi, A. Ogata, Y. Kato, Y. Kitagawa, R. Kodama, K. Mima, H. Shiraga, K. Suzuki, K. Yamakawa, T. Zhang, Y. Sakawa, T. Shoji, Y. Nishida, N. Yugami, M. Downer, and T. Tajima. Observation of ultrahigh gradient electron acceleration by a self-modulated intense short laser pulse. *Phys. Rev. Lett.*, 74:4428–4431, May 1995. doi: 10.1103/PhysRevLett.74.4428. URL <http://link.aps.org/doi/10.1103/PhysRevLett.74.4428>.

- [175] M. Mirzaie, N.A. Hafz, S. Li, T. Sokollik, F. He, Y. Cheng, Z. Sheng, and J. Zhang. Enhanced electron yield from a laser-plasma accelerator using high-Z gas jet targets. *arXiv preprint arXiv:1410.2325*, 2014.
- [176] C. McGuffey, A.G.R. Thomas, W. Schumaker, T. Matsuoka, V. Chvykov, F.J. Dollar, G. Kalintchenko, V. Yanovsky, A. Maksimchuk, K. Krushelnick, V. Bychenkov, I.V. Glazyrin, and A.V. Karpeev. Ionization induced trapping in a laser wakefield accelerator. *Phys. Rev. Lett.*, 104:025004, Jan 2010. doi: 10.1103/PhysRevLett.104.025004. URL <http://link.aps.org/doi/10.1103/PhysRevLett.104.025004>.
- [177] M. Mori, K. Kondo, Y. Mizuta, M. Kando, H. Kotaki, M. Nishiuchi, M. Kado, A.S. Pirozhkov, K. Ogura, H. Sugiyama, S.V. Bulanov, K.A. Tanaka, H. Nishimura, and H. Daido. Generation of stable and low-divergence 10-MeV quasimonoeenergetic electron bunch using argon gas jet. *Phys. Rev. ST Accel. Beams*, 12:082801, Aug 2009. doi: 10.1103/PhysRevSTAB.12.082801. URL <http://link.aps.org/doi/10.1103/PhysRevSTAB.12.082801>.
- [178] P. Forck et al. Minimal invasive beam profile monitors for high intense hadron beams. *IPAC10*, page 1261, 2010.
- [179] M. Putignano, K.-U. Kühnel, C.-D. Schröter, and C.P. Welsch. A fast, low perturbation ionization beam profile monitor based on a gas-jet curtain for the ultra low energy storage ring. *Hyperfine Interactions*, 194(1-3):189–193, 2009. doi: 10.1007/s10751-009-0049-y. URL <http://dx.doi.org/10.1007/s10751-009-0049-y>.
- [180] M. Putignano and C.P. Welsch. Numerical study on the generation of a planar supersonic gas-jet. *Nuclear Instruments and Methods in Physics Research Section A: Accelerators, Spectrometers, Detectors and Associated Equipment*, 667(0):44 – 52, 2012. ISSN 0168-9002. doi: <http://dx.doi.org/10.1016/j.nima.2011.11.054>. URL <http://www.sciencedirect.com/science/article/pii/S0168900211020961>.
- [181] V. Tzoganis, A. Jeff, and C.P. Welsch. Gas dynamics considerations in a non-invasive profile monitor for charged particle beams. *Vacuum*, 109(0): 417 – 424, 2014. ISSN 0042-207X. doi: <http://dx.doi.org/10.1016/j.vacuum.2014.07.009>. URL <http://www.sciencedirect.com/science/article/pii/S0042207X14002450>.
- [182] V. Tzoganis and C.P. Welsch. A non-invasive beam profile monitor for charged particle beams. *Applied Physics Letters*, 104(20):204104, 2014. doi: <http://dx.doi.org/10.1063/1.4879285>. URL <http://scitation.aip.org/content/aip/journal/apl/104/20/10.1063/1.4879285>.

- [183] H. Zhang, A. Alexandrova, A. Jeff, V. Tzoganis, and C. Welsch. Characterizing supersonic gas jet-based beam profile monitors. In *7th International Particle Accelerator Conference (IPAC'16), Busan, Korea, May 8-13, 2016*, pages 357–360. JACOW, Geneva, Switzerland, 2016.
- [184] A. Alexandrova and C.P. Welsch. Laser diode velocimeter-monitor based on self-mixing technique. *Proc. IBIC, Oxford, UK*, 2013.
- [185] LewVac. Fibre optics: Feedthrough, cables and accesories, 2015. URL [http://www.lewvac.co.uk/index\\_files/section%202.pdf](http://www.lewvac.co.uk/index_files/section%202.pdf). original document from LewVac.
- [186] R.J. Tilley. *Colour and the optical properties of materials: an exploration of the relationship between light, the optical properties of materials and colour*. John Wiley & Sons, 2010.
- [187] C. Kittel. *Introduction to solid state physics*. Wiley, 2005.
- [188] S.W. James, R.P. Tatam, and R.L. Elder. Design considerations for a three dimensional fiber optic laser doppler velocimeter for turbomachinery applications. *Review of scientific instruments*, 68(8):3241–3246, 1997.
- [189] H.D. Vom Stein and H.J. Pfeifer. A Doppler difference method for velocity measurements. *Metrologia*, 5(2):59, 1969.
- [190] A. Alexandrova and C.P. Welsch. Beam characterisation using laser self-mixing. In *IBIC*, 2015.
- [191] A. Alexandrova and C.P. Welsch. Laser diode self-mixing technique for liquid velocimetry. *Nuclear Instruments and Methods in Physics Research Section A: Accelerators, Spectrometers, Detectors and Associated Equipment*, 2016.
- [192] H.C. Man, J. Duan, and T.M. Yue. Design and characteristic analysis of supersonic nozzles for high gas pressure laser cutting. *Journal of Materials Processing Technology*, 63(1):217–222, 1997.
- [193] A. Zaitsev, O. Kovalev, A. Malikov, A. Orishich, and V. Shulyatyev. Laser cutting of thick steel sheets using supersonic oxygen jets. *Quantum Electronics*, 37(9):891, 2007.
- [194] M. Nishida, T. Nakagawa, and H. Kobayashi. Density contours of a supersonic free jet. *Experiments in Fluids*, 3(3):181–183, 1985. ISSN 0723-4864. doi: 10.1007/BF00280458. URL <http://dx.doi.org/10.1007/BF00280458>.
- [195] E. Chehura, C.C. Ye, and R.P. Tatam. In-line laser doppler velocimeter using fibre-optic Bragg grating interferometric filters. *Measurement Science and Technology*, 14(6):724, 2003.

- 
- [196] D.G. Jang, Y.S. You, H.M. Milchberg, H. Suk, and K.Y. Kim. All-optical characterization of cryogenically cooled argon clusters in continuous gas jets. *Applied Physics Letters*, 105(2):021906, 2014.